THE UNIVERSITY *of* EDINBURGH

Investigating Excited Electronic States in Fullerenes and Polycyclic Aromatic Hydrocarbons using Femtosecond Laser Photoelectron Spectroscopy

Elvira Bohl

Degree of Doctor of Philosophy

The University of Edinburgh

2016

Abstract

Fullerenes have highly excited electronic states with interesting properties for possible wide ranging applications including in electronics. These highly excited, Rydberg-like states, so-called superatom molecular orbitals (SAMOs), are diffuse low-angular momenta states with molecular orbitals centred on the hollow fullerene core. The SAMOs can be detected by femtosecond photoelectron spectroscopy (PES) and characterised by photoelectron angular distributions (PADs) combined with time-dependent density functional theory (TD-DFT) calculations. The photoelectron spectra of C_{60} and C_{70} show a peak structure below kinetic energies corresponding to the photon energy, superimposed on a thermal electron background. This peak structure was assigned to one-photon ionisation of the SAMO states based on PAD and TD-DFT.

In this thesis, studies of the fullerene species C_{82} and $Sc_3N@C_{80}$ revealed PES and PAD with similar features to C_{60} and C_{70}. The SAMO peaks became less prominent compared to the thermal electron background for increasing molecular size and decreasing symmetry, and were almost absent for the endohedral species. To provide more information about the influence of encapsulated atoms in the fullerene cage on the SAMO states, experiments on $Li@C_{60}$ have been carried out. A lower thermal electron emission temperature and a splitting of the SAMO peaks has been observed for $Li@C_{60}$ compared to C_{60}. Nevertheless the binding energies are remarkably similar in all investigated fullerenes, which is important for any applications. Since the binding energies are about the same, but the ionisation potentials of the fullerenes are different, the excitation energy to the SAMOs scales with the ionisation energy.

The reasons for the well-pronounced peak structure of the SAMO states in the PES of C_{60} could be explained by the similarity of the SAMOs to Rydberg states along with the higher photoionisation probabilities compared to valence states which were modelled by Benoît Mignolet and Françoise Remacle. As the SAMOs are highly excited electronic states, like Rydberg states, the potential energy surface of the neutral molecule and the ionised molecule are similar. Therefore the vibrational energy is conserved in the molecule during the photoionisation on the femtosecond time scale. The TD-DFT calculations on C_{60}, carried out by Benoît Mignolet and Françoise Remacle, revealed the photoionisation probabilities of the SAMOs to be at least three orders of magnitude higher than for non-SAMOs for the applied experimental conditions. To test the prediction of the model, the relative photoionisation probabilities of the s-SAMO to p-SAMO and the s-SAMO to d-SAMO were obtained experimentally from the PES at various photon energies (2-3.5 eV) within this work. The analysis indicates remarkable agreement between the experiment and the theoretical values.

Further quantum chemical calculations on a series of polycyclic aromatic hydrocarbons (PAHs) were carried out within this thesis, which revealed similar Rydberg-like molecular orbitals in analogy to the SAMOs in fullerenes. The first series included benzene, naphthalene, anthracene, tetracene, pentacene

and hexacene. The second series consisted of phenanthrene, pyrene and coronene. Finally, the third series covered cubane, adamantane and dodecahedral C_{20}. All modelled molecules showed diffuse, excited electronic states similar to the SAMOs. Within each series the binding energies of these states decrease with increasing molecular size as well as the ionisation energies, except for the 3rd series. A comparison between all series shows that the binding energies of the states for the 3rd series (the 3-D series) are slightly higher than for the 1st and 2nd series in relation to similar molecular size. The results of the coronene calculations are compared to experimental photoelectron spectra and are shown to be in good agreement with the experiments.

Lay Summary

Fullerenes are molecules of carbon in the form of a hollow sphere, oval, tube and many other shapes. The buckminsterfullerene, C_{60}, resembles the shape of a ball such as used in football. The high symmetry of the C_{60} molecule enables theoretical calculations to be carried out on such a large system compared to an atom. These computational models can be compared to experimental studies to investigate the electronic structure of fullerenes. Since fullerenes are already being used in solar cells and other electronic applications, it is interesting to understand their electronic structure to be able to tune their physical properties in a desirable way.

Previous studies have revealed highly excited states in C_{60} with surprising molecular orbitals. These states were called superatom molecular orbitals (SAMOs) and are located over the whole C_{60} molecule with their centre on the hollow fullerene core. The lifetime of these SAMO states is quite short, so ultra-short laser pulses (10^{-15} second = 1 femtosecond, fs) have to be used to detect them. During the period of such a short fs laser pulse, the electrons of the fullerene molecule are excited into the SAMO states and also ionised out from the SAMOs. These ionised electrons (photoelectrons) can be detected by photoelectron spectroscopy. This method records the speed of the photoelectrons and their radial distribution as they are ejected from the molecule. Theoretical calculations can model the experimental results to enable the assignment of features in the photoelectron spectra (PES). The PES of the fullerenes, C_{60} and C_{70}, showed a peak structure superimposed on an exponentially decaying, thermal electron background. The peak structure was assigned to the SAMO states.

In this thesis, different fullerenes are studied to investigate the influence of molecular size, shape and symmetry or the encapsulation of an atom or molecule inside the fullerene cage on the electronic structure. The studied fullerene species C_{82} and the endohedral fullerene $Sc_3N@C_{80}$ (Sc_3N inside the C_{80} fullerene cage) showed similar features in the PES as C_{60} and C_{70}: a peak structure superimposed on a thermal electron background. However, the SAMO peaks became less prominent compared to the thermal electron background for increasing molecular size and decreasing symmetry, and were almost absent for $Sc_3N@C_{80}$. To get a better understanding of the effect of an encapsulated atom in the fullerene cage on the SAMO states, the endohedral fullerene $Li@C_{60}$ (lithium atom inside the C_{60} fullerene cage) has been analysed by photoelectron spectroscopy. Broader peaks for the SAMO states and a lower thermal electron background have been observed for $Li@C_{60}$ compared to the empty C_{60} fullerene cage. In conclusion the SAMO states can be made more accessible by reducing the ionisation potential (energy needed to ionise the molecule). The ionisation potential of the fullerenes can be tuned by variation of their molecular size or encapsulation of an atom, like for $Li@C_{60}$.

The probability of removing an electron from a SAMO state with respect to an electron from another SAMO state was analysed experimentally. These experimental results were in agreement with theoretical calculations carried out by Benoît Mignolet and Françoise Remacle. This agreement is remarkably consistent and shows the reliability of quantum chemistry computations (a certain type of theoretical calculations).

Theoretical calculations were also done on some smaller molecules than fullerenes with similar structural elements, but in a planar shape, not 3-D. These computations revealed similar SAMO states for the smaller molecules. Most of the results from this study could be matched well with experimental findings in the literature and experiments performed in this thesis.

Declaration

This work is original and my own unless otherwise stated by reference. This thesis has not been previously submitted for any degree at this or any other university.

Elvira Bohl

Publications

Johansson, J. O., Bohl, E., Henderson, G. G., Mignolet, B., Dennis, T. J. S., Remacle, F. & Campbell, E. E. B. Hot electron production and diffuse excited states in C_{70}, C_{82} and $Sc_3N@C_{80}$ characterised by angular-resolved photoelectron spectroscopy. *J. Chem. Phys.* **139,** 084309 (2013).

Bohl, E., Sokół, K. P., Mignolet, B., Thompson, J. O. F., Johansson, J. O., Remacle, F. & Campbell, E. E. B. Relative Photoionization Cross Sections of Super-Atom Molecular Orbitals (SAMOs) in C_{60}. *J. Phys. Chem. A* **119,** 11504–11508 (2015).

Johansson, J. O., Bohl, E. & Campbell, E. E. B. Super-Atom Molecular Orbital Excited States of Fullerenes. *Philos. Trans. R. Soc. A* **374,** 1–13 (2016).

The experimental work and data collection for C_{60}, C_{82} and $Sc_3N@C_{80}$ was conducted in collaboration with Olof Johansson, who built the initial experimental setup which was modified for the rest of the experimental work presented. Olof Johansson also analysed the C_{82} data.

Katarzyna Sokół and Olof Johansson participated and assisted for the investigation of the relative photoionisation probabilities on C_{60}.

In Loving Memory of my Beloved Father

Alexander Dulaschko

Acknowledgements

First of all, I would like to thank Professor Eleanor Campbell for giving me the opportunity to work on this project. She has been a great supervisor throughout my PhD by always having time to give advice and support when needed. I am also grateful for her guidance through ups and downs during the project. It has been a great experience to work on my PhD in Eleanor Campbell's group.

I want to thank Dr Olof Johansson for his detailed introduction to the experimental setup. I have really appreciated his guidance and advice, as well as his help during my work.

I am grateful that Professor Françoise Remacle and Dr Benoît Mignolet (both University of Liege) who have trained me in the theoretical techniques. They have given me the opportunity to visit them for one month to learn and conduct the quantum chemical calculations on the polycyclic aromatic hydrocarbons, which I am very thankful for. Also I want to thank Françoise Remacle and Benoît Mignolet for carrying out previous theoretical studies.

I like to acknowledge Dr David Rogers for his support on my theoretical calculations at Edinburgh, Dr Logan Mackay for helping to take the LD FT-ICR MS data and SIRCAMS: The Scottish Instrumentation and Resource Centre for Advanced Mass Spectrometry, Dr John S. Dennis (Queen Mary University of London) for providing the C_{82} sample.

Thanks to all members of Eleanor Campbell's group for the welcoming and enjoyable working environment. Dr Alexander Bulgakov, Professor Eleanor Campbell and Dr Olof Johansson for the instructive discussions about the cold trap which have helped me with the design. I also thank David Paden for building the cold trap. I thank Dr Andrei Gromov for his help with the sample preparation and other chemistry related procedures. Thanks to Nathan for his cheery company in the lab and office, also for his help and advice, to Arran for his calmness and optimism, to Luke for having nice chats and short distractions from writing.

I also want to thank Kirsten for her early advice on the final PhD years, Oleg for his advice on technical questions about the experimental setup, Kasia for helping me with the photoionisation probability work, James for his help writing a publication, and my fellow PhD students for the joyful coffee breaks, Physchem meetings and demonstrating sessions.

I like to thank my friends near and far, Justyna, Goscha, Steffi, Tina and Christian for their constant support, and especially Gareth for being there for me, understanding, proofreading, encouragement, support and much more. I am really thankful for being with you.

Finally, I want to thank my family, especially my father Alexander, my mother Maria and my brother Alexander. My father was always there for me and supported me. Higher education was important for

him, so he encouraged my brother and me in our educational path. He also assisted me to move to Edinburgh to start my PhD project and had supported me throughout these years. I am grateful for my mother's constant support and help. She has inspired me to follow my intellectual curiosity and to study chemistry. My brother has always supported me during my studies. He has helped me out whenever I needed him. I am really thankful for my family and I deeply appreciate them, as I could have not done this without my family. My thesis is dedicated to my father Alexander Dulaschko, my mother Maria Bohl and my brother Alexander Bohl.

Abbreviations and Acronyms

ATI	above threshold ionisation
BBO	β-barium borate crystal
BS	beam splitter
CCD	charged-coupled device
DFT	density functional theory
E_{bin}	(photo-)electron binding energy
E_{kin}	photoelectron kinetic energy
eV	electron volts
FHG	fourth harmonic generation
FT-ICR	Fourier transform ion cyclotron resonance
HOMO	highest occupied molecular orbital
IC	internal conversion
IP	ionisation potential
ISC	intersystem crossing
LD	laser desorption ionisation
LT-STM	low-temperature scanning tunnelling microscopy
LUMO	lowest unoccupied molecular orbital
MAE	multiple active electrons
MCPs	micro-channel plates
NMR	nuclear magnetic resonance
MO	molecular orbital
MPI	multiphoton ionisation

MS	mass spectrometry/spectrometer
NOPA	non-collinear optical parametric amplifier
PAD	photoelectron angular distribution
PAH	polycyclic aromatic hydrocarbon
PES	photoelectron spectrum/spectra/spectroscopy
REMPI	resonance-enhanced multiphoton ionisation
SAE	single active electron
SAMO	superatom molecular orbital
SHG	second harmonic generation
TD-DFT	time-dependent density functional theory
THG	third harmonic generation
Ti:Sapph	titanium-doped sapphire crystal
TOF	time-of-flight
U_p	ponderomotive shift
VMI	velocity map image/imaging
WLC	white-light continuum
XeVMI	velocity map image of xenon

Table of Content

1. Introduction

The fundamental understanding of the electronic structure and dynamics of molecules and molecular systems is important for the development of new materials with interesting properties for applications, like molecular electronics devices or solar cells.[1,2] Since fullerenes were discovered in 1985,[3] they have become important model systems for the investigation of the fundamental properties of large molecules because they only consist of carbon atoms and have a high symmetry, in particularly C_{60}.[4] Due to the high symmetry of fullerenes, theoretical calculations are simpler to conduct for these systems. Hence, the computed results can complement experimental measurements to draw conclusions from the findings. Furthermore, fullerenes can be chemically modified in a number of ways to tune their properties. For example, they can be synthesised to incorporate atoms or molecules inside the cage (endohedral fullerenes), or functional groups can be added to the outside of the cage (exohedral fullerenes) or the size of the molecule can be simply varied by increasing or reducing the number of carbon atoms. These variations will influence the electronic structure and allow the engineering of the electronic state energies. The manipulation of electronic states can decrease for example the HOMO-LUMO gap to make the molecules suitable for electronic applications.[5]

The properties of fullerenes and modified fullerenes have been investigated in many studies of isolated molecules in the gas phase.[4–15] The advantage of gas phase studies is the observation of molecular characteristics and behaviour without additional interactions like solvent effects, van der Waals interactions or hydrogen bridge bonds. Therefore, the comparison of corresponding calculations to experimental results is simpler as any perturbations are minimised. Furthermore, the molecules can be gradually modified to trace the change in their behaviour and in their electronic energies.

Conventional photoelectron spectroscopy (PES) in the gas phase requires molecules with low vibrational energy to obtain a clear signal or peaks without overlapping vibrational states.[16] However, it has been not possible to prepare single, cold and neutral fullerene molecules in gas phase without encapsulating the molecule in a helium droplet. In the case of the encapsulation interferences still exist between the fullerene molecule and the helium atoms, which influence the characteristics of the single fullerene molecule. For the cooling of a molecular beam of neutral fullerenes supersonic expansion or buffer gas cooling can be used, but during these processes clustering or aggregation occur, which prohibit the preparation of single, cold and neutral fullerene molecules in the gas phase. Single fullerene anions are easier to obtain in the gas phase for example by electrospray ionisation from a solution, however neutral fullerene molecules cannot be prepared using this technique.[17,18] Fortunately, the Rydberg Fingerprint Spectroscopy technique enables the detection of highly excited electronic states, like Rydberg states, in molecules with high vibrational energies. Since the Rydberg states have a similar potential energy surface as the ion, the vibrational energy is conserved during the photoionisation and no vibrational transitions are interfering.[19–22] Hence the Rydberg Fingerprint Spectroscopy technique is

insensitive to the vibrational excitation of the probed molecule. This method will be explained in more detail in chapter 1. 2.

Studies on the electronic structure of fullerenes in the gas phase revealed different excitation and ionisation mechanisms depending on the laser pulse duration and intensity, which will be discussed in detail in chapter 1. 5.[9,23] Hence, mass spectrometry (MS) and PES have been performed on fullerenes on a femtosecond timescale to investigate the processes after the photoionisation of the molecules with a laser pulse.[4,7,14,23–29] For laser excitations at low intensities (10^{10}-10^{13} W/cm^2), pulse durations in the range of 100 femtoseconds (1 fs = 10^{-15} s) and photon energies below the ionisation potential, IP, ($h\nu < IP$) a clear peak structure could be observed in the PES of C_{60}.[30] For longer laser pulses the peak structure becomes less pronounced and disappears for pulses longer than about 200 fs. First this peak structure was assigned to one-photon ionisation of Rydberg series with high orbital angular momenta l ($l \geq 3$).[30] However low-temperature scanning tunnelling microscopy (LT-STM) of C_{60} molecules on copper surfaces revealed highly excited hydrogen-atom-like molecular orbitals.[31] After further measurements and calculations the peaks at lower binding energies of lower-lying Rydberg states could be attributed to these superatom molecular orbitals (SAMOs).[7] The SAMOs have a significant electron density inside the hollow cage so an electron in an excited state is closer to other valence electrons than in a Rydberg state where the excited electron is far away from the molecule and other valence electrons.[31] These SAMO states are large diffuse orbitals which appear to be like hydrogen atomic orbitals.[32] Due to the spatial distribution of the SAMOs, they can form nearly-free-electron bands in aggregates which can be interesting for applications involving charge transfer.[31] The influence on the SAMO states by the modification of the fullerene cage has to be investigated, because the reduction of the energy gap between the HOMO and SAMO states would make the states more accessible for electronic applications.[5,33] Therefore, it is interesting to find out how the electronic structure of fullerenes can be manipulated.

Moreover, the population and ionisation mechanisms of the SAMO states are still unknown.[33] However, studies on smaller molecules than fullerenes will simplify the calculations of excited electronic states and enable computations of the electronic dynamics. In this context it is interesting that quantum chemical calculations of the highly excited states for smaller molecules like hydrocarbons, coronene and pentacene, show molecular orbitals located over the whole molecule in the shape of s, p and d orbitals similar to the SAMOs in fullerenes.[34] The results of previous theoretical studies on the binding energies and photoionisation probabilities for highly excited states of coronene and pentacene were carried out by Benoît Mignolet (University of Liege)[34] and will be discussed in detail in chapter 1. 1. Further theoretical studies on related polycyclic aromatic hydrocarbons (PAHs) combined with experimental measurements can verify these first computed results and reveal SAMO-like states in other PAHs molecules.

The main aim of this thesis is the investigation of the influence of molecular size and structure on SAMO states and the electronic structure in fullerenes. Therefore C_{82}, $Sc_3N@C_{80}$ and $Li@C_{60}$, two endohedral

fullerenes, are probed and the results are compared to previous findings for C_{60} and C_{70}.[7] Femtosecond PES is used to obtain information on the electronic structure of the molecules through the analysis of their photoionisation mechanisms. The fs timescale of the laser pulse enables the observation of the SAMOs, also with the use of the photoelectron angular distributions (PADs) the SAMOs can be characterised (see chapter 1. 4 and 1. 5). Since the population mechanism of the SAMO states is still unknown,[33] the relative photoionisation probabilities of the different SAMOs in C_{60} are analysed and put in comparison with theoretical calculations to get some insight into at the ionisation mechanism.[35] Furthermore, theoretical calculations of excited electronic states have been carried out on a series of PAHs and compared with experimental measurements of coronene, a studied molecule.

For understanding the approach to achieve the project aims, the theory behind the photoionisation mechanisms will be described with previous experiments from the literature at first, followed by a short introduction into the experimental techniques. Then the results from the literature about the gas phase studies on the ionisation mechanisms of fullerenes, in particular C_{60}, are discussed. Subsequently the findings of PES studies on the PAHs, anthracene and naphthalene, from the literature are introduced with a view to the investigation of coronene and pentacene. The next chapter describes the experimental and theoretical methods in detail which have been applied in this project. In the following chapters, the results and findings from this thesis are presented and discussed. Finally, an overall conclusion and an outlook of the project are provided.

1. 1. Photoionisation Mechanisms

In order to study the electronic structure of excited states in the gas phase, the photoionisation mechanisms of atoms and molecules can be probed. For obtaining information about these physical processes, which take place on a very short timescale, it is necessary to use experimental tools that respond on similar timescales. Laser pulses in the fs range are comparable to processes like molecular vibrations (10^{-15} fs) and energy relaxation in larger molecules and bulk solids (10^{-12} fs). Hence, it is important to know the background to the ionisation mechanisms of atoms and molecules in ultrashort, intense laser pulses.

The photoionisation mechanisms of atoms and molecules can be influenced by the electric field of an intense laser pulse. The coupling between an instantaneous laser field and an atom or molecule results in a shift of their energy levels, known as the AC Stark shift.[36] The AC Stark shift can be approximated by the ponderomotive energy, U_p, for the intensity and wavelength range typically used for these kind of experiments.[36] U_p is defined as the average kinetic energy of a free electron in a time varying electric field:

$$U_p = \left(\frac{E_0}{2\omega}\right)^2 = 9.34 \times 10^{-20} \times \lambda^2 \times I \quad \textbf{(1.1)}$$

Where E_0 is the amplitude of the laser electric field, ω is the angular frequency of the laser electric field, λ is the laser wavelength in nanometres (nm) and I is the laser intensity in Watts per square centimetre (W/cm^2). U_p has units of energy and in the case of equation (1.1), the unit is electron volts (eV). The ionisation mechanism for atoms in strong laser fields is determined by the ponderomotive energy of the laser at a certain wavelength and intensity, and the ionisation potential of the atom.[37] There are three ionisation mechanisms that are relevant when the photon energy is much lower than the ionisation potential. The Keldysh parameter, γ, is used to distinguish between these mechanisms:[38]

$$\gamma = \sqrt{\frac{IP}{2U_p}} \quad \textbf{(1.2)}$$

where IP is the ionisation potential. The Keldysh parameter, γ, can also be used to indicate ionisation mechanisms in molecules.[37,38]

For relatively low intensities the Keldysh parameter is larger than 1 ($\gamma > 1$), and direct multiphoton ionisation (MPI) occurs. An atom coherently absorbs the required number of photons to overcome the IP or it can absorb even more photons which is called above threshold ionisation (ATI).[38] This results in equidistant peaks in the PES which are separated by the photon energy.[39]

If intermediate resonances are involved in the ionisation process, the required photons do not need to be absorbed coherently. Therefore the ionisation probability is increased which is also known as resonance-enhanced multiphoton ionisation (REMPI). If no intermediate resonances are involved, the ionisation probability, P_I, is given by:

$$P_I \propto I^n \quad \textbf{(1.3)}$$

with I as the laser intensity and n as the number of photons required to reach the IP. In this description for the ionisation mechanism a single active electron (SAE) model is used. In a molecule like C_{60} experimental results and calculations indicate that more than one electron might be excited during the laser pulse (multiple active electrons, MAE) while elements of a SAE model still exist.[13,26,40] For convenience the following models are discussed for SAE.

For increasing laser intensities, where $\gamma \approx 1$, the ionisation barrier can be suppressed as the magnitude of the electric laser field becomes comparable to the binding potential of the electron. The electron can tunnel through the barrier if the tunnelling period is shorter than the laser period, which is called tunnelling ionisation.

For higher laser intensities, $\gamma < 1$, the laser electric field is strong enough to suppress the binding potential so the electron can classically escape from the potential well, which is known as over-the-barrier ionisation.

In the following chapters the presented spectra and results were obtained for laser intensities that were below the over-the-barrier ionisation threshold. Thus the photoelectrons carry information about their initial state which can help to characterise the occurring ionisation mechanisms.

1. 2. Rydberg Fingerprint Spectroscopy

Rydberg states in atoms or molecules are highly excited electronic states and have been observed in many atomic and molecular systems. The excited electrons are located in Rydberg orbitals with a large distance from the core of the molecule, so they experience the whole molecule like a single charge comparable to a pure coulomb potential in a hydrogen atom. The Rydberg orbitals of the molecules are derived from the electronic states of the hydrogen atom, where the binding energy of the electron, E_{bin}, depends only on the principal quantum number, n:

$$E_{bin} = \frac{Ry}{n^2} \tag{1.4}$$

where Ry is the Rydberg energy of 13.606 eV. The binding energy of a Rydberg electron is the energy difference between the bound electron and the electron at rest at an infinite distance from the ion core (Figure 1.1).

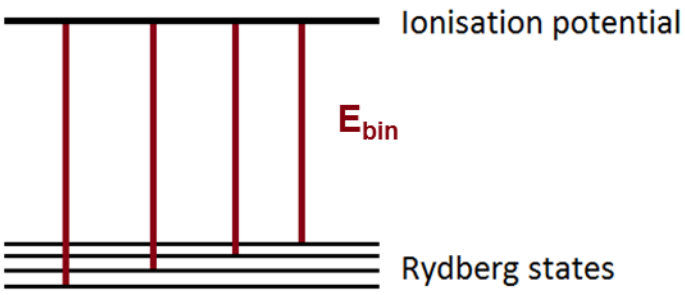

Figure 1.1: Schematic to show the binding energy of a Rydberg electron.

For atoms and molecules with more than one electron, the binding energies of the Rydberg states will deviate from equation (1.4). Due to the fact that the excited electrons have a probability to be near the ion core, they will experience a significantly different potential than from a single charge and therefore

a shift will be introduced to the pure coulomb potential. To a good approximation, the binding energy of a Rydberg electron is given by:

$$E_{bin} = \frac{Ry}{(n - \sigma_l)^2} \quad \textbf{(1.5)}$$

where σ_l is the quantum defect which is approximately constant for a given orbital angular momentum, l, but decreases for higher l.[20] Hence the binding energies of Rydberg electrons are based on the principal quantum number, n, and the quantum defect, σ_l. The quantum defect itself depends on the number and types of atoms in the ion core, their spatial arrangement, the distribution of the positive charge in the ion core, and the angular momentum state of the Rydberg orbital as the wave functions penetrate inner parts of the molecular core.[20,22] Therefore, the binding energies of Rydberg states are sensitive to the local distribution of charges, atoms, and functional groups which influence the charge distribution in the molecule that is experienced by the Rydberg electron.[20,22] Hence, the clear peaks in a spectrum of Rydberg states are characterised by different values of n and σ_l, which are used in the Rydberg Fingerprint Spectroscopy to analyse molecules (an example is given in Figure 1.2).[20,22]

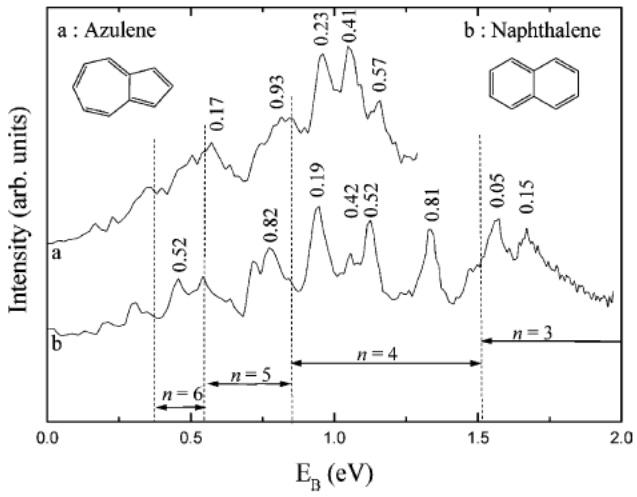

Figure 1.2: Rydberg Fingerprint PES of azulene, top trace, and naphthalene, bottom trace. The principal quantum number is shown at the bottom of the spectra and the quantum defect values are indicated on top of the major peaks. The figure is taken from ref.[22]

First the molecules are excited through single or multiphoton excitation into their Rydberg states and then probed by ionisation of the molecules.[22] The exact population mechanisms of highly excited states for different molecular systems is unknown, including for fullerenes, but in the case of fullerenes it is assumed to be a multiphoton excitation followed by efficient internal conversion (IC).[33] Therefore within one laser pulse the molecule absorbs coherently or non-coherently several photons and is raised into highly excited states.[22] Following excitation the absorbed energy is distributed over different Rydberg states through IC.[22] Subsequently the excited molecules are ionised through absorption of one additional photon and the excess energy is carried away by the photoelectron.[22] An important property

of ionising Rydberg states is the preservation of the vibrational energy from the neutral molecule in the ion (Figure 1.3).[41]

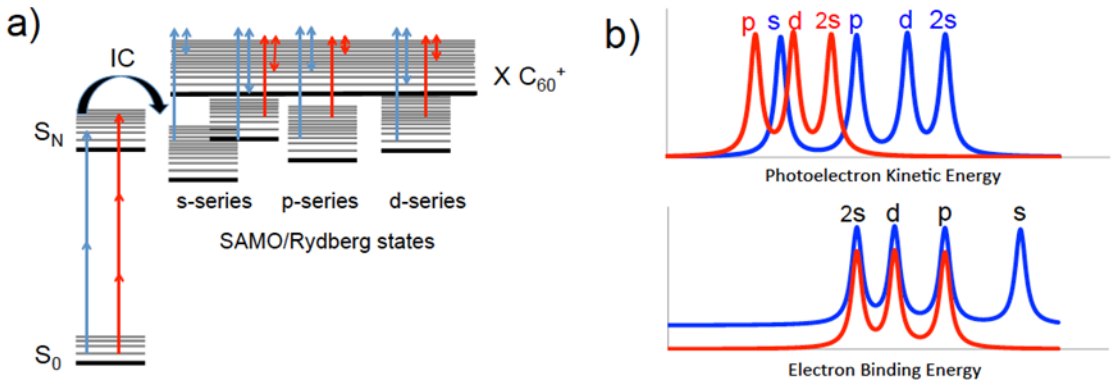

Figure 1.3: Scheme of the Rydberg Fingerprint Spectroscopy, generic for fullerenes, to probe the SAMO and Rydberg excited states: a) multiphoton excitation followed by efficient state couplings to populate many excited states with different vibrational energies (narrow lines demonstrate vibrational excitation). Only s-, p-, d- and 2s-series are shown. Single headed arrows represent two different photon energies, while the double-headed arrows show the photoelectron kinetic energies. Note the ion has the same vibrational level as the excited state; b) upper panel illustrates the PES for the two photon energies in a) and lower panel displays the corresponding electron binding energies.[42]

Due to the excitation of the electron in a Rydberg orbital, the molecular core arranges its global geometry like it is an ion, because the Rydberg electron has a large distance to the core. The potential energy surfaces of the highly excited, neutral parent molecule and the ion are similar, as a result the vibrational energy of the molecular core is preserved during the ionisation.[41,43] At the same time, the Rydberg orbitals are not affected by the initial vibrational excitation due to their large distance from the core ion.[44] Therefore, the binding energy of the Rydberg orbitals, E_{bin}, can be calculated from the PES by subtracting the photon energy, $h\nu$, from the kinetic energy of the electron, E_{kin}:

$$E_{bin} = E_{kin} - h\nu \qquad \textbf{(1.6)}$$

This technique, Rydberg Fingerprint Spectroscopy, or the investigation of Rydberg states in general has been applied to many different molecules.[20,21,45–49] Similar studies have been used to analyse the mechanisms of C_{60} under laser irradiation[7,14,30,50] which will be explained in more detail in chapter 1. 5. The experimental technique for the detection of the photoelectrons will be introduced in the following chapter.

1. 3. Velocity map imaging technique

The velocity map imaging (VMI) technique enables the simultaneous detection of the momentum distribution of the photoionised electrons as well as the angular distribution with respect to the polarisation direction of the laser electric field. This is in contrast to conventional photoelectron spectroscopy methods which show only a single parameter (like magnetic bottle neck photoelectron spectroscopy[51]). The VMI technique was demonstrated for the first time by André Eppink and David H. Parker in 1997 and consists of a set of electrodes and a 2-dimensional (2-D) detector.[52] Due to the experimentally recorded image being a 2-D representation of a 3-dimensional (3-D) distribution of the ejected photoelectrons (Figure 1.4), the image has to be inverted to reconstruct the original 3-D data. This 3-D spherical distribution is called a Newton sphere and emerges after the photoionisation when the released electrons expand from their origin.

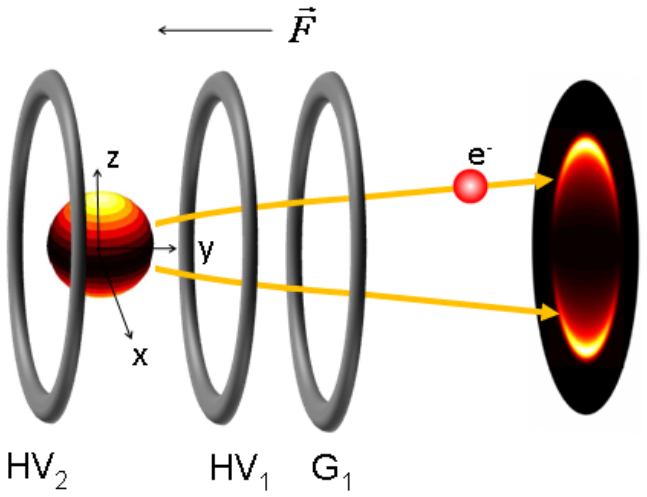

Figure 1.4: VMI principle. The Newton sphere of the photoelectrons after time t elapsed with an applied extraction field. HV1, HV2 and G1 are the electrodes that project the electron distribution onto the position-sensitive detector. The laser propagates in the x-direction and the laser polarisation is along the z-axis.[53]

In a Cartesian coordinate system with the photoelectrons created at the origin and the linearly polarised ionisation laser propagating along the *x*-axis with the polarisation direction in the *z*-direction, photoelectrons with the same initial kinetic energy appear on the surface of the Newton sphere after time *t* (Figure 1.4). The radius of this sphere is the product of the initial photoelectron velocity and the elapsed time *t*. The position of a photoelectron on the Newton sphere depends on its initial momentum and can be described by the polar and azimuthal angles, θ and φ, which give the electron distribution $F(R, \theta, \varphi)$. This sphere is projected onto a position-sensitive detector through the acceleration of the photoelectrons by an electric field anti-parallel to the y-axis towards the detector (Figure 1.4). This electric field is applied by electrodes with typical voltages of HV_1 = –1450 V and HV_2 = –2000 V to focus the photoelectrons on the 2-D plane of the detector.

The electron distribution is rotationally symmetric for linear polarised light around the polarisation direction, so the angular distribution for a specific electron velocity can be simplified:[54]

$$F(R,\theta,\varphi) \rightarrow F(R,\theta) \tag{1.7}$$

This projection makes it possible to recover the original 3-D photoelectron distribution from the measured 2-D image later on with the inverse Abel transformation.[54] For example in Figure 1.4 the projection of the 3-D sphere onto the 2-D detector in the xz plane is illustrated. An electron distribution ($s_z(x,y)$) for a specific z value with the same velocity is projected onto the detector as a line parallel to the xy plane (Figure 1.5):

$$\int_{-\infty}^{\infty} s_z(x,y)dy = 2\int_{0}^{\infty} s_z(x,y)dy \tag{1.8}$$

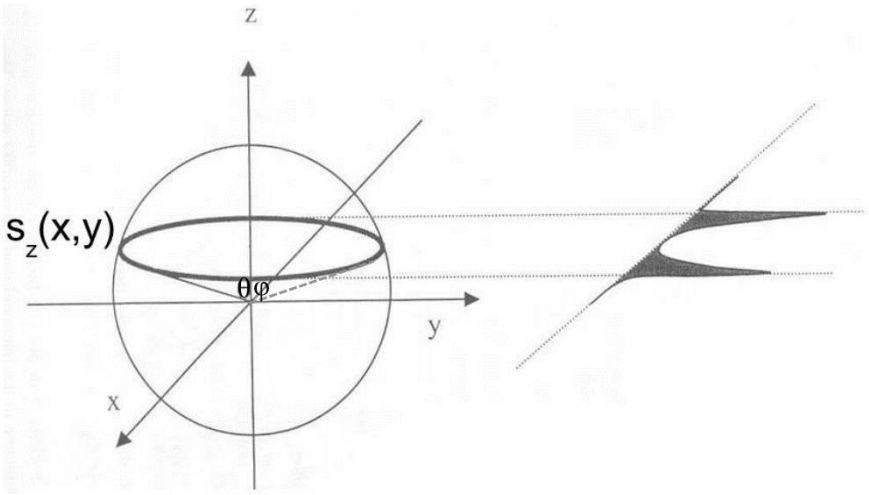

Figure 1.5: Schematic of the Newton sphere spanned by the photoelectrons. The projected distribution of $s_z(x,y)$ as a line on the detector is the Abel transform of this distribution.[54]

Due to the rotational symmetry of the distribution with respect to the z axis, the last step is valid. A substitution of the variables through $r^2 = x^2 + y^2$ can be made:

$$dy = \frac{dy}{dr}dr = \frac{r}{\sqrt{r^2 - x^2}}dr \tag{1.9}$$

This leads to the Abel transformation of $s_z(r)$:

$$2\int_{0}^{\infty} s_z(x,y)dy = 2\int_{0}^{\infty} \frac{rs_z(x,y)}{\sqrt{r^2 - x^2}}dr \tag{1.10}$$

Hence the inverse Abel transformation is used to retrieve the 3-D distribution from the measured image and usually the result is plotted in the xz plane, at $y = 0$. This method will be explained in more detail in chapter 2. 2. 2.

1. 4. Photoelectron Angular Distribution

As mentioned in the previous section the VMI image contains information on the angular distribution of the photoelectrons along with the photoelectron momentum, or kinetic energy. The outgoing photoelectron wavefunction results from the electron scattering off the atomic or molecular ion core and can be expressed as a superposition of spherical harmonic functions, $Y_{lm}(\theta, \phi)$, also known as partial waves, so a general equation of a PAD is:[55,56]

$$I(\theta, \phi) \propto \sum_{L=0}^{L_{max}} \sum_{M=-L}^{L} B_{LM} Y_{LM}(\theta, \phi) \qquad \textbf{(1.11)}$$

With the B_{LM} coefficients being related to the radial dipole matrix elements which contain information on the individual contribution of each partial wave and its coupling with every other partial wave.[56] This equation results from the interference of photoelectron partial waves with orbital angular momenta l and l', where L can take values between 0 and $l + l'$.[56] Expanding equation (1.11) gives the first term B_{00} which is proportional to the angle integrated photoelectron intensity.[56] The subsequent coefficients are usually divided by B_{00} to give a normalised anisotropy parameter, β.[56] Also only even L terms appear in the expansion because odd L terms only have to be considered for chiral molecules or orientated molecules in space.[55,56] The magnetic quantum number M can have values between $-L$ and $+L$, but due to the relation of the polarisation vector of each absorbed photon to the molecular axis, only terms of $M = 0$ can occur.[55] This is a result from the symmetry restrictions of the laboratory frame measurement imposed on the molecule and it also removes the dependence on the angle ϕ due to integration.[55,56] Based on the above restrictions the PADs can be described for a single pulse of linearly polarised light and one photon ionisation of a randomly oriented sample by:[57]

$$I(\theta) = \sigma/4\pi[1 + \beta_2 \mathrm{P}_2(\cos\theta)] \qquad \textbf{(1.12)}$$

Where σ is the total photoionisation cross section, β_2 is the anisotropy parameter, P_2 is the second order Legendre polynomial equal to $\frac{1}{2}(3 \times cos^2\theta - 1)$ and θ is the angle with respect to the laser polarisation direction.

Usually the Cooper-Zare formula is used to calculate the anisotropy value in theoretical studies, when the orbital angular momentum quantum number l is a good quantum number like in the case of an atom, or L for a molecule:[57,58]

$$\beta = \frac{L(L-1)R_{L-1}^2 + (L+1)(L+2)R_{L+1}^2 - 6l(L+1)R_{L+1}R_{L-1}\cos(\delta_{L+1} - \delta_{L-1})}{(2L+1)(LR_{L-1}^2 + (L+1)R_{L+1}^2)} \quad \textbf{(1.13)}$$

$R_{L\pm1} = \int \Psi_f^{L\pm1}(r)\Psi_i^L(r)r^3 dr$ are the radial dipole matrix elements which are overlap integrals of the final *(f)* and initial *(i)* states and δ is the phase shift of the outgoing waves.[57,58] As the selection rule for L in a one-photon transition is $\Delta L = \pm 1$, the free-electron wave from a hydrogen 1*s* orbital ($l = 0$) is given by a single l value of 1, corresponding to a *p* wave. The magnetic quantum number *m* (*m* = –*l*, –*l* + 1, ..., *l* –1, *l*) must remain unchanged when linearly polarised light is used, so only the *m* = 0 component of the *p* wave ($l = 0$) is allowed from an *s* orbital.[59] According to the Cooper-Zare formula the β value for the *s* orbital should be 2. For initial states other than *s* orbitals, higher orbital angular momenta are possible due to the selection rule, so interferences between these free-electron waves occur which can be calculated, e.g. using the Cooper-Zare formula (equation (1.13)). Also due to these interferences the anisotropy value is expected to change with altering kinetic energy of the photoelectron. Hence the photoelectron spectra provide the energy eigenvalues of the parent atom while the PADs reveal characteristics of the corresponding wavefunctions (e.g. a p wave produced from an s orbital).[59]

1. 5. Excitation and Ionisation Mechanisms of Fullerenes

In this section the different photoexcitation and photoionisation mechanisms of C_{60} will be described based on previous studies from the literature.

The excitation and ionisation mechanisms of C_{60} in the gas phase were found to depend on the laser pulse duration and intensity for laser wavelengths below the ionisation potential (IP = 7.6 eV).[4,9,23] If the photon energy of the laser is lower than the ionisation potential, several photons must be absorbed to ionise the molecule, and thus high laser intensities are needed. However, the higher laser intensity can in turn affect the ionisation mechanism as described in chapter 1. 1.[37] First the influence of the laser pulse duration on the excitation and ionisation mechanism of fullerenes will be discussed.

The irradiation of fullerenes with intense laser pulses excites the molecule into highly excited states. The molecules can absorb more energy than they need to remove one electron, and subsequently they can reduce their internal energy by C_2 evaporation, electron emission or photo emission on different timescales.[4,6,11,24]

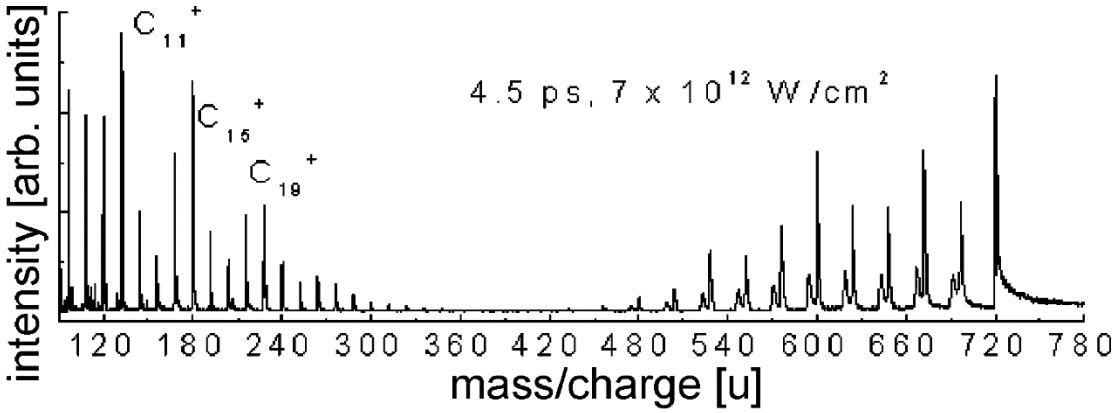

Figure 1.6: Positive ion mass spectrum of C_{60} obtained with 800 nm laser light, pulse duration of 4.5 ps and an approximate laser fluence of ca. 25 – 30 J/cm^2. From ref.[9]

For picosecond (1 ps = 10^{-12} s) or longer laser pulses the time-of-flight (TOF) mass spectra of C_{60} show a tail on the high mass side of the C_{60}^+ peak (Figure 1.6) which can be explained by delayed thermionic emission.[9,25,60] The mass spectrum of Figure 1.6 also shows extensive fragmentation which is caused for higher mass fragments by sequential C_2 evaporation from the excited parent ions while the smaller fragments like carbon rings and chains are due to catastrophic break-up of the fullerene cage with sufficient excitation.[9,25,60] The smaller peaks next to the fullerene fragments on the low mass side are caused by metastable emission of C_2 from ions produced in the extraction region that decay while travelling through the field-free region of the TOF mass spectrometer on the microseconds timescale (1 μs = 10^{-6} s) after excitation.[9] Additionally, the mass spectrum of C_{60} in Figure 1.6 shows only singly charged ions because the gained electronic energy has time to couple to the molecular vibrations during a ps laser pulse as the time constant for the electron phonon coupling of C_{60} was found to be approximately 240 fs.[27] Hence, the electronic system cannot accumulate sufficient energy to cause multiple ionisation.[25,60] For ps laser pulse durations the PES shows an exponentially decreasing intensity with increasing kinetic energy due to the predominance of thermionic electron emission (Figure 1.7 e).[4,7,23,27]

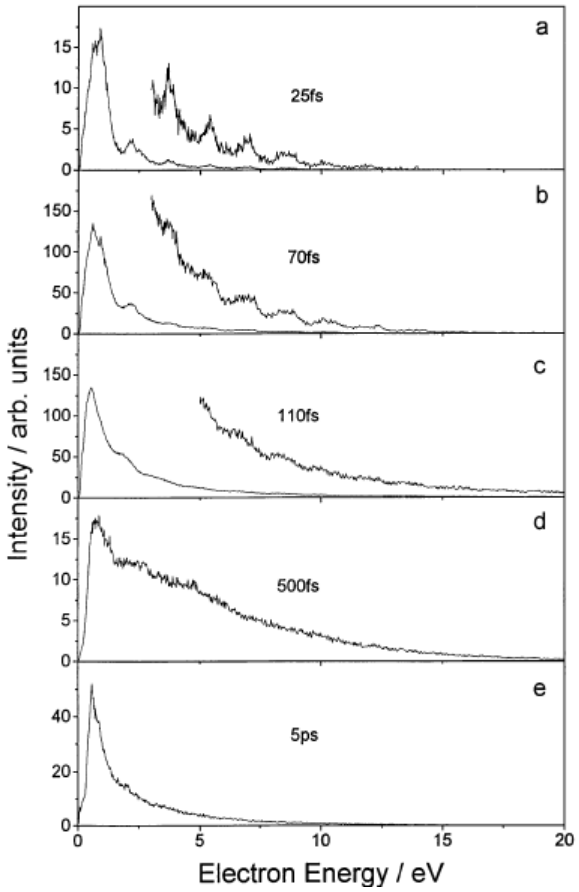

Figure 1.7: PES of C_{60} with different laser pulse durations at laser intensities of a)-d) (80 ± 20) TW/cm^2 and e) 5 TW/cm^2. All spectra were recorded at a laser excitation of 790 nm. From ref.[4]

The delayed thermionic ionisation mechanism appears in systems with low ionisation potential or electron affinity, high dissociation energy of the molecule whilst using a laser photon energy less than the ionisation potential, in which case it has less than the photoionisation energy of the lowest triplet state for fullerenes.[23] For ns laser photon energies below the IP of C_{60} ($IP(C_{60})$= 7.6 eV)[23] but above the IP of the lowest triplet state ($IP(C_{60}^T)$= 5.9 eV)[61,62], a rapid coupling from a photoexcited singlet state to the triplet manifold occurs followed by single photon ionisation, similar to a direct two-photon ionisation mechanism.[23] In case of a delayed thermionic mechanism, photons are absorbed at a relatively low rate during the laser pulse, so the electronic excitation energy is quickly coupled to vibrations, while more energy is still being absorbed.[4,23,27,33] The total energy gained by the molecule is equilibrated over electronic and vibrational degrees of freedom until the vibrational energy is high enough to eject an electron. This process is not direct with respect to the laser pulse, so the ionisation can occur up to microseconds after the excitation.[4] The electron emission and fragmentation can be described by statistical models assuming the energy is equilibrated over all degrees of freedom.[25] Hence, calculating the temporal evolution of the internal energy, $E(t)$, of the electronic system can be used as an input to model the electron emission to obtain emission rate constants, that can be used to calculate experimental

observables like the apparent electron temperature.[63] The internal energy, $E(t)$, is calculated by solving the following differential equation (1.14):[12,64,65]

$$\frac{dE(t)}{dt} = \sigma_p I(t) - \frac{E(t)}{\tau} \qquad \textbf{(1.14)}$$

With σ_p as a constant, average photon absorption cross-section, $I(t)$ as the laser intensity and τ as the time constant for coupling to vibrational degrees of freedom.[27,63] This model assumes a single decay constant, τ, independent of the energy difference between the electronic and vibrational systems for the energy relaxation to vibrational degrees of freedom. The thermionic emission model is based on the Weisskopf formalism applying the principles of detailed balance, which gives an Arrhenius-type rate constant for the electron emission, $k(E)$:[28,33,66–68]

$$k(E) \cong A(E) \exp\left(-\frac{\Phi}{k_B T_a(E)}\right) \qquad \textbf{(1.15)}$$

With E as the total internal energy of the molecule, A is a scaling factor including the photoelectron yield, Φ is the ionisation energy, k_B is Boltzmann's constant and T_a is the apparent temperature.[33] The temperature is a microcanonical temperature of the electronic subsystem of the molecular ion because fullerenes in the gas phase can be considered as isolated systems in the high vaccum.[33] Also the model predicts an exponentially decreasing electron emission probability with increasing electron kinetic energy, E_{kin}, resembling a Boltzmann distribution, so the PES can be described by:[33,66–68]

$$I(E_{kin}) \propto A \exp\left(-\frac{E_{kin}}{k_B T_a}\right) \qquad \textbf{(1.16)}$$

with I as the intensity of the emitted electrons and E_{kin} is the electron kinetic energy.[68]

For laser pulse durations from 50 fs up to about 1 ps the mass spectra of C_{60} show less fragmentation, but multiply charged species appear (Figure 1.8).[4,15]

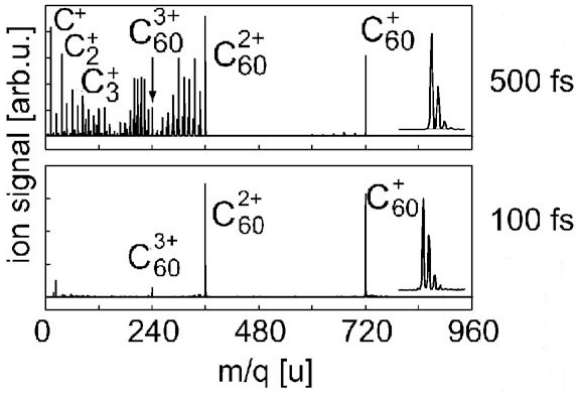

Figure 1.8: Positive ion mass spectra of C_{60} obtained with 797 nm laser pulses and pulse durations as indicated on the right side (for upper panel 500 fs and for lower panel 100 fs) at 40 TW/cm². From ref. [15]

The resulting PES show a thermal background (Figure 1.7 b-d) which can also be fitted by the exponential distribution (1.16).[27,33] The observed apparent temperatures for thermionic emission, seen for few-ps pulses, (3000 - 4000 K) are significantly lower than at a pulse duration from 50 fs to 1 ps (Figure 1.7 b) T_a = 32000 K, c) T_a = 39000 K). [4,27] At this pulse duration it is thought that enough energy can be accumulated in the electronic system to induce thermal ionisation from highly excited electrons, described as a transient thermal electron emission model.[4,27,64] According to this model the electrons are highly excited but the vibrations are hardly affected by the electronic excitation as the ionisation occurs before coupling to the vibrational degrees of freedom takes place.[4,27] This is possible due to the time constants for the energy equilibration in the electronic subsystem being less than 50 fs[15] whilst the time constant for the coupling between the electronic and vibrational states is assumed to be 240 fs.[27] Thus the ionisation occurs for short laser pulses (50 – 1000 fs) from a hot electron cloud before the energy couples to the vibrations, leaving the vibrational system "cold".[27] After the ionisation the remaining internal energy will couple to vibrations leading to fragmentation. As a result the electron apparent temperatures are much higher for the transient thermal electron emission because the heat capacity of the electronic subsystem is lower than the combined capacity of the electronic and vibrational subsystem.[27] This mechanism is analogous to the two-temperature model which is used to describe the energy equilibration in bulk metals after laser excitation.[69]

1. 5. 1. Thermal Ionisation after Femtosecond Laser Pulses

As mentioned previously in this chapter, the PES of C_{60} for ps or longer laser pulse durations shows an exponentially decreasing intensity with increasing kinetic energy (Figure 1.7 e) and the corresponding VMI images show a completely homogeneous distribution of the photoelectrons (Figure 1.9 c).[4,7,12,23,27,64] Time dependent studies of the C_{60} PES, under conditions in which thermionic emission is expected to take place, by Bordas and co-workers using VMI have shown a clearly thermal nature of the emission which would be expected from a completely statistical emission mechanism.[33,70,71] However, an angular anisotropy of the thermal electron signal is observed for VMI images of C_{60} at certain laser wavelengths for pulse durations in the fs range (Figure 1.9).[12,64]

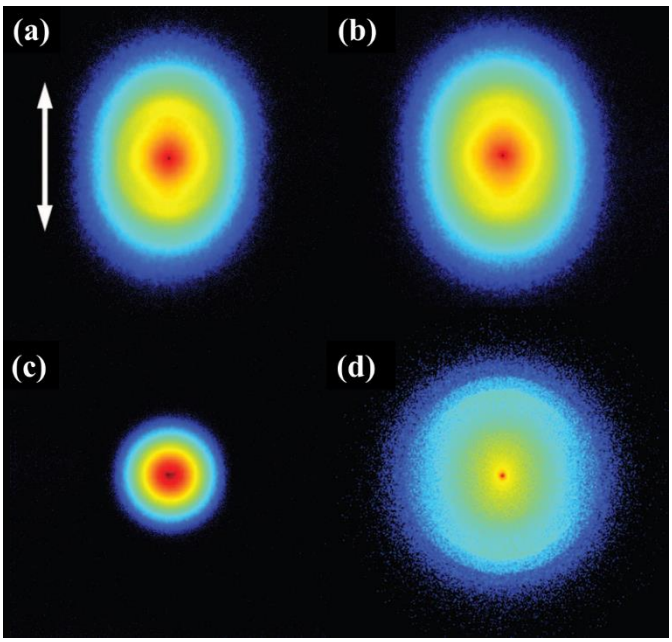

Figure 1.9: Raw VMIs with logarithmic colour scale of C_{60}(a, c-d) and C_{70} (b).The laser settings are a) 800 nm, 180 fs, 5.4 TW/cm^2, b) 800 nm, 180 fs, 6.1 TW/cm^2, c) 532 nm, ns range, d) 400 nm, 120 fs, 0.26 TW/cm^2 and the direction of the laser polarisation is parallel to the white arrow. From ref.[64]

The PES of C_{60} and C_{70} obtained with 800 nm and 180 fs laser pulses show a clear anisotropic image (Figure 1.9 a and b) while the PES of C_{60} from ns laser pulses is isotropic (Figure 1.9 c).[64] As mentioned previously, for laser pulses on the order of ps or ns the equilibration among all degrees of freedom (vibrational and electronic system) occurs and therefore the PES is expected to be isotropic as shown in Figure 1.9 c.[7] The laser intensities for the shown VMIs in Figure 1.9 (a) 5.4 TW/cm^2 and b) 6.1 TW/cm^2) are below the threshold for field ionisation of fullerenes (> 13.3 TW/cm^2).[26] Also, additional screening effects due to the high electron density in C_{60} are suggested to increase this field ionisation threshold and to hinder the barrier suppression.[26,72] Hence, the thermally emitted electrons are expected to be isotropic and show no change of the apparent temperature with the emission angle.[33,64] Further investigations of this asymmetry of the thermal electron emission have revealed that the thermally emitted electrons can get an extra "push" along the laser polarisation direction which can be explained by classical electrodynamics.[33,64] According to the thermal model based on the Weisskopf formula, the photoionisation rate can be extracted and correlated with the fragmentation pattern of C_{60} in the mass spectra.[27] Hence, the electrons are assumed to be emitted on a timescale on the order of 100 fs, so during the laser pulse.[4] Therefore the released electron will receive a momentum kick from the vector potential of the transient time-varying electric field.[33,64] The maximum increase that the electron can experience in its kinetic energy is $2U_p$, if the electron is ejected at the peak of the vector potential, corresponding to zero instantaneous electric field.[33] If the electron is emitted outside the temporal envelope of the time-varying field or at the peak of the electric field, it will not get a momentum kick in the direction of the laser electric field.[33] The kinetic energy of the photoelectrons from direct photoionisation are not affected as they are typically emitted at the peak of the electric field.[33] As a result, the kinetic energy of

the photoelectron produced via direct photoionisation can be related directly to its electron binding energy (equation (1.6)).[33] As described previously, the maximum momentum kick, that the emitted electron can receive, is proportional to U_p, so the asymmetry depends on the wavelength (equation (1.1)).[33] Figure 1.10 shows the clearly asymmetric electron distribution at 800 nm (d, e) in contrast to the spectra using 400 nm (a, b).[33,64]

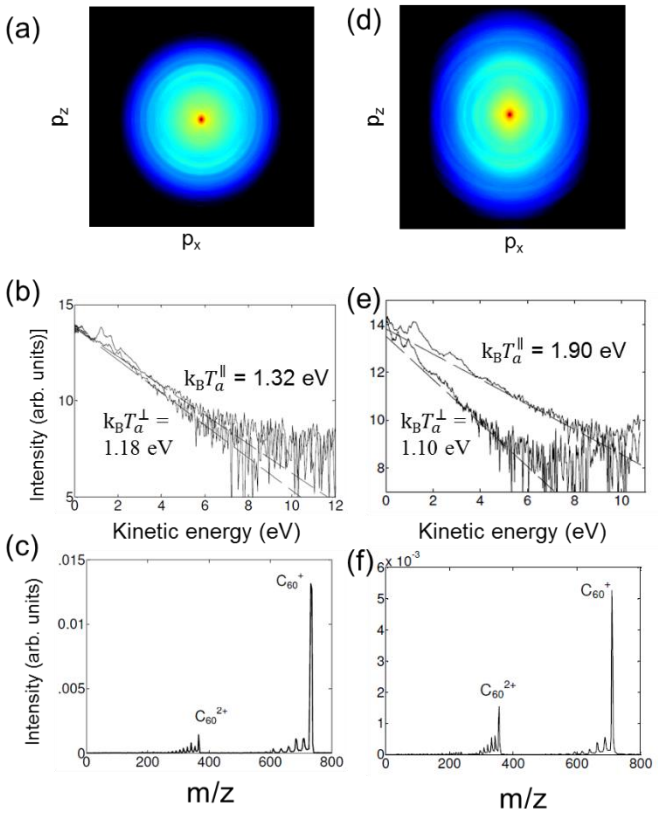

Figure 1.10: Experimental results of C_{60} using 400 nm, 120 fs, (1.4 ± 0.2) TW/cm² (a, b, c) and 800 nm, 182 fs, (6.7 ± 0.2) TW/cm² (d, e, f) laser pulses. The first row (a, b) displays the inverted VMIs (plotted in logarithmic colour scale for display purposes) with the laser polarisation direction along the p_z axis. In the second row the angular-resolved PES parallel and perpendicular to the laser polarisation are shown (b, e). The corresponding mass spectra are displayed in the bottom row.[63]

Despite the laser intensities being different for the two measurements in Figure 1.10, the mass spectra and the perpendicular temperatures are similar, which indicates the fullerenes have absorbed the same total amount of energy.[33] Hence, the perpendicular temperature can be used to measure the absorbed energy which has also been proposed by Huismans *et al.* using angular-resolved PES and a statistical model based on the Weisskopf formalism similar to the previously described thermal model.[63,73]

The asymmetry in the PES can be characterised by comparing the apparent temperatures obtained parallel and perpendicular to laser polarisation direction. The difference of the parallel and perpendicular apparent temperatures, $\Delta k_B T_a$, is plotted against U_p in Figure 1.11.

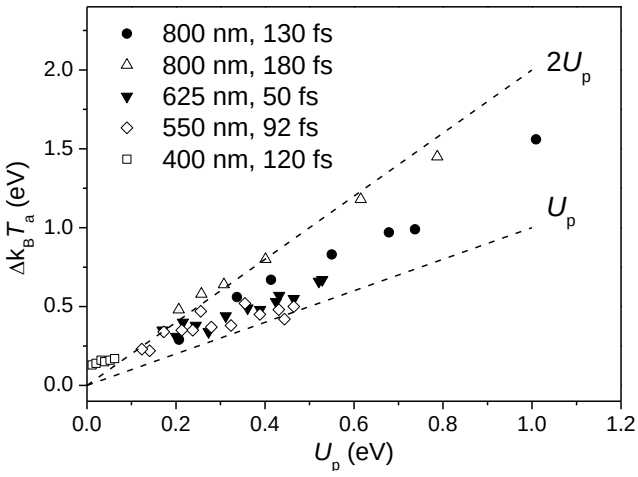

Figure 1.11: Difference of the parallel and perpendicular apparent temperatures, $\Delta k_B T_a$, plotted against U_p for a range of wavelengths and pulse durations.[63]

The graph in Figure 1.11 supports the proposed mechanism because the difference in the apparent temperatures, $\Delta k_B T_a$, falls approximately between U_p and $2U_p$ for a range of wavelengths.[63] The thermal emission model could also reproduce the trend in asymmetry although the apparent temperatures along the laser polarisation direction were consistently underestimated (Figure 1.12).[4,27,64]

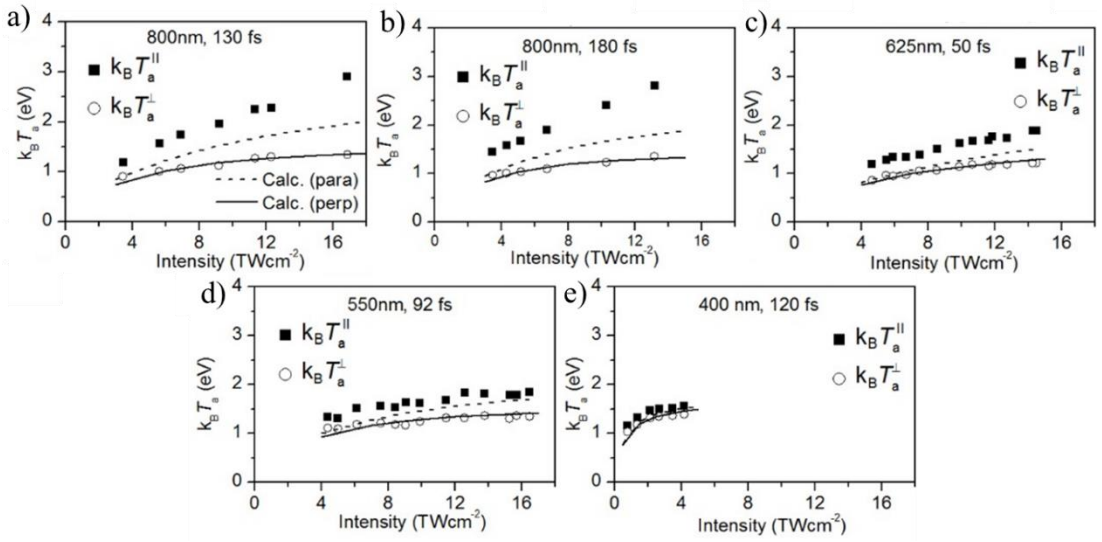

Figure 1.12: Parallel (squares for experimental data and dashed lines from computations) and perpendicular (circles are experimental data and solid lines from computations) apparent temperatures plotted against the laser intensity for different laser wavelengths and pulse durations.[63]

Although the model is simple, the calculated temperatures fit quite well with the experimental values. The discrepancies between the model and the experimental apparent temperatures parallel to the laser polarisation direction may be due to other effects, which are not considered in the applied model, like internal polarisation, recollision effects or unresolved ATI peaks.[33,63] Nevertheless the proposed simple model agrees qualitatively well with the observed trends in the experimental data.[33,63]

Beside the difference between the parallel and perpendicular apparent temperatures, the PES of C_{60} also show that more electrons are emitted parallel than perpendicular to the laser polarisation direction (Figure 1.13).[74]

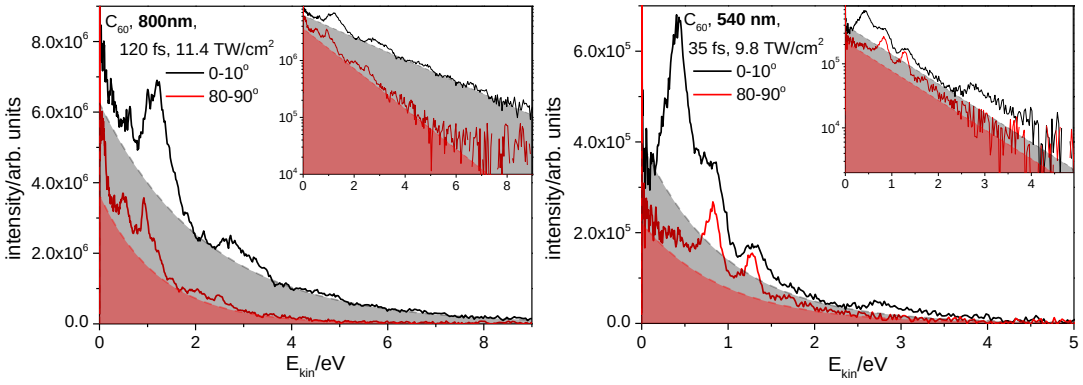

Figure 1.13: Angular-resolved PES of C_{60} showing 0-10° (black line) and 80-90° (red line) segments in respect to the laser polarisation direction at 800 nm (left) and 540 nm (right) excitation. The inset shows the same PES, respectively, with the intensity plotted on a logarithmic scale. The area underneath the distributions is related to the emitted electron number for the 0-10° (black area) and the 80-90° (red area) slice.

The area underneath the distribution is correlated to the number of emitted electrons. Figure 1.13 shows clearly that the area for the 0-10° distribution (grey area) is much larger than for 80-90° (red area) with respect to the laser polarisation direction. Also, the difference between the number of emitted electrons at 0-10° and 80-90° is clearly greater for 800 nm pulses than for 540 nm pulses. To characterise this difference, the ratios between the number of counts for 0-10° and for 80-90° are plotted against the laser intensity for various wavelengths in Figure 1.14.[74]

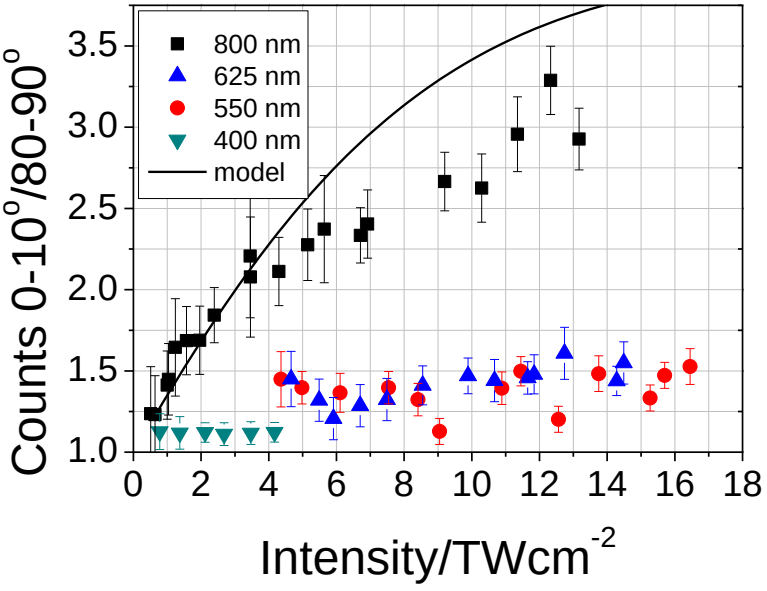

Figure 1.14: The ratios between the number of counts for 0-10° and 80-90° angular segments plotted as a function of laser intensity for different wavelengths including the modelled ratios.[74]

From Figure 1.14 a clear intensity dependence of the count ratio for the 800 nm measurement can be noticed as the count ratio increases with higher laser intensities.[74] This observation is interpreted as a suppression of the confining ionisation barrier by the electric field.[74] It is similar to the field ionisation described in chapter 1. 1, in which case the ionisation potential oscillates in time with the electric field of the laser.[74] The greatest suppression will be parallel to the polarisation axis because the suppression of the barrier is directional.[74] The modelled values are overestimating the experimental ratios for higher laser intensities, so this model needs further refinement to take account of variables such as the laser wavelength.

If a molecule has undergone a statistical energy equilibration, it will have a distribution of highly excited electrons, so the needed electric field strength is lower than for an unexcited molecule to overcome the ionisation potential.[74] Although the Keldysh parameter is much higher than 1, even for the highest experimental intensities (according to the equation (1.2)), which indicates the intensities are below the threshold for field ionisation.[74] However, the electrons can be excited enough to decrease their binding energy greatly, so the ionisation potential is effectively decreased, allowing field ionisation to occur.[74] It is important that the frequency of the electric field is not too high, so the electrons have time to tunnel through the suppressed barrier before the field changes sign and the barrier is back at its maximum.[74] Therefore the field ionisation is dependent on the wavelength and this effect is seen clearly in the measurements using 800 nm, but not for shorter wavelengths.[74] This effect was called the electric-field-induced barrier suppression and the model was developed by Gordon Henderson.[74] As part of this thesis the electric field-induced barrier suppression model will be complemented by experiments on C_{60} using 700 nm laser pulses and the results will be presented in chapter 4. 3. 1.

1. 5. 2. Highly Excited Electronic States in Fullerenes

Another feature in the PES of fullerenes is a peak structure superimposed on the thermal electron emission background (Figure 1.7 a-c).[23] The small peaks above the photon energy can be described by ATI as the peaks are separated by the photon energy.[4] The peak structure below the photon energy showed 3 to 4 prominent peaks which were assigned initially to Rydberg series with angular momenta of l = 3, 5, 7 (Figure 1.15).[30]

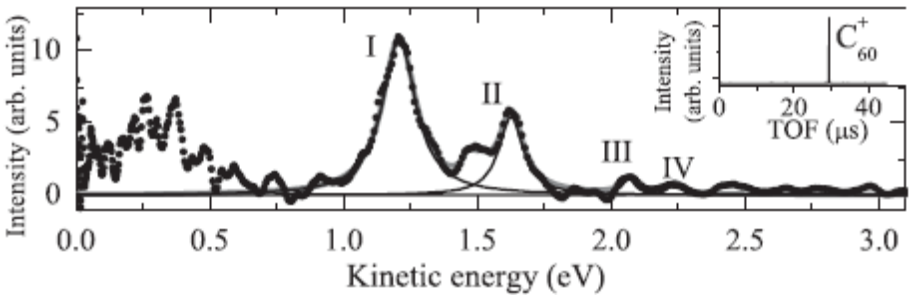

Figure 1.15: Angular-resolved PES (angular segment 0°-10°, parallel to laser polarisation) of C_{60} with the thermal background removed, with mass spectrum as an insert; 400 nm, 120 fs laser pulses of intensity 0.3 TW/cm^2.[7]

After the detection of SAMOs in C_{60} using low-temperature scanning tunnelling spectroscopy (LT-STS) (Figure 1.16)[31] and recent studies in the gas phase combined with density functional theory (DFT)[5], by Hartree-Fock,[32] and time-dependent DFT (TD-DFT) calculations, the peaks at lower kinetic energies could be assigned to the single-photon ionisation of SAMOs (Figure 1.15).[7]

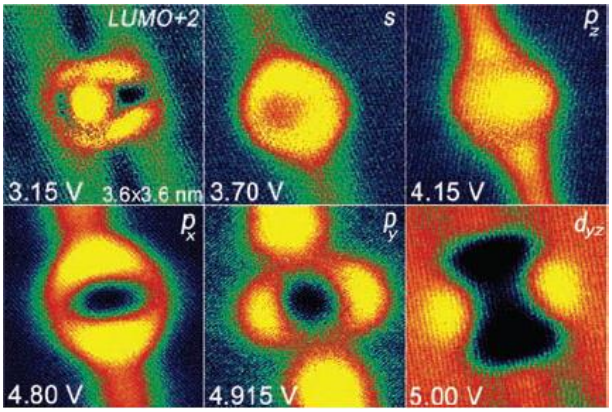

Figure 1.16: LT-STS of a C_{60} molecule isolated on a Cu surface. These dI/dV images evolve from the LUMO+2 with a π^* molecular character to the *s*, p_x, p_y, p_z and d_{yz} SAMO character as the measurement voltage is increased while the current is kept constant. From ref.[31]

The SAMOs are similar to low-lying members of low angular momentum Rydberg series.[33] However, they are different to conventional Rydberg states because the electron density is centred on the centre of the hollow cage and not on the atoms in the molecule, also they have a significant charge density inside the cage, at least for the lowest s and p SAMOs.[33] The SAMO states will converge to conventional Rydberg series if the principal quantum number increases.[33] Hence, the electron density will move farther away from the molecule until the Coulomb force will dominate the interactions.[33] The SAMOs are populated and ionised during the same laser pulse in the gas phase due to their high ionisation rate and short lifetime as shown in a recent model based on Fermi's golden rule and TD-DFT calculations.[7,75] On the basis of these results the peaks I to IV in the PES of C_{60} (Figure 1.15) could be identified as 3s, 3p, 3d and 4s SAMO states (*n* based on the number of nodes).[7,33,75] These assignments were possible by determination of the PADs and the anisotropic values, β, of the peaks supported by TD-DFT calculations

(Figure 1.17).[7] The β values range from –1 to 2 and represent the interference between the outgoing free-electron waves at the ionisation (see chapter 1. 4). The precise analysis of the PADs will be described in chapter 2. 2. 2.

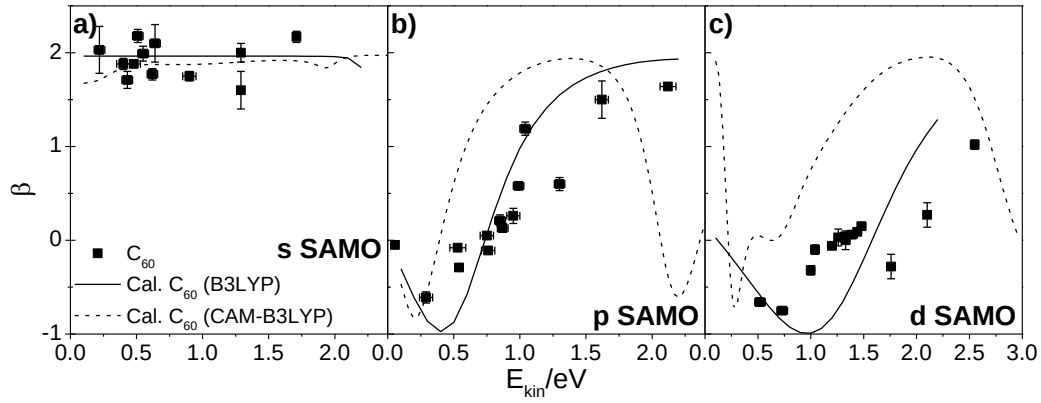

Figure 1.17: β of C_{60} (points) as a function of photoelectron kinetic energy for a) s SAMO, b) p SAMO and c) d SAMO. The lines are showing the computed β values at the TD-DFT/B3LYP/6-31+G(d) (solid line) and at the TD-DFT/CAM-B3LYP/6-31+G(d) level.[75]

The clear peak structure of the SAMOs in the PES (Figure 1.15) can be explained by the modelled photoionisation widths and photoionisation lifetimes using TD-DFT.[75] The photoionisation widths, Γ, are computed for a given kinetic energy of the photoionised electron, ε, and integrated over all angular distributions using following equation (1.17):[75,76]

$$\Gamma_I(\varepsilon) = \rho(\varepsilon) \int |\langle \Psi_{GS}^{cat}, \varepsilon | -E \cdot \mu | \Psi_I^{neut} \rangle|^2 d\Omega \qquad \textbf{(1.17)}$$

Where $-E \cdot \mu$ is the dipolar coupling due to the electric field of the excitation pulse and the density of states, $\rho(\varepsilon)$, is given by

$$\rho(\varepsilon) = k \left(\frac{L}{2\pi}\right)^3 \qquad \textbf{(1.18)}$$

With k referring to the wavevector in the k- space and L is the dimension of a box to which the electron wavefunction is normalised as a plane wave.[75]

The photoionisation lifetime, $\gamma(\varepsilon)$, is inversely proportional to the photoionisation widths:

$$\gamma(\varepsilon) = \frac{2\pi}{\Gamma_I(\varepsilon)} \qquad \textbf{(1.19)}$$

The results of the calculated photoionisation widths for C_{60} of the SAMO states are orders of magnitude larger than those of isoenergetic non-SAMO states (the lowest 500 excited states were computed) (Figure 1.18 a).[75]

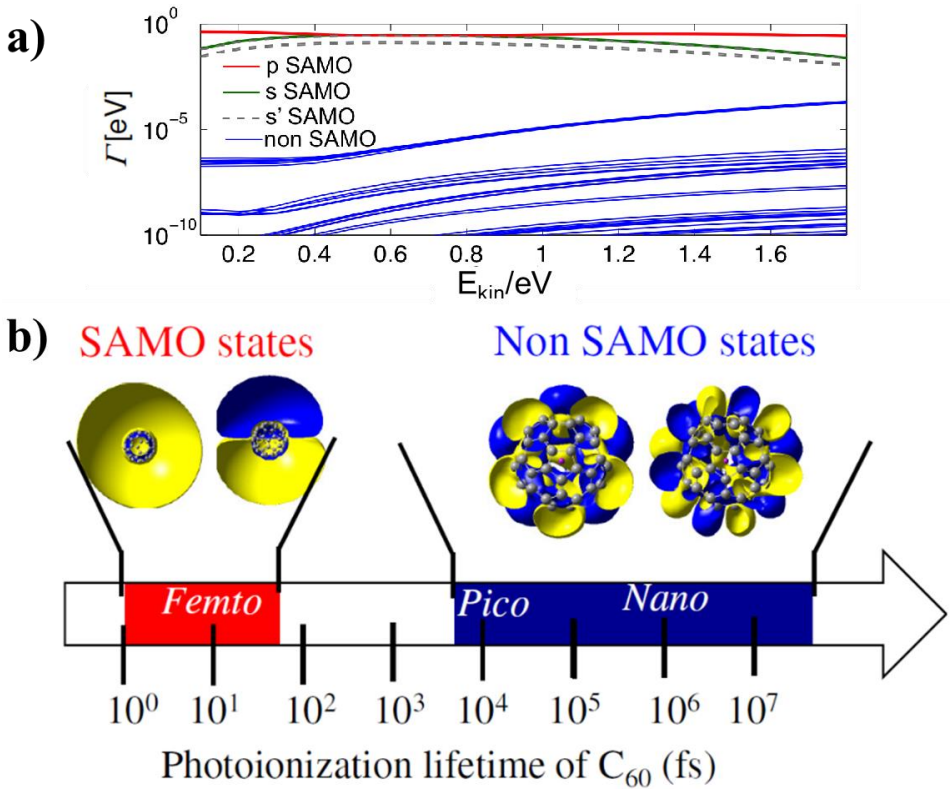

Figure 1.18: a) Computed photoionisation widths, Γ, as a function of the photoelectron kinetic energy of all calculated excited states (first 500 states) and b) displaying the photoionisation lifetime of SAMO and non-SAMO states including a few corresponding Dyson orbitals (isocontour at about 0.00002 $|e|/a^3$). These calculations were conducted by Benoît Mignolet using TD-DFT.[35,75]

Furthermore, the TD-DFT calculations showed that only the SAMO states will photoionise on the timescale of the laser pulse (Figure 1.18 b).[75] As a result the PES is dominated by single-photon ionisation of SAMOs for relatively low laser intensities.[75] In the laser focus, where other excited states do not photoionise within the fs laser pulse timescale due to their very low ionisation widths, these excited valence states can contribute to the excitation leading to thermal electron emission, as described previously in this chapter.[75,77] The exact population mechanism of the SAMOs and isoenergetic states is unknown, but it is assumed that the states are probably populated through multiphoton processes which involve different mechanisms like IC from intermediate states.[50,77] Additionally, high vibrational energy in the molecule supports rapid distribution of energy into the Rydberg and SAMO states since PES experiments on vibrationally "cold" C_{60} (80 K) by Boyle *et al.* showed no significant Rydberg population.[14,78]

1. 6. Studies on Polycyclic Aromatic Hydrocarbons (PAHs)

Previous PES studies on PAHs have revealed a similar thermal ionisation mechanism as for fullerenes.[12,63] Since the PAHs are smaller, it is easier to calculate their electron dynamics and due to their lower density of states, the timescale may be longer for equilibration which makes it possible to probe experimentally. This approach would enable theoretical calculations on the electron dynamics which could complement the experimental measurements to get a better understanding of the mechanism. This is in contrast to fullerenes which are large molecules and therefore calculations on the electron dynamics in C_{60} are impossible to conduct due to the immense computational costs.

Additionally, quantum mechanical studies on coronene and pentacene conducted by Benoît Mignolet showed molecular orbitals with similar electron density to the SAMOs in fullerenes (Figure 1.19).[34]

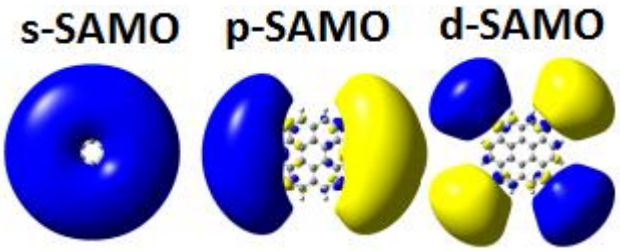

Figure 1.19: A few calculated molecular orbitals of coronene that are similar to the indicated orbitals at the TD-DFT/CAM-B3LYP/6-31(2+)+G(d) level by Benoît Mignolet.[34]

Coronene and pentacene are smaller molecules than fullerenes and contain an additional kind of atom, hydrogen atoms. As mentioned above, theoretical studies on the electronic states of coronene and pentacene show highly excited molecular orbitals with diffuse electron density features resembling the SAMOs in fullerenes.[34] Mignolet *et al.* computed the electronic structure of the 200 lowest excited states of the coronene molecule (D_{6h}) at the TD-DFT/CAM-B3LYP/6-31(2+)+G(d) level.[34] Three of the calculated molecular orbitals are shown in Figure 1.19 that are similar to the s-, p- and d-SAMO of C_{60}.[34] The pentacene molecule has been optimised at the DFT/B3LYP/6-31++G(d,p) level by Mignolet *et al.*[34] The theoretical studies also revealed that the photoionisation cross-sections of the SAMOs in coronene and pentacene are significantly higher than for non-SAMO states under experimental conditions typically used in this thesis, even if the difference is much smaller than for fullerenes (Figure 1.20).[34] According to these studies, measurements of the PES of coronene and pentacene should show peaks originated from the photoionisation of these states, in analogy to fullerene SAMOs.

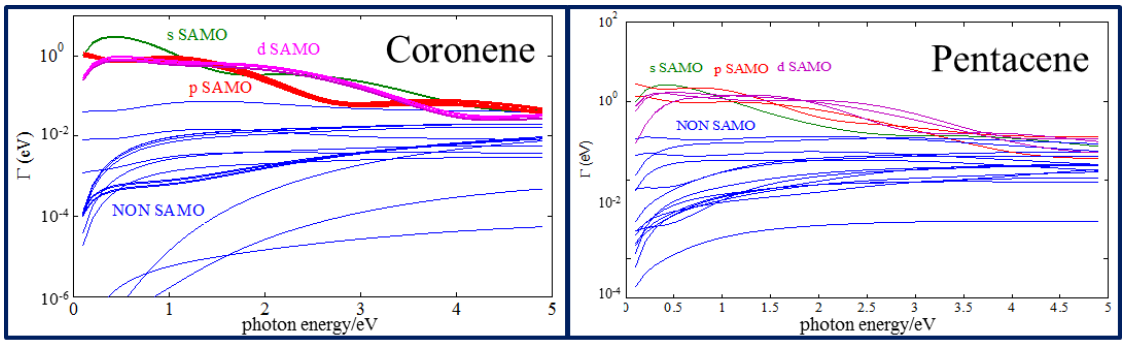

Figure 1.20: Calculated photoionisation widths of coronene and pentacene plotted against the photon energy. The computations were conducted by Benoît Mignolet at the TD-DFT/CAM-B3LYP/6-31(2+)+G(d) level for coronene and at the TD-DFT/B3LYP/6-31++G(d,p) level for pentacene.[34]

In this context it is also worthwhile to take a look at similar studies on the excitation and photoionisation mechanisms of other PAHs like naphthalene and anthracene after ultrashort laser irradiation. PES studies on Rydberg states of naphthalene and anthracene identified two different ionisation mechanisms, a direct ionisation and ionisation after IC similar to Rydberg Fingerprint Spectroscopy.[48,79] Also, the comparison of the results revealed a higher IC rate for anthracene than naphthalene which was explained by more degrees of freedom in anthracene than naphthalene.[48,79] Therefore, studies on the photoionisation of molecules are good probes for highly excited states and their dynamics. Similar studies on fullerenes or other PAHs can lead to analogous results in respect to the molecular size dependency. Hence conclusions from the mechanisms in PAHs might be transferred to fullerenes, because the exact population mechanism of the Rydberg states and SAMOs is still unknown for fullerenes and needs to be identified.[33]

PES studies on PAHs will give a better understanding of the properties of highly excited states like Rydberg states or SAMOs and their dynamics. In addition the excitation and ionisation mechanisms of these excited states may be easier to be identified and probed using the comparison of theoretical models and experimental results. This gave the motivation to theoretically investigate the excited electronic states of a series of different PAHs and to compare the calculations to PES results, which will be presented in chapter 1.

2. Experimental and Theoretical Methods

In this work mass spectrometry and photoelectron spectroscopy are used to determine the electronic structure, along with the excitation and ionisation mechanisms of the studied molecules. The experimental setup consists of a fs laser system and a vacuum chamber equipped with a VMI detector and a TOF-MS which are described in the following sections. The theoretical methods applied to study the excited states of PAHs are explained in the last part of this chapter.

2. 1. Laser System

In the laser system, an oscillator with a titanium-doped sapphire crystal (Ti:Sapph) (Coherent Mantis) creates the fs laser pulses. The Ti:Sapph crystal as the gain medium has an emission of the required bandwidth to generate a fs Gaussian shape pulse according to the Fourier relationship:[80]

$$\Delta t \times \Delta \upsilon = 0.441 \quad \textbf{(2.1)}$$

with Δt as the FWHM pulse width in time and $\Delta \upsilon$ as the FWHM spectral width in frequency space. Hence the Ti:Sapph oscillator used provides the fundamental sub-35 fs laser pulse at 800 nm with a corresponding bandwidth of 80 nm and a repetition rate of 80 MHz after mode-locking.[81] The Ti:Sapph crystal is pumped by a quantum well laser (Coherent OPS) to excite the titanium atoms and to produce a continuous wave (CW) output.[81] For the generation of fs pulses the cavity length is changed at an appropriate speed to induce high-power fluctuations.[81] Once a power fluctuation becomes sufficiently high, a slight Kerr lens effect is formed in the gain medium.[80,81] Due to the arrangement of the cavity this instantaneous power fluctuation is amplified and results in the dominant pulse which will form the mode-locked laser pulses.[81] This method is referred to as passive mode-locking and a spectrum of the output laser beam after the Mantis is shown in Figure 2.1.[80,81]

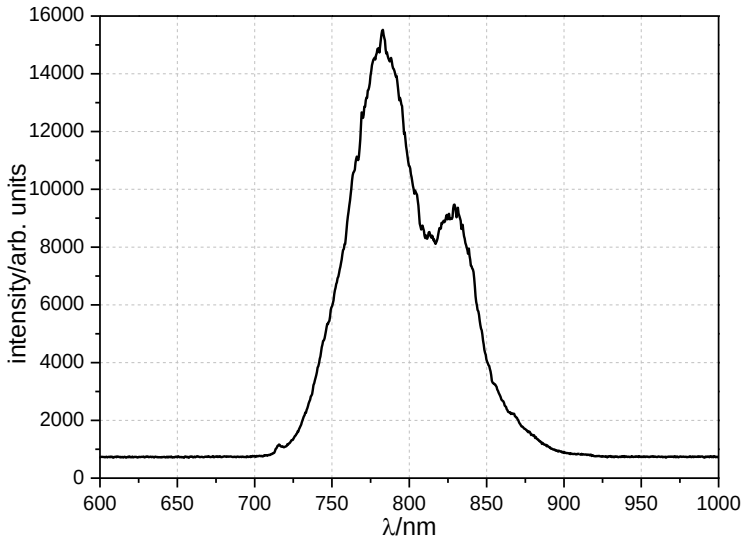

Figure 2.1: Spectrum of Mantis output taken with Ocean Optics HR2000 spectrometer showing a central wavelength of 800 nm and a FWHM of about 80nm.

In Figure 2.1 the spectrum of the fs laser beam shows a local minimum around 810 nm that is due to spectral hole burning in the gain medium.[82] The mode-locked average output power from the Mantis is typically about 500 mW which is not sufficient power for the operation of the non-collinear optical parametric amplifier (NOPA) or the experiments. Therefore the fs laser beam from the oscillator is directed to a Ti:Sapph regenerative amplifier (Coherent Legend Elite) to be amplified (Figure 2.2).

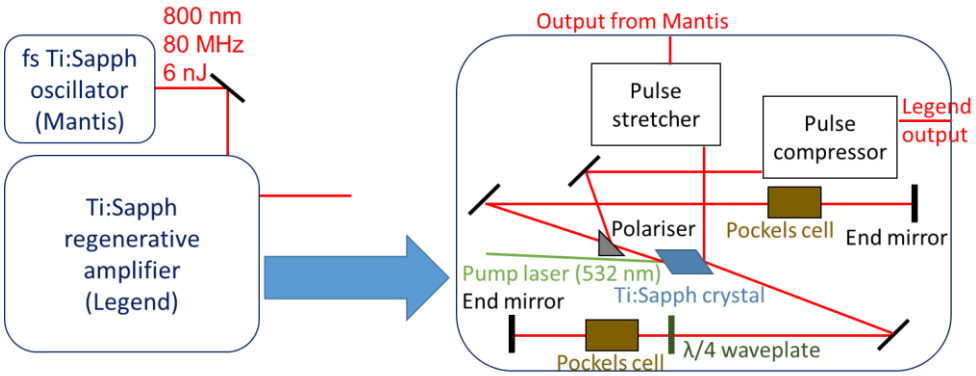

Figure 2.2: Fs laser setup of the oscillator and the amplifier. On the right hand side the cavity of the amplifier is shown.

Initially the pulses are stretched over time to reduce their intensity as the peak intensities are very high due to the short pulse duration. The stretched pulses are amplified in a cavity containing a Ti:Sapph crystal which is pumped by a frequency doubled Nd:YAG ns laser (Coherent Evolution). Pockels cells in front of each of the two end mirrors of the cavity control the polarisation of the pulses to time the entry and the pulse ejection in the cavity. Therefore, the vertically polarised seed pulse enters the cavity and passes through a λ/4 waveplate and an inactive Pockels cell. Then it is reflected off the end mirror and the pulse double-passes the waveplate and Pockels cell becoming horizontally polarised.

Immediately after the pulse leaves the Pockels cell, a voltage is applied to negate the effect of the λ/4 waveplate. Hence the pulse is trapped in the cavity and can be transmitted by the Ti:Sapph crystal. The pulse takes typically 20–30 round trips in the cavity for maximum amplification. Afterwards a quarter-wave voltage is applied to the Pockels cell's output changing the pulse polarisation back to vertical to allow it to leave the cavity through the reflection off a broadband polariser. The Pockels cell electronics' timing is controlled by a signal delay generator (Coherent, SDG) with respect to the pump laser. After the amplification the laser pulses are recompressed to shorter pulse durations again which have a central wavelength of 800 nm with a bandwidth of about 10 nm, a pulse duration of about 120 fs, an average power of 3.5 W at a repetition rate of 1 kHz and a horizontal polarisation. The spectrum of the output beam from the regenerative amplifier is shown in Figure 2.3.

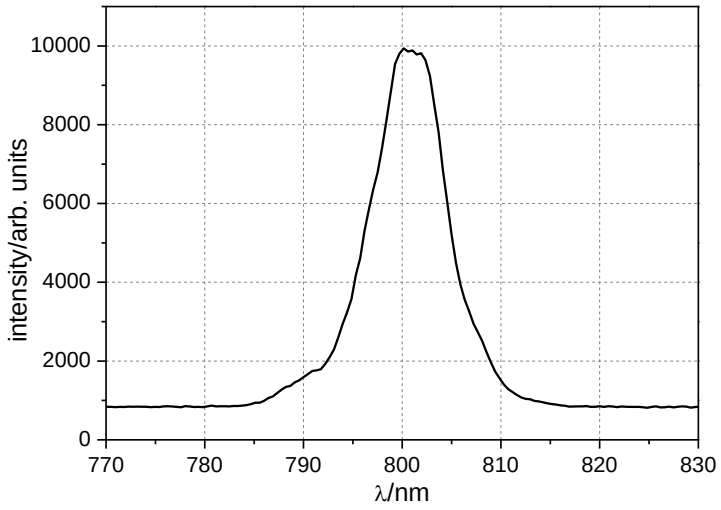

Figure 2.3: Spectrum of Legend output taken with Ocean Optics HR2000 spectrometer with a central wavelength of about 800 nm and a FWHM of about 9 nm.

The amplified laser beam can be split and directed to the desired optical elements depending on the experiment (Figure 2.4).

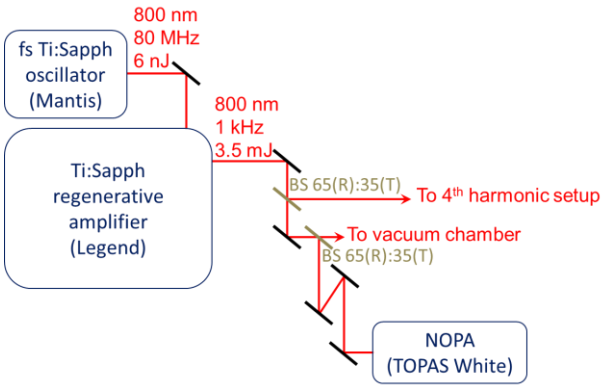

Figure 2.4: Fs laser setup of oscillator, amplifier and NOPA where BS stands for beam splitter.

For experiments using wavelengths between 490 nm and 1100 nm the amplified laser beam is directed into a commercial NOPA (Light Conversion TOPAS White) which produces sub-35 fs pulses of about 30-50 mW average power at a repetition rate of 1 kHz (Figure 2.5).[83]

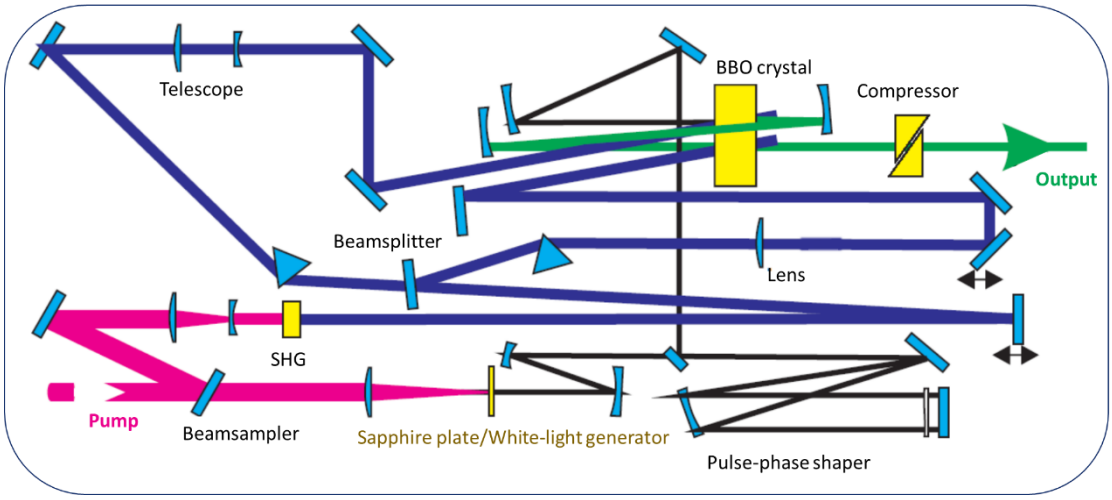

Figure 2.5: Schematic of the optical layout of TOPAS White.[83]

In the NOPA 2% of the incoming pump beam is focussed onto a sapphire plate to generate a fs white-light continuum (WLC).[83] This WLC pulse serves as a seed for a two-stage NOPA that employs a single β-barium borate (BBO) crystal.[83] The main part of the incoming beam is directed to a different BBO crystal to generate the second harmonic (SHG), 400 nm, as a pump beam.[83] This pump beam is split and used to pump the first and second stage of the parametric amplifier.[83] In the first stage the signal pulse is produced by non-collinear overlapping of the seed pulse with the first pump pulse in the BBO crystal.[83] Depending on the delay of the first pump pulse with respect to the chirped seed pulse the wavelength of the signal pulse can be tuned.[83] In the second stage the created signal pulse is overlapped with the second pump pulse in the same BBO crystal to be amplified.[83] The amplified signal pulse is passed through a compressor which is composed of two fused silica prisms to optimise for the shortest pulse duration.

2. 1. 1. One-colour Experiment

For measurements using 800 nm the output from the Legend is aligned through a λ/2 plate to rotate the laser polarisation axis 90° so the laser beam is vertically polarised. The laser power is controlled either through rotating the waveplate followed by a polariser which transmits vertically polarised light or a neutral density attenuator before the waveplate. The laser beam is then focussed into the vacuum chamber using a lens with a focal distance of 30 cm. On the other side of the vacuum chamber the laser power is recorded with a power meter.

The optical setup for the 800 nm experiments on $Sc_3N@C_{60}$ and C_{82} is shown in Figure 2.6 a). For later measurements the height of the vacuum chamber was adjusted and the periscope could be removed. The modified optical setup used for $Li@C_{60}$ (and coronene) measurements is shown in Figure 2.6 b).

a)

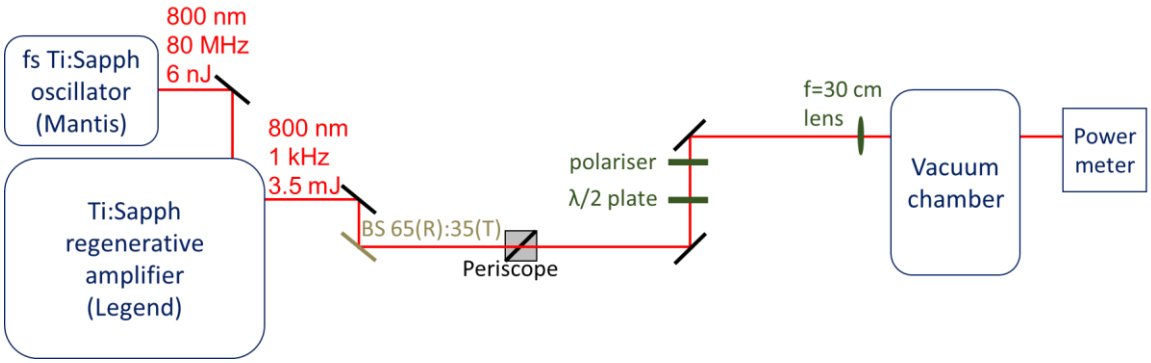

b)

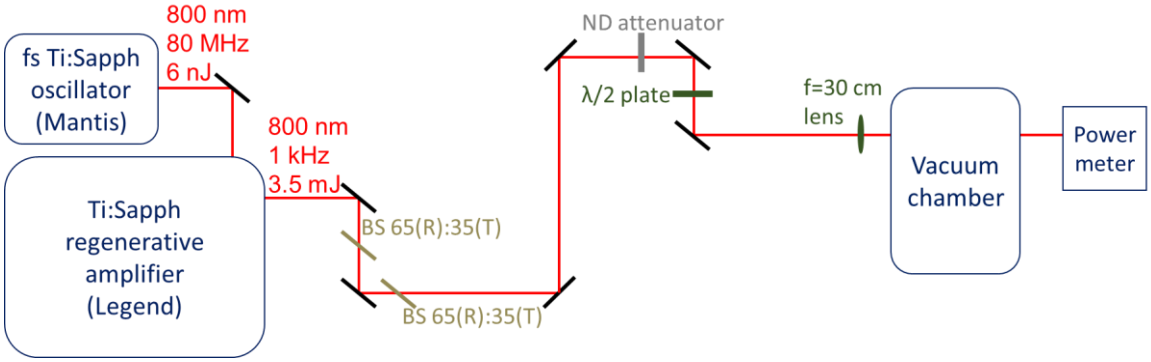

Figure 2.6: Optical setups for experiments using 800nm for a) $Sc_3N@C_{80}$ and C_{82} as well as for b) $Li@C_{60}$ and coronene.

The optical layouts using the output beam of the NOPA are shown in Figure 2.7 a) for $Sc_3N@C_{80}$ and C_{82} measurements. As mentioned above the optical setup was slightly changed after the adjustment of the chamber height, so the optical setup using the NOPA output for $Li@C_{60}$ and coronene was modified (Figure 2.7 b).

a)

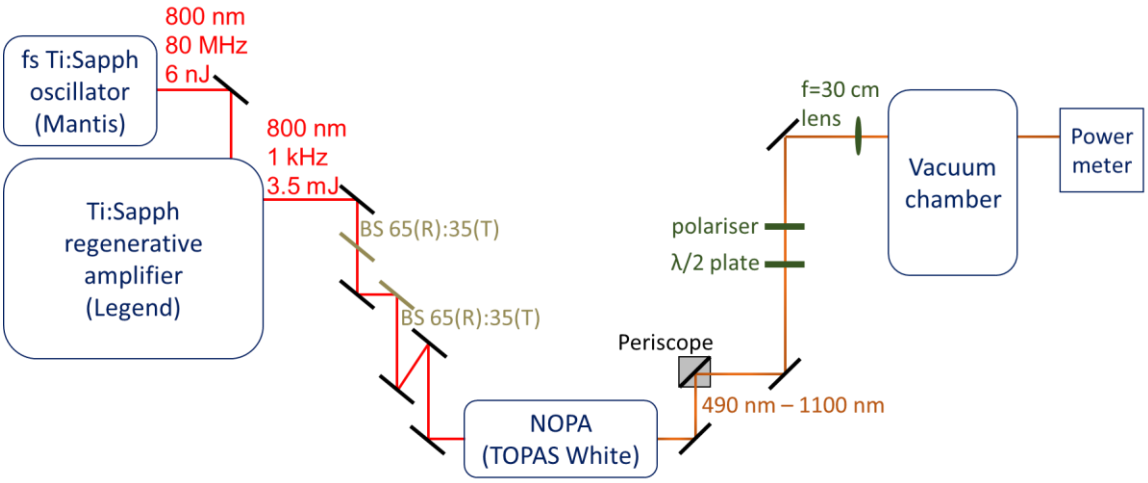

b)

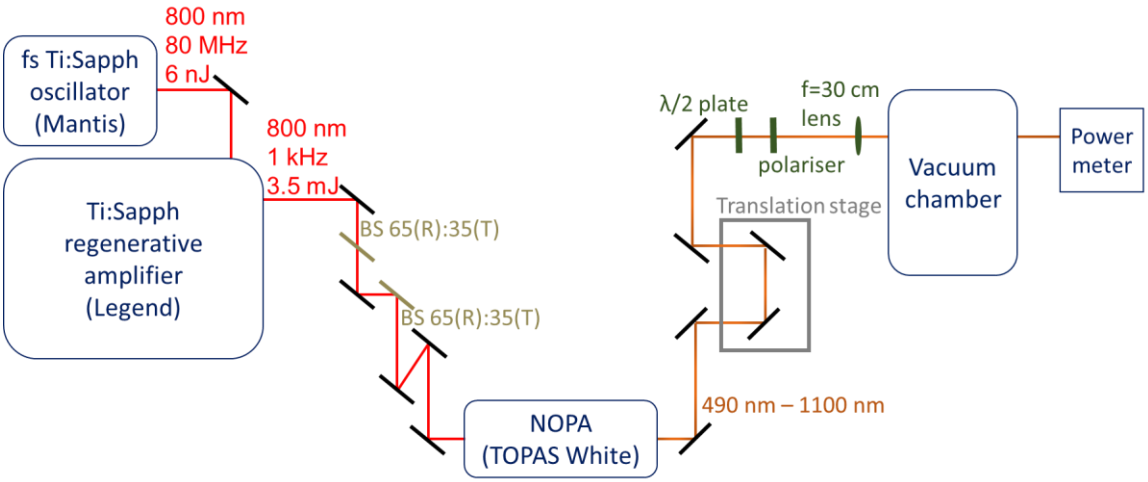

Figure 2.7: Optical setups for experiments using NOPA for a) $Sc_3N@C_{80}$ and C_{82} as well as for b) $Li@C_{60}$ and coronene.

2. 1. 2. Two-colour Experiment

For pump-probe experiments the fundamental output of the Ti:Sapph regenerative amplifier was split into two beams by a 65:35 beam splitter (BS). The transmitted beam is directed to the NOPA to adjust the desired wavelength for the probe pulse (Figure 2.8). The reflected beam is aligned through an assembly of optics to generate the 4th harmonic (200 nm) of the fundamental (800 nm) as shown in Figure 2.8.

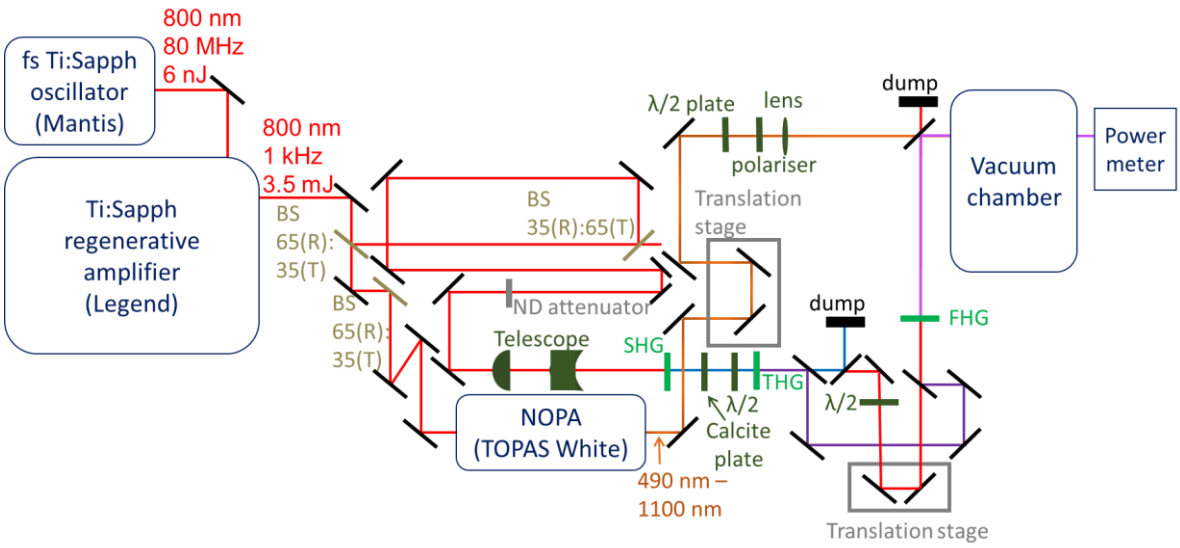

Figure 2.8: Scheme of the 4th harmonic laser setup

The setup to generate the 4th harmonic starts with directing the fundamental beam over a long path using 7 mirrors and 2 beam splitters, so the pump (4th harmonic) and probe pulse (NOPA output) overlap in time in the vacuum chamber (Figure 2.8). The laser pulse power is decreased by one neutral-density filter (79% transmission for 800 nm) before the beam size is reduced by a telescope (M = 0.5) using a convex (f = 10 cm) and a concave (f = -5 cm) lens. After the telescope the laser is aligned through a SHG BBO crystal to generate the 2nd harmonic (400 nm) of the fundamental. As the fundamental travels faster through the optical elements than the generated 2nd harmonic, a calcite plate is used to compensate for the group velocity delay so the pulses overlap temporally again. The formed 2nd harmonic has a polarisation axis perpendicular to the fundamental input and therefore the polarisation axis of the fundamental has to be rotated through a dual waveplate (zero order λ/2 at 800 nm and λ at 400 nm) by 90°. Hence both pulses reach the third harmonic generation (THG) BBO crystal at the same time with the same polarisation axis to produce the 3rd harmonic (267 nm).

After the 3rd harmonic setup the laser light is separated by a dichroic mirror where the 3rd harmonic is reflected, but the fundamental and the 2nd harmonic are transmitted (Figure 2.8). The 3rd harmonic beam is directed to a fourth harmonic generation (FHG) BBO crystal. The fundamental is separated from the 2nd harmonic by a dichroic mirror and its polarisation axis is rotated through a λ/2 plate to match with the 3rd harmonic polarisation axis. Also the fundamental is aligned through two mirrors on a translation stage to ensure the time overlap of the fundamental and the 3rd harmonic in the FHG BBO crystal. Consequently, the 4th harmonic (200 nm) is produced and directed into the vacuum chamber by a dichroic mirror which simultaneously separates the fundamental and a part of the 3rd harmonic from the 4th harmonic.

The beam output of the NOPA is aligned through mirrors on a translation stage to vary the time delay between the pump and probe pulse (Figure 2.8). Subsequently the probe pulse is focused into the vacuum chamber through a 50 cm-focal lens.

Figure 2.9 shows the experimental laser setup for the pump-probe studies in this work.

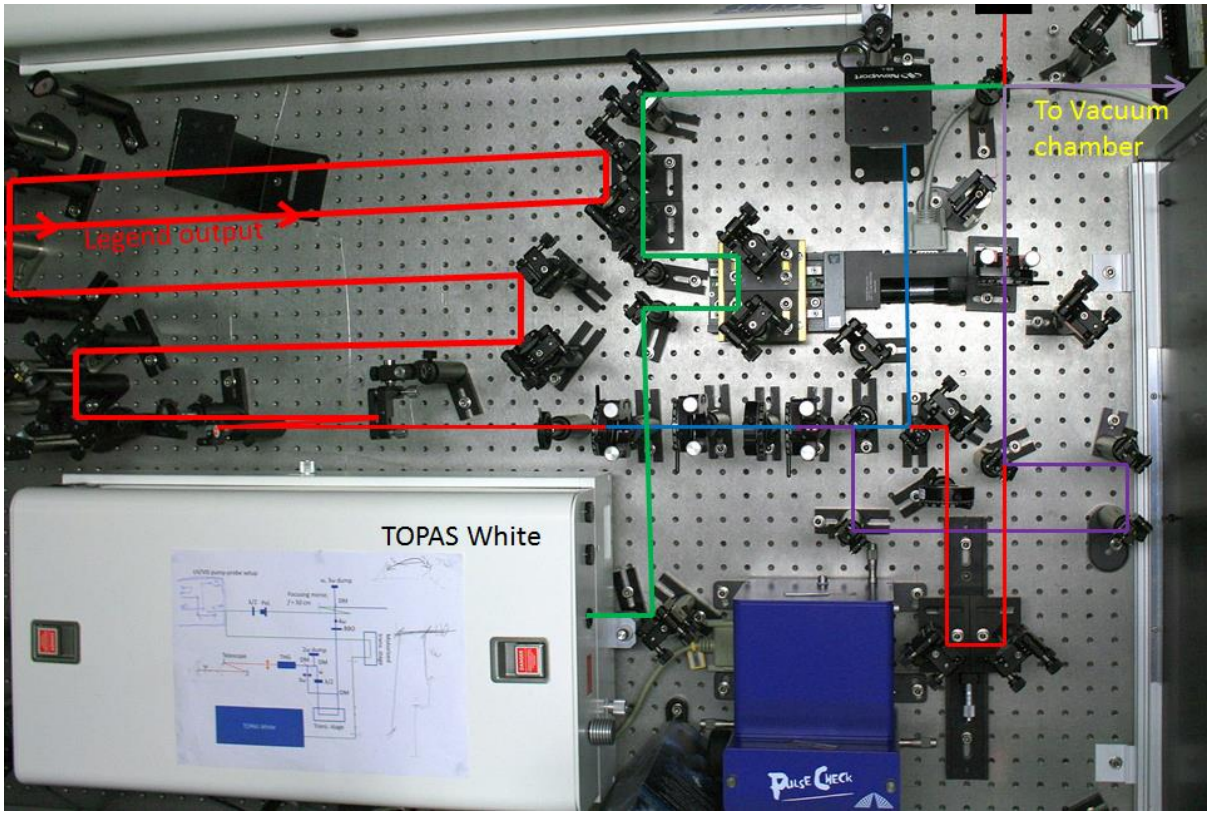

Figure 2.9: Experimental laser setup for 4th harmonic generation and TOPAS White output alignment through the translation stage. The two concave mirrors before the SHG have been replaced by a telescope (M = 0.5) using a convex (f = 10 cm) and a concave (f = -5 cm) lens as described in the text and in Figure 2.8.

2. 1. 3. Laser Beam Characterisation

The pulse duration, beam waist and laser intensity of the laser beam were determined for all laser wavelengths applied in the measurements.

The laser pulse duration was measured using a commercial autocorrelator (APE Pulsecheck) after the laser beam had passed through most of the optics used in an experiment, such as the attenuator, waveplate, polariser and optical viewport such as the one on the vacuum chamber which lets the laser beam pass through to the interaction region. The technique applied by the autocorrelator is an optical method to determine the pulse duration as a fs laser pulse cannot be measured by an electronic device

due to their typical measurable timescale being just below one nanosecond (about 7 GHz). In this approach the beam is split into two parts and recombined in a SHG BBO crystal to produce the 2nd harmonic of the incoming beam.[80] The 2nd harmonic will be most intense when both fundamental pulses overlap in time because the generation of the 2nd harmonic depends on the square of the intensity of the fundamental. Hence, the signal of the 2nd harmonic can be recorded as a function of the delay between the two fundamental pulses to obtain a second order autocorrelation. A Gaussian function gives the best fit for the temporal profile of the input laser beam, so the full width at half maximum (FWHM) of the fundamental can be deconvoluted from the measured FWHM dividing it by 1.414.[80] Typical autocorrelations measured for the output beam from the Legend and the TOPAS White set to 625 nm are displayed in Figure 2.10. For other wavelength settings than 635 nm of the TOPAS White the pulse duration is different due to the intensity profile of the WLC spectrum.

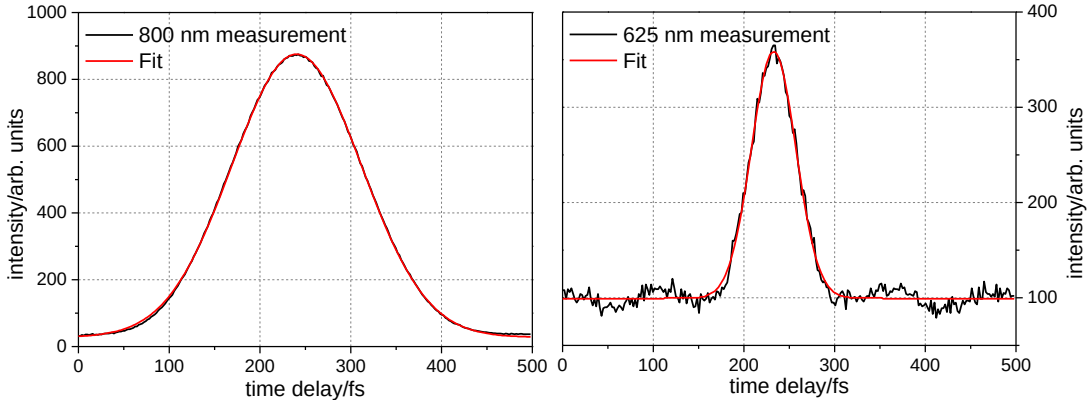

Figure 2.10: Autocorrelation of Legend output (left-hand side) and TOPAS White output set to 625 nm (right-hand side). The obtained pulse duration of the Legend output (800 nm) was (123 ± 5) fs and (44 ± 5) fs for the TOPAS White output of 625 nm.

The laser intensity has to be determined in the focus for every measurement to get comparable data for experiments conducted with different laser systems. Various techniques can be used to obtain the laser intensity such as observing the multiphoton ionisation of xenon at 800 nm via Freeman-type resonances for different laser powers which will be explained in detail in chapter 2. 2. 2. The approach used to estimate the laser intensity in this work for laser wavelengths other than 800 nm was to measure the beam waist in the focus to obtain the laser intensity by equation (2.2).

$$I_0 = \sqrt{\frac{16ln(2)}{\pi}} * \frac{E_p}{\Delta t * \pi * {w_0}^2} \approx 1.8789 * \frac{E_p}{\Delta t * \pi * {w_0}^2} \quad \textbf{(2.2)}$$

Where I_0 is the peak intensity of the laser pulse given in W/cm^2, E_p is the total pulse energy measured in J, Δt is the pulse duration and w_0 is the beam waist of the laser beam. Since the laser beam has a Gaussian spatial profile, the beam waist is the radius from the propagation axis at which the intensity decreases to 1/e^2 of the maximum peak intensity. Therefore, the intensity profile of a Gaussian beam can be described by equation (2.3) assuming the laser beam propagation is along the z axis.[84–86]

$$I(x,y) = I_0 \exp\left(-2 * \frac{(x-x_0)^2 + (y-y_0)^2}{w_0^2}\right) \quad \textbf{(2.3)}$$

With x_0 and y_0 located at the centre of the beam, while x and y are transverse Cartesian coordinates.

The total power P_0 of the laser beam is given by:

$$P_0 = I_0 \int_{-\infty}^{\infty} \int_{-\infty}^{\infty} I(x,y)dxdy = \frac{\pi}{2} I_0 w_0^2 \quad \textbf{(2.4)}$$

In this thesis the knife-edge method was employed to measure the beam waist in the focus after the lens.[84,85] For this a razor blade was placed perpendicular to the beam propagation at the focal point and behind it a power meter recorded the laser power. The experimental setup for this approach is shown in Figure 2.11.

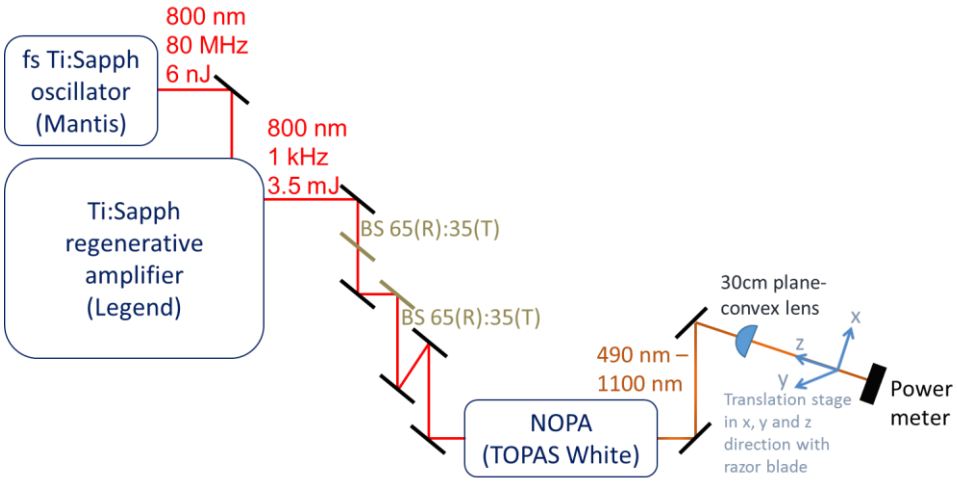

Figure 2.11: Optical setup to determine the laser beam waist in the focus using a 30 cm lens by the knife edge method.

First the razor blade was positioned at the focus of the laser beam along the z axis. Then the razor blade was moved along either the x axis or the y axis and the change of the pulse energy of the laser beam was recorded. If the knife edge is moved along the x axis, the transmitted power $P(x_a)$ is obtained by the integral:

$$P(x_a) = P_0 - I_0 \int_{-\infty}^{\infty} \int_{-\infty}^{x_a} I(x,y)dxdy \quad \textbf{(2.5)}$$

Which can be solved by applying equation (2.4) and (2.5) to:

$$P(x_a) = \frac{P_0}{2}\left[1 - erf\left(\frac{\sqrt{2}(x-x_0)}{w_0}\right)\right] \quad \textbf{(2.6)}$$

This equation can be fitted to the experimental data to obtain the beam waist in the focus or unfocussed beam. This procedure was repeated for two other positions of the razor blade along the z axis, slightly off the focus. Then the smallest measured beam waist was taken as the laser beam waist in the focus. A typical result of a beam waist measurement is shown in Figure 2.12 for 540 nm unfocussed and using a 30 cm lens.

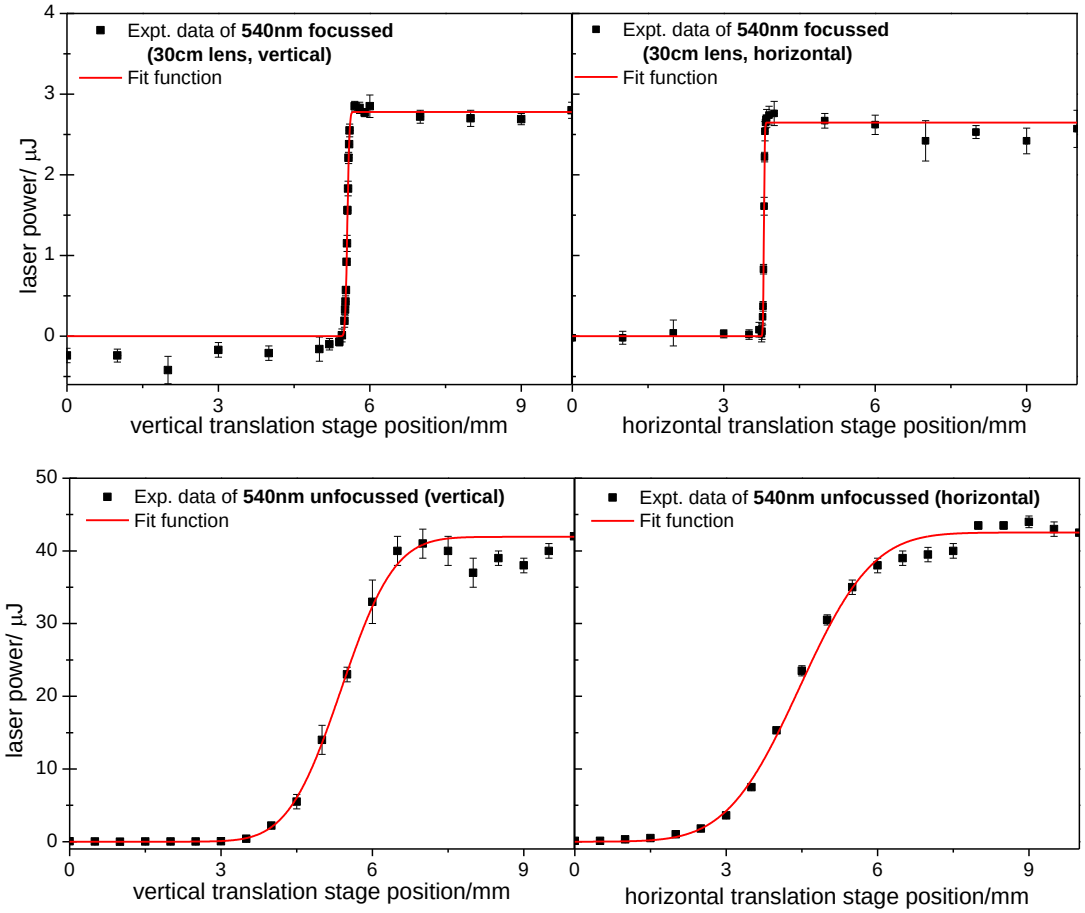

Figure 2.12: Experimental result for the focussed (top row) and unfocussed beam waist (30 cm lens) (bottom row) measurement of 540 nm using the knife edge method. The unfocussed beam waist in the vertical direction (along the x axis according to Figure 2.11) is (1.66 ± 0.10) mm and (2.27 ± 0.09) mm in the horizontal direction (along the y axis). The focussed beam waist (30 cm lens) waist in the vertical direction is (0.067 ± 0.005) mm and (0.029 ± 0.001) mm in the horizontal direction.

The focussed beam waist,w_0, can also be calculated from the measured unfocussed beam waist, w_x, with the following equation, again under the assumption of a Gaussian beam profile:

$$w_0 = \frac{2\lambda}{\pi} \times \frac{f}{2 \times w_x} \tag{2.7}$$

With λ as the laser wavelength and f as the focal length of the lens, which is 30 cm in the described setup. The calculated focussed beam waist is compared to the measured focussed beam waist in Table 2.1.

Table 2.1: Summary of the focal beam waists and areas based on the experimental measurement of the unfocussed and focussed 540 nm laser beam waist using a 30 cm lens.

Method	Vertical focussed beam waist (f=30 cm), $w_{0,v}$	Horizontal focussed beam waist (f=30 cm), $w_{0,h}$	Area in focus $A = w_{0,v} \times w_{0,h} \times \pi$
Calculated from unfocussed beam waist	(31.1 ± 1.9) µm	(22.8 ± 0.9) µm	(2228 ± 223) µm^2
Measured focussed beam waist	(67 ± 5) µm	(29 ± 1) µm	(6104 ± 666) µm^2

For the comparison it is easier to calculate the area in the focus based on the beam diameter for each axis because the laser beam spot is oval, not perfectly round (Table 2.1). Hence the measured focussed beam area is about twice as large as the estimated area from the unfocussed beam waist. However, the focal area estimated from the unfocused beam waist measurements is based on the assumption of using a perfect lens, so this estimation only gives the smallest possible focussed beam area, but in reality this focussed beam area or waist is typically larger. The results of the unfocussed beam waist measurement will still be included in further calculations of the laser intensity and the according calibration factor to have an upper limit for the laser intensity.

The obtained beam areas in the focus (Table 2.1) are used to calculate the laser intensity in the focus using equation (2.2), for example for a pulse energy of $E_p = 7.5\ \mu J$ and a pulse duration of $\Delta t =$ (35 ± 1) fs, results are shown in Table 2.2:

Table 2.2: Calculated laser intensity in the focus of a 540 nm, 7.5 µJ and (35 ± 10) fs laser beam using a 30 cm lens applying equation (2.2).

Method	Calculated laser intensity in the focus using 540 nm and a 30 cm focal lens
Estimated focal beam area	(18.1 ± 2.8) TW/cm^2
Measured focal beam area	(6.6 ± 1.1) TW/cm^2

The errors are calculated by the error propagation of the experimentally obtained values.

Subsequently the conversion factor, S_I, from the pulse energy to the laser intensity can be obtained for this particular wavelength, pulse duration and focal lens by:

$$S_I = \frac{I_0}{E_p} \tag{2.8}$$

in units of $\frac{W}{\mu J \times cm^2}$.

The results for the determination of the conversion factors of the laser intensity for 540 nm and 800 nm are summarised in Table 2.3, and are also compared to the conversion factors obtained by the xenon VMI (XeVMI) which will be explained further on in chapter 2. 2. 2.

Table 2.3: Summary of the conversion factors for the laser intensity obtained by 3 different methods for 800 nm and 540 nm.

Laser wavelength, pulse duration and focal length of the lens / Method used to determine laser intensity in the focus	800 nm, 120 fs, 30 cm lens	540 nm, 35 fs, 30 cm lens
Measured unfocussed beam waist and calculated laser intensity in the focus using the perfect lens equation (equation (2.7))	$(9.2 \pm 1.8) \cdot 10^{11} \frac{W/cm^2}{\mu J}$	$(2.4 \pm 0.5) \cdot 10^{12} \frac{W/cm^2}{\mu J}$
Measured focussed beam waist and calculated laser intensity using equation (2.2)	$(2.48 \pm 0.54) \cdot 10^{11} \frac{W/cm^2}{\mu J}$	$(8.8 \pm 1.8) \cdot 10^{11} \frac{W/cm^2}{\mu J}$
Measured laser intensity in focus using XeVMI (see chapter 2. 2. 2)	$(6.21 \pm 0.13) \cdot 10^{11} \frac{W/cm^2}{\mu J}$	$(9.36 \pm 0.10) \cdot 10^{11} \frac{W/cm^2}{\mu J}$

The comparison shows that the method of using the unfocussed beam waist measurement assuming a perfect lens gives the highest conversion factor and therefore the highest possible laser intensity. As mentioned previously this intensity conversion factor can only be used as an upper limit because the realistic experimental value is lower due to the perfect lens assumption.

In the case of the 800 nm laser beam directly from the legend output (Figure 2.6) the conversion factor calculated from the focussed beam waist measurements is less than half of the factor determined by the XeVMI method (chapter 2. 2. 2). This is probably due to the fundamental laser beam not having a perfect Gaussian beam profile, which is assumed for the laser intensity calculation based on the beam waist measurements. Therefore, these intensity conversion factors will differ more from the factor obtained by the XeVMI method because this method is based on experimental literature results of the xenon ionisation using fs laser pulses. This could also explain the larger spread of the conversion factors for 800 nm compared to 540 nm, as the output from the TOPAS White has a beam profile closer to a Gaussian beam (Table 2.3). In conclusion, for the fundamental laser beam of 800 nm the XeVMI method is more reliable for the determination of the laser intensity conversion factor than measuring the laser beam waist, probably due to the fundamental output diverting from a Gaussian beam profile.

For the 540 nm laser beam, which is the output of a NOPA (TOPAS White, see chapter 2. 1. 1) pumped by the fundamental, the conversion factor obtained by the XeVMI method lies within the error of the factor calculated from the focussed beam waist measurement (Table 2.3). Hence, the output of the NOPA has a beam shape closer to a Gaussian beam than the fundamental laser beam. Therefore, the measurement of the beam waist in the focus can be used to calculate the conversion factor for the laser intensity of the NOPA output. However, the conversion factor calculated from the beam waist measurement of the unfocussed laser beam gives only an upper limit of the conversion factor as mentioned above and should not be used for the conversion of the pulse energy into the laser intensity. The laser intensity calibration factors, which were determined for other wavelengths used in this thesis, are summarised in the appendix 8. 1.

After the laser intensity is determined and the laser pulse duration has been measured, the laser fluence, F, can be calculated in the focus:

$$F = \sqrt{\frac{\pi}{4\ln(2)}} \times \Delta t \times I_0 \approx 0.94 \times \Delta t \times I_0 \qquad \textbf{(2.9)}$$

The fluence, F, is the time-integrated intensity and usually given in units of $\frac{J}{cm^2}$.

2. 2. Photoelectron Spectrometry

This section will introduce the vacuum chamber and briefly describe where the mass spectrometer, the VMI detector and the cold trap are placed.

The vacuum chamber consists of an interaction chamber with a hot source located underneath it (Figure 2.13). The pressure in the whole vacuum chamber is usually kept below 10^{-8} mbar for the measurement.

For calibration measurements xenon gas is introduced into the chamber so the pressure is adjusted to be between 2×10^{-6} to 2×10^{-7} mbar.

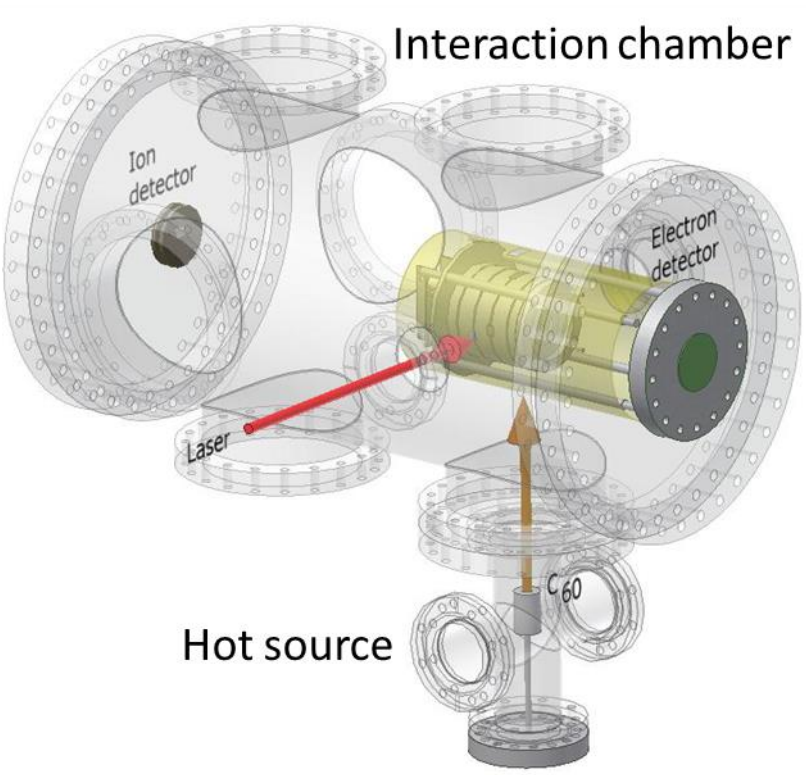

Figure 2.13: Scheme of the vacuum chamber

The hot source contains the sample which is heated to a certain temperature depending on the substance, producing a molecular beam. The C_{60} powder of 99.95 % purity and the $Sc_3N@C_{80}$ powder of 97 % purity was purchased from SES Research. The C_{82} sample was kindly provided by John S. Dennis (Queen Mary University of London). The $Li@C_{60}$ sample was provided by Idea International as a $Li@C_{60}^{+}[PF_6]^{-}$ salt of 95% purity. The coronene sample was purchased from Sigma Aldrich at 97% purity. The C_{60}, $Sc_3N@C_{80}$, $Li@C_{60}$ and coronene powders were filled into a quartz ampoule without further purification. The received C_{82} sample was dissolved in freshly distilled carbon disulphide (CS_2). The solution was then filled into a quartz ampoule and the solvent evaporated by applying a light nitrogen gas flow into the ampoule. This procedure was repeated ten times to ensure that a sufficient amount of the C_{82} sample was placed in the ampoule. The quartz ampoule containing the sample was placed in the heating rod of the hot source which is made of molybdenum. Then the C_{60}, C_{82} or $Sc_3N@C_{80}$ sample is heated to about 450 to 500 ^{o}C to transfer the molecules into the gas phase. The $Li@C_{60}$ powder is carefully heated to about 350-370 ^{o}C to sublime it whilst avoiding decomposition of the endohedral fullerene.[87] The coronene sample is also carefully heated to about 180-195 ^{o}C to avoid decomposition of the molecule during the sublimation. In this manner an effusive molecular beam is created which rises up to the interaction chamber. The laser beam is focused between the extraction plates (HV_1 and HV_2), so the molecules can be ionised and their photoproducts can be extracted to the

corresponding detector, depending on the applied potential to the extraction plates (Figure 2.13 and Figure 2.14).

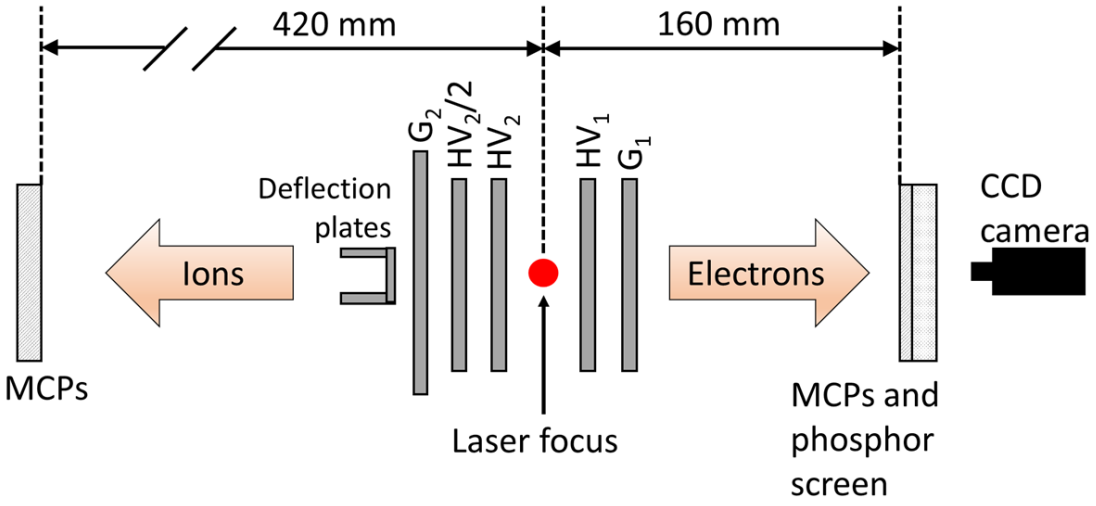

Figure 2.14: Schematic setup of the TOF-MS and the VMI

Mass spectra of positive ions can be recorded if the extraction plate HV_1 (typically about 2000 V) has a higher positive potential than HV_2 (typically about 700 V) according to the Wiley-McLaren extraction scheme.[88] The electrode $HV_2/2$ has half of the applied voltage to HV_2 to ensure a smoother potential drop. The electrode G_2 is grounded, so after the ions have been accelerated, they can enter the field free region of the TOF-MS. At the end of the TOF region the ions are detected by a pair of micro-channel plates (MCP) in the chevron configuration (Figure 2.14).

VMIs of the photoelectrons can be recorded when the extraction plate HV_2 (usually about –2000 V) has a higher negative potential than HV_1 (usually about –1450 V) whereas the electrode G_1 is grounded. The signal of the accelerated electrons is amplified by two MCPs and visualised by a phosphor screen. The image on the phosphor screen is detected by a charged-coupled device (CCD) camera (Figure 2.14).

The extraction plates are located in a horizontal µ-metal cylinder as shown in Figure 2.13 to protect the electron trajectories from outside influences like the earth's magnetic field. This µ-metal cylinder has a square opening for the laser to enter the interaction region and another opening on the other side to exit the chamber again. In the same way the µ-metal cylinder has an opening to the hot source and another one on the top side of the cylinder, so the effusive molecular beam can access the extraction plates and exit the cylinder again.

A cold trap was constructed to freeze-out the background gas and improve the signal to noise ratio in the measurements. It is either placed above the µ-metal cylinder or the TOF region of the mass spectrometer. The designed cold trap consists of a lower container and an upper container and all parts are made of stainless steel (Figure 2.15).

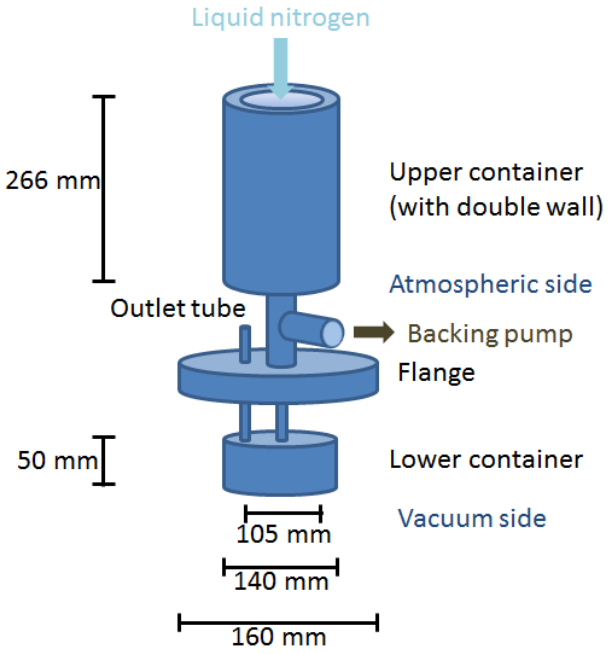

Figure 2.15: Outline of the cold trap

The upper container was taken from an old experimental setup and is double walled. The double walled space is pumped down to a pressure of about 10^{-2} mbar and is separated from the vacuum chamber. The lower container is connected with the upper container through a stainless steel tube with an inner diameter of about 6 mm. Liquid nitrogen (LN_2) is poured into the upper container to fill the lower container which is located in the vacuum chamber right above the square opening of the µ-metal cylinder for the molecular beam or above the TOF region. Trials using the cold trap showed that the pressure in the vacuum chamber decreased during the sublimation of the sample from the hot source (typically 5×10^{-8} mbar to below 10^{-8} mbar) as well as the background in the recorded mass spectra (Figure 2.16).

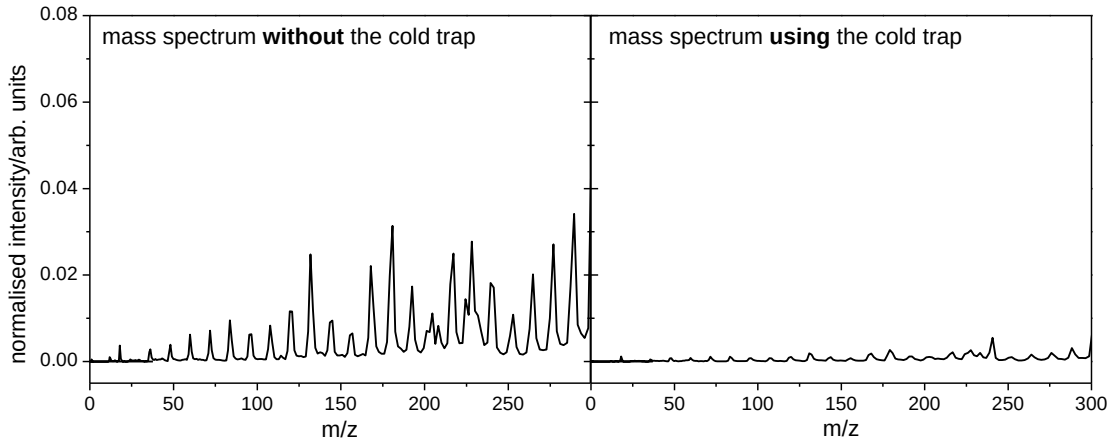

Figure 2.16: Mass spectra recorded under the same experimental conditions, except in the left spectrum the cold trap has not been used as it has been used to record the right spectrum. It is clearly that the cold trap reduced the noise in the range of about 100 – 300 *m/z* significantly.

2. 2. 1. Mass Spectrometry

As mentioned in the previous chapter a linear TOF-MS with a Wiley-McLaren arrangement of the extraction plates was used to analyse the positive ions under the same conditions as used for recording the photoelectron experiments.[88] In this manner the positive ions are extracted from the ionisation spot and accelerated into a field-free region using a two-stage acceleration, where the flight time of the ions is measured over a known distance to determine their mass to charge ratio (*m/z*).

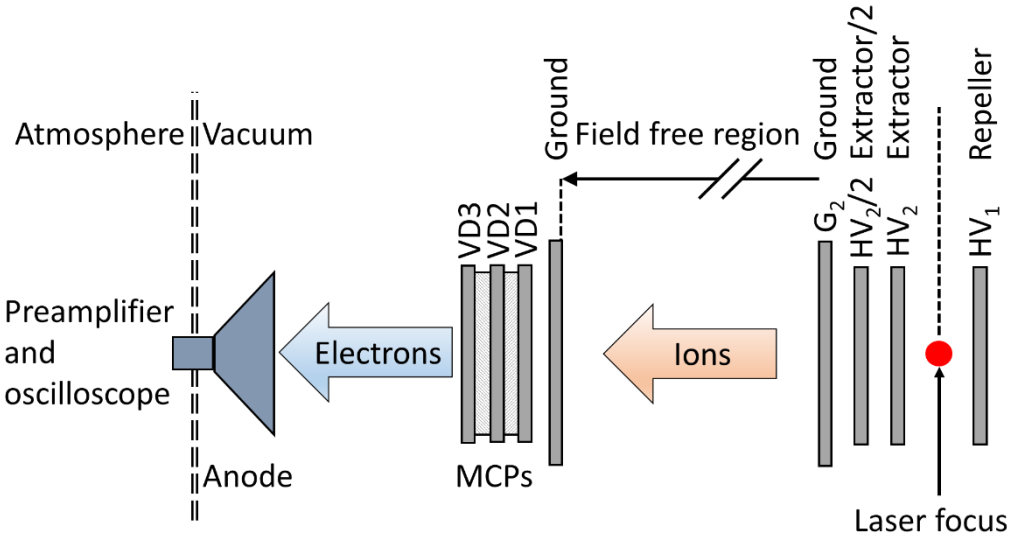

Figure 2.17: Schematic setup of the linear TOF-MS with Wiley-McLaren extraction region

The energy (E_p) gained by the ion in the extraction and acceleration region is equal to its charge (z) multiplied by the applied potential (U) which is converted into kinetic energy (E_k) in the field-free region:

$$E_p = z \cdot U \rightarrow E_k = \frac{1}{2} m \cdot v^2 \qquad \textbf{(2.10)}$$

Hence, the time the ions take to travel through the TOF tube is dependent on their *m/z* ratio. However, the ions are not being produced in a point source, so there is some geometrical variation on where the ions can be created. The Wiley-McLaren extraction arrangement compensates for this variation as the ions go through two electric fields with different strengths. Hence ions created closer to the field-free region will gain less energy and have slower velocity in the field-free region than ions produced further away from the TOF tube. The extraction voltages are optimised for the best mass resolution so the ions created with the same *m/z* ratio but at different points get to the detector at the same time. The detector used is a commercial MCP detector (Jordan TOF Products Inc., part no. C-0701) with a pair of Chevron-style MCPs (Photonis USA, part no. MCP 18/12/5 D 40:1 (PS30220)). The voltage applied to the detector, typically -4.3 kV, is divided by a voltage divider to apply voltages of about -1946 V, -1061 V

and -176 V over the electrodes VD1, VD2 and VD3, respectively. In this manner the voltage across a single MCP is not greater than 1kV and the electron cascade generated by the impact of the ion is accelerated towards the anode through each MCP (Figure 2.17). The anode detects the current produced by the electron cascade on the vacuum side and on the atmosphere side the signal is directed to a 1.8 GHz preamplifier (TA1800, FAST ComTec). The signal is amplified ten times and sent to a digital 500 MHz oscilloscope (MS06054A, Agilent Technologies) which is triggered by the photodiode signal from inside the Legend. The oscilloscope usually accumulates 200 spectra and sends them to a computer via a USB cable. A LabVIEW program (*Mass_spec.vi*) is used to control the oscilloscope and add the accumulated spectra. The TOF mass spectra are converted to *m/z* ratio through the calibration of known mass peaks in the spectrum like the xenon isotope distribution or C_{60}^{+} peaks (Figure 2.18).

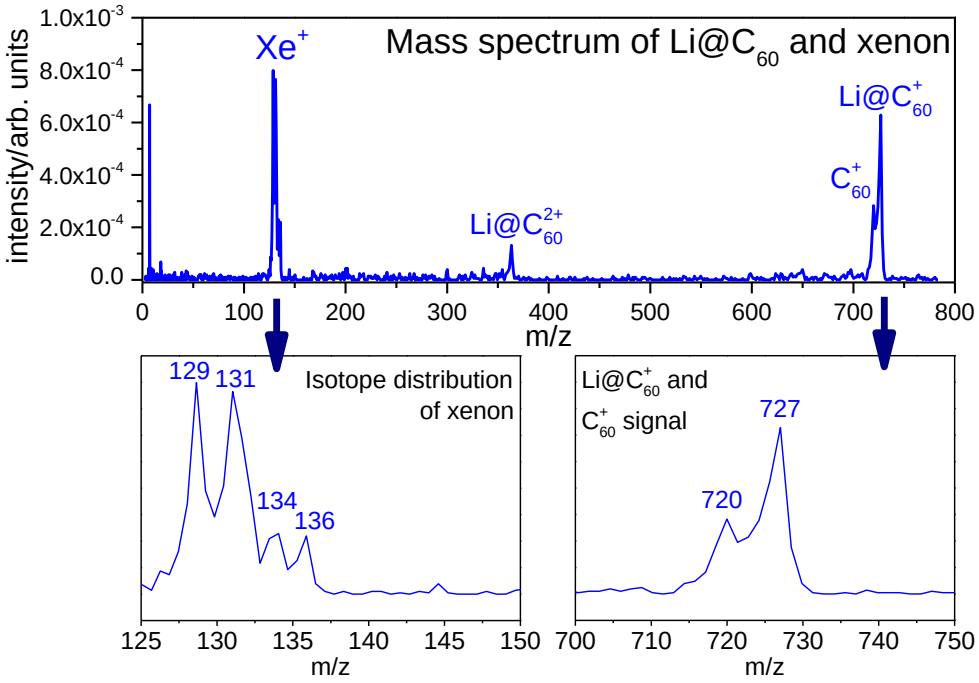

Figure 2.18: Mass spectrum of Li@C_{60} using xenon as the calibration of the mass scale.

2. 2. 2. Velocity Map Imaging

The VMI technique will be explained in this section. Also a description of how the PES and PADs are obtained will be given.

After photoionisation the released photoelectrons are detected using the VMI technique to obtain the photoelectron kinetic energy and angular distribution information. The VMI method focuses electrons with the same initial momentum through electrostatic lenses onto a single spot of a detector regardless of their original extraction position, within a few millimetres (Figure 1.4).[52] These photoelectrons are

detected using a commercial detector (Photonis USA Inc., part no. 31376). The detector consists of a pair of Chevron-style MCPs and a phosphor screen which is coupled with fibre optics to the atmospheric side. An additional electrode before the MCPs ensures a proper grounding of the field-free region in front of the detector (Figure 2.19). Typical voltages applied across the electrodes in the detector are V_{MCP} = 1750 V and $V_{Phosphor}$ = 4750 V (Figure 2.19).

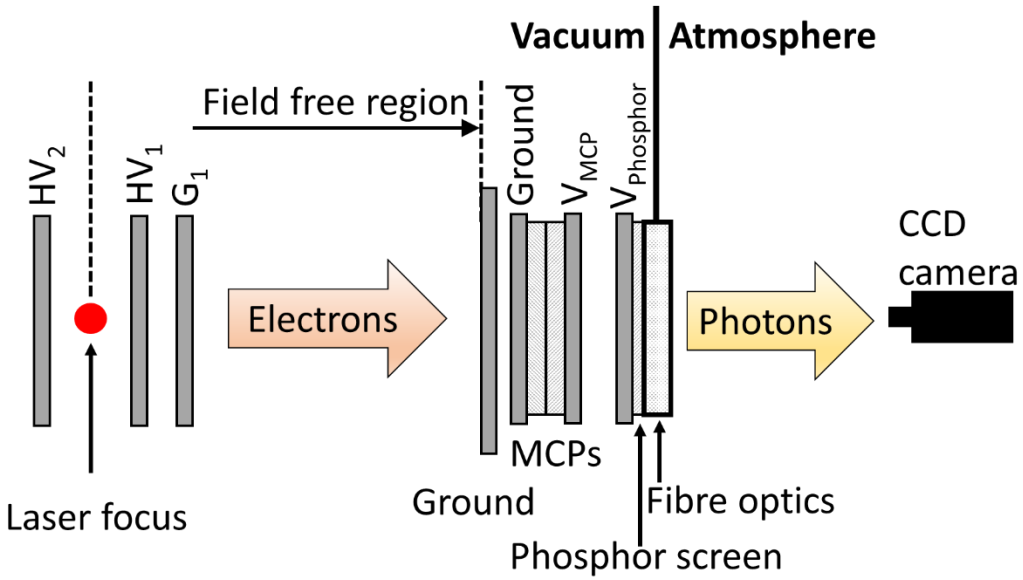

Figure 2.19: Schematic showing the arrangement of the VMI detector.

On the atmospheric side the generated image is recorded by a CCD camera (Allied Vision Technology, Stingray Model F146B) which is connected through a FireWire cable to a computer.[52] The camera resolution is 1388 x 1038 pixels with a maximum transfer rate of 15 frames per second and a maximum shutter speed of 82 ms. The images are accumulated using two different programs, one for continuous acquisition and one for single count acquisition, written in LabVIEW by Dr J. O. Johansson.[53] The continuous_acquisition.vi program adds up images over many laser shots, typically about 100,000 images. An equivalent number of images is taken as background measurements while the laser beam is blocked in front of the chamber. Afterwards the background images are subtracted from the signal images and the resulting images are summed using a MATLAB program written by Dr J. O. Johansson.[53] In the continuous acquisition measurements the number of counts per image is on the order of 10^7; however, for experiments using lower laser power the typical counts per image are 0 – 30. In this case a single count acquisition program is used which applies a user-defined threshold to each image to record only true counts and set all other pixels to zero. The centre of mass for each spot is found by a built-in routine and added as one count to the corresponding coordinate in the new image. This technique is referred to as centroiding and obtains a higher resolution as a typical one electron spot of about 5 to 10 pixels in diameter is reduced to one pixel.[89,90] Usually the centroided images have to be smoothed along the polar angle but not the radii to maintain the radial resolution before the inversion

(Figure 2.20). For this procedure a further MATLAB program is used which is adapted from work by Linda Winkler.[91]

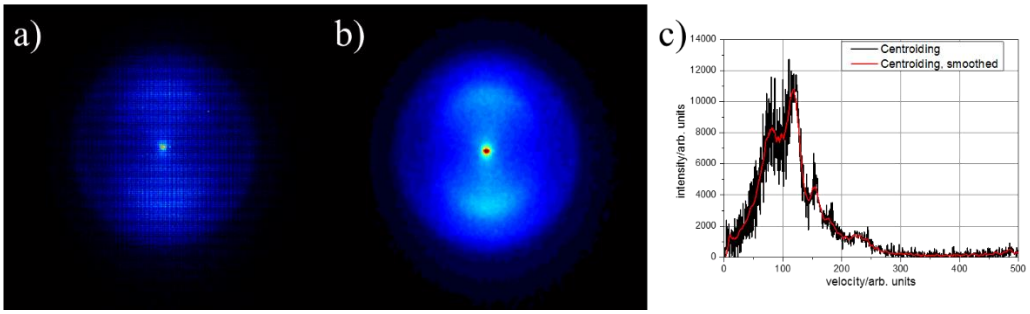

Figure 2.20: Comparison between a) a raw VMI image of C_{60} using 570 nm recorded with centroiding, b) the same VMI image smoothed and c) their corresponding angle integrated PES vs. velocity of the photoelectrons.

Any raw VMI image has to be inverted because it is a 2-D representation of a 3-D distribution of the ejected photoelectrons (for more details see chapter 1. 3). A modified version of the Polar Onion Peeling program (POP)[92] is used to perform the inversion of the raw image. Firstly the program converts the raw 2-D projection from Cartesian, G(x,z), to polar coordinates, $h(r,\theta)$. Then the contribution of events outside the x/z plane at y=0 (centre slice through the 3-D distribution), to the 2-D projection are subtracted having incrementally decreasing radii using the Abel integral (Figure 2.21 and equation (1.10)).

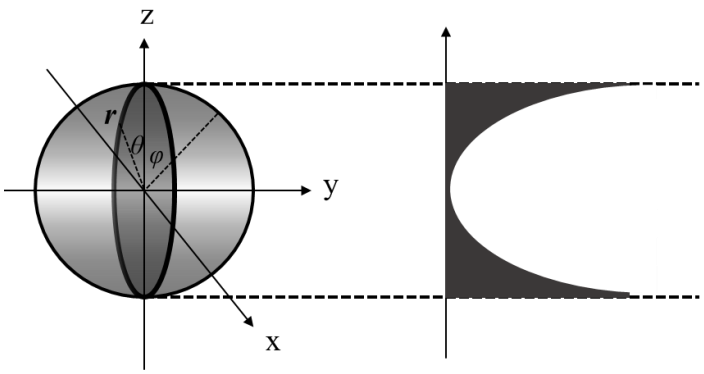

Figure 2.21: A sketch of a newton sphere showing the centre slice at *y*=0 and its projection onto a detector using the Abel transform of this distribution.

This method is based on onion peeling in polar coordinates.[93] Starting from the maximum radius $h(r_{max},\theta)$ where it is assumed that no electrons are present with kinetic energy radii larger than the detector. The intensity of the $h(r_{max},\theta)$ distribution is fitted to the angular distribution:

$$I(\theta) = N(r)\sum_{n}\beta_n(r)P_n(\cos(\theta)) \qquad (2.11)$$

with $P_n(\cos(\theta))$ as a Legendre polynomial of the *n*-th order (up to *n*=4 in the original POP program)[92], $N(r)$ as an intensity factor and $\beta_n(r)$ as the anisotropy parameter. The basis function used for a certain

radius is an idealised radial distribution function to generate an isotropic polar image, $h_{ideal}(r,\theta)$ for electrons at the radius r_{max}, in brief $h_{ideal}(r_{max};r,\theta)$. This image is used with the experimentally observed intensity factor and anisotropy parameter to get the idealised image:

$$h_{fit}(r_{max};r,\theta) = h_{ideal}(r_{max};r,\theta)\, N(r) \sum_{n} \beta_n(r) P_n\left(\frac{r}{r_{max}}\cos(\theta)\right) \qquad \textbf{(2.12)}$$

With the $\frac{r}{r_{max}}$ factor accounting for the polar pixel number at radius, r, compared to the number at the maximum radius, r_{max}. $h_{fit}(r_{max};r,\theta)$ represents the φ-contribution of electrons with the same kinetic energy as electrons at r_{max} which is subtracted from the raw image, $h(r,\theta)$. This procedure is repeated for incrementally decreasing radii until the centre is reached. Whenever the h_{fit} image has been calculated for each radius and removed from the raw $h(r,\theta)$ image, the centre slice of the 3-D distribution in the x/z plane at y=0, or $\varphi = 0$ respectively, will be left and is described as an inverted image.

As previously mentioned, only Legendre polynomials up to *n*=4 are used in the original POP program. The authors of the original POP program were mainly concerned with one- or two-photon processes and included only up to *n*=4 because the number of the polynomials depends on the amount of the photons absorbed during the process. Since the processes concerning the results of this thesis contain the absorption of more photons, the program has been modified by Dr Gordon Henderson to include Legendre polynomials up to *n*=10.[74] The modified program, POP_092011.m, is written in MATLAB and named GPOP.

The inverted image is retrieved as a function of the measured values which are proportional to the number of electrons arriving at a certain point. The corresponding velocity distribution is extracted through the integration over all angles as a function of CCD camera pixels. To obtain the PES as a function of the kinetic energy of the electrons, the inverted image is calibrated with a well-known PES like the spectrum of xenon at the same measurement settings.[92,94] The resonant photoionisation of xenon via Freeman Resonances has been extensively studied and the electronic structure of xenon is well known.[94–97] Therefore the characteristic PES of xenon can be used to calibrate the velocity scale of PES[94] recorded at different laser wavelengths and also the laser intensity for a wavelength of 800 nm.[96]

2. 2. 2. 1. Calibration of Photoelectron Kinetic Energy Distributions

For the conversion of the kinetic energy scale from CCD camera pixels to eV in the PES usually the difference between two peaks in the XeVMI is used to calculate the calibration factor. Direct multiphoton absorption in xenon atoms, resulting in ATI peaks, can be used for calibration because the peaks are separated by the energy of one photon due to the atom absorbing one or more photons

coherently than are needed to ionise it. Depending on the laser wavelength used for the ionisation of xenon, either the peak of the $^2P_{3/2}$ ion state and the following ATI peaks of the same state can be analysed for the calibration or the energy difference of 1.306 eV between the two xenon ion fine structure levels, $^2P_{3/2}$ and $^2P_{1/2}$, can be used.[94,98] An example of a XeVMI calibration spectrum using 570 nm, (39 ± 1) fs, 29 µJ with extraction voltages set to HV1= -1450 V and HV2= -2000 V is shown in Figure 2.22.

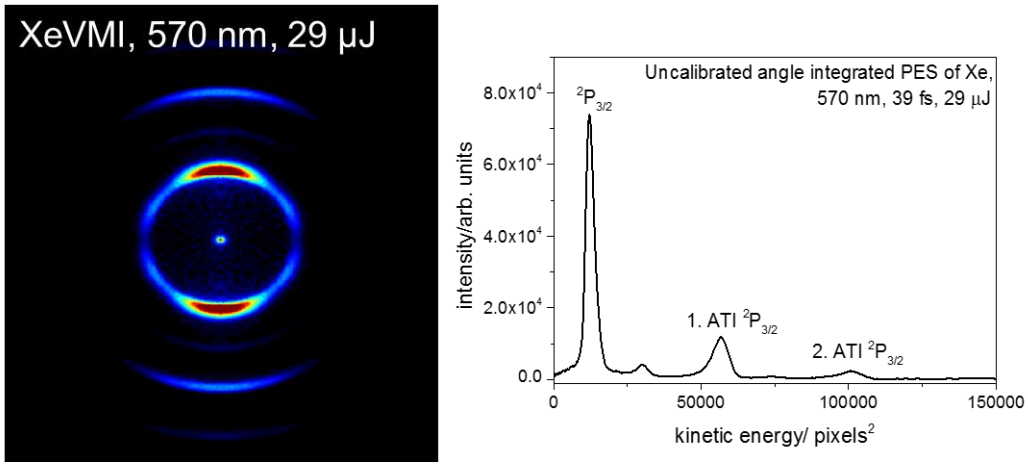

Figure 2.22: Inverted XeVMI on the left and on the right the corresponding angle integrated PES using 570 nm, (39 ± 1) fs, 29 µJ with an uncalibrated kinetic energy scale in pixels^2.

On the basis of the fit functions the peak positions are found to be at (12319 ± 13) pixels^2, (56408 ± 39) pixels^2 and (100183 ± 113) pixels^2 for the $^2P_{3/2}$, 1. ATI $^2P_{3/2}$ and 2. ATI $^2P_{3/2}$ state respectively. Assuming the average distance between the analysed peaks in pixels^2

$$\Delta_{P-1ATI} = x_c\left(1.ATI\ \ ^2P_{3/2}\right) - x_c\left(\ ^2P_{3/2}\right) = (56408 - 12319) = 44089 \pm 41 \quad \textbf{(2.13)}$$

$$\Delta_{1ATI-2ATI} = x_c\left(2.ATI\ \ ^2P_{3/2}\right) - x_c\left(1.ATI\ \ ^2P_{3/2}\right) = (100183 - 56408) = 43775 \pm 120 \quad \textbf{(2.14)}$$

$$\emptyset(\Delta) = \frac{\Delta_{P-1ATI} + \Delta_{1ATI-2ATI}}{2} = 43932 \pm 63 \quad \textbf{(2.15)}$$

is equal to the photon energy (2.18 eV), the calibration factor *k* is calculated as follows:

$$k = \frac{2.18\ eV}{43932\ pixels^2} = (4.962 \pm 0.007) \times 10^{-5}\ \frac{eV}{pixels^2} \quad \textbf{(2.16)}$$

The resulting calibration factor is applied to the kinetic energy scale and the calibrated PES is obtained as shown in Figure 2.23.

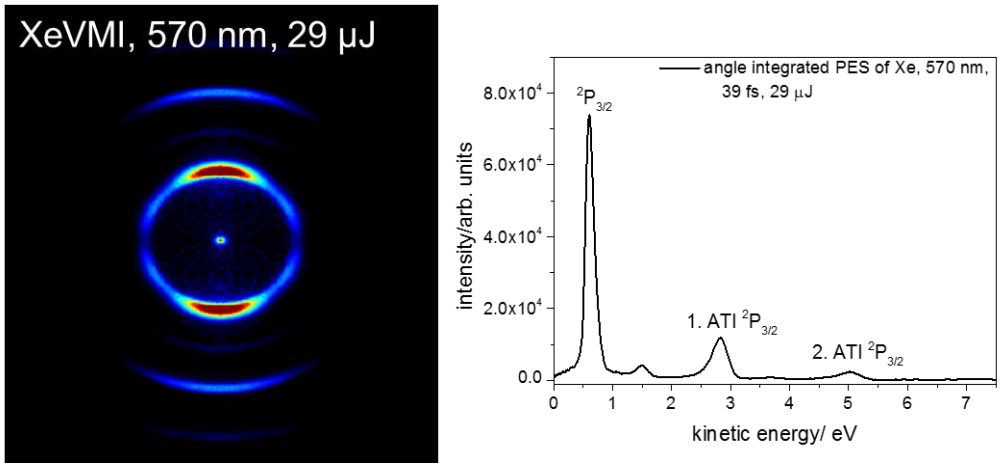

Figure 2.23: Inverted XeVMI on the left and on the right the corresponding angle integrated PES using 570 nm, (39 ± 1) fs, 29 µJ with a calibrated kinetic energy scale in eV.

Likewise the calibration factor can be obtained from the XeVMI for some other wavelengths using the energy difference of 1.306 eV between the xenon ion peak states, $^2P_{3/2}$ and $^2P_{1/2}$.[94,98] An example for a resulting calibrated PES of xenon is shown in Figure 2.24 for 540 nm, (35 ± 10) fs, 36 µJ.

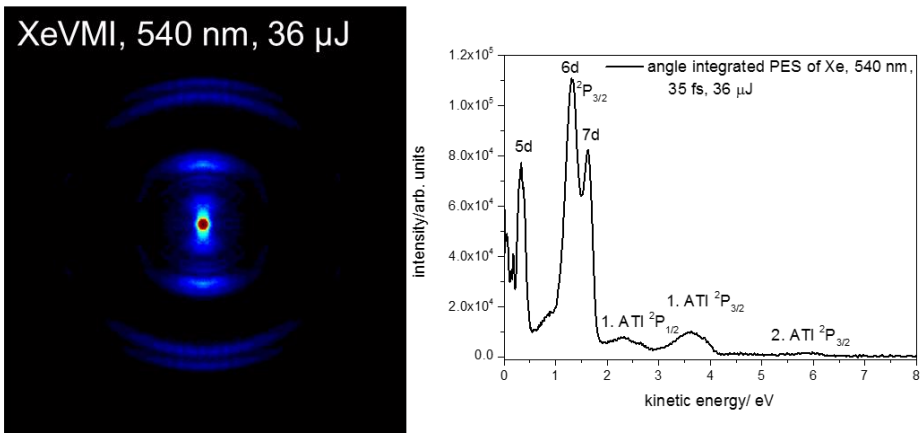

Figure 2.24: Inverted XeVMI on the left and on the right the corresponding angle integrated PES using 540 nm, (35 ± 10) fs, 36 µJ with a kinetic energy scale in eV using a calibration factor of $k = (4.8 \pm 0.1) \times 10^{-5} \frac{eV}{pixels^2}$.

In the same manner the calibration of the kinetic energy scale is conducted for every measurement series performed where the laser wavelength or alignment or the extraction voltages have been changed.

2. 2. 2. 2. Laser Intensity Calibration using Multiphoton Ionisation of Xenon

As mentioned previously, the laser intensity in the focus cannot be only determined by the measurement of the laser beam waist but also through the analysis of a series of XeVMI spectra as a function of laser power. This approach is based upon the approximation of the AC Stark shift as the ponderomotive shift, U_p, of the states in the xenon atom introduced by the electric field of the fs laser beam (chapter 1. 1). Therefore, the Stark shift will increase with laser intensity and certain states can be shifted into resonance which will open different ionisation channels, termed as REMPI.[94,96] This principle is shown in the following schematic diagram of some xenon Rydberg states shifting with increasing laser intensity (Figure 2.25).[96,98]

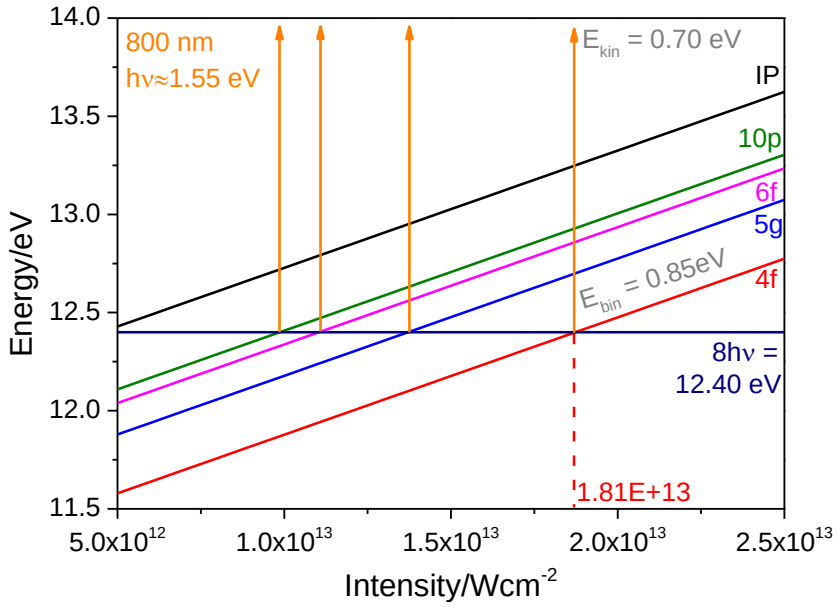

Figure 2.25: Schematic diagram of resonance shifting in xenon at 800 nm of the 4f (red line), 5g (blue line), 6f (pink line) and 10p (green line) states considering the ponderomotive shift depending on the laser intensity.[98]

On the basis of this scheme and the literature[96] the 4f Rydberg state of xenon will be shifted into resonance at a laser intensity of about 18.1 TW/cm^2 using 800 nm. Therefore, a series of XeVMIs using 800 nm, (120 ± 5) fs laser pulses are taken as a function of laser power and the results are shown in Figure 2.26.

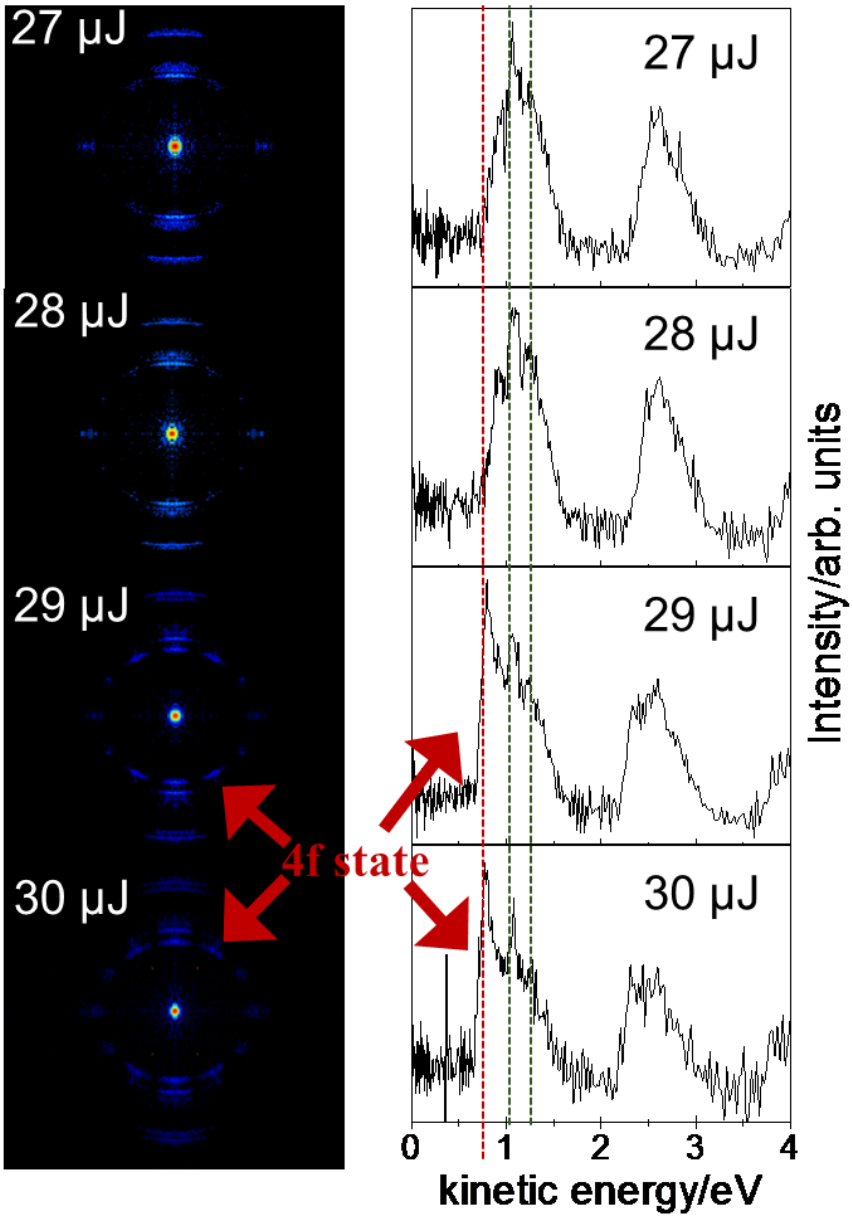

Figure 2.26: Inverted VMI images of xenon and the corresponding angle integrated PES for different laser pulse energies (as labelled in the figure) using 800 nm, 120 fs and a 30 cm focal lens. The 4f state is indicated with the arrows when it shifts into resonance. The green dashed lines show the position of the 5g (1.00 ± 0.05 eV) and 6f (1.17 ± 0.05 eV) or 10p (1.23 ± 0.05 eV) state respectively.

The angular distribution of the 4f Rydberg state displays four pronounced nodal planes which is a distinctive pattern for the contribution of partial waves of at least $l = 4$ (g waves) to this photoionisation channel.[96] This characteristic is detected in the VMIs in Figure 2.26 at a laser pulse energy of 29 µJ and 30 µJ, but not for a pulse energy of 28 µJ and 27 µJ. Also, the PES (Figure 2.26) show a peak appearing around 0.7 eV for laser intensities of 29 µJ and 30 µJ which is expected for the 4f state (see Figure 2.25).[96] On the basis of these results it can be estimated that a pulse energy of 29 µJ for the fundamental laser output from the regenerative amplifier of 800 nm, 120 fs using a 30 cm focal lens corresponds to

a peak laser intensity of 18.1 TW/cm^2 in the interaction region. This leads to a laser peak intensity calibration factor of

$$S_I = \frac{18.1 \times 10^{12}\ W/cm^2}{29\ \mu J} = (6.21 \pm 0.21) \times 10^{11}\ \frac{W/cm^2}{\mu J} \qquad \textbf{(2.17)}$$

This obtained intensity calibration factor is compared to the calibration factors calculated from the laser beam waist measurement and discussed in more detail in section 2. 1. 3, Table 2.3. The conclusion of this comparison is that the calibration factor using the XeVMI is most accurate for the laser intensity calibration in the case of the 800 nm laser beam directly from the regenerative amplifier and falls in between the values estimated from the measurements of the beam waist focussed and unfocussed (see chapter 2. 1. 3).

According to this principle a similar laser intensity calibration is conducted to determine the calibration factor for the laser beam of 540 nm from the NOPA (TOPAS White) output (Figure 2.7). In this case a photon energy of about 2.30 eV (540 nm) cannot reach an f Rydberg state in the xenon atom resonantly through multiphoton ionisation, but at a laser intensity of about 13.1 TW/cm^2 the 6d Rydberg state should be shifted into resonance using 540 nm (see Figure 2.27) resulting in the $^2P_{3/2}$ state of the xenon ion.

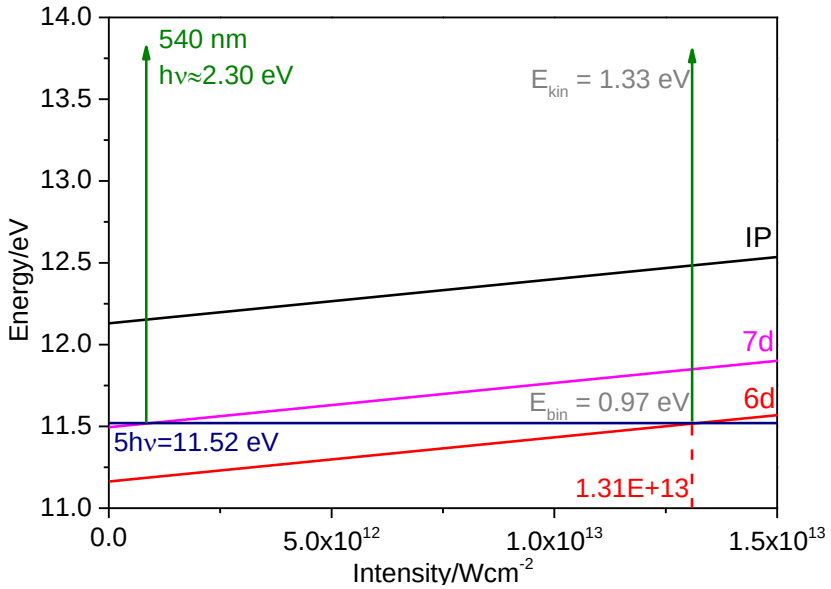

Figure 2.27: Schematic diagram of resonance shifting in xenon at 540 nm of the 6d (red line) and 7d (pink line) states considering the ponderomotive shift depending on the laser intensity.

Therefore, a series of XeVMIs has been recorded for different laser pulse energies (12 µJ, 14 µJ, 20 µJ and 36 µJ) using 540 nm to observe at which laser pulse energy the 6d Rydberg state is shifted in resonance and becomes visible in the spectrum (Figure 2.28).

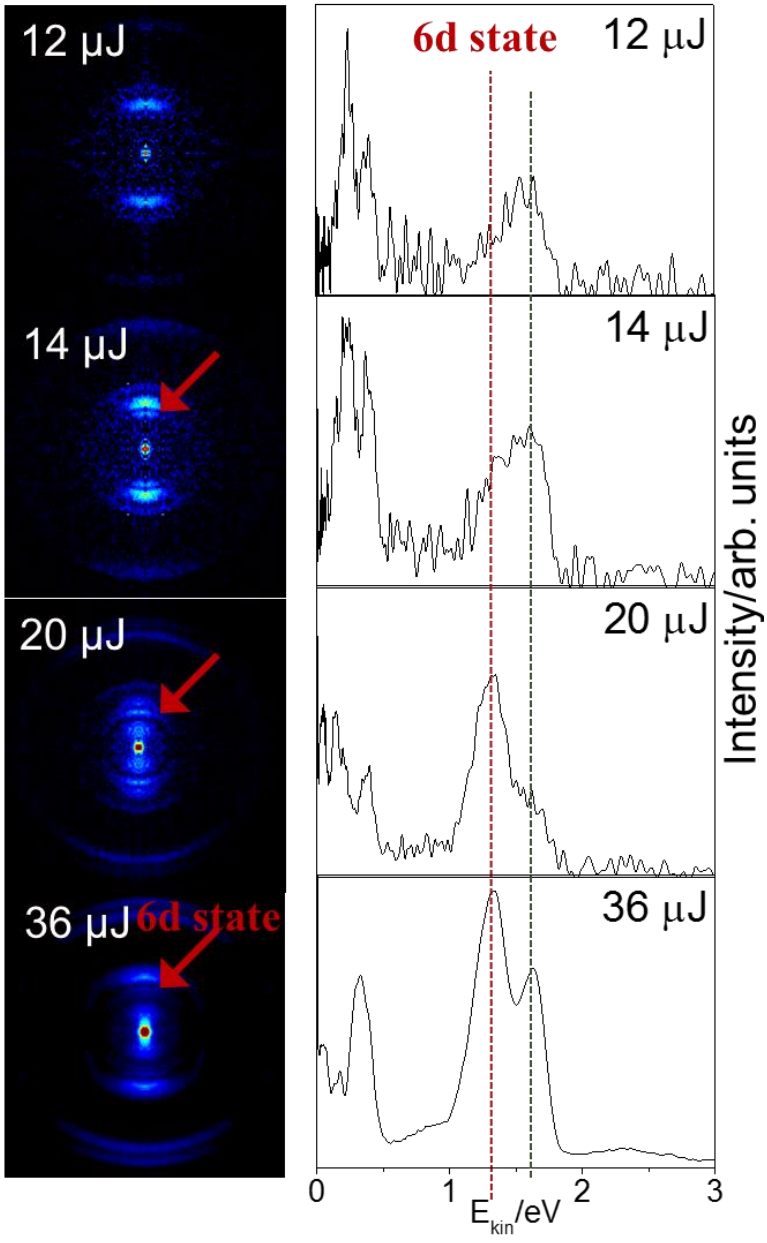

Figure 2.28: Inverted VMI images of xenon and the corresponding angle integrated PES for different laser pulse energies (as labelled in the figure) using 540 nm, (35 ± 10) fs and a 30 cm focal lens. The 6d state is indicated with the arrows when it shifts in resonance and a red dashed line in the PES.

According to the results in Figure 2.28 the 6d Rydberg state of xenon appears in the spectra at a laser pulse intensity of 14 µJ. Therefore, the pulse energy of 14 µJ can be estimated to correspond to a laser intensity of 13.1 TW/cm^2 for a laser output from the NOPA (TOPAS White) of 540 nm, (35 ± 10) fs using a 30 cm focal lens. The resulting calibration factor is

$$S_I = \frac{13.1 \times 10^{12}\, W/cm^2}{14\ \mu J} = (9.36 \pm 0.67) \times 10^{11} \frac{W/cm^2}{\mu J} \qquad \textbf{(2.18)}$$

In section 2. 1. 3, Table 2.3 this calibration factor is compared to another method used to obtain the laser intensity calibration factor in more detail, as mentioned previously. The outcome of the comparison for the laser beam from the NOPA (TOPAS White) is that the beam waist measurements of the focus are reasonably good to determine the calibration factor for the laser intensity. The calibration factor which has been obtained by measuring the focal beam waist and will be used further on for experiments using a 30 cm focal lens and a 540 nm, (35 ± 10) fs laser beam, is

$$S_I = (8.8 \pm 1.8) \times 10^{11} \frac{W/cm^2}{\mu J} \qquad \textbf{(2.19)}$$

After the laser intensity has been determined, the laser fluence, *F*, can be calculated as previously described in chapter 2. 1. 3.

2. 2. 2. 3. Analysing Photoelectron Angular Distributions

The position-sensitive VMI detector (Figure 2.19) does not only provide angle integrated PES but also provides information on the angular distribution of the photoelectrons. This information can be accessed through the division of the VMI image into angular segments of 10° intervals using the MATLAB program Pizza_PES_from_inverted_VMI.m written by Dr Olof Johansson to extract the angular-resolved PES (Figure 2.29).

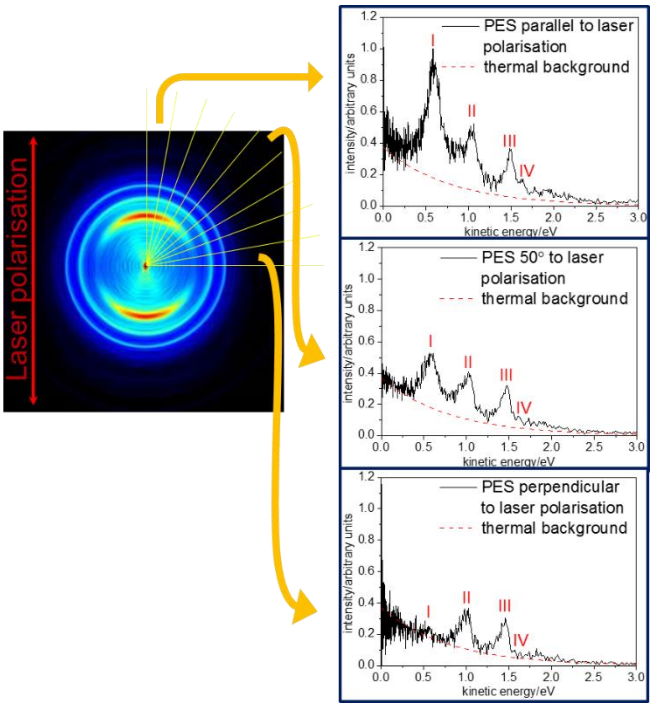

Figure 2.29: Inverted VMI of C_{60} using 500 nm, (4.5 ± 0.3) TW/cm² and (90 ± 10) fs laser pulses and the corresponding angular-resolved PES. Adapted from ref.[77]

After the subtraction of the thermal electron background Lorentzian peaks are fitted to the peaks in the angular-resolved PES by eye (fitting procedure is explained in appendix 8. 2).[30] Then the PAD for a specific kinetic energy can be experimentally obtained by plotting the area of a particular peak as a function of polar angle (Figure 2.30) and fitting equation (1.12) to the data points to determine the β value (see chapter 1. 3).[56–59]

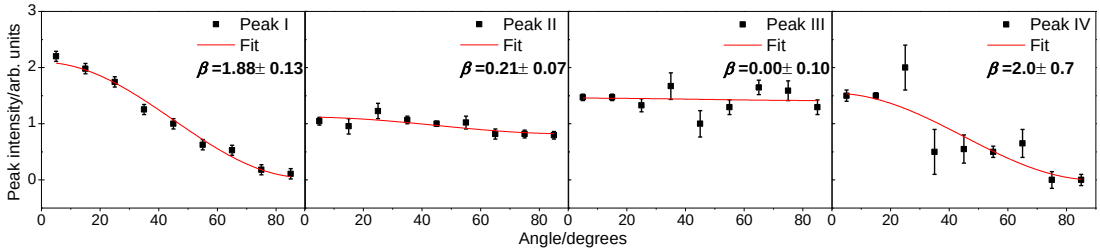

Figure 2.30: PAD of the labelled peaks in Figure 2.29 at 540 nm, (10 ± 1) TW/cm^2, (35 ± 10) fs laser irradiation of C_{60}.

The experimentally determined β value can be compared to results of TD-DFT calculations of the anisotropy parameter calculated for a given excited state to aid the assignment of the peaks. These theoretical calculations have been carried out by Prof Françoise Remacle and Dr Benoît Mignolet and the results are discussed in chapter 3. 1.[7,75,77]

2. 3. Theoretical Methods

In this thesis time-dependent (TD) and time-independent DFT was used to investigate the electronic structure of PAHs. The time-independent DFT method is based on the two Hohenberg-Kohn theorems.[99] The first Hohenberg-Kohn theorem shows that an electron density, $\rho(r)$, depending on three spatial coordinates, determines the ground state properties of a many-electron system. This gives the basis for decreasing a many-body problem of N electrons with $3N$ spatial coordinates to a problem with just three spatial coordinates, by using functionals of the electron density. Furthermore, the time-dependent DFT is developed through the extension of this theorem to the time-dependent domain (which will be described later on). The second Hohenberg-Kohn theorem, also called the variational theorem, shows that the energy functional, $E[\rho(r)]$, is minimal when the electron density corresponds to the density in the ground state. Hence the Kohn-Sham approach is introduced with a system of non-interacting electrons moving in an effective potential.[100] However, the created density of this fictitious non-interacting system is the same as for a system of interacting electrons. The Kohn-Sham equation[100] is:

$$\varepsilon_i \varphi_i = \left(-\frac{\hbar^2}{2m}\nabla_i^2 + V_{ext}(r) + \int d^3r' \frac{\rho(r')}{|r-r'|} + V_{XC}(r_i) \right) \varphi_i \qquad \textbf{(2.20)}$$

In which the first term is the kinetic energy of an electron in the orbital φ_i, the second term, $V_{ext}(r)$, describes the classical attractive electron nuclei Coulomb potential, the third terms stands for the Coulomb interaction between the charge distribution of all other electrons with the electron in the orbital φ_i (classical Coulomb repulsion) and the last term represents the exchange correlation potential that is given by the first functional derivative of the exchange-correlation energy functional:

$$V_{XC}(r) = \frac{\delta E_{XC}[\rho(r)]}{\delta \rho(r)} \tag{2.21}$$

$V_{XC}(r_i)$ depends on the density, so equation (2.21) has to be solved self-consistently. The exact exchange correlation potential is not known, therefore, approximations are made to find an expression for $V_{XC}(r_i)$. There are many different functionals and the choice of a functional should depend on the character of the states of interest and its intended application. For the study of diffuse excited states and Rydberg states, long-range corrected functionals such as CAM-B3LYP are used in this work.

The wavefunction is expressed by a single Slater determinant composed of Kohn-Sham orbitals $\varphi_i(r)$ and therefore the density is given by the sum over all occupied orbitals:

$$\rho(r) = \sum_{j=1}^{n} |\varphi_i(r)|^2 \tag{2.22}$$

For the calculation of the excited states time-dependent DFT is used, so the time-dependent Schrödinger equation has to be solved to analyse the response of the molecule to a time-dependent perturbation, in this case for a time-dependent electric field.

$$i\hbar \frac{\partial}{\partial t} \Psi(r,t) = \hat{H} \Psi(r,t) \tag{2.23}$$

The Runge Gross theorem[101] is the foundation of TD-DFT and shows that there is a unique mapping for a given initial wavefunction between its time-dependent density, $\rho(r,t)$, and the time-dependent external potential. Since the potential is defined up to an additive purely time-dependent function, only the phase of the wavefunction can change but not its density. Including the analogues of the first and second Hohenberg-Kohn theorems[99], which were described previously, the time-dependent wavefunction $\Psi(r,t)$ is determined up to a time-dependent phase factor $\alpha(t)$:

$$\Psi(r,t) = \Psi[\rho(t)](t) e^{-i\alpha(t)} \tag{2.24}$$

Hence the one electron time-dependent Schrödinger equation is expressed as:

$$i\frac{d}{dt}\varphi_i(r,t) = \left(-\frac{\hbar^2}{2m}\nabla_i^2 + v(r,t) + \int d^3r' \frac{\rho(r',t)}{|r-r'|} + \frac{dA_{XC}[\rho]}{\delta\rho(r,t)}\right)\varphi_i(r,t) \tag{2.25}$$

The term $v(r,t)$ states the sum of the classical Coulomb potential and the external time-dependent potential which contains the electric field $V(r,t)$. In the parenthesis the last term describes the exchange and correlation effects and is also known as the exchange-correlation kernel, i.e. the functional derivative of the exchange-correlation potential. As well as in the time-independent case, the time-dependent Kohn-Sham theory is accurate but the exchange correlation action function, $A_{XC}[\rho]$, is unknown and approximations have to be made.

As previously described for the time-independent case, the time-dependent wavefunction is represented by a single Slater determinant composed of time-dependent single electron orbitals, $\varphi_i(r)$, and the time-dependent density is the sum of the density of each occupied orbital.

$$\rho(r,t) = \sum_{j=1}^{n} |\varphi_i(r,t)|^2 \qquad \textbf{(2.26)}$$

The program Gaussian 09[102] was used which included the quantum chemistry Kohn-Sham DFT implementation with different functionals and Pople basis sets (in particular split valence double zeta basis sets). In this case each basis function consists as a sum of Gaussian primitives. The calculations were performed at Prof. Françoise Remaçle's computational facilities at the University of Liège.

In the first run the electronic structure with excited states was modelled for a smaller PAH using different functionals and basis sets to analyse the best agreement with literature data and to keep the computational time short. In this case naphthalene was chosen to investigate the most suitable functional and basis set. The functional CAM-B3LYP and the basis set 6-31(2+)+G(d,p) were found to have the best agreement with the literature and the shortest computational time (for more details on the results see chapter 1), this combination was then used to model other PAHs.

Firstly, a ground state optimisation was conducted and the resulting structure was used for the TD-DFT calculations with its symmetry superimposed. The excited states were calculated up to the first 100 states. The output orbitals were viewed in GaussView, adjusting the isocontour value, and the visual shape of the electron density was used to determine the orbital as s, p_z, p_x, p_y, d_{xy}, d_{yz}, d_{x2-y2} and d_{z2} states.

Furthermore, Benoît Mignolet computed the Dyson orbitals of the SAMO-like excited states identified in the studied PAHs, and modelled the PAD of these states depending on the kinetic energy of the outgoing electron.[75] Dyson orbitals correspond to the wavefunction of the ionised electron.[75,103] They are defined as the one-electron wavefunction (also called quasi-particle wavefunction) obtained from the overlap of the many-electron wavefunction of the neutral molecule and that of the cation.[75,103] A given Dyson orbital consists of several SAMO/Rydberg orbitals since the excited states are composed of several transitions from the HOMO to SAMO and/or Rydberg orbitals of the same symmetry.[75,103] The SAMO states consists predominantly of SAMO excitations and the Rydberg states of Rydberg excitations.[75,103]

3. Investigation of Superatom Molecular Orbitals (SAMOs) in Fullerenes

3. 1. Introduction

The SAMOs are diffuse excited electronic states similar to Rydberg orbitals with low angular momentum quantum numbers, l = 0, 1, 2, and a principal quantum number, n, of at least 3 (based on the number of nodes).[7] In contrast to conventional Rydberg states, the SAMOs are centred in the middle of the fullerene cage and possess electron density inside the cage, due to the hollow cage structure (Figure 3.1).[7,33,75]

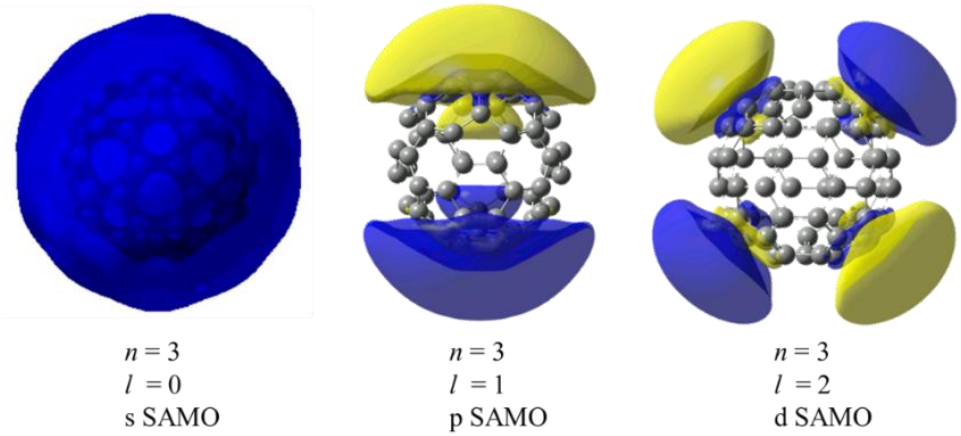

Figure 3.1: Isocontour amplitudes (0.002 $|e|/a^3$) of the SAMOs of C_{60} calculated at the TD-DFT/CAM-B3LYP/6-31+G(d) level.[75]

These states were originally assigned in C_{60} by Petek *et al.* using STM on a single C_{60} molecule absorbed on a copper surface (see chapter 1. 5, Figure 1.16).[31] In the gas phase the SAMO states could be identified in C_{60} and C_{70} by Johansson *et al.* using angular-resolved photoelectron spectroscopy (which was described in chapter 1. 5).[7] A typical VMI image and the corresponding PES of C_{60} are given in Figure 3.2.[7]

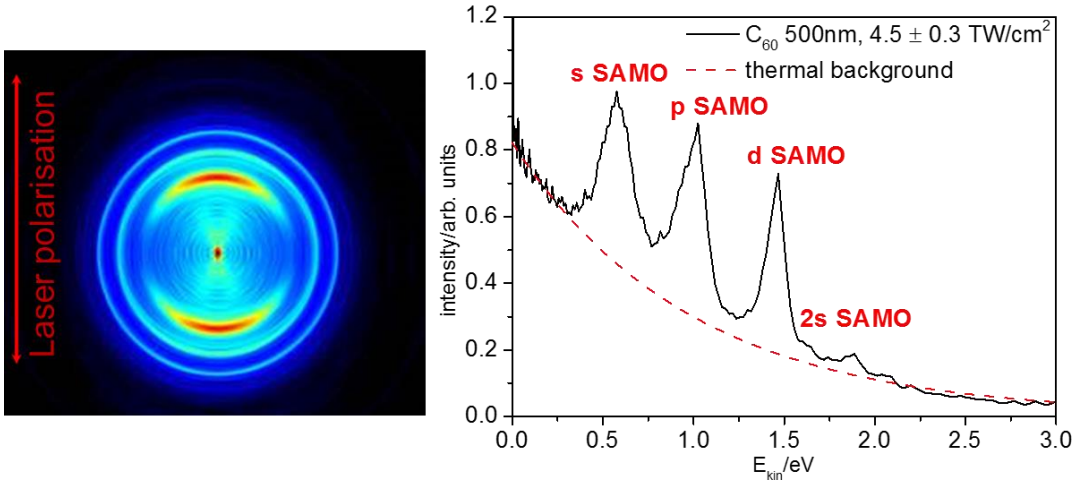

Figure 3.2: Inverted VMI image of C_{60} at 500nm, (90 ± 10) fs, (4.5 ± 0.3) TW/cm² is shown on the left hand side and the corresponding angle-integrated PES on the right hand side. The thermal electron background and the peak assignment is displayed in the PES (adapted from ref.[74]).

The spectrum shows a thermal electron background (red dashed line in Figure 3.2, also for C_{70}[7,74]) which is caused by thermal emission of electrons from the electronic subsystem before the absorbed energy couples to the vibrational subsystem, as introduced in chapter 1. 5 and will be discussed in further detail in chapter 1. The second feature of the C_{60} and C_{70} PES is the peak structure superimposed on the thermal background (Figure 3.2) which has been determined to originate from the SAMO states (as introduced in chapter 1. 5). As mentioned in chapter 2. 2. 2, after the subtraction of the thermal electron background, Lorentzian peaks are fitted to the peak structure (explained in detail in appendix 8. 2) to analyse their properties, like peak position, width and the PAD of the peak. In Figure 3.3 an example of a peak fit result is shown for C_{60} at 500 nm.

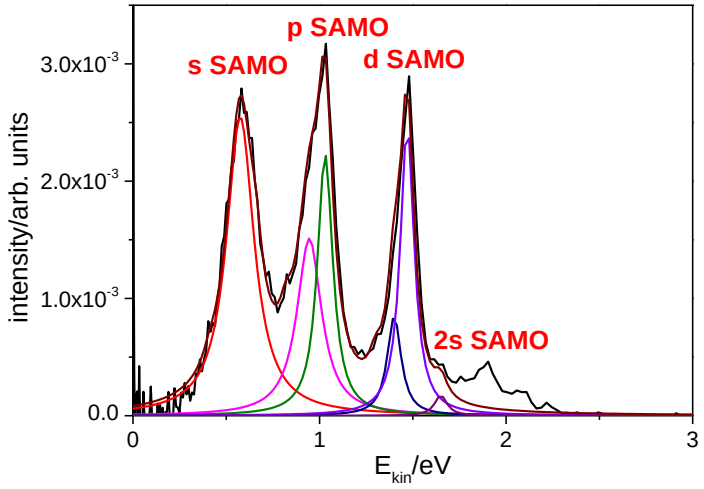

Figure 3.3: The C_{60} PES from Figure 3.2 (from ref.[74]) with the peak fitting results of the present work. For peaks fitted by 2 functions the mean value of the two peak positions is taken for the position of the state; s SAMO (red line), p SAMO (pink and green line), d SAMO (blue and violet line), 2s SAMO (purple line); the brown line is the sum of all peak fits.

The photoelectron kinetic energies of the SAMOs from the spectrum in Figure 3.3 are summarised in the following table (Table 3.1) with the associated binding energies and anisotropy values.[7,75,77] The errors in the peak position are estimated during the fitting procedure which is done by hand, while the errors of the β values are obtained by error propagation.

Table 3.1: Summary of the experimental data of the SAMO peaks from the PES in Figure 3.3 comparing to the calculated electron binding energies at the TD-DFT/B3LYP/6-31+G(d) and the TD-DFT/CAM-B3LYP/6-31+G(d) level.[7,75,77]

Peak		s SAMO	p SAMO	d SAMO	2s SAMO
exp. E_{kin} (kinetic energy)		(0.62 ± 0.02) eV	(0.99 ± 0.02) eV	(1.44 ± 0.02) eV	(1.65 ± 0.03) eV
exp. E_{bin} (binding energy)		**(1.86 ± 0.02) eV**	**(1.49 ± 0.02) eV**	**(1.04 ± 0.02) eV**	**(0.83 ± 0.03) eV**
calc. E_{bin} (binding energy)	B3LYP	**2.14 eV**	**1.26 eV**	**0.77 eV**	--
	CAM-B3LYP	**2.10 eV**	**1.14 eV**	**0.62 eV**	--
exp. β value (anisotropy value)		1.97 ± 0.06	0.30 ± 0.04	0.17 ± 0.01	1.75 ± 0.06
calc. β value (anisotropy value)	B3LYP	1.96	0.98	-0.22	--
	CAM-B3LYP	1.87	1.79	1.52	--

Table 3.1 also shows the computed electron binding energies of the SAMO states using the TD-DFT/B3LYP/6-31+G(d) level and the TD-DFT/CAM-B3LYP/6-31+G(d) level.[7,75] In case of C_{70} the experimentally obtained SAMO binding energies are also compared to calculations at the TD-DFT/B3LYP/6-31+G(d) level (Table 3.2).[74,77]

Table 3.2: Comparison of the C_{70} experimental data on the E_{bin} of SAMOs to the computational results at the TD-DFT/B3LYP/6-31+G(d) on C_{70}.[77]

State	s SAMO	p SAMO	d SAMO	2s SAMO
exp. E_{bin}	(1.86 ± 0.02) eV	(1.42 ± 0.02) eV	(0.99 ± 0.03) eV	--
calc. E_{bin}	2.20 eV	1.19 – 1.24 eV	0.73 – 0.79 eV	--

The experimentally obtained anisotropy values are also compared to theoretically modelled values for C_{60} and C_{70} vs the kinetic energy of the photoelectron, as seen in Figure 3.4.[77]

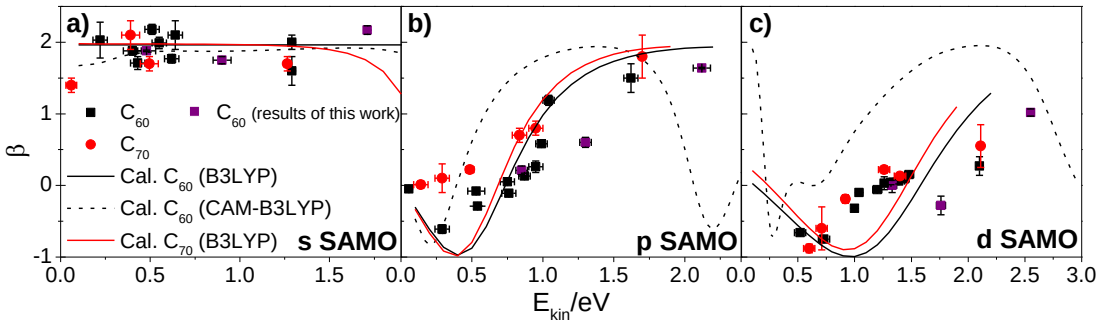

Figure 3.4: Comparison between the experimentally obtained and theoretically modelled (TD-DFT/B3LYP/6-31+G(d) and TD-DFT/CAM-B3LYP/6-31+G(d)) anisotropy values for the s (a), p (b) and d (c) SAMO plotted against the kinetic energy of the photoelectron.[75,77] The purple data points were obtained in the present work to complement previous studies from ref.[75,77]

It is obvious that the trend of the calculated β values is following the experimental values, but there are a few small discrepancies between the experimental data and the modelled as well as between the results of the calculations using different functionals (Figure 3.4). First of all, the anisotropy parameters for the s SAMO state ($\beta \approx 2$) are well described by the theoretical model at both computation levels using CAM-B3LYP and B3LYP (Figure 3.4 (a)). According to the Cooper-Zare formula (see chapter 1. 4) and these results, the s SAMO was thus clearly identified in C_{60} and C_{70}.[77] The theoretical β values for the p SAMO are still in good agreement with the experimental values for the calculation using B3LYP whereas the computational results using CAM-B3LYP differ (Figure 3.4 (b)). This is the same case for β values of the d SAMO where the variation even increases between the theoretical results using CAM-B3LYP and B3LYP (Figure 3.4 (c)). While the experimental anisotropy parameters are in better agreement with the theory using the B3LYP functional, the electron binding energies seem to comply with the results of the CAM-B3LYP functional better (Table 3.1 and Figure 3.4). On the basis of the CAM-B3LYP including corrections for the long-range interactions the excitation energies for Rydberg states are given relatively accurately, but the modelling of other properties might deteriorate using this functional.[104,105] In which case the B3LYP functional shows a better description of the anisotropy values than the CAM-B3LYP functional. Nevertheless, overall the experimental and computational results are in a fairly good agreement with the result that four of the well pronounced peaks in the PES of C_{60} and C_{70} have been assigned to s, p, d and 2s SAMO with experimental binding energies of (1.9 ± 0.2) eV, (1.5 ± 0.1) eV, (1.0 ± 0.1) eV and (0.9 ± 0.1 eV) respectively.

The identification of the SAMO states in C_{60} and C_{70} in the gas phase provides incentive to study their properties and in which way those can be tuned. In this regard other fullerene systems, like C_{82} and endohedral fullerenes like $Sc_3N@C_{80}$ and $Li@C_{60}$, were investigated to analyse the existence of SAMOs in these molecules, their characteristics, and how the change in the molecular structure affected the SAMO states. The results are summarised in the following sections.

3. 2. Results

3. 2. 1. C_{82} - Results on SAMOs

The fullerene C_{82} has 9 possible isomers, based on the isolated-pentagon rule, of which 6 of them are supposed to be stable due to their closed electronic shell, but only 1 isomer, 3 (C_2) (Figure 3.6 based on theoretical studies), has been extracted experimentally without any stabilising exohedral derivatives or any encapsulated metal atoms or ions.[106–108] A typical mass spectrum recorded of the C_{82} sample is displayed in Figure 3.6. The mass spectrum of C_{82} always showed a small C_{84}^+ mass peak next to the C_{82}^+ peak, but the C_{82}^+ signal dominated the spectrum throughout the measurements by a C_{82}/C_{84} ratio of about 3:1. Hence we can assume that the main contribution to the PES is caused by the first ionisation of the C_{82} molecule.

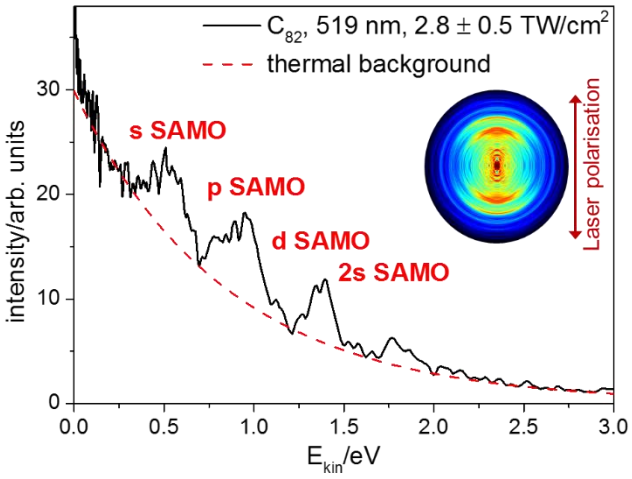

Figure 3.5: Angle integrated PES of C_{82} at 519 nm, (90 ± 10) fs, (2.8 ± 1.0) TW/cm² with the according inverted VMI image. The thermal electron background and the peak assignment is displayed in the PES.[77]

C_{82}
isomer 3 (C_2)

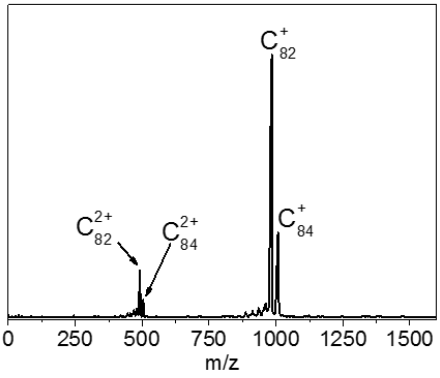

Figure 3.6: Molecular structure of C_{82} isomer 3 (C_2) based on theoretical studies[107] **on top and mass spectrum of C_{82} using 400 nm, (120 ± 10) fs, (0.56 ± 0.50) TW/cm².**[77]

The PES of C_{82} were recorded at different laser wavelengths (400 nm, 520 nm, 544 nm, 632 nm and 694 nm) and the mass spectra were taken at the same experimental condition as the corresponding PES. Figure 3.5 shows a typical PES of C_{82} at 519 nm.

The PES of C_{82} shows a peak structure superimposed on a thermal electron background which is similar to the features in the C_{60} PES (compare to Figure 3.2). The thermal electron emission of C_{82} will be discussed and compared to C_{60} and C_{70} in detail in chapter 4. 4.

For the analysis of the superimposed peak structure the fitted thermal electron background is subtracted from the PES which gives a background-subtracted spectrum as shown in Figure 3.7.

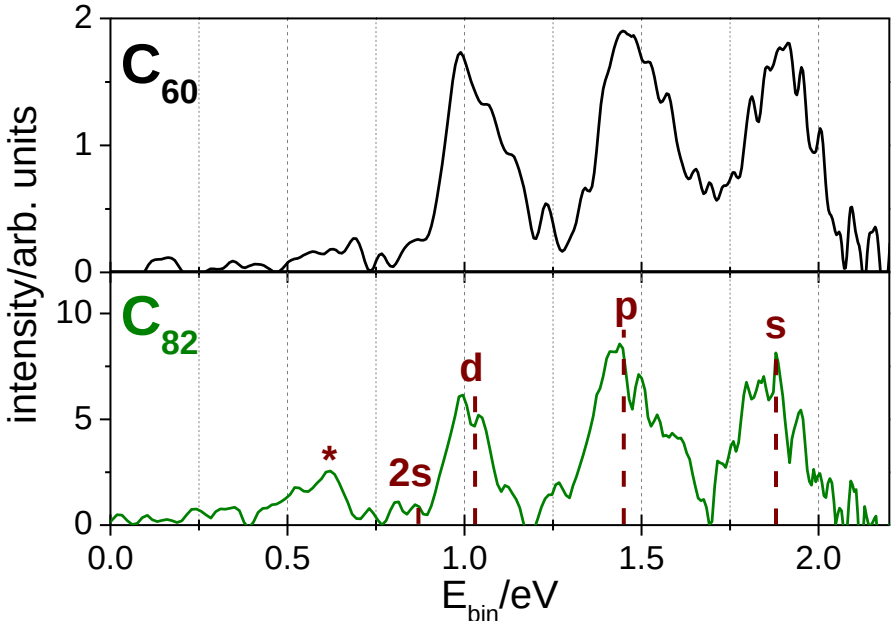

Figure 3.7: Comparing a thermal background subtracted, angle integrated PES of C_{60}, 514 nm, (90 ± 10) fs, (2.7 ± 0.8) TW/cm² to C_{82}, 519 nm, (90 ± 10) fs, (2.8 ± 1.0) TW/cm² plotted against the electron binding energy (E_{bin}) (according to the method described in chapter 1. 2). The peak assignment to the corresponding SAMO of the C_{82} spectrum is shown in the graph, but the peak around 0.60 eV with the asterisk is unidentified.

The PES of C_{82} and C_{60} are plotted against the electron binding energy, E_{bin}, which can be done due to the assumption of a one photon ionisation from the excited electronic state as described in chapter 1. 2 (Rydberg Fingerprint Spectroscopy). All the PES of C_{82} show a similar peak structure to the PES of C_{60} at the studied wavelengths and the peaks are observed at the same binding energies for C_{82} as for C_{60} (Figure 3.7 and Table 3.3).[77] The peak at E_{bin} = (0.60 ± 0.04) eV (marked with an asterisk in Figure 3.7) has not been identified in the C_{82} PES, however it also appears in the C_{60} spectrum. In previous studies on C_{60} using PES the peak at E_{bin} = (0.57 ± 0.02) eV was assigned to the 4h Rydberg state, but the peak around E_{bin} = (0.61 ± 0.02) eV could not be assigned unambiguously either to the 5f or 6d Rydberg state.[14,30,78] The assignment of the peaks at higher E_{bin} (> 0.75 eV, Figure 3.7) to certain SAMOs in the C_{82} spectrum has been based on their electron binding energy and their anisotropy values, β, compared to the previously studied C_{60} PES (see section 3. 1). Therefore, the 2s SAMO assignment has been indicated in the C_{82} PES even though no identifiable peak coincide with it (Figure 3.7). The s SAMO peak seems to be slightly shifted to lower binding energies for C_{82} compared C_{60} but this possible shift is still within the experimental error (Table 3.3). The errors of the peak positions are estimated through a fitting procedure of Lorentzian functions to each peak by eye. However, the peak pattern seems to be slightly more structured in C_{82} than in C_{60} which could be due the lower symmetry of C_{82} introducing a splitting of the p and d SAMO states that are degenerate in the symmetric C_{60}. For a better comparison,

the E_{bin} of the SAMO states are summarised in Table 3.3 for C_{60}, C_{70} and C_{82}, as well as the TD-DFT results on C_{84}.[77]

Table 3.3: Summary of the binding energies of the lowest SAMO states in C_{60}, C_{70} and C_{82} observed experimentally and theoretically for C_{60}, C_{70} and C_{84} at the TD-DFT/B3LYP/6-31+G(d) level.[77]

Fullerene		E_{bin}/eV			
		s SAMO	p SAMO	d SAMO	2s SAMO
C_{60}	Expt.	1.90 ± 0.01	1.47 ± 0.02	1.02 ± 0.01	0.87 ± 0.02
	B3LYP	2.14	1.26	0.77	--
C_{70}	Expt.	1.86 ± 0.02	1.42 ± 0.02	0.99 ± 0.03	0.83 ± 0.03
	B3LYP	2.20	1.19 - 1.24	0.73 – 0.79	0.61
C_{82}	Expt.	1.90 ± 0.04	1.42 ± 0.05	1.03 ± 0.03	0.86 ± 0.03
C_{84}	B3LYP	2.12	1.22 – 1.28	0.72 – 0.83	--

The experimental results for C_{82} can be matched with the TD-DFT outcomes for C_{84}, because the computations showed very similar energies of the SAMOs in C_{84} compared to C_{60}, so it can be assumed that the same applies to C_{82}.[77] On the contrary Zhao *et al.* have reported that the binding energy of the s SAMO is 0.2 eV higher in C_{82} than C_{60} based on their DFT studies.[5] Nevertheless, laser spectroscopy results are more comparable to TD-DFT calculations which give excitation energies to the different states whereas DFT calculations only provide the energy of occupied and virtual MO. Therefore, experimental results for C_{82} can be compared to TD-DFT studies on C_{84}.[77] Sometimes the theoretical calculations give a range of E_{bin} as in the case of p and d SAMOs of C_{70} and C_{84}, which is a result of suppressing the degenerate p and d states compared to C_{60}, as mentioned previously.

Table 3.3 clearly shows that all experimental electron binding energies are similar for each state and the values are in some cases even within the stated error. The calculations predict higher binding energies for the s SAMO state than observed experimentally but lower energies for the p and d SAMOs. However, the computed values are in reasonable agreement with the experiment.

Furthermore, the PAD of these peaks were determined using the technique described in chapter 2. 2. 2 for their assignment to the particular SAMO state. The obtained β values are plotted against E_{kin} and compared to the findings of C_{60} and C_{70} (Figure 3.8).

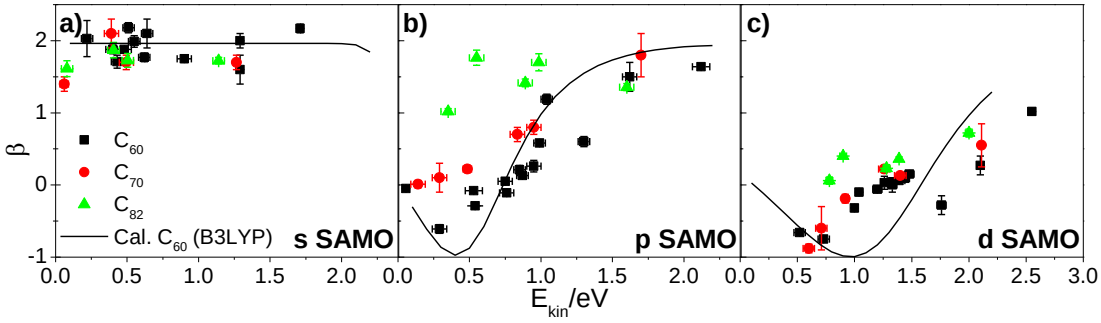

Figure 3.8: Experimentally obtained anisotropy values for the s, p and d SAMOs in C_{60} (black squares), C_{70} (red circles) and C_{82} (green upwards pointing triangles) plotted against the electron kinetic energy.[77] The graphs also include only the theoretically modelled β values for C_{60} at the TD-DFT/B3LYP/6-31+G(d) (black line) level.[77]

On the basis of the obtained anisotropy value of $\beta \approx 2$ (Figure 3.8) and the electron binding energy of ~ 2 eV (Table 3.3) the s SAMO state could be clearly assigned in the C_{82} PES (Figure 3.7).[77] The PAD for the p SAMO in C_{82} is slightly different to the PAD of C_{60} and C_{70} as it has been observed likewise for the PAD of the p state in C_{70} compared to C_{60}.[77] It seems like the β-values of the p SAMO in larger or less symmetric fullerenes (like C_{82}) start to increase at lower kinetic energies than for smaller fullerene cages with higher symmetry (like C_{60}). The same observation of PAD is noticeable for the d SAMO comparing C_{82} to C_{60} just less distinctive. These differences in the PADs can be explained by the known sensitivity of the PADs to small changes to the molecular potential like molecular size or symmetry, however in this case these disparities are not large enough to influence the binding energies (Table 3.3).[77] Due to the properties of Rydberg states (see chapter 1. 2) which are independent of the molecular structure, only small changes in the binding energies of fullerenes may arise as the fullerenes have a similar molecular structure.[77] In return, the calculated binding energies also support this conclusion by not showing larger differences from each other than the experimentally observed ones.[7,75,77]

3. 2. 2. $Sc_3N@C_{80}$ - Results on SAMOs

The investigation of C_{82} revealed the influence of the fullerene cage size on the highly excited electronic states, in particular the SAMOs. For studying the effect of encapsulated atoms or molecules in the fullerene cage on their electronic structure, endohedral fullerenes have to be probed. The highly excited states of the endohedral fullerene $Sc_3N@C_{80}$ have been analysed to investigate the effect of the trapped molecule. In this case the previously discussed results in section 3. 2 have to be considered regarding the impact of a change in the fullerene cage size and symmetry on the electronic structure as the findings from $Sc_3N@C_{80}$ are compared to the results of C_{60}, C_{70} and C_{82}. A direct comparison between the electronic structure of $Sc_3N@C_{80}$ and of an empty C_{80} fullerene cage is not possible due to the different symmetry point groups of the fullerene cage containing a molecule (I_h)[109] and the empty cage (D_{5d} and D_2) (based on experimental NMR (nuclear magnetic resonance) studies).[110–112]

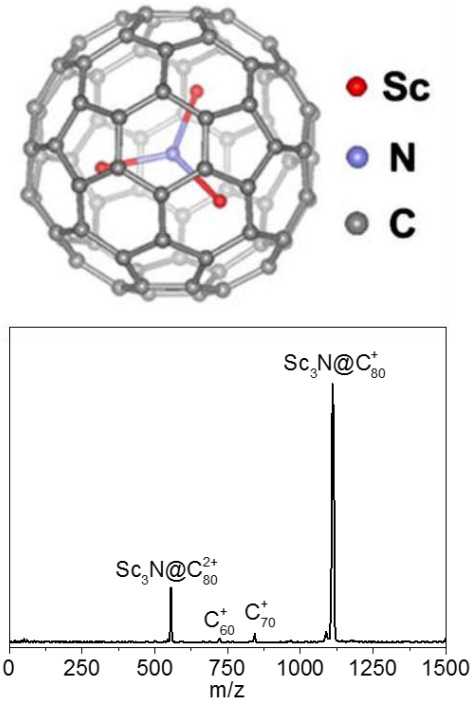

Figure 3.9: Molecular structure of $Sc_3N@C_{80}$ based on DFT calculations[113,164] as well as experimental NMR studies[109] on top and mass spectrum of $Sc_3N@C_{80}$ using 503 nm, (90 ± 10) fs, (3 ± 1) TW/cm².[77]

A typical mass spectrum of $Sc_3N@C_{80}$ is shown in Figure 3.9 which has the singly charged $Sc_3N@C_{80}^+$ species as the dominant signal. This was the case for all investigated experimental conditions including different laser wavelengths (400 nm, 503 nm, 506 nm, 547 nm, 600 nm and 800 nm). The traces of C_{60} and C_{70} in the mass spectra may be due to contamination in the original $Sc_3N@C_{80}$ sample. Therefore, the main contribution to the photoelectron spectra is assumed to be from the first ionisation of the $Sc_3N@C_{80}$ molecule. Figure 3.10 is an example for a typical PES of $Sc_3N@C_{80}$ with the corresponding inverted VMI image as an insert. The PES of $Sc_3N@C_{80}$ shows the same features as in the PES of the previously discussed fullerenes C_{60}, C_{70}

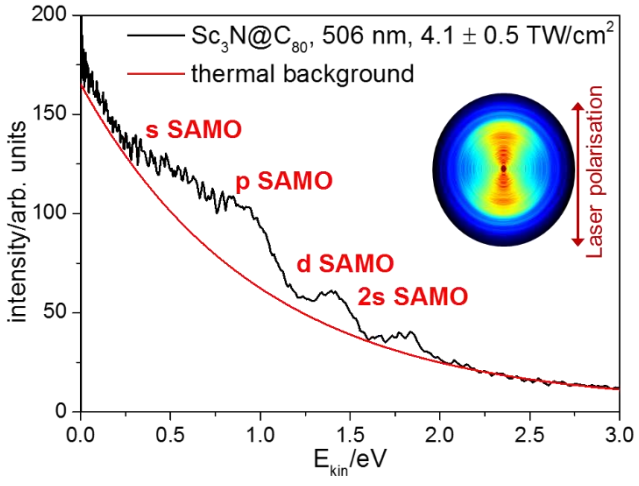

Figure 3.10: Angle integrated PES of $Sc_3N@C_{80}$ at 506 nm, (90 ± 10) fs, (4.1 ± 0.5) TW/cm² with the corresponding inverted VMI. The thermal electron background and the peak assignment is shown in the PES.[77]

and C_{82}: a peak structure below the photon energy superimposed on a thermal background.[77] The comparison between the thermal background subtracted PES of $Sc_3N@C_{80}$ and the PES of C_{60} clearly points out that the peak structure is less pronounced and the peaks are broader for $Sc_3N@C_{80}$ than for C_{60} (Figure 3.11).

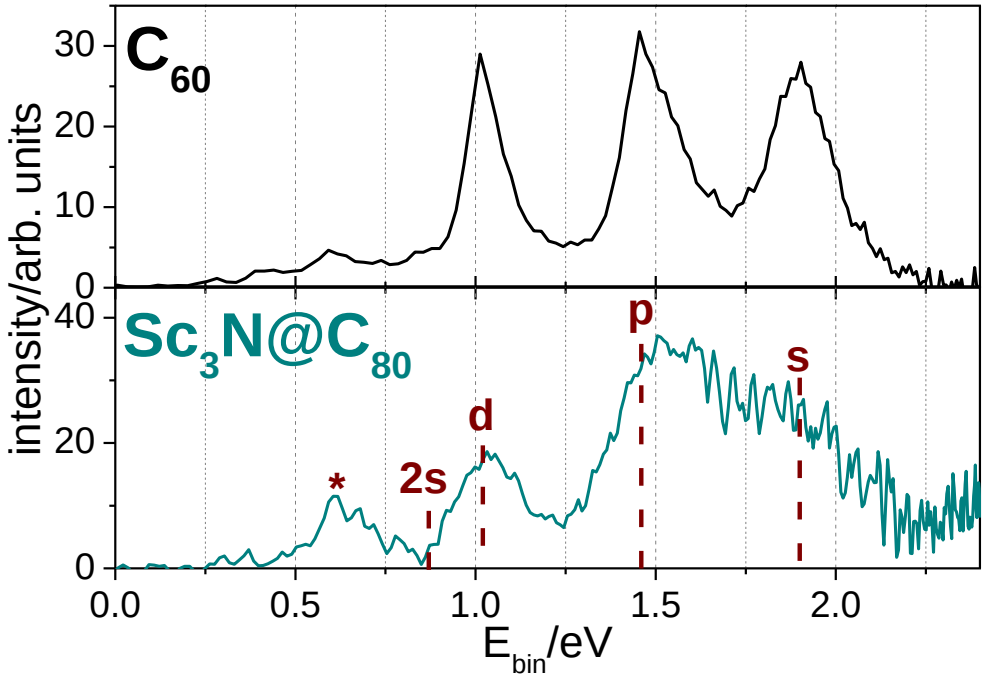

Figure 3.11: Comparing a thermal background subtracted, angle integrated PES of C_{60}, 500 nm, (90 ± 10) fs, (4.5 ± 0.3) TW/cm² to $Sc_3N@C_{80}$, 506 nm, (90 ± 10) fs, (4.1 ± 0.5) TW/cm² plotted against the E_{bin} (according to the method described in chapter 1. 2). The peak assignment to the corresponding SAMO of the $Sc_3N@C_{80}$ spectrum is shown in the graph, but the peak around 0.60 eV with the asterisk is unidentified.

Analogous to the assignment in the C_{82} PES (see section 3. 2. 1 or 3. 1), the peaks in the $Sc_3N@C_{80}$ spectrum (Figure 3.11) have been assigned to certain SAMOs based on their electron binding energy and their anisotropy values, β, compared to C_{60} PES. Hence, the s SAMO could be identified by fitting a Lorentzian function at E_{bin} = (1.96 ± 0.08) eV and obtaining its PADs, which resulted in β = 2.12 ± 0.09, even without an unresolved s peak in the PES of $Sc_3N@C_{80}$ (Figure 3.11). The 2s SAMO has been indicated in the $Sc_3N@C_{80}$ PES without an identifiable peak, but unfortunately no β value could be determined due to the absence of an coinciding peak. The SAMO peaks are broader in the $Sc_3N@C_{80}$ PES than compared to the C_{60} (Figure 3.11). This broadening of the SAMO peaks can be caused by the lower symmetry of the $Sc_3N@C_{80}$ which introduces a splitting of the different p and d states as discussed for C_{82}. Additionally, the encapsulated Sc_3N molecule probably has an effect on the binding energy and electron density of the states. The peaks of the $Sc_3N@C_{80}$ PES have been characterised by analysing the binding energies and PAD of the peaks (Table 3.4 and Figure 3.12).

Table 3.4: Summary of the SAMO binding energies of C_{60}, C_{70}, C_{82} and $Sc_3N@C_{80}$ observed experimentally.[77]

Fullerene		E_{bin}/eV			
		s SAMO	p SAMO	d SAMO	2s SAMO
C_{60}	Expt.	1.90 ± 0.01	1.47 ± 0.02	1.02 ± 0.01	0.87 ± 0.02
C_{70}	Expt.	1.86 ± 0.02	1.42 ± 0.02	0.99 ± 0.03	0.83 ± 0.03
C_{82}	Expt.	1.90 ± 0.04	1.42 ± 0.05	1.03 ± 0.03	0.86 ± 0.03
$Sc_3N@C_{80}$	Expt.	1.96 ± 0.08	1.50 ± 0.05	1.04 ± 0.08	0.68 ± 0.09

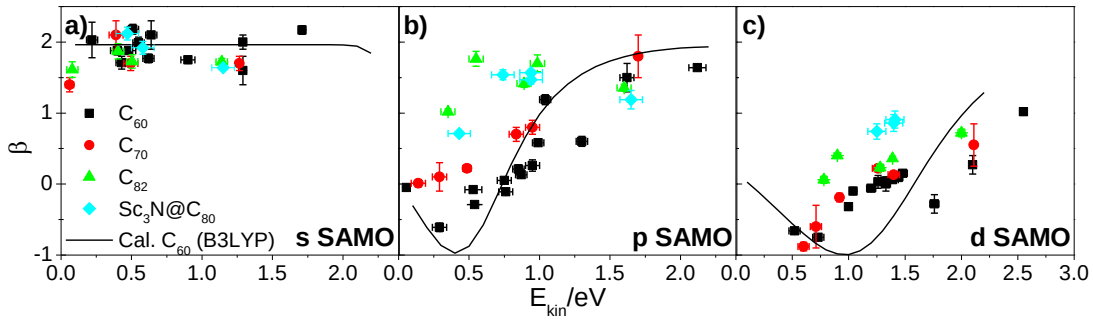

Figure 3.12: Anisotropy values of C_{60} (black squares), C_{70} (red circles), C_{82} (green upwards pointing triangles) and $Sc_3N@C_{80}$ (cyan squares) plotted against E_{kin}.[77] **The graphs also include only the theoretically modelled β values for C_{60} at the TD-DFT/B3LYP/6-31+G(d) (black line) level.**[77]

Table 3.4 summarises the determined binding energies of the SAMO states in $Sc_3N@C_{80}$. Due to the broadening of the peaks it has been difficult to determine the peak position, so this uncertainty is included in the estimated error. These binding energies are similar to the ones observed in C_{60}, C_{70} and C_{82} which supports the conclusion that the structural change between these molecules is not large enough to affect the binding energies of the SAMO states.[77] DFT calculations by Huang *et al.* showed a smaller relative energy difference between the SAMO states (about 0.2 eV between s and p SAMO) compared to the experimental results of this work.[113] However, as it was mentioned previously in this chapter, TD-DFT calculations are needed to model excitation energies because DFT computations only provide the electronic structure of the ground state. Comparing the anisotropy values of $Sc_3N@C_{80}$ to the other studied fullerenes a difference in the trend for the p SAMO can be seen in Figure 3.12. This observation follows the tendency previously observed for C_{82} where the β values are slightly higher and increase at lower kinetic energies for larger fullerenes with lower symmetry (chapter 3. 2 and Figure 3.12). However the anisotropy values for the s SAMO and d SAMO states seem to be consistent for all studied fullerenes.[77]

3. 2. 3. Li@C_{60} - Results on SAMOs

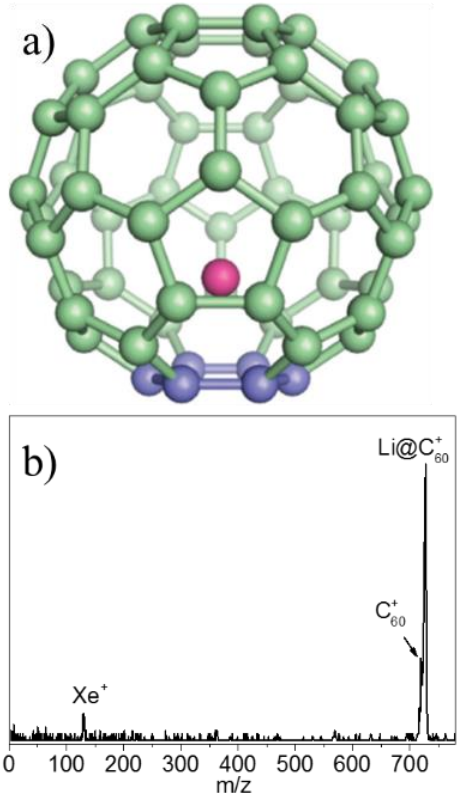

Figure 3.13: a) Idealised molecular structure of Li@C_{60} based on experimental studies[117,118]; b) a mass spectrum of Li@C_{60}[PF_6] sample at T_{oven} = 329 °C using 540 nm, (35 ± 10) fs and (8.9 ± 0.8) TW/cm².

Until now the influence of the fullerene cage size on the electronic structure has been investigated and a first step has been made to analyse the effect of an encapsulated atom, or molecule, on the excited electronic states of the fullerene, by probing the endohedral fullerene $Sc_3N@C_{80}$. Unfortunately, the results obtained from $Sc_3N@C_{80}$ cannot be compared directly to an empty C_{80} fullerene cage to give an unambiguous conclusion on the impact of an encapsulated molecule (see chapter 3. 2. 2). Therefore, another endohedral fullerene with a lithium atom inside a C_{60} fullerene cage was studied, Li@C_{60}. In the ground state the Li atom is located about 0.15 nm off centre of the cage on the inner surface of a C_6 ring of the fullerene (Figure 3.13 a). This is in contrast to some other endohedral fullerenes where the encaged atom or molecule is located in the centre of the cage, like for La@C_{60} and $Sc_3N@C_{80}$.[114–116] Nevertheless, another intriguing fact about the Li@C_{60} molecule is that the fullerene cage has the same symmetry group as the empty C_{60} cage, I_h, in contrast to other metallo-endohedral species.[117,118] Hence a direct comparison of Li@C_{60} to C_{60} is possible to determine the effect of an atom encapsulation on the electronic structure, unlike $Sc_3N@C_{80}$ where a direct comparison of the same cage is not possible.

Previous studies on the Li@C_{60} material showed that the encapsulated Li atom donates an electron to the C_{60} cage[119,120] and the electronic ground state is ionic in nature, so the molecule is essentially composed of a Li^+ ion and a C_{60}^- cage.[121–123] Experimental studies on Li@C_{60} from the literature have reported that the molecule behaves like the C_{60} anion.[120,124] The pure Li@C_{60} material is believed to exist as a combination of dimer and trimer structures, which may be precursors to polymers.[117,125] However, the relatively weak inter-cage bonds are believed to break on evaporation which results in endohedral fullerene radicals.[115,126] Therefore, these radicals can decompose or react with oxygen or polymerise, which has been observed in particular in presence of solvent impurities.[115,120,125,127] The neutral Li@C_{60} has been reported to be a better radical and electron acceptor than C_{60}, so the Li@C_{60} molecule has to be stabilised in ambient conditions, e. g. with an appropriate counter anion like PF_6^-.[118,128] Hence, the stabilised Li@C_{60}[PF_6] salt was used for the experiments in this thesis.

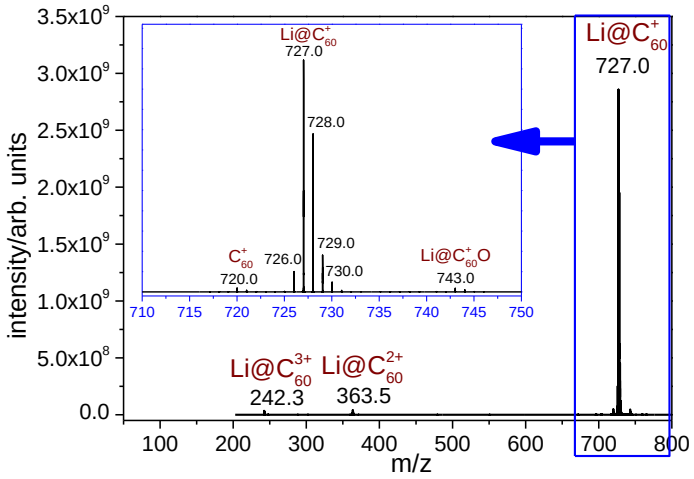

Figure 3.14: LD FT-ICR mass spectrum of the Li@C$_{60}$[PF$_6$] sample.

A typical mass spectrum of the Li@C$_{60}$[PF$_6$] is shown in Figure 3.13 under experimental conditions where the Li@C$_{60}^+$ mass peak is most dominant. For all studied wavelengths a C$_{60}^+$ mass peak was present in the spectra which could be due to contamination of the original sample. Nevertheless, a check of the sample in a Laser Desorption Fourier transform ion cyclotron resonance mass spectrometer (LD FT-ICR MS) did not show any noticeable C$_{60}$ contamination (Figure 3.14, for negative mode see appendix 8. 3, Figure 8.4).

In the context of this result an examination of the applied oven temperature for the hot source during the recorded measurement for Li@C$_{60}$ is needed, which has been about 350 - 370 °C (see chapter 2. 2). However, the experiments on C$_{60}$ have had an oven temperature of about 500 °C (see chapter 2. 2) and the oven temperature has had to be raised to at least 470 °C to obtain a C$_{60}^+$ signal in the mass spectrum. Therefore, it is possible that Li@C$_{60}$ decomposes during the evaporation process, or the sample decomposes slowly in the hot source over time. Additionally, the presence of the Li@C$_{60}$ lowers the evaporation temperature of C$_{60}$ according to a positive deviation from Raoult's law.

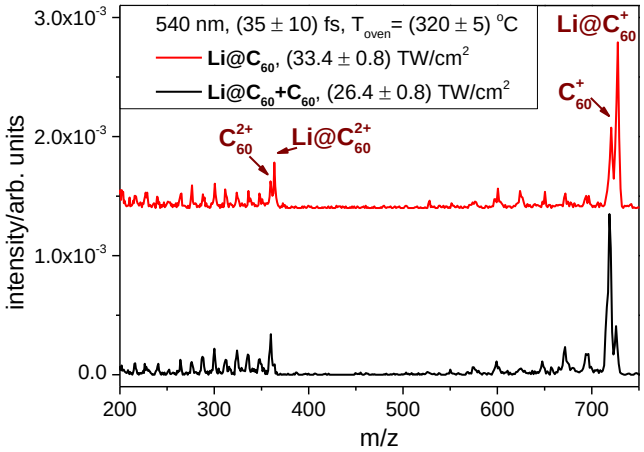

Figure 3.15: Mass spectra taken of pure Li@C$_{60}$[PF$_6$] and Li@C$_{60}$[PF$_6$] with C$_{60}$ sample at an oven temperature of (320 ± 5) °C using 540 nm, (35 ± 10) fs, (33.4 ± 0.8) TW/cm^2 and (26.4 ± 0.8) TW/cm^2, respectively.

To test if the presence of Li@C$_{60}$ has an effect on the C$_{60}$ evaporation temperature, a small amount of C$_{60}$ powder has been added to the Li@C$_{60}$ sample and mass spectra have been taken (Figure 3.15). After the C$_{60}$ addition the C$_{60}^+$ mass peak has clearly increased. The ratio of the Li@C$_{60}^+$/C$_{60}^+$ peak also shifted towards C$_{60}^+$ despite the oven temperature being just around 320 °C. The same change can be observed for the doubly ionised species Li@C$_{60}^{2+}$/C$_{60}^{2+}$. The outcome of this results shows that Li@C$_{60}$ lowers the evaporation temperature of C$_{60}$ so even neutral C$_{60}$, which is not a decomposition product of Li@C$_{60}$, can be present in the molecular beam at oven temperatures below the usual sublimation temperature of pure C$_{60}$.

However, a decrease of the $Li@C_{60}^+$ signal relative to the C_{60}^+ has been observed over many days. This has been previously documented and an approximate half-life of 40 minutes at a temperature of 500 °C has been determined due to destruction or polymerisation of the sample in the oven.[125,129] Additionally the ever-present Li^+ peak in the mass spectrum, which cannot be detected in the chamber without the sample, supports the constant degradation of the $Li@C_{60}$ during the heating of the sample (Figure 3.13 and Figure 3.16). Therefore, a $Li@C_{60}$ sample batch in the oven can be used over a period of about two months.

The C_{60}^+ peak in the mass spectrum can also result from any fragmentation of the $Li@C_{60}^+$ ions in the gas phase due to the loss of the Li^+ ion.[125] This has also been previously postulated on the basis that the emission of C_2 will strongly compete with the Li emission because the insertion energy for a Li^+ ion is about 5 – 6 eV[130] and the C_2 emission has a significantly higher activation energy of about 10.6 eV[131,132].[87,125] The mass spectra of $Li@C_{60}$ at 800 nm at varied laser intensities show a fragmentation pattern which can be analysed in this context (Figure 3.16).

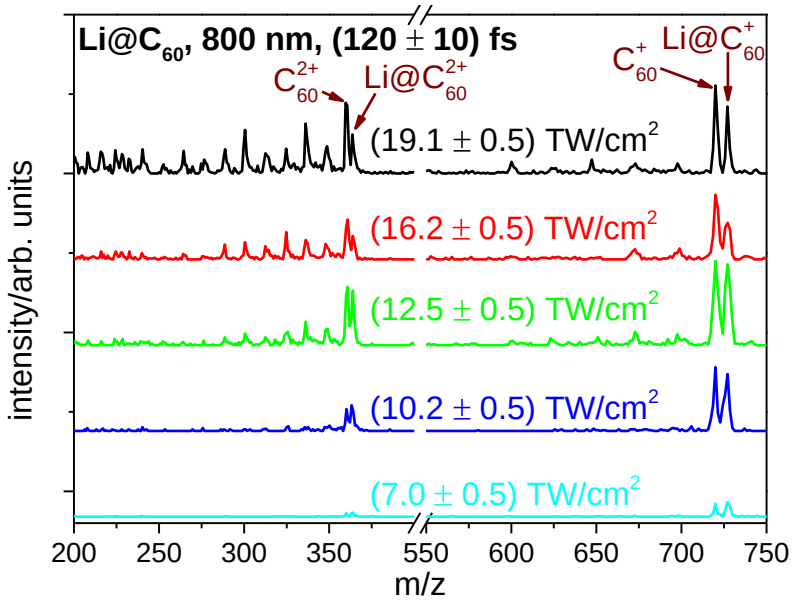

Figure 3.16: TOF-MS of $Li@C_{60}$ acquired using 800 nm, (120 ± 10) fs and laser intensities of (19.1 ± 0.5), (16.2 ± 0.5), (12.5 ± 0.5), (10.2 ± 0.5) and (7.0 ± 0.5) TW/cm² (black, red, green, blue and cyan solid line respectively). The spectrum at (16.2 ± 0.5) TW/cm² has been taken at an oven temperature about 25 °C lower than the other measurements.

For laser intensities higher than (10.2 ± 0.5) TW/cm² the fragmentation through C_2 loss from the fullerene cage increases but the fragment distribution of the empty C_{60} cage is higher in intensity than for the endohedral $Li@C_{60}$, as seen in Figure 3.16. Also from lower laser intensities upwards (> (10.2 ± 0.5) TW/cm²) the amount of doubly charged parent cation increases as a function of laser intensity, but the C_{60}^{2+} peak is higher in intensity than the $Li@C_{60}^{2+}$ peak. In comparison to the $Li@C_{60}^+/C_{60}^+$ peak relation (Figure 3.16) it shows a stronger tendency to the Li-loss channel than to the double ionisation path which may be due to the higher excitation energy of the doubly charged species.[125] Furthermore, the singly charged C_{60}^+ and Li^+ peaks increase in relation to the $Li@C_{60}^+$ peak at increasing laser

intensities (> (7.0 ± 0.5) TW/cm^2) which indicates that the Li atom is being ejected from the C_{60} cage by the laser pulse for higher pulse intensities (Figure 3.16). However, the mass peak ratio of the Li@C_{60}^+ to C_{60}^+ is equal up to a laser intensity of about (12.5 ± 0.5) TW/cm^2. From a laser intensity of about (16.2 ± 0.5) TW/cm^2 the Li@C_{60}^+ to C_{60}^+ ratio shifts slightly towards C_{60}^+ (Figure 3.16) but this change can be still within the experimental fluctuations. A further test of the Li@C_{60}^+/C_{60}^+ mass peak ratio has been conducted using 540 nm, (35 ± 10) fs and a range of different laser intensities (Figure 3.17).

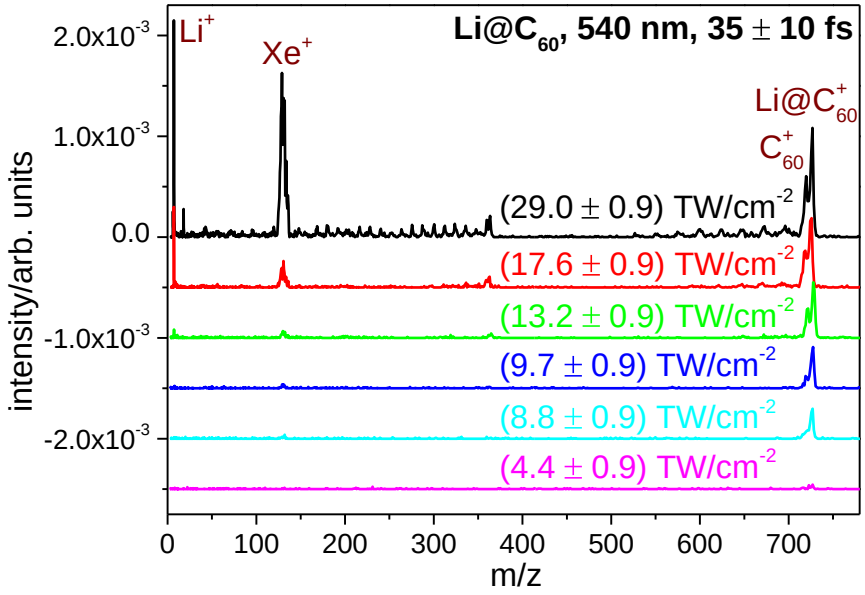

Figure 3.17: Mass spectra series of Li@C_{60}[PF_6] at several laser intensities (as labelled in the graph) using 540 nm, (35 ± 10) fs at T_{oven} = (328 ± 2) °C. The *m/z* axis has been calibrated using the Xe^+ signal.

The recorded mass spectra series displayed in Figure 3.17 shows that the Li@C_{60}^+/C_{60}^+ mass peak ratio does not depend on the laser intensity, but the Li@C_{60}^+ mass peak is definitely higher than the C_{60}^+ peak. Similar results have also been obtained for a series of mass spectra using laser wavelengths of 600 nm at various laser intensities (see appendix 8. 4, Figure 8.5). On the basis that the Li@C_{60}^+/C_{60}^+ mass peak ratio does not depend strongly on the laser intensity, it can be concluded that the C_{60}^+ mass peak is probably not only due to the fragmentation of Li@C_{60} caused by the laser pulse but mainly a consequence of neutral C_{60} present in the molecular beam being ionised by the laser, as discussed before.

The variation of the Li@C_{60}^+/C_{60}^+ mass peak ratio at different laser wavelengths (Figure 3.16 and Figure 3.17) could be due to the different first ionisation energy for C_{60}^+ (IP(C_{60})= 7.6 eV)[23] and Li@C_{60} (IP (Li@C_{60})≈ 6.4 eV)[119,125]. Hence a series of Li@C_{60} mass spectra, similar to the one in Figure 3.17, has been recorded but for lower laser intensities (before fragmentation occurs, see appendix 8. 5, Figure 8.6) to investigate the laser intensity dependence of the ion yield.[26,87] Since the ionisation probability, P_n, depends on the laser intensity as I^n, with n being the number of photons needed to ionise the

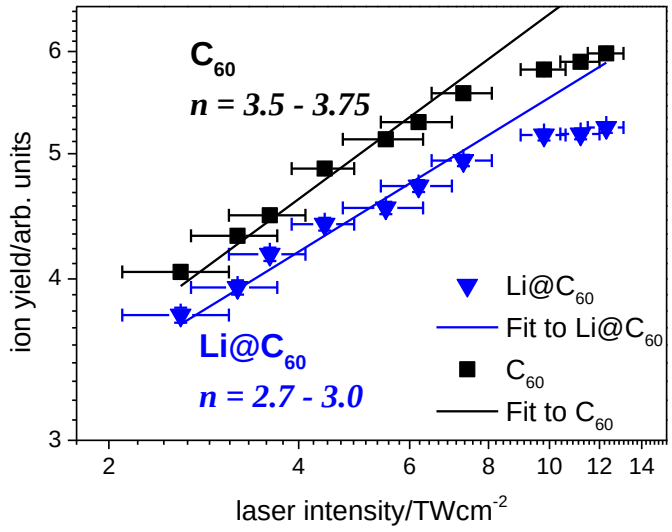

Figure 3.18: Ion yield of Li@C_{60} and C_{60} plotted against the laser intensity in a double logarithmic scale. The graph includes the obtained slope, *n*, from the manual fit of the data. The ion yields were extracted from the mass spectra series in appendix 8. 5, Figure 8.6.

molecule, if no intermediate resonances are involved in the ionisation process (see chapter 1. 1), a double logarithmic plot of the ion yield against the laser intensity should give the photon order needed to ionise the molecular species.[26,39,87] In this experiment a photon energy of 2.30 eV (540 nm) has been used to ionise the sample. Therefore, four photons are needed to ionise the C_{60} molecule ($IP(C_{60})$ = 7.6 eV)[23] whereas only three photons of the same energy are necessary to ionise the endohedral Li@C_{60} fullerene ($IP(Li@C_{60}) \approx 6.4$ eV)[119,125]. The experimentally obtained plot for the Li@C_{60} mass spectra series using 540nm, (35 ± 10) fs at different laser intensities (see appendix 8. 5, Figure 8.6) is shown in Figure 3.18. On the basis of this graph a gradient of about 3.7 ± 0.3 for C_{60} was extracted indicating a four-photon ionisation process, while the gradient for Li@C_{60} of 2.9 ± 0.3 consistent with a three-photon ionisation process. Hence these results supports the existence of both C_{60} and Li@C_{60} in the used sample.[87]

The comparison of the mass spectra of Li@C_{60} at similar laser intensities but different laser wavelengths should show the photon order needed to photoionise the molecule through a multiphoton process (Figure 3.19).

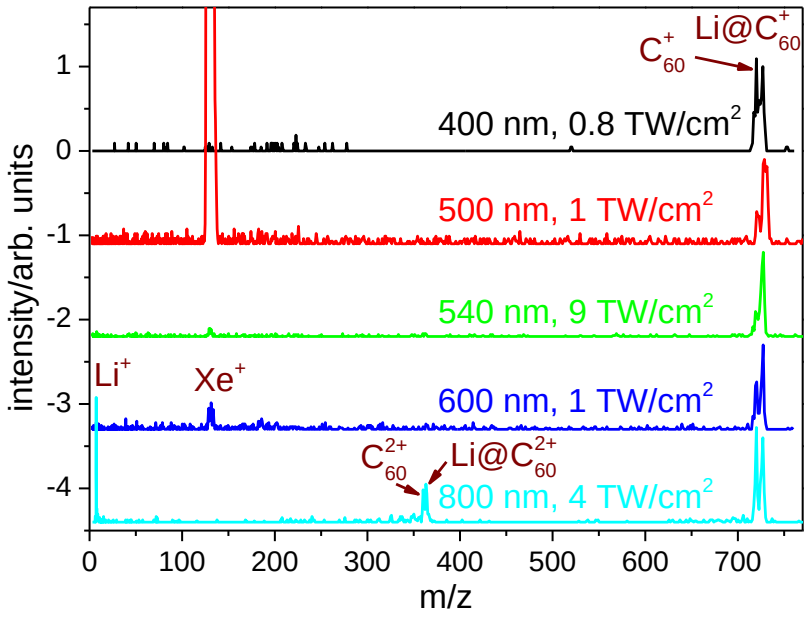

Figure 3.19: Mass spectra of Li@C_{60}[PF_6] at different laser wavelengths: 400 nm, (120 ± 10) fs, (0.8 ± 0.3) TW/cm², 383 °C (black line), 500 nm, (90 ± 10) fs, (1.0 ± 0.5) TW/cm², 337 °C (red line), 540 nm, (35 ± 10) fs, (9.0 ± 0.8) TW/cm², 329 °C (green line), 600 nm, (90 ± 10) fs, (1.0 ± 0.5) TW/cm², 300 °C (blue line), 800 nm, (120 ± 10) fs, (4.0 ± 0.6) TW/cm², 382 °C (cyan line). Xenon was used in situ for the mass scale calibration. The assignment of the mass peaks is given in the graph.

The spectra clearly show that the mass peak ratio of $Li@C_{60}^+/C_{60}^+$ is the same for 400 nm and 800 nm whereas for the other laser wavelengths the ratio shifts towards $Li@C_{60}^+$ (Figure 3.19). This outcome suggests that less photons are needed to multiphoton ionise Li@C_{60} than C_{60} with 500 nm, 540 nm and 600 nm but for 400 nm and 800 nm the same number of photons is necessary for Li@C_{60} as for C_{60} (Table 3.5).

Table 3.5: Summarising the photon order needed to multiphoton ionise Li@C_{60} (*IP* ≈ 6.4 – 6.2 eV)[119,125] and C_{60} (*IP* = 7.6 eV)[23] at different photon energies.

Wavelength	Photon energy	Li@C_{60}		C_{60}	$Li@C_{60}^+/C_{60}^+$ mass ratio (integrated mass peaks) from Figure 3.19
		IP ≈ 6.4 eV	*IP* ≈ 6.2 eV	*IP* = 7.6 eV	
400 nm	3.10 eV	2.06 ≈ 3	2	2.45 ≈ 3	1:1
500 nm	2.48 eV	2.58 ≈ 3	2.5 ≈ 3	3.06 ≈ 4	5:1
540 nm	2.30 eV	2.78 ≈ 3	2.70 ≈ 3	3.30 ≈ 4	3:1
600 nm	2.07 eV	3.09 ≈ 4	3.00	3.67 ≈ 4	2:1
800 nm	1.55 eV	4.13 ≈ 5	4	4.90 ≈ 5	1:1

According to Table 3.5 the ionisation energy of Li@C_{60} has to be between 6.4 - 6.2 eV to fit the photon order related to the rough mass peak ratio of the integrated mass peak area shown in Figure 3.19. This result is in agreement with the literature in which the *IP* of endohedral Li@C_{60} has been calculated to be around 6.0 eV using DFT and experiments estimated an *IP* of about 6.4 eV.[87,119,125] Additionally, the findings based on Figure 3.18 are validating the calculated photon orders for the multiphoton ionisation of Li@C_{60} and C_{60}.

In the following comparisons between the PES of Li@C_{60} to C_{60} or to other fullerenes it should to be noted that photoelectrons originating from C_{60} are always present and overlapping with the photoelectrons from the Li@C_{60} ionisation, as seen in the mass spectra (Figure 3.16, Figure 3.17 and Figure 3.19). First the PES of Li@C_{60} and C_{60} are compared for laser wavelengths of 400 nm and 540 nm where the photon order is the same, or different, for the two molecules, respectively (Figure 3.20).

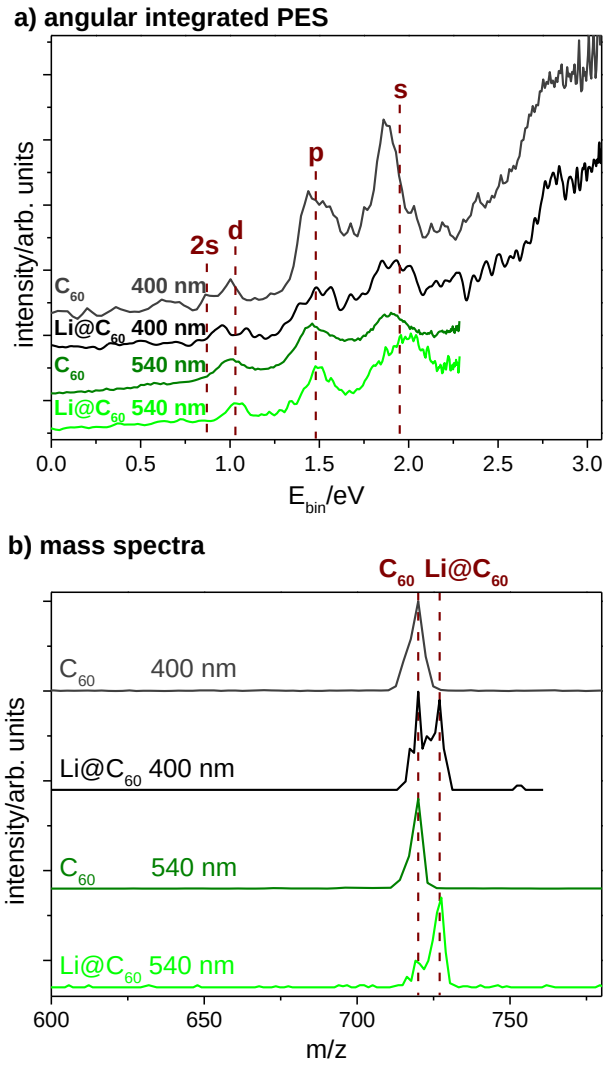

Figure 3.20: Comparing a) the PES of Li@C_{60} at 400 nm, (120 ± 10) fs, (0.8 ± 0.3) TW/cm^2 and 540 nm, (35 ± 10) fs, (9.0 ± 0.8) TW/cm^2 to C_{60} (similar laser conditions) and b) the according mass spectra. The assignment of the SAMO states for Li@C_{60} are shown in the PES.

The angle integrated PES of Li@C_{60} shows a thermal electron background with a superimposed peak structure similar to C_{60} and the other studied fullerenes (Figure 3.20, chapter 3. 2. 1 and chapter 3. 2. 2). The thermal electron background will be discussed in more detail in chapter 4. 3. 2, whilst this chapter focusses on the peak structure or SAMO states.

Comparing the PES at 540 nm of Li@C_{60} and C_{60} a shift in the s SAMO peak to a higher binding energy is observed while the other SAMO peaks seem to stay at the same binding energies as for C_{60} (Figure 3.20). This observation is less clear in the comparison of the PES at 400 nm but still visible. Taking into account the observed mass spectra (Figure 3.19 and Figure 3.20) and the lower photon order of the photoionisation of Li@C_{60} vs C_{60} at 540nm compared to 400 nm (Table 3.5), it is best to compare the PES of the two compounds at 540 nm to find any effects on the electronic structure or SAMO states caused by the encapsulated Li atom.

Figure 3.21 compares the angle integrated, thermal background subtracted PES of Li@C_{60} and C_{60} at 540 nm.

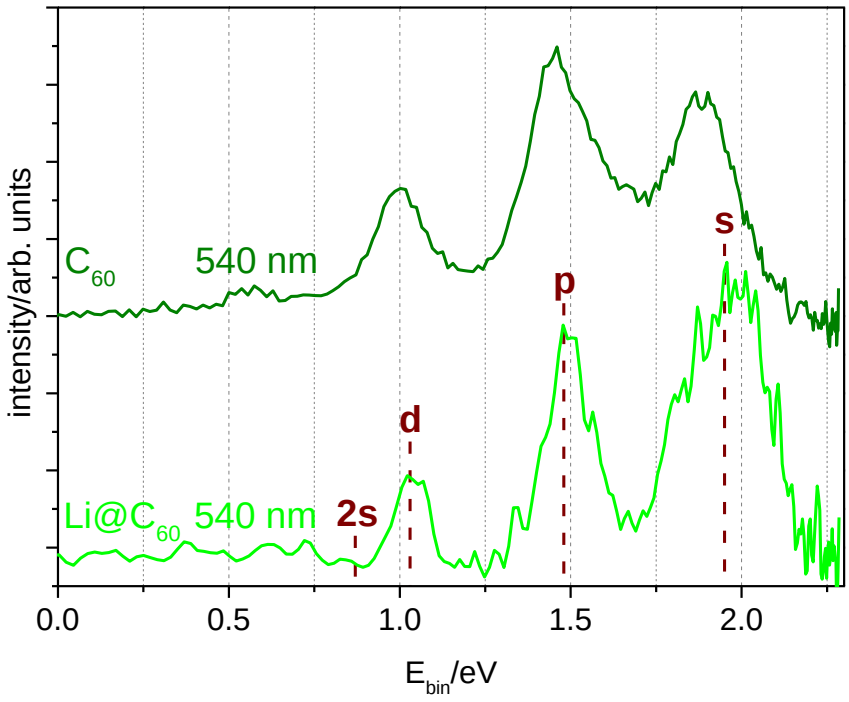

Figure 3.21: Angle integrated and thermal background subtracted PES of Li@C_{60} (green line) and C_{60} (olive line) at 540 nm, (35 ± 10) fs, (9.0 ± 0.8) TW/cm^2. The assignment of the SAMO states for Li@C_{60} is indicated on top of the PES.

Analogous to the peak assignment for C_{82} and $Sc_3N@C_{80}$ (see section 3. 2. 1 and 3. 2. 2), the peaks in the Li@C_{60} spectrum (Figure 3.21) have been assigned to certain SAMOs based on their electron binding energy and their anisotropy values, β, compared to C_{60} PES. Therefore, the 2s SAMO assignment has been indicated in the Li@C_{60} PES without an identifiable peak assuming the same E_{bin}

as for C_{60} (Figure 3.21). For other laser wavelengths, like 600 nm and 800 nm (see appendix 8. 6, Figure 8.7), the Li@C_{60} PES show an identifiable 2s SAMO peak at E_{bin} = (0.87 ± 0.06) eV.

The s SAMO peak in the Li@C_{60} PES is much broader and shifted to higher binding energies, as mentioned previously, than in the C_{60} PES (Figure 3.21). The broadening of the s peak could be due to a splitting of this peak which cannot be resolved due to the relatively broad spectral bandwidth of the laser pulse (about 0.17 eV) and the close spacing of the two features. This splitting is maybe caused by the overlapping photoelectron signal from the Li@C_{60} and the C_{60}.

The electron binding energies of the SAMO states obtained from the PES of Li@C_{60} are compared to other fullerenes in Table 3.6.

Table 3.6: Summarising the experimentally obtained electron binding energies of the SAMO states of C_{60}, C_{70}, C_{82}, $Sc_3N@C_{80}$ and Li@C_{60}.

Fullerene		E_{bin}/eV			
		s SAMO	p SAMO	d SAMO	2s SAMO
C_{60}	Expt.	1.90 ± 0.01	1.47 ± 0.02	1.02 ± 0.01	0.87 ± 0.02
C_{70}	Expt.	1.86 ± 0.02	1.42 ± 0.02	0.99 ± 0.03	0.83 ± 0.03
C_{82}	Expt.	1.90 ± 0.04	1.42 ± 0.05	1.03 ± 0.03	0.86 ± 0.03
$Sc_3N@C_{80}$	Expt.	1.96 ± 0.08	1.50 ± 0.05	1.04 ± 0.08	0.68 ± 0.09
Li@C_{60}	Expt.	1.93 ± 0.07	1.47 ± 0.06	1.03 ± 0.04	0.87 ± 0.06

The binding energy shown in Table 3.6 for the s SAMO of Li@C_{60} is the average of the E_{bin} obtained from the PES at 400 nm, 500 nm, 540 nm and 600 nm (not for 800 nm as the photon energy is not enough to one-photon ionise the s SAMO). Since it is not possible to separate the component due to Li@C_{60} from the one due to C_{60}, the difference between the s SAMO binding energy of Li@C_{60} and C_{60} is small. However, this shift of the s SAMO binding energy is more credible for Li@C_{60} than for $Sc_3N@C_{80}$ because the peak position of the s state is clearly visible in the Li@C_{60} PES (compare Figure 3.11 and Figure 3.21). Theoretical studies on the neutral Li@C_{60} using DFT have also shown an increase of the s SAMO binding energy due to endohedral doping of the C_{60} cage with a lithium atom.[5,31] However, the shift of s SAMO state has been calculated to be about 2 eV which is much higher than the experimentally obtained shift of the binding energy.[5,31] For the other SAMO states (p, d and 2s) the calculations have also yielded the same binding energies as for an empty C_{60} cage, in agreement with the experimental results presented here.[5,31]

Additionally, the PADs of the SAMO peaks in the PES of Li@C_{60} have been identified and compared to the anisotropy values of C_{60} (Figure 3.22).

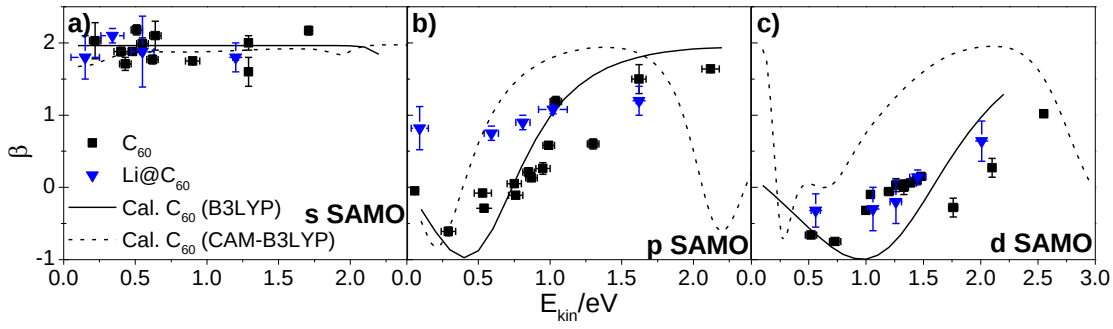

Figure 3.22: Anisotropy values of C_{60} (black squares) and Li@C_{60} (blue triangles) plotted against E_{kin}.[77] The graphs also include the theoretically modelled β values for C_{60} at the TD-DFT/B3LYP/6-31+G(d) (black solid line) and at the TD-DFT/CAM-B3LYP/6-31+G(d) (black dashed line) level.[77]

The β value for the s SAMO of Li@C_{60} is about 2 for the measured range of the kinetic electron energies which is also in agreement with the experimental and calculated β values for C_{60} (Figure 3.22 a). This outcome corresponds to the theory of the PAD as only one partial wave is expected (p wave) from an s orbital, unless a significant contribution of non s type molecular orbitals is added (see chapter 1. 4). Also the obtained β values for the d SAMO in the Li@C_{60} are very close to the C_{60} equivalent and have the same behaviour along the measured kinetic energy (Figure 3.22 c). The similarity of the PAD for the s and d state between Li@C_{60} and C_{60} can be explained by the theoretically calculated Dyson orbitals of these states for Li@C_{60}^+ ion (Table 3.7). These computations have been conducted by Prof Françoise Remacle and Dr Benoît Mignolet on the Li@C_{60}^+ which enabled more cost-effective closed shell TD-DFT calculations, since the neutral Li@C_{60} molecule exists as a radical that implies using open shell calculations.

Table 3.7: Comparison of the SAMO Dyson orbitals calculated for C_{60} and $Li@C_{60}^{+}$.[77]

	C_{60}	$Li@C_{60}^{+}$
s SAMO (isocontour C_{60}= 0.00002 $\lvert e\rvert/a^3$ and $Li@C_{60}$= 0.002 $\lvert e\rvert/a^3$)	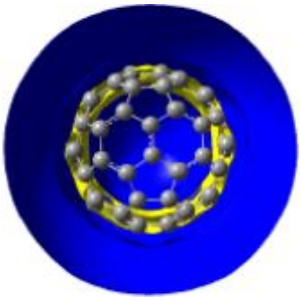	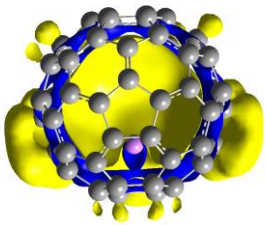
p SAMO (isocontour 0.002 $\lvert e\rvert/a^3$)	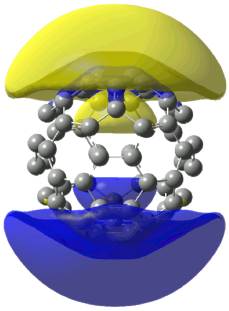	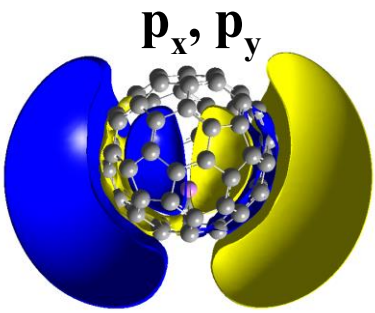 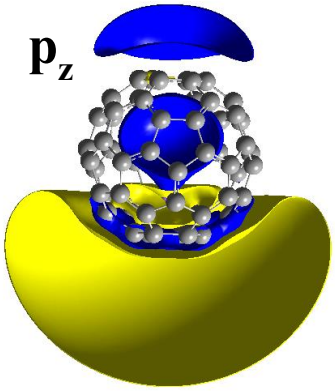
d SAMO (isocontour 0.002 $\lvert e\rvert/a^3$)	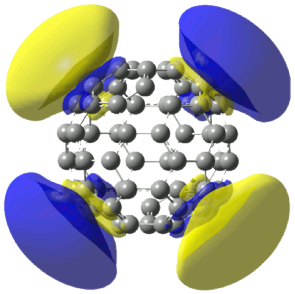	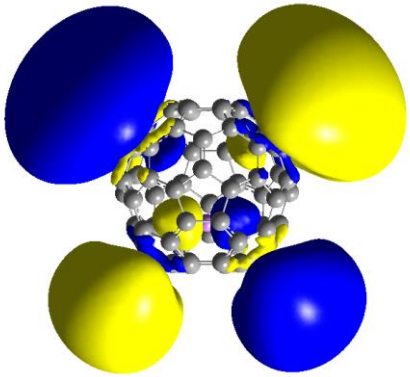

The comparison between the Dyson orbitals for the s and d SAMOs of C_{60} and Li@C_{60} shows only a slight influence of the Li atom on the electron densities (Table 3.7). In particular, for the d SAMO the majority of the electron density appears to be outside the fullerene cage where the influence of the Li atom is notably screened. Therefore, just a small effect of the Li atom on the s and d SAMO is detected (Figure 3.22). In case of the p SAMO state in Li@C_{60} the Dyson orbital differs from an empty C_{60}, especially for the p_z orbital (Table 3.7). Since the Li atom breaks the icosahedron of the fullerene cage, the degeneracy of the p states is lifted and removed for the p_z orbital. The encapsulated Li atom clearly interferes with the p_z SAMO state and deforms its electron density. This influence of the encapsulated Li atom alters the core potential of the molecule which affects the relative phase shift of the outgoing photoelectron partial waves due to scattering. Hence this effect is reflected in the PAD of the p states where the anisotropy values of Li@C_{60} show a difference for $E_{kin} < 1.0$ eV in contrast to C_{60} (Figure 3.22 b).

3. 2. 4. Photoionisation Probabilities of SAMOs in C_{60}

In the previous subchapters the effects of fullerene cage symmetry, size and insertion of an atom or molecule into the cage on the electronic structure, in particular on the SAMO states, were analysed and discussed. But even looking at the PES of C_{60} using different photon energies, variations in the peak intensities of the SAMO peaks can be clearly observed (Figure 3.23) which can have characteristic information about the SAMO states.

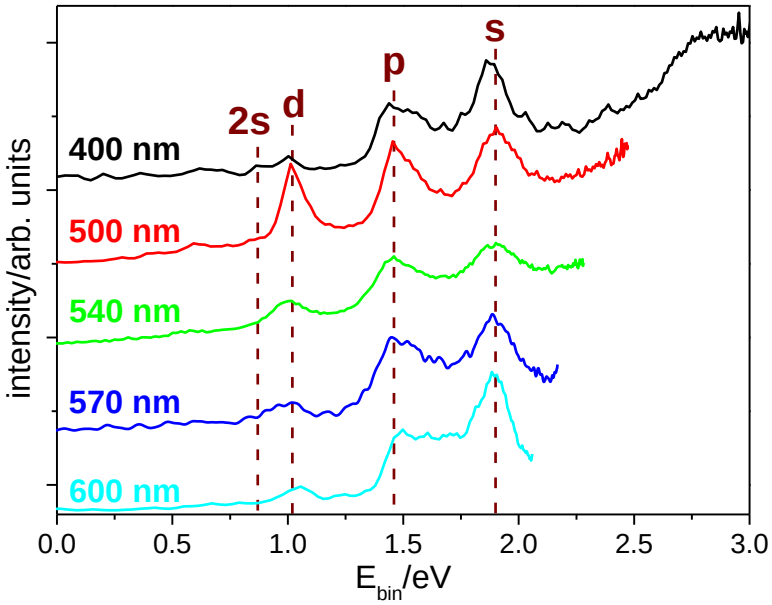

Figure 3.23: Angle integrated PES of C_{60} at various wavelengths plotted against the electron binging energy.[35,133]

In order to find out about these properties the relative photoionisation cross sections of the SAMOs in C_{60} have been determined experimentally and compared to results from TD-DFT calculations conducted by Benoît Mignolet.[35]

The result of the theoretical model is shown in Figure 3.24 where the calculated photoionisation widths (previously explained in section 1. 5. 2) of the lowest SAMO states are plotted against the kinetic energy of the photoelectron.[35] The calculated photoionisation width is proportional to the photoionisation rate and directly related to the photoionisation cross-section.

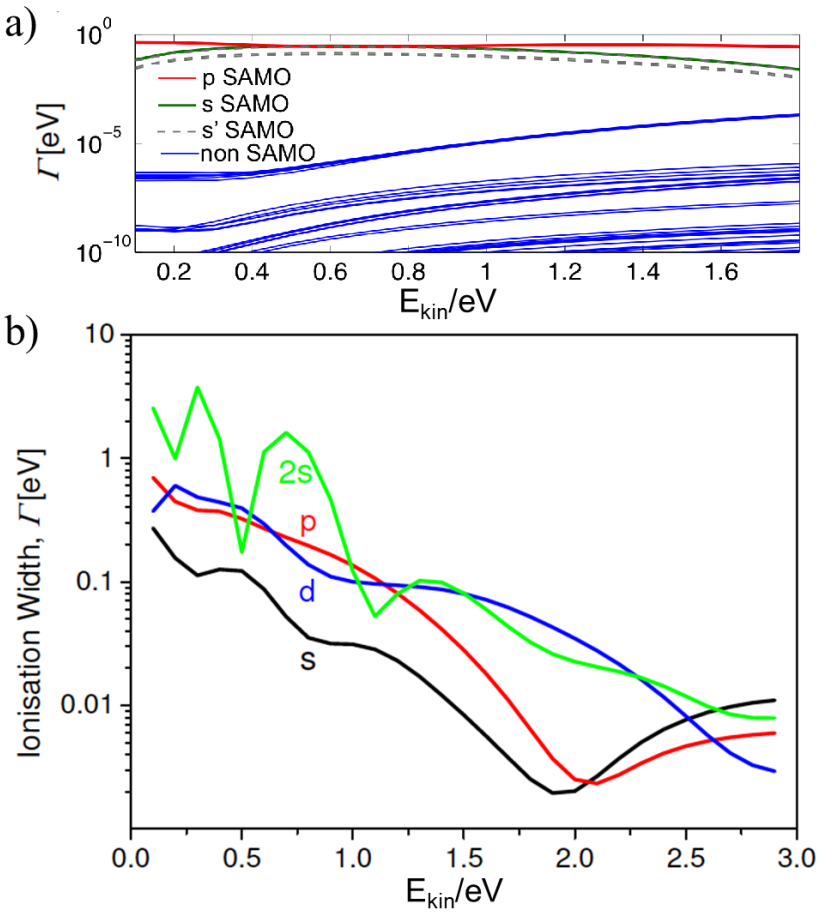

Figure 3.24: a) Computed photoionisation widths as a function of the photoelectron kinetic energy of all calculated excited states (first 500 states) and b) of the lowest-lying SAMO states using TD-DFT conducted by Benoît Mignolet.[35,75]

The comparison of the photoionisation widths for the first 500 excited states (Figure 3.24 a) reveals that the photoionisation width of the non-SAMO states increases with increasing photoelectron kinetic energy.[35,75] In contrast to the photoionisation widths of the SAMO states which decrease with increasing kinetic energy of the photoelectron according to Figure 3.24 b).[35] This result is in agreement with previously identified trends in absolute photoionisation cross-sections for different molecular systems, where the photoionisation widths are predicted to be similar for SAMO and non-SAMO states converging to a value of ≤ 0.01 for photoelectron energies above 2.5 eV.[75,134–137] Because the absolute photoionisation widths could not be determined in the conducted experiments, the relative photoionisation ratios of the s and p SAMO as well as the s and d SAMO were identified for the experimental data and compared with the corresponding ratios of the calculated photoionisation widths.[35]

For the experimental data of the photoionisation probabilities of the C_{60} SAMOs it was crucial to make sure the ratio of the SAMO peak intensities were not critically dependent on the oven temperature of the hot source, the laser pulse duration or the laser pulse intensity within the ranges typically used in the photoionisation experiments (Figure 3.25, Figure 3.26 and Figure 3.27).[133]

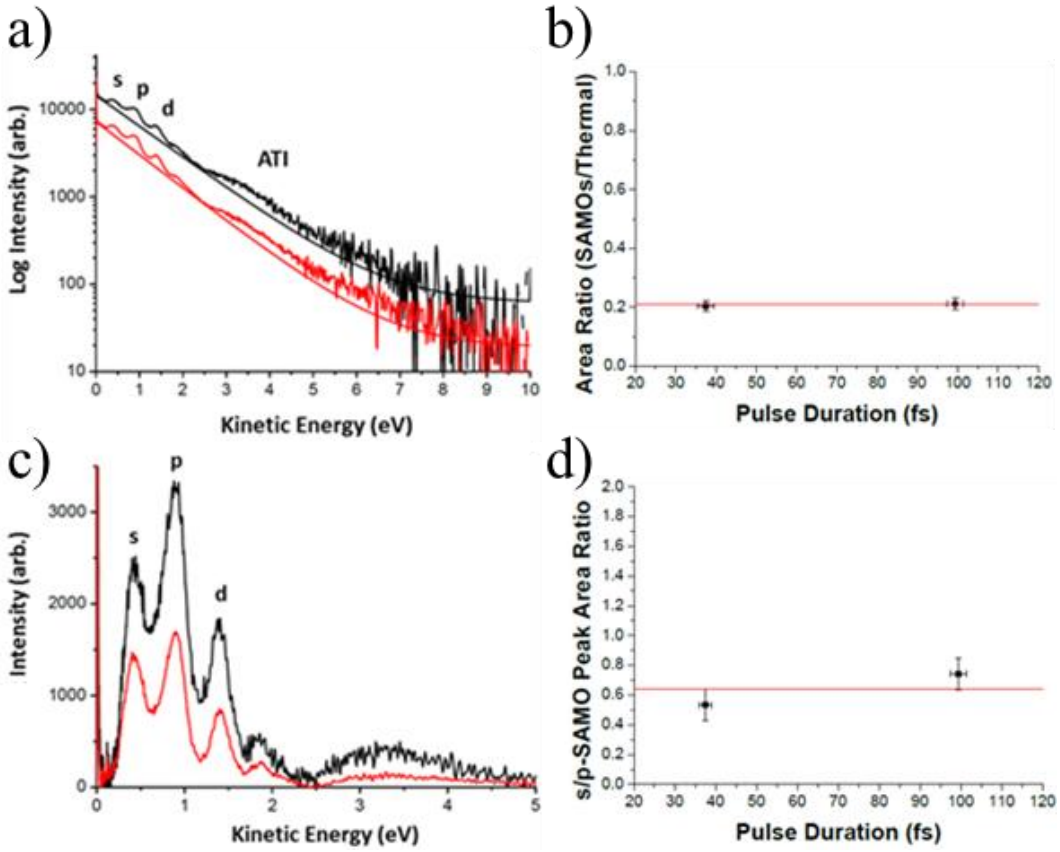

Figure 3.25: a) C_{60} PES using 540 nm plotted on a logarithmic scale for the intensity; c) same PES after thermal electron background subtraction on a linear scale. The spectra in black and red correspond to a pulse duration of (38 ± 10) fs, (10.5 ± 0.5) TW/cm² and (99 ± 2) fs, (4 ± 1) TW/cm² respectively. The comparison of the two different pulse durations for b) the overall s, p and d SAMO to thermal background signal area ratio and d) s to p SAMO peak area ratio including red, horizontal lines to guide the eye.[133]

According to the results in Figure 3.25 from measurements at a set wavelength (542 nm), oven temperature (505 °C) and laser fluence (~ 0.4 J/cm²) but different laser pulse durations, (38 ± 1) fs and (99 ± 2) fs, the ratio of the SAMO signal to the thermal background and the s to p SAMO ratio do not change distinctively within the experimental error. Therefore it can be concluded that the pulse duration is not a significant factor for the analysis of the relative intensity of the SAMO states.[133]

Since earlier studies have shown the importance of initial vibrational energy for the population and detection of the SAMO peaks,[14] measurements are performed to investigate any influence of the oven temperature and hence the internal energy of C_{60} on the SAMO ratios. PES of C_{60} are recorded at a set wavelength (540 nm), pulse duration, (35 ± 10) fs, and laser intensity, (8.20 ± 0.05) TW/cm², for a series of different oven temperatures (505 °C, 485 °C, 460 °C and 435 °C) which still induce significantly higher vibrational temperatures than the low temperature molecular beam experiments performed by Boyle *et al*.[14,133]

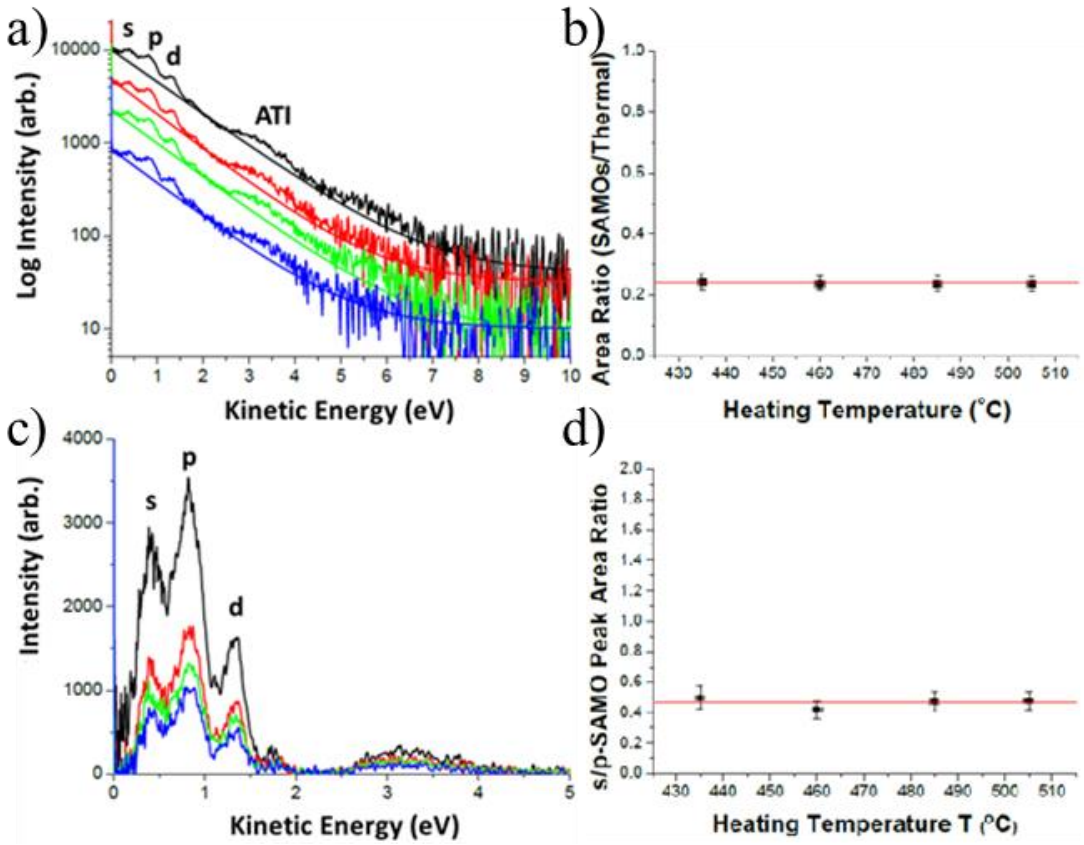

Figure 3.26: PES of C_{60} using 540 nm, (35 ± 10) fs, (8.20 ± 0.05) TW/cm^2 laser pulses a) on a logarithmic intensity scale and c) after thermal electron background subtraction on a linear scale are shown for different oven temperatures, 505 °C (black line), 485 °C (red line), 460 °C (green line) and 435 °C (blue line). The comparison of the different oven temperatures for b) the overall s, p and d SAMO to thermal background signal area ratio and d) s to p SAMO peak area ratio including red, horizontal lines to guide the eye.[133]

The measurements in Figure 3.26 show that the oven temperature in the studied temperature range is not a critical factor for the relative difference in the observed photoelectron intensities of the SAMO states, whilst it is an important factor for optimising the total count rate by controlling the target density.[133]

Furthermore, the influence of variable the laser power density on the SAMO peak ratio has been investigated at a set laser wavelength (540 nm), pulse duration, (35 ± 10) fs, and oven temperature (505 °C) for a number of different laser intensities, (5.8 ± 0.1) TW/cm^2, (4.7 ± 0.1) TW/cm^2, (3.9 ± 0.1) TW/cm^2, (3.2 ± 0.1) TW/cm^2 and (1.8 ± 0.1) TW/cm^2.[133]

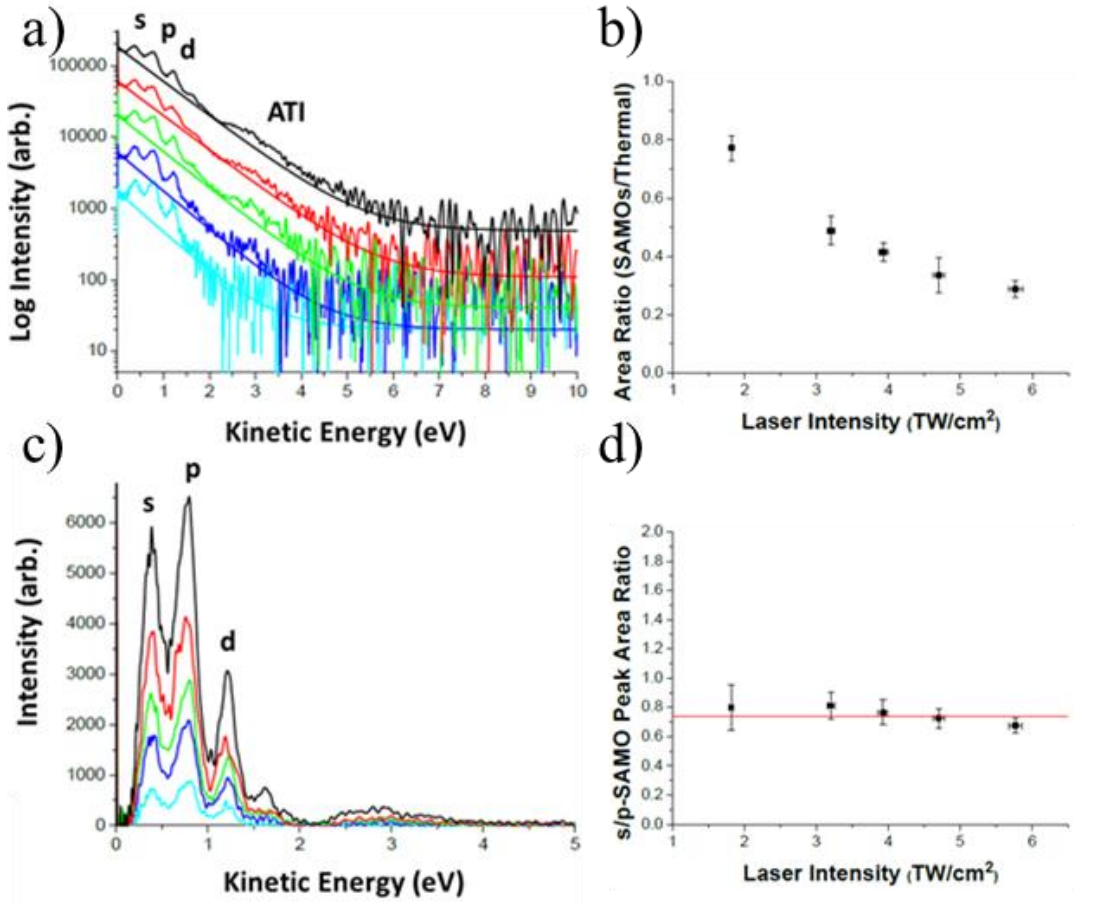

Figure 3.27: a) PES of C_{60} plotted on a logarithmic scale for the intensity and c) the PES after thermal electron background subtraction. b) Displaying the laser intensity dependence of the overall s, p, and d SAMO photoionisation intensity relative to the thermal electron emission and d) the s/p SAMO photoionisation intensity ratio dependence on the laser intensity.[133]

The laser pulse intensity affects the relative magnitude of the SAMO states with respect to the total thermal background significantly (Figure 3.27).[133] The total thermal electron background increases with a rising electron temperature for increasing laser intensity or fluence[12,27] more rapidly than for the SAMO signal. Nevertheless, the relative intensities of the SAMO states remain constant for the range of laser pulse intensities studied.[133]

The outcomes of the above measurements testing the influence of the pulse duration, oven temperature and laser intensity on the relative SAMO peak ratio show no dependency on these experimental parameters in the studied range which corresponds to the typical variety of the measurement parameters used in this thesis. Therefore, the relative photoionisation probabilities can be analysed experimentally and the obtained results are reliable in the range of the studied experimental parameters.

To obtain the experimental photoionisation probability ratios the thermal background was subtracted from the obtained PES and Lorentzian functions were fitted to the SAMO peaks.[35] The assignment of the peak structure in the studied PES to the SAMO states has been done previously in the Campbell

group on the basis of the binding energies and PAD compared to theoretical calculations.[7] A summary of some of the analysed angle integrated PES of C_{60} is shown in Figure 3.28.

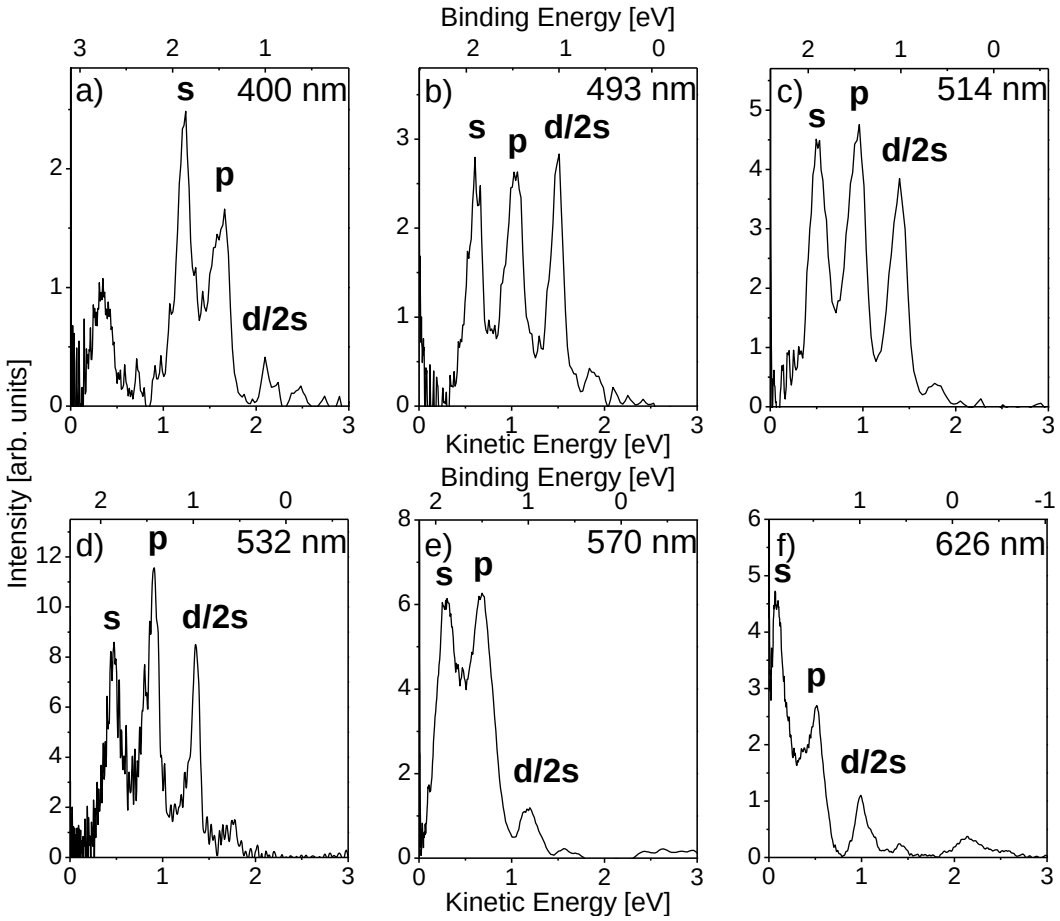

Figure 3.28: A few of the studied angle integrated PES of C_{60} after thermal background subtraction at the indicated laser wavelength.[35]

The electron binding energies of these peaks are identical for all investigated laser wavelengths. The first s SAMO peak corresponds to a binding energy of about 1.9 eV, the first p SAMO band has a binding energy of about 1.5 eV, the following peaks for the d SAMO band and the second s SAMO state cannot be clearly distinguished in these angle-integrated PES because their binding energies of about 1.0 eV and 0.9 eV are very close.[7,35] During the manual fitting process the binding energies and peak widths were kept constant for each SAMO state while the relative intensities were adjusted to the spectrum.[35]

The obtained photoionisation ratios of s to p SAMO and s to d SAMO states are compared to the theoretically calculated ratios in Figure 3.29.

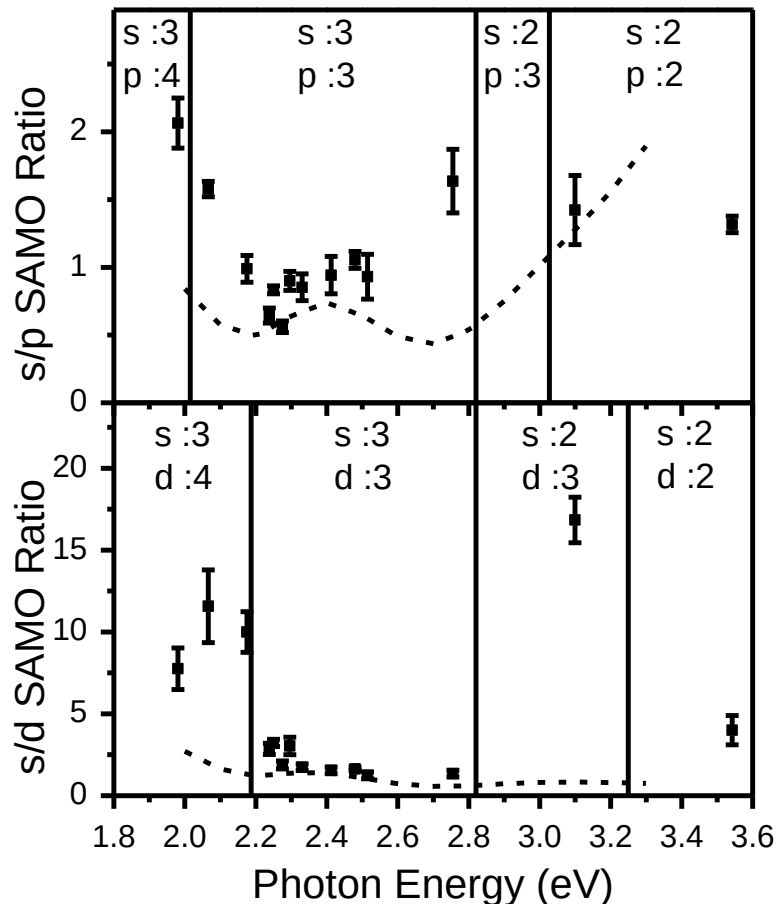

Figure 3.29: Comparison of relative experimental SAMO peak intensities (squares) and the theoretical photoionization width ratios of SAMO states plotted as a function of laser photon energy. Upper panel: ratio of the s and p peak intensities. Lower panel: ratio of the s and d peak intensities. Theoretical values shown by dashed lines (ratio of average values calculated for each band).[75] The numbers at the top of the plots indicate the number of photons needed to access the s and the p or d SAMO states, respectively (not taking into consideration the substantial amount of vibrational energy that is present in the hot fullerenes from the oven).[35]

The comparison shows a clear correlation between the predicted trend and the experimentally obtained results within the region where the excited states can be accessed by the same number of photons, as indicated by the numbers at the top of each plot (Figure 3.29).[35] Beyond these regions the s SAMO can be reached by one less photon than the higher states and therefore the s SAMO peak intensity is expected to be significantly higher than the peak for the higher-lying states.[35] This assumption is supported by the measured SAMO ratios which are correspondingly higher in the described case.[35] However the calculations do not predict this occurrence as the exact population mechanism is not considered but just an equal population of all states with the same probability is assumed.[35,75] The findings show that the simple assumption of equally populated SAMO states is holding as long as the same photon order is needed to energetically access the states.

Considering that the same photon order is needed to access the d and 2s SAMO states, they should be expected to give photoionisation ratios comparable to the calculations because these states have similar binding energies and therefore would be accessible by the same number of photons throughout the photon range investigated.[35] Nevertheless, due to the similar binding energies of the d and 2s SAMOs the peaks are very difficult to distinguish and to assign in the experimental spectra.[35] Also the calculations indicate strong oscillations in the 2s photoionisation width (Figure 3.24 b). Therefore, it is not surprising that the experimentally obtained photoionisation ratios of the d and 2s SAMO do not agree with the calculations as well as the s/p and s/d SAMO ratios as shown in Figure 3.30.

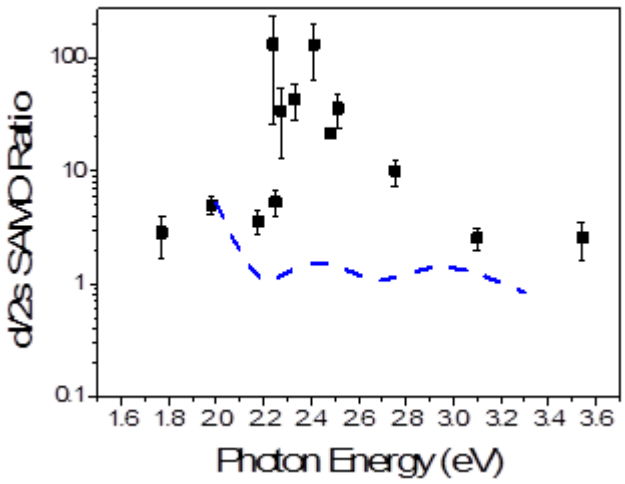

Figure 3.30: Comparison of relative experimental d and 2s SAMO peak intensities with theoretical ionisation width ratios (average band values) as a function of photon energy.[35]

3. 3. Discussion and Conclusions

3. 3. 1. Discussion

For the discussion of the results on the SAMO states of the investigated fullerenes, the PES and corresponding mass spectra are compared (Figure 3.31).

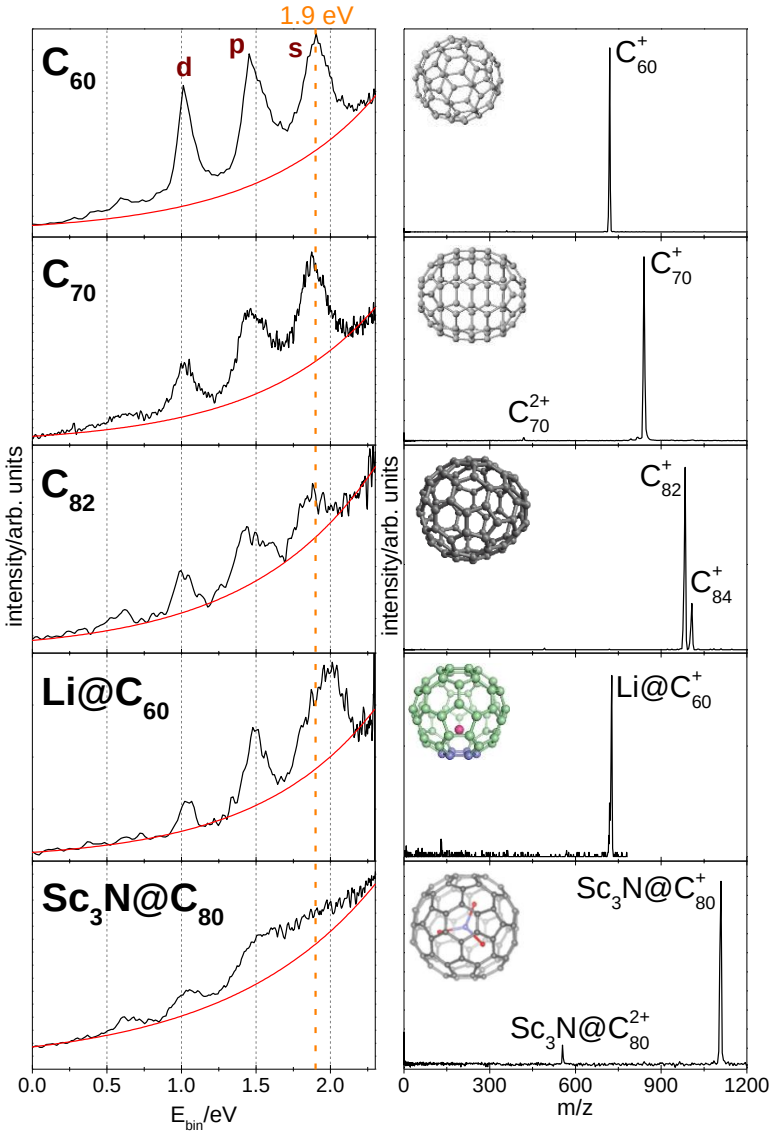

Figure 3.31: Angle integrated PES (left column) and corresponding mass spectra (right column) for C_{60} (top row) excited with 500 nm, (90 ± 10) fs, (4.7 ± 0.3) TW/cm^2; C_{70} (second row) excited with 520 nm, (90 ± 10) fs, (2.9 ± 0.5) TW/cm^2; C_{82} (third row) excited with 519 nm, (90 ± 10) fs, (2.8 ± 1.0) TW/cm^2; Li@C_{60} (fourth row) excited with 540 nm, (35 ± 10) fs, (9.0 ± 0.8) TW/cm^2 ; and Sc_3N@C_{80} (bottom row) excited with 506 nm, (90 ± 10) fs, (4.1 ± 0.5) TW/cm^2.[77] The thermal electron background fit is shown as a red line in each PES and the assignment of the peak structure is shown in the C_{60} PES, top row.

As mentioned in the previous chapters all the PES of the analysed fullerenes (Figure 3.31) show a thermal background with a superimposed peak structure which has been assigned to the s, p and d SAMO states.[77] On the basis of Figure 3.31 it is obvious that the SAMO peaks become broader and less pronounced with increasing size of the fullerene cage ($C_{60} \rightarrow C_{70} \rightarrow C_{82}$) and decreasing symmetry ($I_h \rightarrow D_{5h} \rightarrow C_2$).[77] Due to the breaking of the I_h symmetry a splitting of the degenerate p and d orbitals occurs which is shown in the computational results for C_{70} through a range of E_{bin} of the p and d SAMOs (Table 3.8).[77]

Table 3.8: Summary of the experimentally obtained E_{bin} of the SAMO states for the examined fullerenes, C_{60}, C_{70}, C_{82}, Li@C_{60} and Sc_3N@C_{80}. The computed E_{bin} of the SAMOs are also shown at the TD-DFT/B3LYP/6-31+G(d) level for C_{60}, C_{70} and C_{84}, as well as at the TD-DFT/CAM-B3LYP/6-31+G(d) level for C_{60}.[75,77]

Fullerene		E_{bin}/eV			
		s SAMO	**p SAMO**	**d SAMO**	**2s SAMO**
C_{60}	**Expt.**	**1.86 ± 0.02**	**1.49 ± 0.02**	**1.04 ± 0.02**	**0.83 ± 0.03**
	Calc. B3LYP	2.14	1.26	0.77	0.54
	Calc. CAM-B3LYP	2.10	1.14	0.62	0.39
C_{70}	**Expt.**	**1.86 ± 0.02**	**1.42 ± 0.02**	**0.99 ± 0.03**	**0.83 ± 0.03**
	Calc. B3LYP	2.20	1.19 – 1.24	0.73 – 0.79	0.61
C_{82}	**Expt.**	**1.90 ± 0.04**	**1.42 ± 0.05**	**1.03 ± 0.03**	**0.86 ± 0.03**
C_{84}	Calc. B3LYP	2.12	1.22 – 1.28	0.72 – 0.83	--
Li@C_{60}	**Expt.**	**1.93 ± 0.07**	**1.47 ± 0.06**	**1.03 ± 0.04**	**0.87 ± 0.06**
Sc_3N@C_{80}	**Expt.**	**1.96 ± 0.08**	**1.50 ± 0.05**	**1.04 ± 0.08**	**0.68 ± 0.09**

According to Table 3.8 the encapsulation of an atom or molecule inside a fullerene cage seems to increase the E_{bin} of the s SAMO, like in the case of Li@C_{60} and Sc_3N@C_{80}, while the binding energies of the p and d state are unaffected. Nevertheless, it has to be pointed out that the s SAMO peak is not well resolved in the PES of Sc_3N@C_{80} and it has been only possible to determine the s state through its PAD. In terms of the Li@C_{60} PES the s SAMO can be resolved with a clear shift to higher E_{bin} (Figure 3.31).

Furthermore, the variation of the anisotropy values of the different SAMOs states plotted against the photoelectron kinetic energy provides a more stringent test of the theoretical calculations on the electronic structure of the molecule (Figure 3.32).[77]

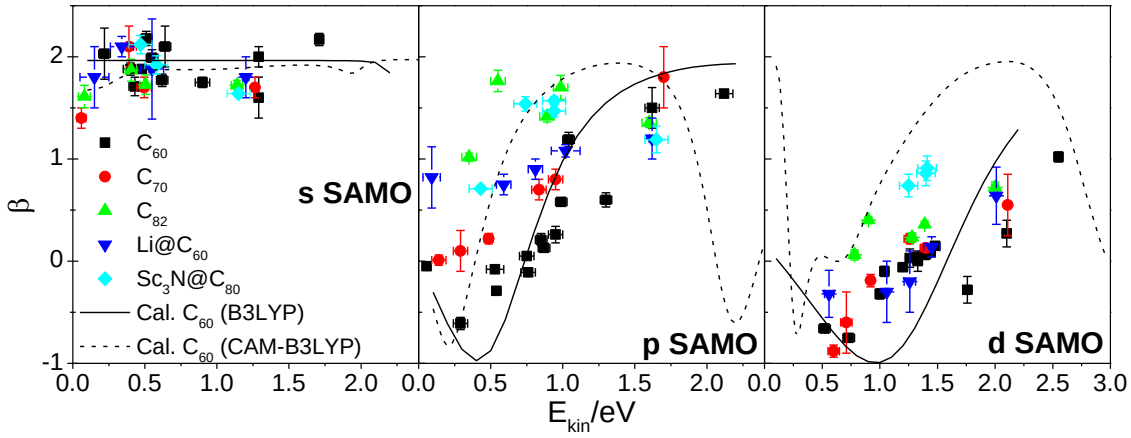

Figure 3.32: Anisotropy values of C_{60} (black squares), C_{70} (red circles), C_{82} (green upwards pointing triangles), $Li@C_{60}$ (blue downwards pointing triangles) and $Sc_3N@C_{80}$ (cyan squares) plotted against E_{kin} for the s (left plot), p (middle plot) and d SAMO (right plot).[77] The graphs also include the theoretically modelled β values for C_{60} at the TD-DFT/B3LYP/6-31+G(d) (black solid line) and at the TD-DFT/CAM-B3LYP/6-31+G(d) level (black dashed line).[77]

Firstly the anisotropy values for the s SAMO states (Figure 3.32 left plot) are consistent for all studied fullerenes with $\beta \approx 2$, as the electron-electron correlation between the residual electrons and the outgoing electron does not have a significant contribution to the photoionisation of this state.[77] However for the p SAMO the trend of the β values shows a difference between the studied fullerenes, especially below 1 eV (Figure 3.32 middle plot).[77] It seems like the β values increase at lower E_{kin} for larger fullerenes ($C_{60} \rightarrow C_{70} \rightarrow C_{82}$),[77] as well as for the encapsulation of an atom ($C_{60} \rightarrow Li@C_{60}$). It is also interesting to point out that the anisotropy values of the p state of C_{82} follow closely the values of $Sc_3N@C_{80}$ whilst the trend in the β values of the $Sc_3N@C_{80}$ seems to be very similar to the alteration in the PADs of $Li@C_{60}$. For the d SAMO (Figure 3.32 right plot) the β values are not affected until the fullerene cage size is increased significantly (C_{60}, $C_{70} \rightarrow C_{82}$) which is also the case for $Sc_3N@C_{80}$, but again the endohedral molecule might have an influence on the β value which cannot be distinguished from the effect of the increasing cage size. Nevertheless, the anisotropy values of the d state of $Li@C_{60}$ are almost identical with the values of C_{60}, so the encapsulated atom or molecule does not have a significant influence on the d SAMO.

3. 3. 2. Conclusions

All studied fullerenes show a peak structure superimposed on a thermal background in the PES. The peaks have been identified as s, p and d SAMOs based on the comparison of the E_{bin} and the corresponding PAD to previous studies on C_{60}.

The observed broadening of the SAMO peaks for bigger fullerenes can be caused by the splitting of the degenerate p and d bands due to the breaking of the I_h symmetry. Unfortunately, this splitting cannot be resolved in the experimental PES because of the broad bandwidth of the used laser pulses and the close spacing of the non-degenerate states. The increasing number of atoms in higher fullerene molecules increase the number of electronic states as well, which may enhance the energy distribution into the electronic subsystem after the initial excitation.[77] This explanation would support the assumption that the thermal electron emission mechanism becomes more dominant in the photoionisation of larger fullerenes.[77] However, this would have an effect on the apparent temperature of the thermal electron background which will be analysed in detail in chapter 1.

The $Sc_3N@C_{80}$ PES indicates a shift of the s SAMO to higher E_{bin}, however the s peak is not well resolved. The PES of the endohedral $Li@C_{60}$ shows a clear shift of the well-pronounced s SAMO peak to higher E_{bin} compared to C_{60}. Therefore, the conclusion can be made that the encapsulation of an atom or molecule increases the binding energy of the s SAMO for the studied fullerenes, $Li@C_{60}$ and $Sc_3N@C_{80}$, but does not significantly affect the E_{bin} of the p and d SAMOs.

Although the binding energies of the SAMO states are not changing significantly, the ionisation energies of the studied fullerenes are different. The ionisation potential of $Li@C_{60}$ ($IP(Li@C_{60}) \approx 6.4$ eV)[119,125] is about 1 eV lower than of C_{60} ($IP(C_{60}) = 7.6$ eV)[23]. Since the E_{bin} of the SAMOs stay about the same for $Li@C_{60}$ and C_{60}, but the IPs vary, the excitation energies for the SAMOs are changing. Hence, it is possible to tune the excitation energies by adjusting the ionisation energy via functionalisation. Also, the accessibility of the SAMO states can be improved by the fullerene size or functionalisation.

From the PAD of the SAMOs it can be concluded that the anisotropy values of the s SAMOs are not affected by changing the fullerene cage size neither the symmetry nor by encapsulating an atom or molecule inside the cage. However, the PAD of the p and d SAMO states are influenced by a variation in the size of the fullerene or the insertion of an atom or molecule inside the fullerene.

The effect of the fullerene cage size on the PAD can be explained by the lower symmetry for other fullerenes than C_{60} which causes a splitting of the degenerated p and d SAMOs. Therefore, the correlation between the outgoing electron and the residual electrons will change and this will definitely differ the anisotropy value. For the β values of the d SAMO the increase of the fullerene cage has to be bigger than for the p SAMO, possibly, because the electron density is expected to be located further from the cage for the d state than for the p state.

The encapsulation of an atom (or molecule) alters the PAD of the p SAMO but not the PAD of the d SAMO. The encaged atom does probably modify the core potential of the endohedral fullerene so the relative phase of the outgoing photoelectron partial waves is varied due to scattering. As mentioned, before the electron density of the d state is assumed to be outside the fullerene cage, thus the endohedral atom is effectively screened and has no significant effect on the orbital. This is also confirmed by the modelled Dyson orbitals of $Li@C_{60}$ and C_{60}. On the other hand, the endohedral fullerene $Sc_3N@C_{80}$ shows a different PAD for the d SAMO compared to C_{60} but this is mainly due to the effect of the larger fullerene cage (C_{80}) as explained previously, and the β values are closer to C_{82}.

For a further characterisation of the SAMO states the photoionisation probability ratios of the s/p and s/d SAMOs have been obtained experimentally (section 3. 2. 1).[35] These experimentally identified SAMO ratios have been reproduced by the ratios of the theoretically calculated photoionisation widths using TD-DFT.[35] The successful modelling of the ionisation properties of such a large and complex system like a fullerene is remarkable and substantiates the predictive potential of quantum chemistry techniques for analysing the electronic dynamics of complex molecular systems.[35]

4. Thermal Electron Emission from Fullerenes

4. 1. Introduction

The transient thermal electron emission and the electric field-induced barrier suppression models were established to describe the thermal electron emission in the PES of C_{60} and C_{70} for laser pulse durations between 50 fs to a few hundred fs and were introduced in chapter 1. 5.[4,27,33,63,64] As part of this thesis, measurements on C_{60} have been carried out to reproduce and to verify the thermal electron model. The thermal electron background in the PES of fullerenes can be fitted by an exponential distribution, $I(E_{kin}) \propto \exp(-\frac{E_{kin}}{k_B T_a})$, (equation (1.16)) which is characterised by an apparent temperature T_a with k_B as the Boltzmann constant (as described in chapter 1. 5). As the thermal electron emission from fullerenes has been studied previously in C_{60} and C_{70}, it is reasonable to assume that other fullerenes will behave similarly in this regard.[12,125] Furthermore, the experimental thermal electron emission of the endohedral Li@C_{60} has been compared to the thermal electron distribution of C_{60}. The model has been applied to Li@C_{60}, by Eleanor Campbell, to reproduce the experimentally obtained apparent temperatures of the thermal electron background. At the end of this chapter the experimentally obtained apparent temperatures of the thermal electron emission for all investigated fullerenes (C_{60}, C_{70},[64,74,77] C_{82}, $Sc_3N@C_{80}$ and Li@C_{60}) are compared and trends are discussed.

4. 2. Analysis Procedure

Firstly the procedure for the analysis of the thermal electron background in the PES will be explained. The PES is plotted on a log-lin scale so the apparent temperature can be determined by fitting a straight line to the distribution by eye. The inverse of the slope yields the apparent temperature according to the equation (converted from equation (1.16)):

$$\log(I) = -\frac{E_{kin}}{k_B T_a} \qquad \textbf{(4.1)}$$

Due to other features in the PES like direct ionisation of SAMO peaks of E_{kin} below the photon energy and ATI peaks at higher E_{kin} than the photon energy, an automated least-squares fitting procedure cannot be used. Therefore, the fits are made by eye and the errors are also estimated by eye. An example of a fitted temperature and estimated errors is displayed in Figure 4.1. The upper limit is estimated by taking

ATI peaks into account of the thermal background and the lower limit is assessed by fitting the lowest possible temperature with a reasonable agreement with the spectrum.

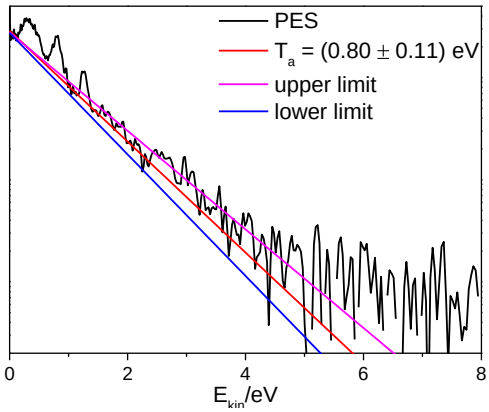

Figure 4.1: Fitting procedure of the electron apparent temperature to an angle integrated PES of Li@C_{60} using 540 nm, (35 ±10) fs, (9.0 ± 0.8) TW/cm^2 of the present work. The fitted temperature is (0.80 ± 0.11) eV obtained from the red line. The pink and blue line represent the upper and lower limits for the error estimation, respectively.

4. 3. Results

4. 3. 1. C_{60} - Verification of the Thermal Electron Emission Model

For the verification of the thermal electron model, experiments on C_{60} have been conducted using 700 nm, (78 ± 10) fs and 800 nm, (120 ± 10) fs laser pulses at different laser intensities. A typical angular-resolved PES and its corresponding mass spectrum of C_{60} at 700 nm is shown in Figure 4.2.

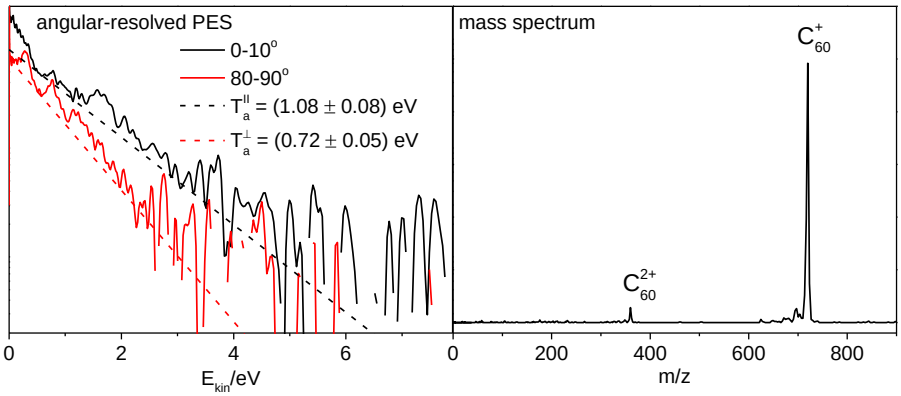

Figure 4.2: Angular-resolved PES (left) and corresponding mass spectrum (right) of C_{60} using 700 nm, (78 ± 10) fs, (5.1 ± 1.0) TW/cm^2 of the present work. The electron distributions along (0-10°, black solid line) and perpendicular (80-90°, red solid line) to the laser polarisation direction are shown including the fit of the thermal electron background (according dashed line).

The difference between the parallel and perpendicular apparent temperatures, $\Delta k_B T_a$, which have been obtained from the experiments using 700 nm and 800 nm, are plotted against U_p in Figure 4.3 and compared to literature values[63].

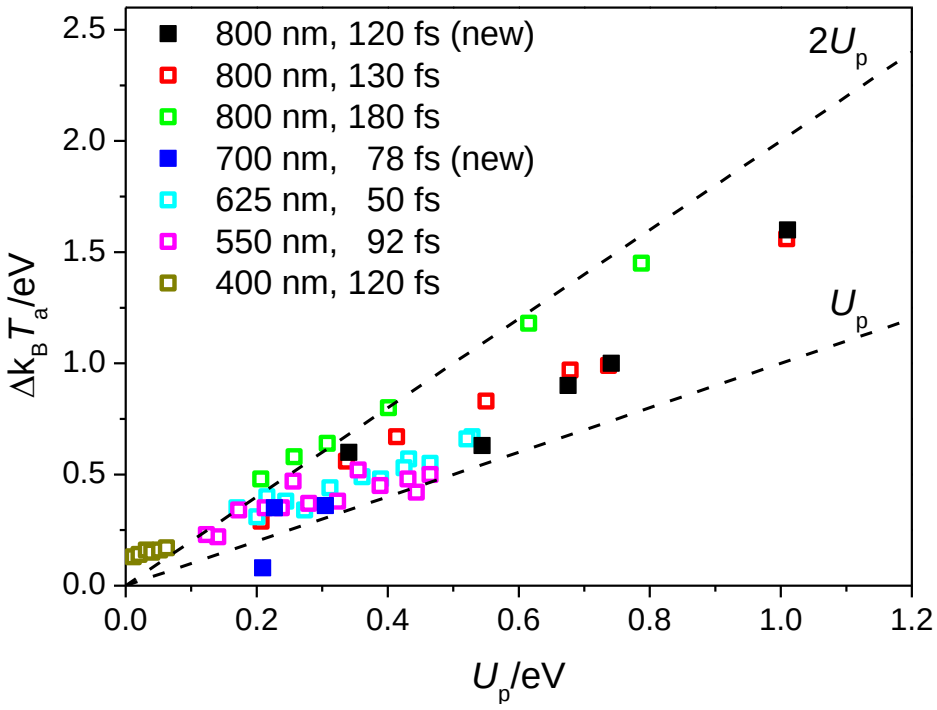

Figure 4.3: Difference of the parallel and perpendicular apparent temperatures, $\Delta k_B T_a$, of C_{60} is plotted against U_p for a range of wavelengths and pulse durations. The solid data points are newly obtained while the open squares are from ref.[63]

The new measurements using an 800 nm excitation wavelength have reproduced the values from the literature for 130 fs laser pulses. Additionally, the experimental results at 700 nm lie between U_p and $2U_p$, except the value for the lowest laser intensity (Figure 4.3). This deviation can be explained by the high noise level, which is present at such a low laser intensity at 700 nm, so the fitting of the thermal electron temperature was difficult and the result has a large error (see appendix 0, Figure 8.8).

The experimentally obtained parallel and perpendicular apparent temperatures have also been compared to literature values. The results from the experiment using 800 nm, (120 ± 10) fs laser pulses is compared to the literature values at 800 nm, 130 fs (Figure 4.4 a). The experimental results at 700 nm, (78 ± 10) fs laser excitation are compared to literature values at 625 nm, 50 fs (Figure 4.4 b).

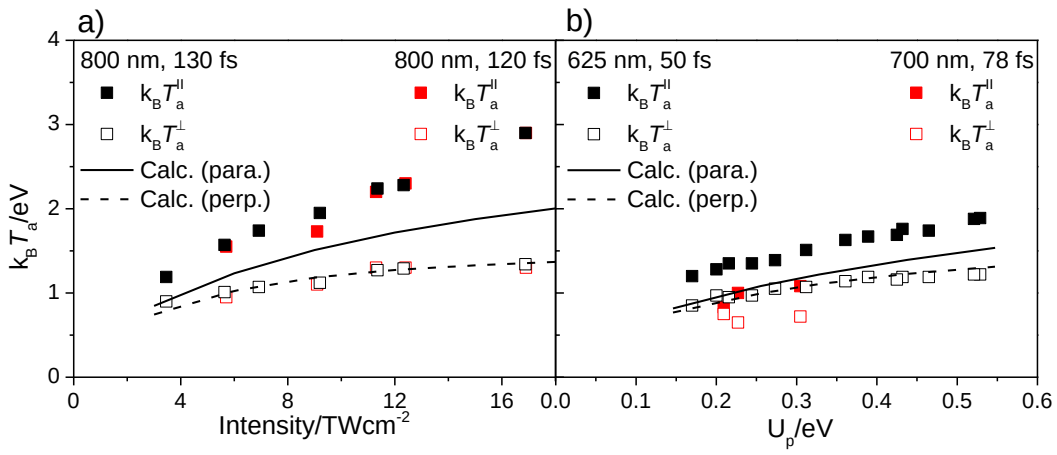

Figure 4.4: Experimental apparent temperatures of C_{60} (red points) obtained for a) 800 nm, (120 ± 10) fs plotted against the laser intensity and b) 700 nm, (78 ± 10) fs plotted against U_p (equation (1.1)). The obtained data points are compared to literature values (black points and lines) from ref.[63]

In chapter 1. 5 the consistent underestimation of the experimental temperatures parallel to the laser polarisation by the thermal model (Figure 4.4) has been explained by possible effects which are not considered in the model.

In the case of the 800 nm measurements, the obtained apparent temperatures are in a good agreement with the experimental literature values (Figure 4.4 a). Only the parallel temperature at a laser intensity around 9 TW/cm^2 is lower than the literature value but the deviation is still within the error.

The determined apparent temperatures of the PES using 700 nm cannot be compared directly to the literature values from ref.[63] as the 700 nm measurements have been conducted to complement the previous results and the model. However, the new temperatures can be compared to literature values at 625 nm to gain conclusions on any trend (Figure 4.4 b). The apparent electron temperatures increase with increasing laser intensity and seem to follow a similar trend to the values of 625 nm. The onset of the 700 nm values is at slightly lower temperatures than for 625 nm which may be due to the difference in photon absorption cross-section, as this is the only fit parameter used in the computational model for the thermal electron emission (section 1. 5, equation (1.14)).[63]

On the basis of Figure 4.3 and Figure 4.4, the thermal electron emission model has been verified by reproducing the experimental data for 800 nm and by complementing the literature values with the apparent temperatures from the 700 nm experiment, especially for the perpendicular apparent temperatures. In the case of the modelled parallel temperatures, the deviations to the experimental values need further investigation to determine additional effects which have to be considered in the model as mentioned in chapter 1. 5.

The electric field-induced barrier suppression model was introduced by Gordon Henderson[74] and is previously described in chapter 1. 5. The model attempts to provide an explanation for the increased

counts of thermal photoelectrons in PES segments along the laser polarisation compared to segments perpendicular to it for mainly longer wavelengths.[74] The above mentioned measurements on C_{60} using 700 nm laser pulses have also been used to test this model. The obtained data points have been displayed with the previous results from Figure 1.14 from chapter 1. 5 (Figure 4.5).[74]

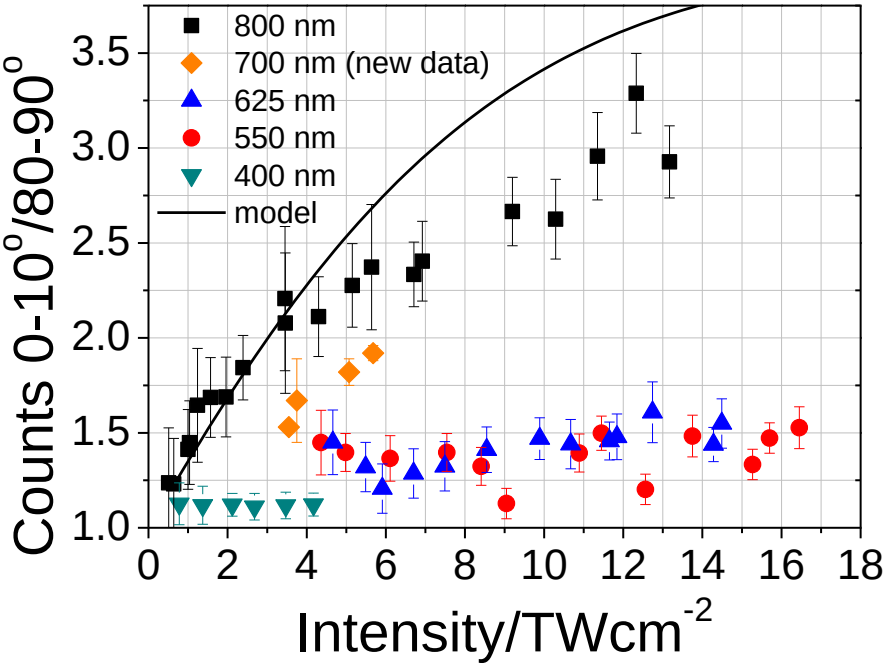

Figure 4.5: The ratios between the number of counts for 0-10° and 80-90° angular segments plotted as a function of laser intensity for different wavelengths taken from ref.[74], same as Figure 1.14, but also includes the new data points for 700 nm (orange points).

The experimentally determined count ratios for C_{60} using 700 nm are between the ratios for 800 nm and 625 nm or 550 nm, respectively (Figure 4.5). Also the 700 nm data points seem to follow the same trend as the 800 nm data points. However, the modelled values show a larger deviation for laser intensities >4 TW/cm^2 for the values at 800 nm. Therefore, the electric field-induced barrier suppression model has to be refined to fit better to the experimental values, e. g. the laser wavelength dependence has to be included. Then this model can be implemented into the transient thermal electron emission model.

4. 3. 2. Thermal Electron Emission from Li@C_{60}

Since the PES of Li@C_{60} also shows a thermal electron background as mentioned previously in chapter 3. 2. 3, the thermal electron emission can also be characterised by the transient thermalisation model (using IP(Li@C_{60}) ≈ 6.5 eV[87], assuming the same time constant for coupling to vibrational degrees of freedom as for C_{60} with 240 fs[27], with a photon absorption cross-section of 0.15 Å^2, 241 valence

electrons, and 3.5 Å^2 as the radius of the fullerene cage[122,138]). In Figure 4.6 the apparent temperatures of the thermal electron background of Li@C_{60} and C_{60} are compared for 800 nm, 120-130 fs laser pulses at various laser intensities, as well as the differences between the parallel and perpendicular electron temperatures with respect to the laser polarisation direction.

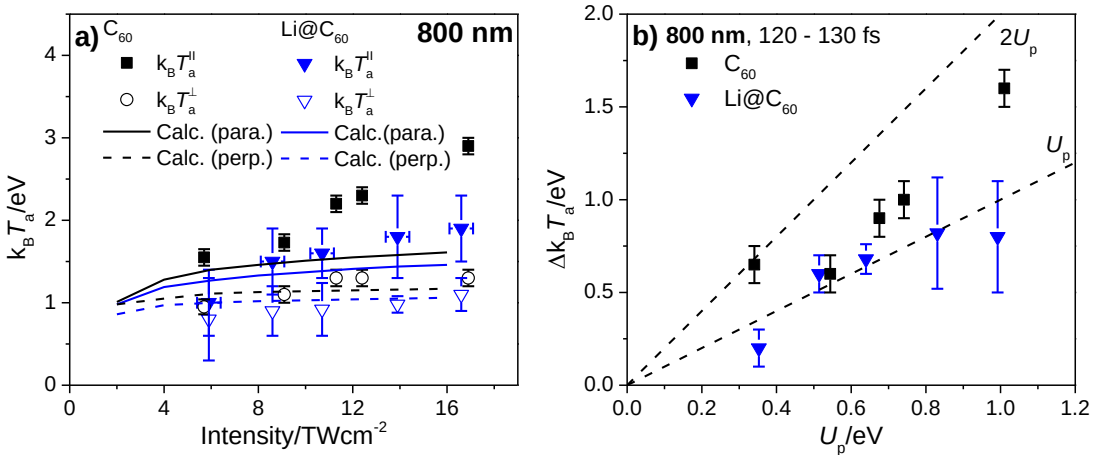

Figure 4.6: a) Plot of experimental apparent temperatures (points) obtained for Li@C_{60} (blue points) and C_{60} (black points) using 800 nm, (120 ± 10) fs against the laser intensity and compared to results from the transient thermal electron emission model[4,27,64] (lines) calculated by Eleanor Campbell (see chapter 1. 5). b) Difference between the parallel and perpendicular electron temperatures, obtained from plot a), plotted against the ponderomotive shift (equation (1.1)). The dashed lines in b) indicated the maximal gain in kinetic energy of the electrons from the vector field, $2U_p$, and a gain of U_p (see chapter 1. 5).

The apparent temperatures are lower for Li@C_{60} than C_{60} which is reproduced by the thermal model (Figure 4.6). Also the asymmetry of the thermal electron background seems to be lower for Li@C_{60} than C_{60} according to Figure 4.6. The lower apparent temperatures of Li@C_{60} may be due to the lower ionisation potential of Li@C_{60} (IP(Li@C_{60}) ≈ 6.4 eV)[119,125] than C_{60} (IP(C_{60}) = 7.6 eV)[23], so less energy is needed to ionise Li@C_{60} and therefore the electron temperature is lower. It has also to be noted that the oven temperature for the Li@C_{60} (T_{oven} = 380 °C) has been lower than for the C_{60} experiments (T_{oven} = 500 °C) and the mass peak ratios of Li@C_{60}^+/C_{60}^+ has been roughly about 1:1 constantly (see Figure 3.16, chapter 3. 2. 3). This already indicates that the Li@C_{60} signal is overlapped by the C_{60} signal (as discussed in chapter 3. 2. 3). Therefore, the thermal electron signal may be originated mainly from C_{60} which only has a lower apparent temperature due to the lower oven temperature. To test this, the ratio of the thermal electron counts of the parallel to the perpendicular PES segments with respect to the laser polarisation is compared to the 800 nm data points from Figure 4.5.

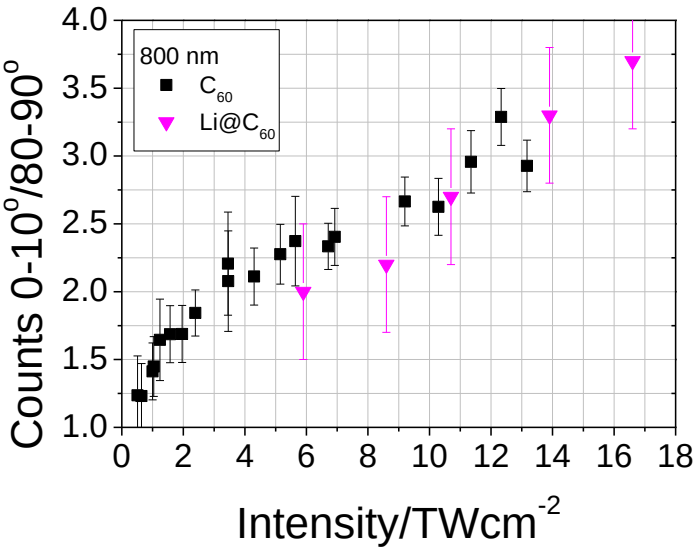

Figure 4.7: The ratios between the thermal electron counts for 0-10° and 80-90° angular segments plotted as a function of laser intensity for C_{60} (black points, data taken from ref.[74]) and Li@C_{60} (pink points) at 800 nm.

The thermal count ratio for Li@C_{60} fits well to the ratio for C_{60} for higher laser intensities from about 10 TW/cm^2 upwards based on Figure 4.7. For lower laser intensities the count ratio seems to be lower for Li@C_{60} than C_{60}, but the C_{60} ratios are still within the error of the Li@C_{60} measurement. The errors are estimated to be quite large for the Li@C_{60} count ratios due to the lower signal and higher noise in the measurements, especially for lower laser intensities. Nevertheless, for a laser wavelength of 540 nm, where the Li@C_{60}^+ is more dominant than the C_{60}^+ mass peak (see chapter 3. 2. 3, Figure 3.19), the apparent temperatures are still lower for Li@C_{60}^+ than C_{60}^+ (Figure 4.8 b) which supports the findings from the experiments at 800 nm, too.

4. 4. Comparison of the Studied Fullerenes

The thermal electron temperatures of all the studied fullerenes can be compared to C_{60} and C_{70} for different wavelengths and some data points are available at a few varying laser intensities. Therefore, the apparent temperatures perpendicular to the laser polarisation direction are compared for a range of wavelengths (Figure 4.8).

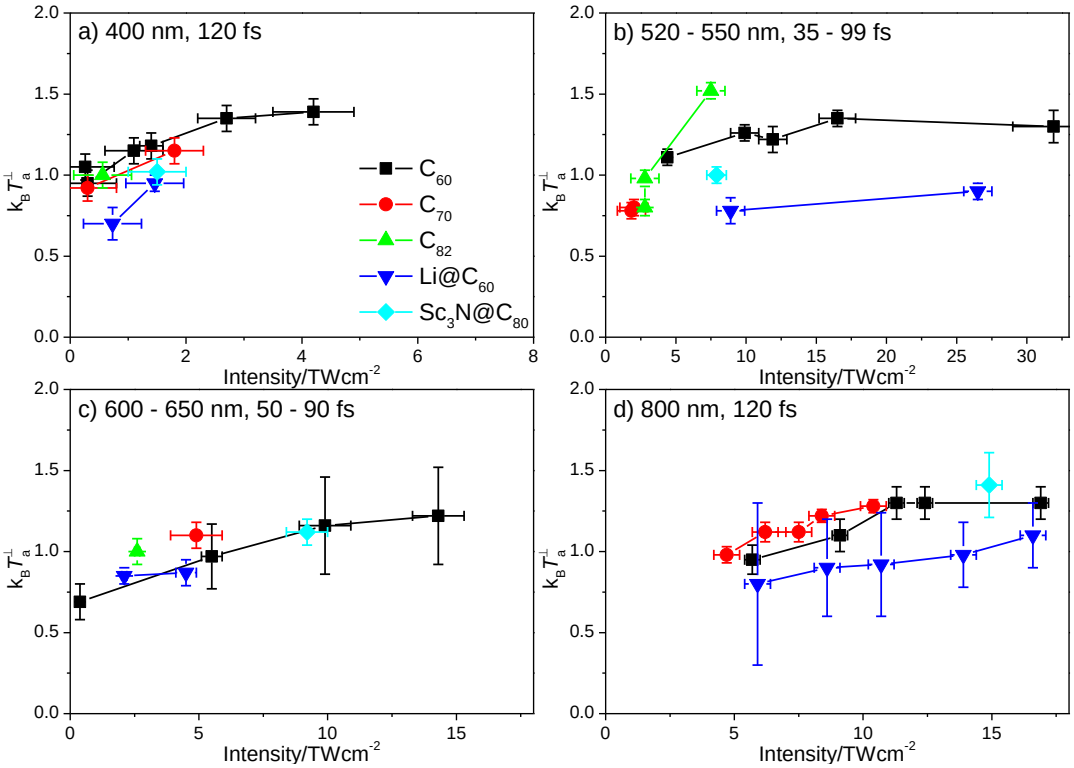

Figure 4.8: Comparison of the apparent temperatures perpendicular to the laser polarisation for C_{60}[35,64,74,77], C_{70}[74,77], C_{82}[77], Li@C_{60} and $Sc_3N@C_{80}$[77] using laser wavelengths of a) 400 nm, 120 fs; b) 520 – 550 nm, 35 – 99 fs; c) 600 – 650 nm, 50 – 90 fs; d) 800 nm, 120 fs.

For an excitation wavelength of 400 nm C_{60} shows the highest perpendicular electron temperature in relation to the other displayed fullerenes (Figure 4.8 a).[12,77] For C_{70} and C_{82} the temperatures seem to be slightly lower than for C_{60} but the values are still within the errors for the C_{60} temperatures (Figure 4.8 a), whereas the Li@C_{60} temperatures are clearly lower than for C_{60}. In the case of a laser wavelength 520 – 550 nm the difference between the thermal temperatures of Li@C_{60} and C_{60} is even clearer (Figure 4.8 b). For this wavelength the C_{70} temperature as well as the $Sc_3N@C_{80}$ temperature are lower than for C_{60} (Figure 4.8 b). However, the thermal temperature of C_{82} seems to rise more rapidly with increasing laser intensity than for C_{60} for wavelengths of 520 – 550 nm which needs to be verified, since this measurement has only been taken once (Figure 4.8 b). This supports the reliability of the C_{82} thermal temperature for the 600 – 650 nm measurement being higher than for C_{60} (Figure 4.8 c). For this wavelength (600 – 650 nm) the thermal electron temperature of C_{70} also seems to be higher in comparison to C_{60} but is still within the estimated error of the C_{60} temperature. On the contrary, the thermal electron temperatures of Li@C_{60} and $Sc_3N@C_{80}$ are the same as for C_{60} at a wavelength range of 600 – 650 nm (Figure 4.8 c). In the case of the thermal electron temperatures using 800 nm, Li@C_{60} has lower values than C_{60} though are still within the error of the C_{60} temperatures (Figure 4.8 d). Interestingly, the apparent temperatures of C_{70} are higher than for C_{60} at 800 nm, but the difference between the values is very small and close to the range of the errors (Figure 4.8 d).

Comparing the difference in the apparent temperatures parallel and perpendicular to the laser polarisation, $\Delta k_B T_a$, provides information on the degree of asymmetry in the thermal electron emission (Figure 4.9).

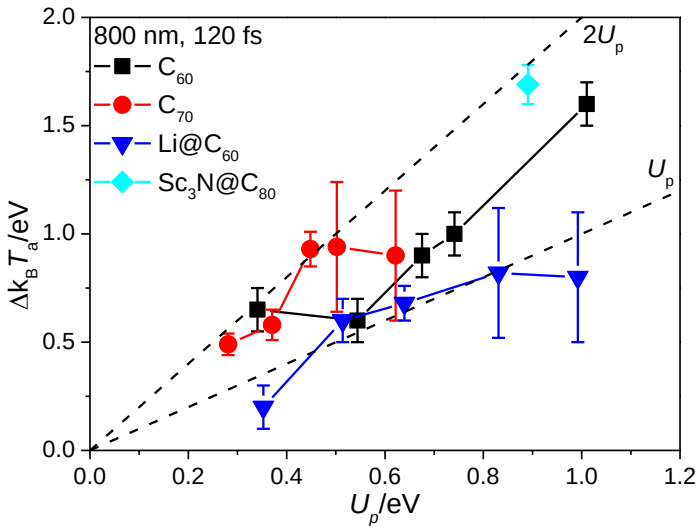

Figure 4.9: Difference between the parallel and perpendicular electron temperatures, $\Delta k_B T_a$, of C_{60}, C_{70}[64,74], $Li@C_{60}$ and $Sc_3N@C_{80}$[77] using 800 nm, 120 fs laser pulses plotted against the ponderomotive shift (equation (1.1)). The dashed lines indicated the maximal gain in kinetic energy of the electrons from the vector field, $2U_p$, and a gain of U_p (see chapter 1. 5).

In Figure 4.9, the apparent temperature difference, $\Delta k_B T_a$, are compared for the studied fullerenes, as shown in Figure 4.8, only for the laser wavelength of 800 nm, as the largest degree of asymmetry in the thermal electron background is expected for this longer wavelength than for lower ones (650 nm, 600 nm etc.) (as explained in chapter 1. 5). The comparison shows that almost all data points fall between U_p and $2U_p$, as previously shown in chapter 1. 5 in Figure 1.11. Hence, this result also supports the transient thermal electron emission mechanism for the studied fullerenes in which case the emitting electrons can receive a momentum kick along the laser polarisation direction.[63] The apparent temperature difference of $Li@C_{60}$ for the highest and lowest ponderomotive shift are slightly lower than U_p (Figure 4.9). However, the data point for the highest ponderomotive shift has an error range including a value of U_p. The deviating apparent temperature difference of $Li@C_{60}$ needs to be reproduced to assure if their variance from the model is true.

Overall the similarity of the temperatures and the asymmetry of the VMI provide support for the thermal electron emission mechanism because the excitation spectrum of each molecule should have little effect on it.[77] Nevertheless, according to the transient thermal electron emission model the apparent temperature of $Li@C_{60}$ is expected to be lower than for C_{60} (see Figure 4.6 a) which has reproduced the trends obtained in Figure 4.8 for comparing $Li@C_{60}$ to C_{60}. The lower electron temperature of $Li@C_{60}$ can be explained by its lower ionisation potential compared to C_{60} (as explained previously in this chapter), so $Li@C_{60}$ ionises with less energy and probably quicker. Hence the thermal electron

temperature decreases as seen in Figure 4.8. Expanding on this explanation all fullerenes larger than C_{60} would be expected to have a lower thermal temperature due to the higher heat capacity based on more available electrons, but this is not clear looking at Figure 4.8. A slightly higher electron temperature for C_{60} had been observed previously in comparison to C_{70}, which had been explained by the lower heat capacity of C_{60}.[12,77] This observation is in agreement with the experimental results using 400 nm and 520 – 550 nm (Figure 4.8 a, b), but not for 600 – 650 nm and 800 nm (Figure 4.8 c, d). Therefore, especially the increase in the electron temperature for C_{82} (Figure 4.8 b, c) and C_{70} (Figure 4.8 d) requires further investigation.

5. Computational and Experimental Studies on Polycyclic Aromatic Hydrocarbons (PAHs)

5. 1. Introduction

Previous studies on PAHs revealed similar photoionisation mechanisms and excited electronic states (in analogy to SAMOs) to fullerenes (see chapter 1. 1). Based on these findings theoretical calculations have been conducted on various PAHs using TD-DFT in the program Gaussian 09[102] (see chapter 2. 3). The outcomes of this computational investigation will be presented in this chapter.

5. 2. Computational Studies

5. 2. 1. Benchmarking

Firstly a variety of different functionals and basis sets (Pople, split valence double zeta basis sets) have been tested to get the best comparable results to literature values with an acceptable calculation time (not more than 24 hours for the excited state calculation). For this test run, naphthalene was chosen because experimental data on the Rydberg states were available from the literature.[22,139] The following table (Table 5.1) summarises the tested functional and basis sets with a short description:

Table 5.1: Summary of the tested functionals and basis set on naphthalene.

Functional used with 6-31(2+)+G(d,p) basis set	**Description**
wB97XD	long range corrected functional including empirical dispersion[140]
M06HF	full Hartree-Fock exchange which eliminates self-exchange interactions at long range[141]
B3LYP	most commonly used hybrid functional including a mixture of Hartree-Fock and DFT functional[142]
CAM-B3LYP	long range corrected version of B3LYP using the Coulomb-attenuating method[143]
Basis set used with CAM-B3LYP	**Description**
6-31++G(d,p) used wB97XD functional	- core orbital basis (1s) function: 6 gaussian primitives - inner valence orbital basis functions: 3 gaussian primitives; outer valence orbitals basis functions: 1 gaussian primitive - **non-hydrogen atoms: 1 sets of p(sp)-type diffuse basis functions (4 diffuse basis functions per atom); H atoms: 1 s-type diffuse function** - heavy atoms: 1 set of d orbitals as polarisation functions; H atoms: 1 set of p orbitals as polarisation
6-31(2+)+G(d,p)	- same as above except the following - **non-hydrogen atoms: 2 sets of p(sp)-type diffuse basis functions; H atoms: 1 s-type diffuse function**
6-31(2+)(2+)G(d,p)	- same as above except the following - **non-hydrogen atoms: 2 sets of p(sp)-type diffuse basis functions; H atoms: 2 sets of s-type diffuse basis functions**
6-31(3+)(3+)G(d,p)	- same as above except the following - **non-hydrogen atoms: 3 sets of p(sp)-type diffuse basis functions; H atoms: 3 sets of s-type diffuse basis functions**

The procedure to obtain the binding energies of the excited electronic states was as follows. First the ground state structure is optimised using the chosen functional and basis set with the symmetry point group imposed. In the case of naphthalene, the symmetry point group is C_{2v}. As a quick test of the reliability of the computational result, the calculated vertical *IP* is compared to the literature value, where the variance should not exceed 5% of the value. The adiabatic *IP* has been calculated only for a few functionals and basis sets as further verification of their accuracy. The computed *IPs* of the different functionals and basis sets are summarised in Table 5.2 for naphthalene.

Table 5.2: Comparing computed *IPs* of naphthalene to literature values at different theory levels.

Naphthalene	vertical *IP*/eV	adiabatic *IP*/eV
Experimental literature values	**8.15 ± 0.02** [144]	**8.14 ± 0.01** [145]
Calculated values	**vertical *IP*/eV**	**adiabatic *IP*/eV**
wB97XD/6-31(2+)+G(d,p)	**7.99**	**--**
M06HF/6-31(2+)+G(d,p)	**8.51**	**--**
B3LYP/6-31(2+)+G(d,p)	**7.91**	**--**
CAM-B3LYP/6-31(2+)+G(d,p)	**8.05**	**7.94**
wB97XD/6-31++G(d,p)	**8.31**	**--**
CAM-B3LYP/6-31(2+)+G(d,p)	**8.05**	**7.94**
CAM-B3LYP/6-31(2+)(2+)G(d,p)	**8.05**	**7.94**
CAM-B3LYP/6-31(3+)(3+)G(d,p)	**8.05**	**--**

All computed *IPs* are within 5% of the literature value and below the experimental *IP*, except at the M06HF/6-31(2+)+G(d,p) and wB97XD/6-31++G(d,p) level (Table 5.2). The M06HF[141] functional neglects the self-exchange interactions at long range and uses the full Hartree-Fock exchange (Table 5.1) which may lead to a larger deviation. However, the wB97XD functional is long-range-corrected and includes empirical dispersion (Table 5.1), but the complementing basis set also needs to be large enough to enable a good approximation. In Table 5.2 the outcomes show that the basis set 6-31(2+)+G(d,p) has to be used with the wB97XD functional to obtain reasonably good results, whereas the 6-31++G(d,p) basis set is probably too small for the calculation of the *IP* of naphthalene. Altogether the best results are obtained with the CAM-B3LYP functional and a basis set of 6-31(2+)+G(d,p) at least (Table 5.2). Larger basis sets with the CAM-B3LYP functional do not give a noticeable improvement in the *IPs* (Table 5.2).

Then the optimised ground state structure is used to calculate the excited electronic states using TD-DFT. The resulting MO are viewed in the GaussView program and by eye it is determined if the electron density has a shape similar to s, p or d orbitals. An example of excited states which have been identified as s, p or d SAMO-like orbitals in naphthalene are shown in Figure 5.1.

a) s state b) p state c) d state

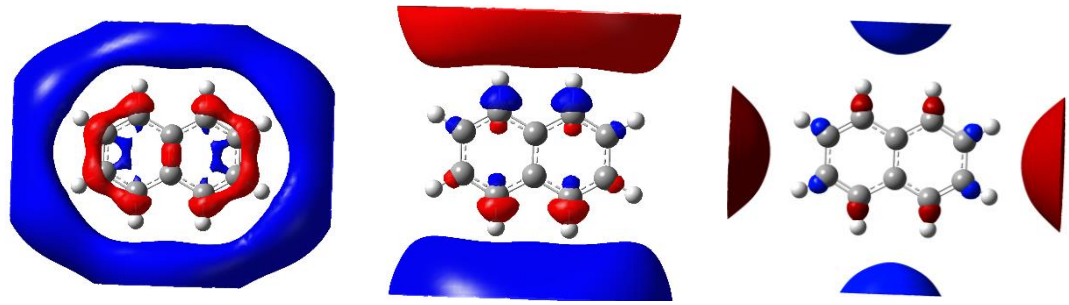

Figure 5.1: SAMO-like orbitals (isocontour value of 0.003 $|e|/a^3$) identified in naphthalene as a) s, b) p and c) d states. The MOs are larger than the computational cells, so the orbitals are cut at the cell borders.

The binding energies of these states is obtained through the subtraction of the excitation energy from the vertical *IP* for each state. The resulting binding energies can be compared to literature values as shown in Table 5.3 for naphthalene.

Table 5.3: Calculated binding energies of different excited states of naphthalene at the CAM-B3LYP/6-31(2+)+G(d,p) level compared to literature values.

Orbital:	LUMO+1	LUMO+2	LUMO+3	LUMO+4
identified orbital shape as	**s**	**p_z**	**p_y**	**p_x**
calc. vertical *IP*	8.05 eV			
Excitation energy	5.55 eV	5.91 eV	5.94 eV	5.94 eV
Binding energy	**2.50 eV**	**2.14 eV**	**2.11 eV**	**2.11 eV**
Experimental literature values for the binding energies	**(2.57 ± 0.09) eV**[21] **(2.55 ± 0.09) eV**[146]	**(2.14 ± 0.09) eV**[21] **(2.35 ± 0.09) eV**[146]		

This procedure was conducted on naphthalene for the different functionals and basis sets (see Table 5.1), so that the binding energies of some states could be compared. The obtained binding energies at the various theory levels are summarised graphically in Figure 5.2.

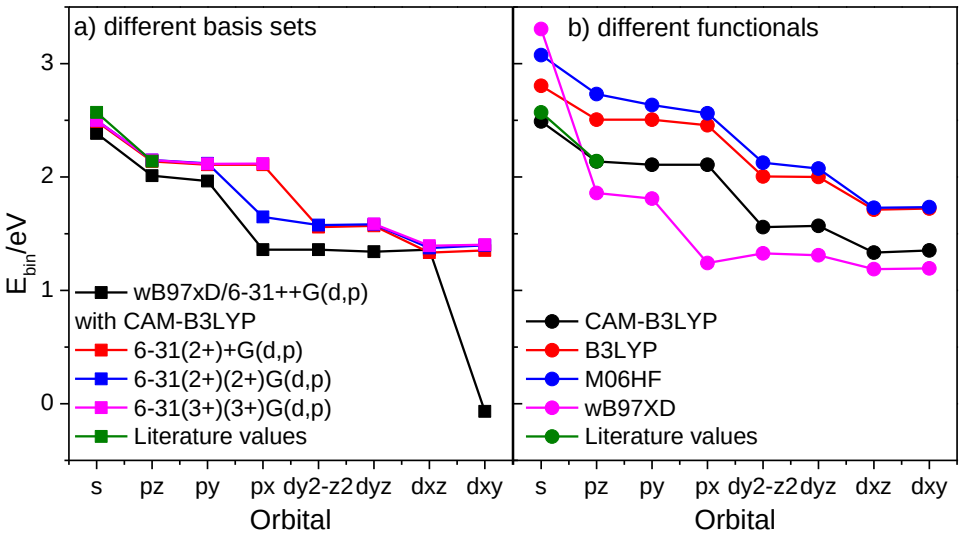

Figure 5.2: Comparing the calculated binding energies of different excited states of naphthalene obtained using various a) basis sets and b) functionals (with 6-31(2+)+G(d,p) basis set). The computed results are also compared to literature values from ref.[22]

On the basis of Figure 5.2 the functional CAM-B3LYP with the basis set 6-31(2+)+G(d,p) was chosen as the most suitable theory level. The larger basis sets (Figure 5.2 a) increase the computational time, but do not have a significant improvement on the binding energies because the basis set 6-31(2+)+G(d,p) already gives values close to the literature. The CAM-B3LYP functional shows the best agreement with the literature values for the binding energies of the s and p state, while the other functionals, which also include long range interactions like wB97XD and M06HF, are farther off the literature values as well as B3LYP (Figure 5.2 b).

Therefore the excited states of the following PAHs were calculated at the CAM-B3LYP/6-31(2+)+G(d,p) level. The molecules for the 1st series, called linear series, were benzene, naphthalene, anthracene, tetracene, pentacene and hexacene. The molecules of the 2nd series, also called planar series, were phenanthrene, pyrene and coronene. The molecules of the 3rd series, also called 3-D series, were cubane, adamantane and dodecahedral C_{20}.

5. 2. 2. Computational Results on PAHs

All molecules revealed excited states with electron densities located over the whole molecule in analogy to the SAMO states in fullerenes. Some Dyson orbitals (see chapter 2. 3) of these excited states are displayed in Table 5.4.

Table 5.4: Displaying a few s and p_z Dyson orbitals of naphthalene, pentacene, phenanthrene and cubane computed by Benoît Mignolet based on TD-DFT calculations from this thesis. The isocontours (isocontour value of 0.002 $|e|/a^3$) of the orbitals are shown as a cut through and along the molecular plane.

compound	s state	p_z state
naphthalene	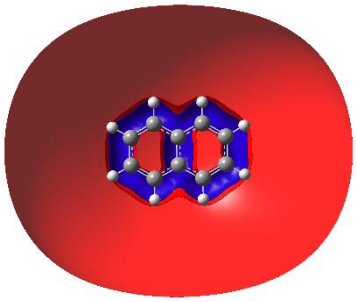	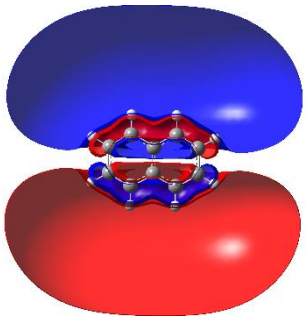
pentacene	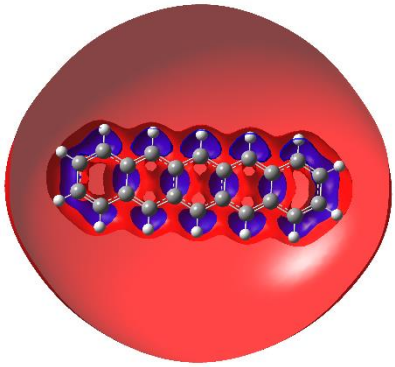	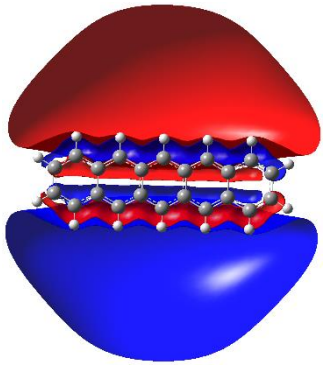
phenanthrene	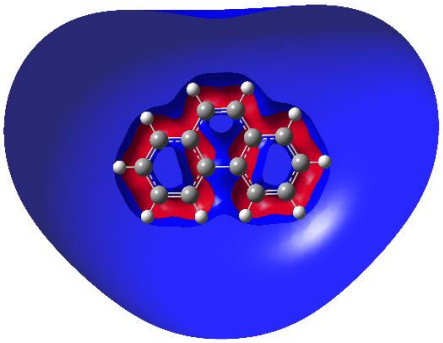	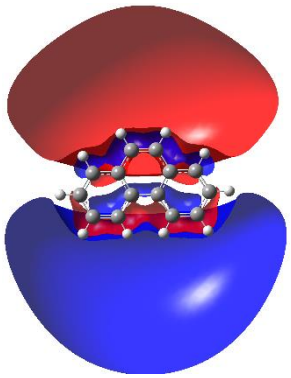
cubane	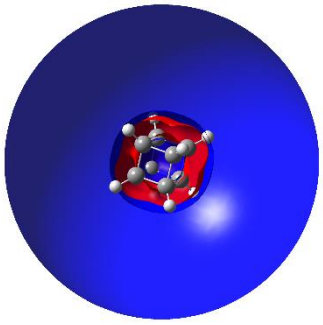	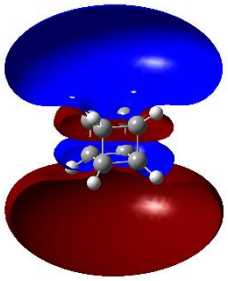

The three series will be discussed separately to analyse the variation of the binding energies for the excited states. First the binding energies of the identified s, p and d SAMO-like states are compared for the several compounds within the 1st series in Figure 5.3.

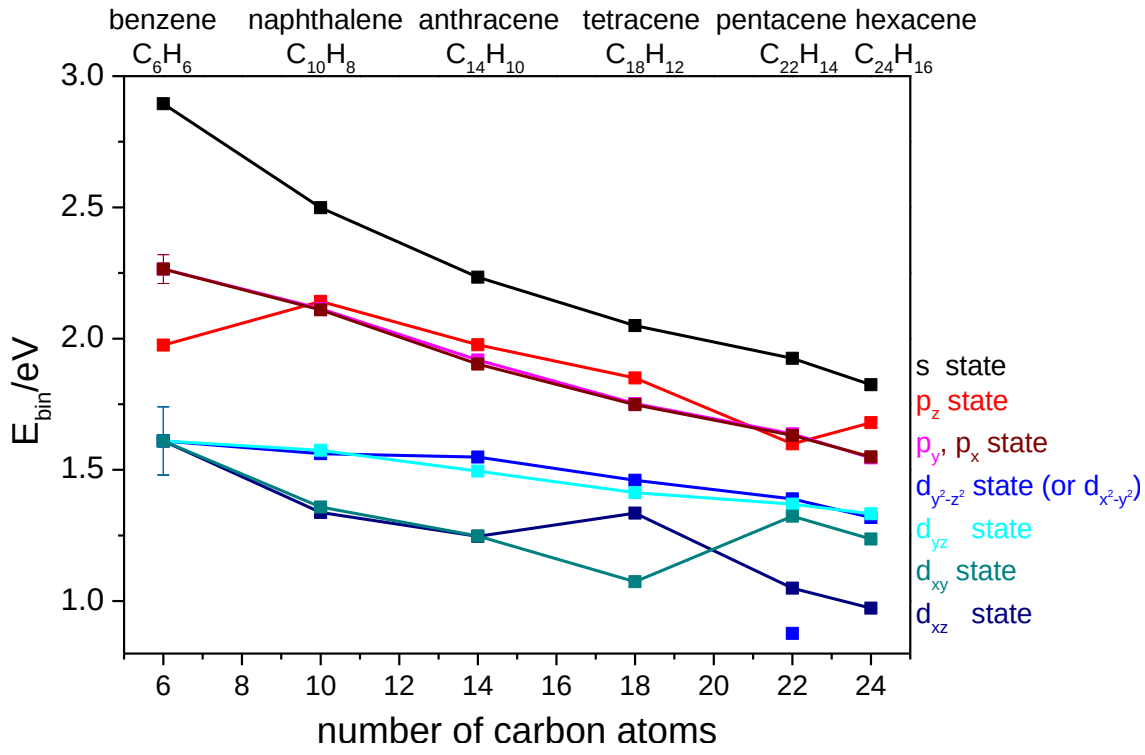

Figure 5.3: E_{bin} comparison of the first s, p and d SAMO-like states for the 1st series of PAHs plotted against the number of carbon atoms in the corresponding molecule. The compound names and chemical formula are summarised on top of the graph.

The error bars in the E_{bin} for some states indicate the range of the binding energies which the states may have as the precise assignment has been difficult. The trend in the binding energies is obvious that the energies decrease with increasing molecular size while the symmetry of the molecules remains the same (D_{2h}), except for benzene (D_{6h}) (Figure 5.3). This trend is clear for the s, p_y, p_x, d_{y2-z2} and d_{yz} state, whereas the p_z, d_{xz} and d_{xy} states show fluctuations in their binding energies. For molecules larger than anthracene it became difficult to distinguish between the different d states which could have resulted in misinterpretation of some MOs, which can be seen by the additional d_{xy} state energy for pentacene. Nevertheless, the binding energies of naphthalene can be compared to experimental literature values which show a good agreement as shown in Table 5.3. This supports the findings of the computations on the 1st series of PAHs.

The comparison of the binding energies for the 2nd series is shown in Figure 5.4.

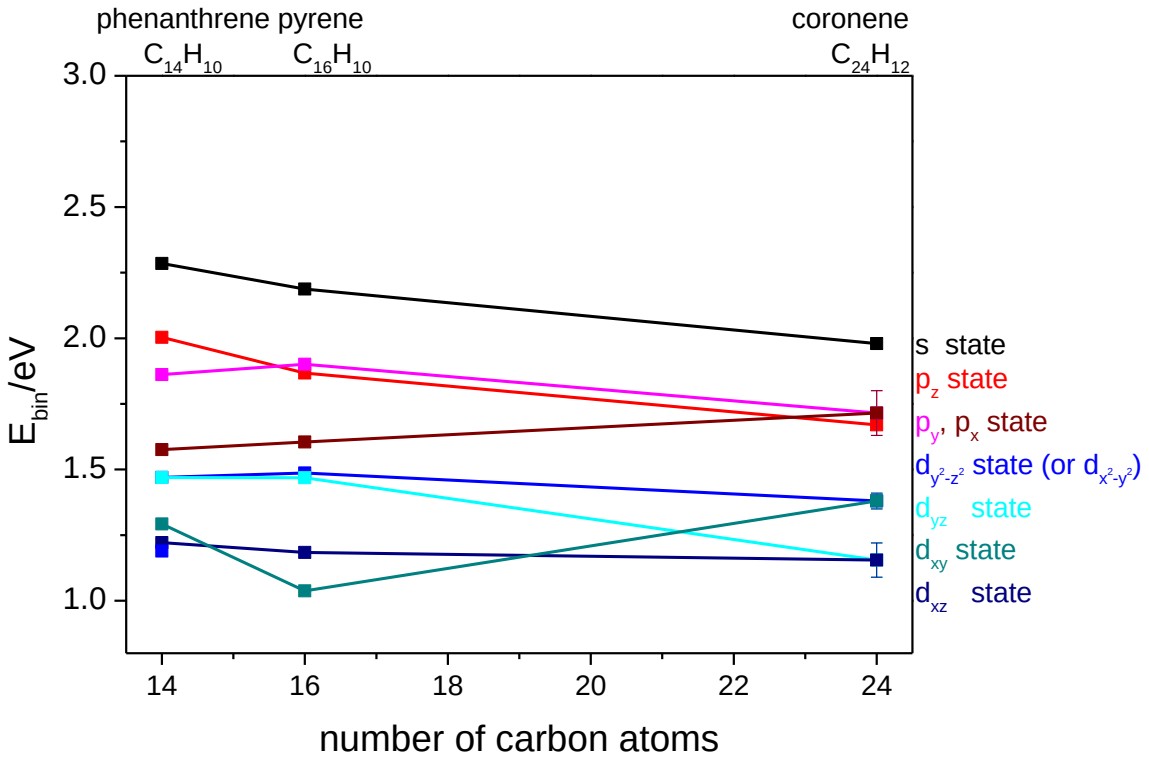

Figure 5.4: E_{bin} comparison of the first s, p and d SAMO-like states for the 2nd series of PAHs plotted against the number of carbon atoms in the corresponding molecule. The compound names and chemical formula are summarised on top of the graph.

Due to the increasing symmetry within the 2nd series from phenanthrene (C_{2h}) via pyrene (D_{2h}) up to coronene (D_{6h}), the p and d states become more degenerate which makes the comparison from molecule to molecule more difficult (Figure 5.4). The s and p_z orbitals are decreasing in their binding energies for larger molecules while the energies of the other states are either fluctuating (p_y, d_{xy}) or increasing (p_x). The fluctuations can be caused by the different symmetry groups of the molecules where the assignment of the various p and d orbitals changes (e.g. d_{yz} orbital of pyrene becomes d_{xy} orbital of coronene with respect to the molecular plane).

The 3rd series of PAHs has mainly degenerate p and d orbitals due to the high symmetry of the molecules. The E_{bin} of the various states are compared in Figure 5.5 for the 3rd series.

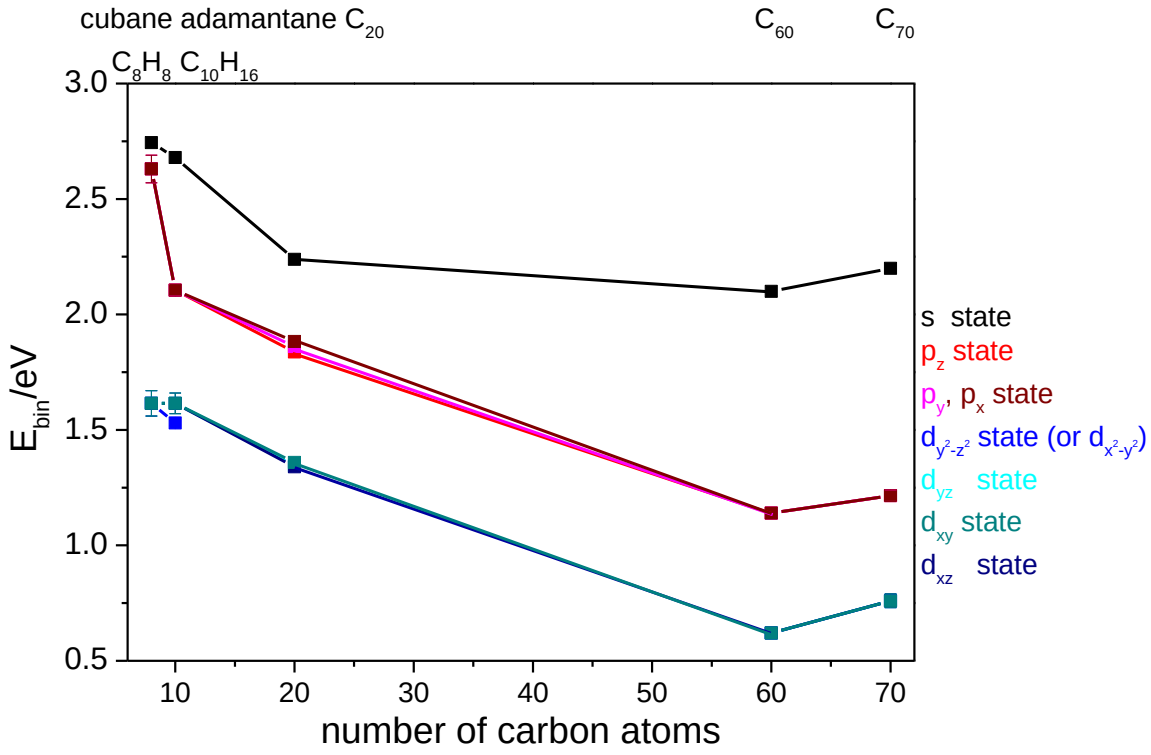

Figure 5.5: E_{bin} comparison of the first s, p and d SAMO-like states for the 3rd series of PAHs plotted against the number of carbon atoms in the corresponding molecule. The literature E_{bin} of the first SAMOs in C_{60} and C_{70} are also included in the graph but note C_{60} and C_{70} were computed at the CAM-B3LYP/6-31+G(d) and the B3LYP/6-31+G(d) level, respectively.[77] The compound names and chemical formula are summarised on top of the graph where appropriate.

Also the molecules in this series have different symmetry groups, O_h, T_d and I_h for cubane, adamantane and C_{20}, respectively. Nevertheless, for larger molecules the binding energies of the SAMO-like states are decreasing which is consistent for molecules of the same symmetry group like I_h, C_{20} and C_{60} (Figure 5.5).

Overall a common trend in the binding energies of the SAMO-like states within each PAH series is seen where E_{bin} decreases with increasing molecular size regardless of the symmetry, especially noticeable for the s and some p orbitals (Figure 5.3, Figure 5.4 and Figure 5.5). Hence the energies of the s and p_z orbitals are compared for all studied PAHs in Figure 5.6.

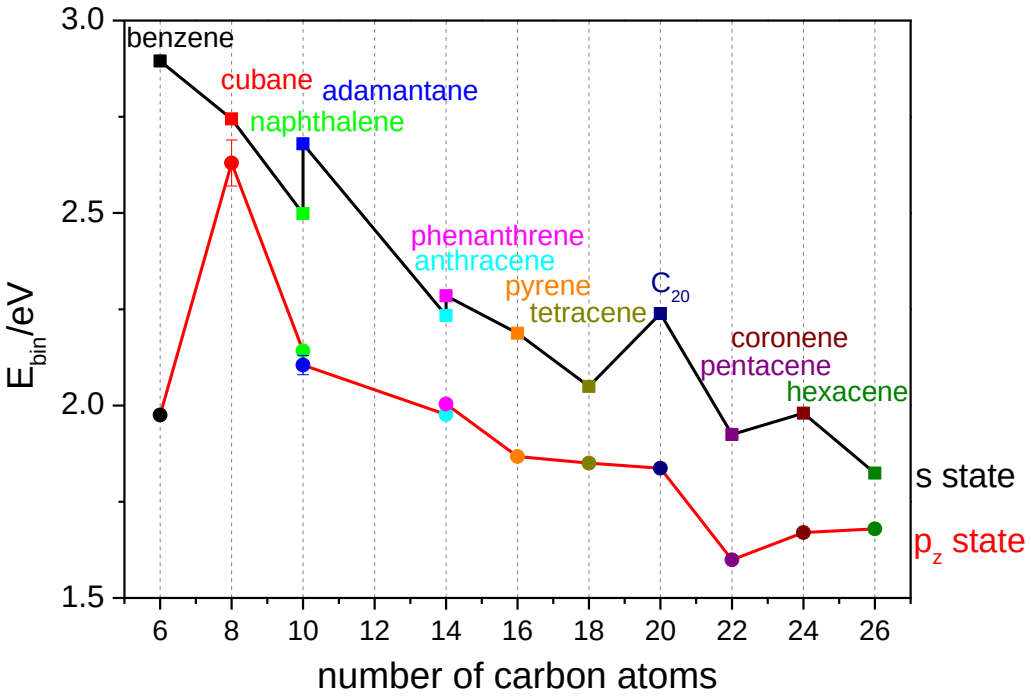

Figure 5.6: E_{bin} comparison of the first s and p_z SAMO-like states for all studied PAHs scaled according the number of carbon atoms in the corresponding molecule.

The binding energies of the s and p_z SAMO-like states clearly decrease with increasing molecular size (Figure 5.6). However, the molecules with the highest symmetry point groups, which have also a hollow core, show a higher E_{bin} for the s and p_z orbitals than compounds of similar molecular size (naphthalene $C_{10}H_8$ compared to adamantane $C_{10}H_{16}$, or C_{20} (dodecahedral) compared to tetracene $C_{18}H_{12}$ or pentacene $C_{22}H_{14}$).

The calculated results on naphthalene could be verified by experimental values from the literature as mentioned in the beginning of this chapter. For pentacene, hexacene and pyrene no relevant experimental studies could be found in the literature. Cubane is thermodynamically unstable and highly strained, so the studies in the literature cover only theoretical calculations or experiments on its derivatives.[147] PES spectra of anthracene from the literature show two peaks at a binding energy of 1.15 eV and 1.38 eV.[48,79] These peaks may correspond to a d state with a calculated E_{bin} = 1.25 – 1.55 eV. The photoionisation of tetracene has been studied in the literature with intense laser pulses.[148] The PES of tetracene have been obtained at high laser intensities (780 nm, 80 fs, 100 TW/cm^2) and show a smooth, exponentially decreasing signal with some structure below a photoelectron kinetic energy of about 10 eV.[148] Unfortunately, the spectra are not well resolved for lower electron kinetic energies, so no peaks can be identified.[148] Experimental PES studies on the C_{20} anion in the literature show a peak structure for binding energies above 2.2 eV.[149,150] A peak around E_{bin} = 2.25 eV[149,150] has a similar binding energy as the calculated E_{bin} of the s state at 2.24 eV. However, the binding energies of the SAMO-like state can be different for the anion due to the additional electron and negative charge, which may explain the absence of peaks with comparable E_{bin} for the p and d states, 1.84 – 1.88 eV and 1.34

– 1.36 eV respectively. Absorption spectroscopy results from the literature of phenanthrene isolated in a neon matrix identified excited electronic states (E_{bin} (S_8) = 1.80 eV and E_{bin} (S_7) = 2.04 eV) with binding energies similar to the p_y and p_z states, 1.86 eV and 2.00 eV respectively.[151] The Rydberg states of adamantane have been extensively studied in the literature, but the experimental electron binding energies do not match the computed one for the SAMO-like states.[152–154] However, some peaks in the excitation spectrum of adamantane ($IP \approx 9.25$ eV)[152] have not been assigned yet.[155] A relatively strong peak around 6.58 eV in the spectrum may correspond to the s SAMO-like state with a binding energy of 2.68 eV.[155] However another PAH, coronene, has been investigated within this thesis work by fs PES to obtain experimental validation of the computational results. In the following part the experimental findings on coronene will be presented.

5. 3. Experimental Results on Coronene

The angle integrated PES of coronene have been recorded at a laser wavelength of 400 nm and 800 nm (Figure 5.7) with the experimental setup as described in chapter 2. 1. 1.

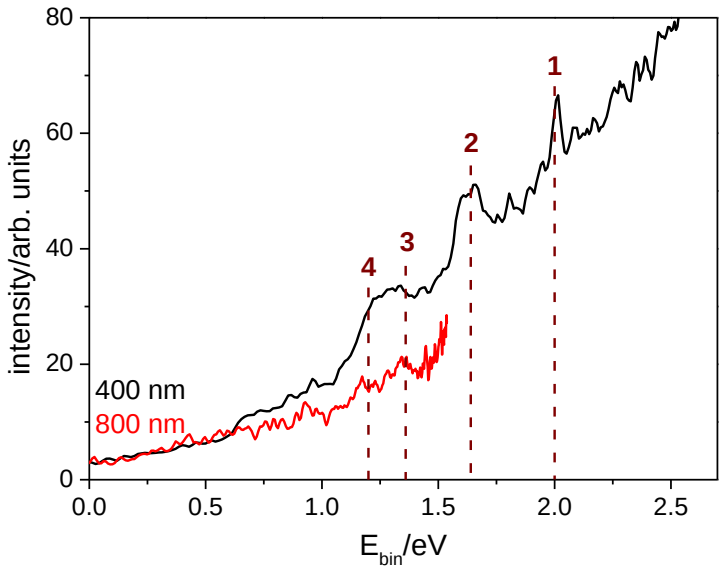

Figure 5.7: Angle integrated PES of coronene using 400 nm, (120 ± 10) fs, (0.7 ± 0.1) TW/cm² (black line) and 800 nm, (120 ± 10) fs, (4.0 ± 0.1) TW/cm² (red line) laser pulses. The dashed brown lines indicate the peak position of 1 to 4.

The spectra of coronene show a thermal electron background with peaks superimposed on it, similar to the fullerene spectra (Figure 3.31). Hence, Lorentzian functions are fitted to the four peaks in Figure 5.7 after the thermal background subtraction to identify these peaks. The obtained E_{bin} and anisotropy values of the four peaks are summarised and compared to the modelled values in Table 5.5.

Table 5.5: Summary and comparison of the experimentally obtained binding energies and anisotropy values, β, to theoretically modelled values.

	Experimental results		Theoretical results		
Peak	E_{bin}/eV	β	E_{bin}/eV	β	State
1	2.00 ± 0.05	1.00 ± 0.03	1.98	1.70	s
2	1.64 ± 0.03	0.95 ± 0.06	1.67	0.96	p_z
	1.77 ± 0.03	1.07 ± 0.63	1.63-1.80	2.00, 1.84	p_x, p_y
3	1.36 ± 0.05	0.80 ± 0.11	1.35-1.41	--	d_{y2-z2}
4	1.20 ± 0.10	0.86 ± 0.11	1.09-1.22	1.32	d

The binding energies of the peaks are in good agreement with the E_{bin} of the s, p and d states of the theoretical calculations (Table 5.5). However, the experimental β values do not match well with the modelled anisotropy values, except for the p_z state and peak 2. It has to be mentioned that the analysis of the anisotropy values has been difficult due to a broad signal underlying the peaks 1-4 even after the thermal background subtraction (Figure 5.8).

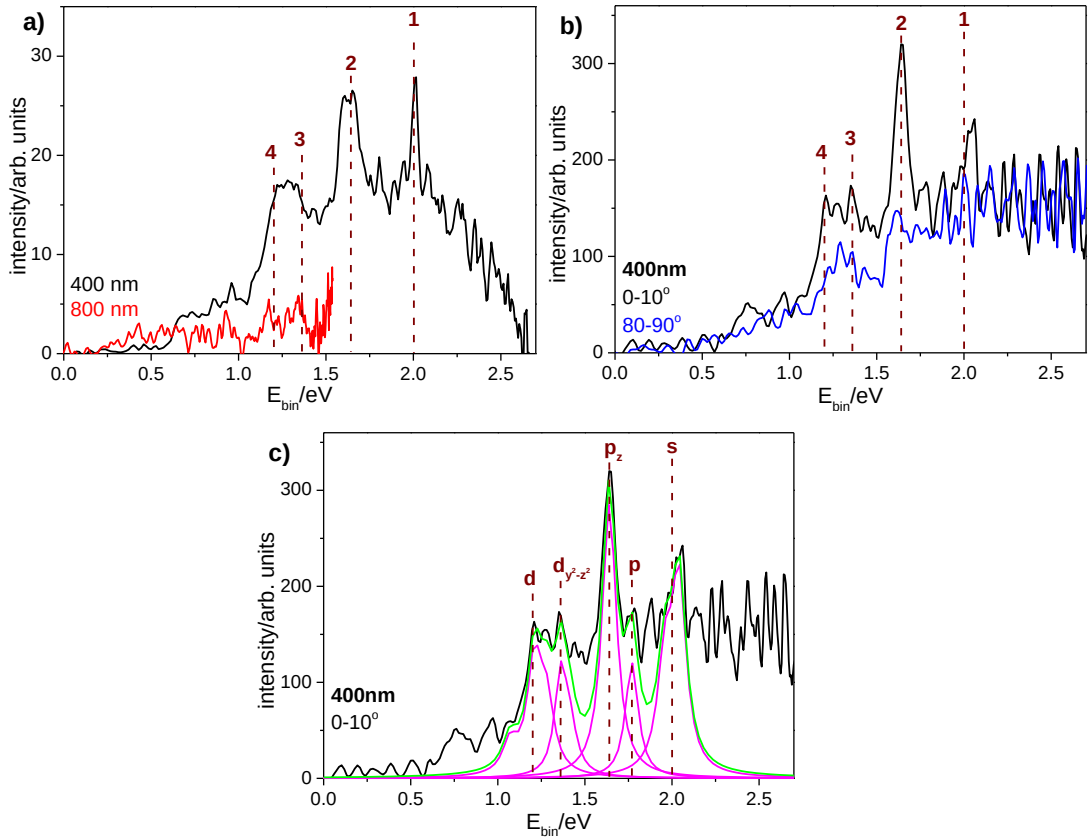

Figure 5.8: PES of coronene: a) angle integrated, thermal background subtracted spectra using 400 nm, (120 ± 10) fs, (0.7 ± 0.1) TW/cm² (black line) and 800 nm, (120 ± 10) fs, (4.0 ± 0.1) TW/cm² (red line) laser pulses; b) angular-resolved, thermal background subtracted PES parallel (0-10°, black line) and perpendicular (80-90°, blue line) to the laser polarisation direction obtained from a) 400 nm; c) 0-10° spectrum from b) including the peak fit for each state (magenta) and the sum (green). The dashed brown lines in both spectra indicate the peak position of 1 to 4 or the assigned states, respectively.

Therefore, the anisotropy of the peaks 1-4 can be distorted by this broad signal which could not be removed. This may result in a reduced β value of these peaks as the broad signal is present for all angular segments of the PES (Figure 5.8 b). Additionally, the photoionisation widths or probabilities of the SAMO-like states and non-SAMO-like states in coronene (see chapter 1. 1, Figure 1.20) are closer and almost overlapping, unlike the large difference in magnitude for C_{60} (see chapter 3. 2. 1, Figure 3.24). This makes it more likely to detect signals from valence states in the PES, too. Therefore, the broad signal might be originated from valence states as observed similarly for other molecules like 2,5-norbornadiene and phenol.[43,156,157] This described influence of the valence states on the anisotropy values of the peaks 1-4 in coronene has to be considered for the following discussion.

In this context it is worthwhile to take a look at the theoretically calculated β values of the SAMO-like states for coronene (Figure 5.9).

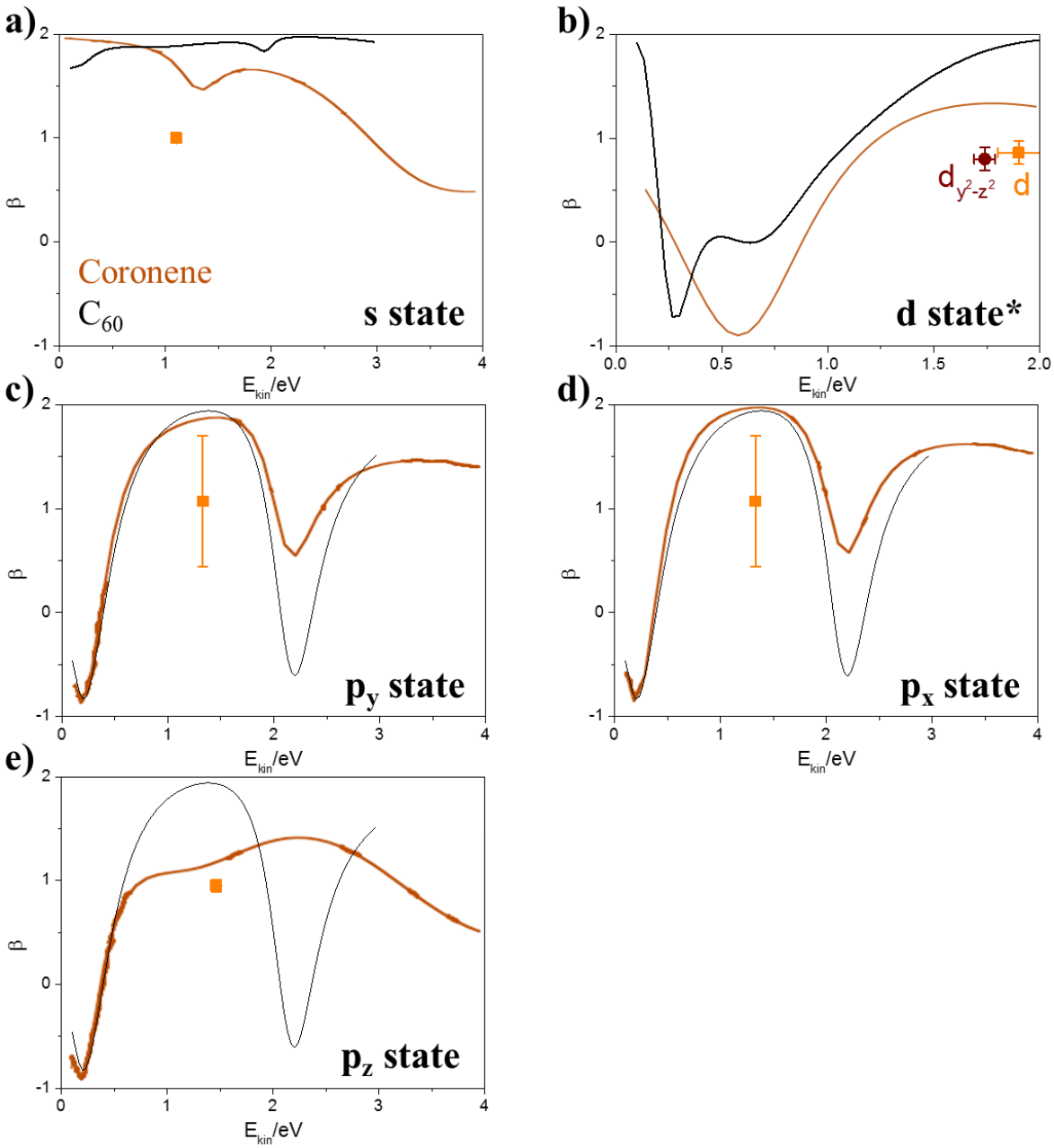

Figure 5.9: Modelled anisotropy values of coronene (orange line) and C_{60} (black line) plotted against the photoelectron kinetic energy for the a) s, c-e) p and b) d states, including the experimental results from Table 5.5. The computed values were obtained by Benoît Mignolet at the TD-DFT/CAM-B3LYP/6-31(2+)+G(d,p) level for coronene and at the TD-DFT/CAM-B3LYP/6-31+G(d) level for C_{60}.[77] The asterisk at the d state points out that the β values for coronene of the d state are taken from previous calculations of Benoît Mignolet at the TD-DFT/CAM-B3LYP/6-31(2+)+G(d) level (chapter 1. 1).

Comparing the anisotropy values of coronene s, p and d states to C_{60}, it is noticeable that the β values are similar, except for the p_z state, and have just a slight derivation from the C_{60} β values (Figure 5.9). In the case of the s state the β values of coronene diverge from 2 for higher kinetic energies which indicates that the s state of coronene has a larger amount of non s type MO character than for C_{60} (see chapter 1. 4 and 3. 3). For the two p_y and p_x states, the anisotropy values of coronene follow the same

trend as the ones for the p SAMO of C_{60}, as well as for the d state (Figure 5.9 b-d). However, the β values of the p_z state of coronene vary significantly from C_{60} (Figure 5.9 e). This is probably caused by the planar symmetry of the coronene which is lower and lifts the degeneracy of the p states compared to C_{60}. Hence the states with an electron density located over the molecular plane (p_z) are stabilised compared to MO with density within the molecular plane (p_y, p_x). These findings are also supported by the shapes of the corresponding Dyson orbitals which are displayed in Figure 5.10.

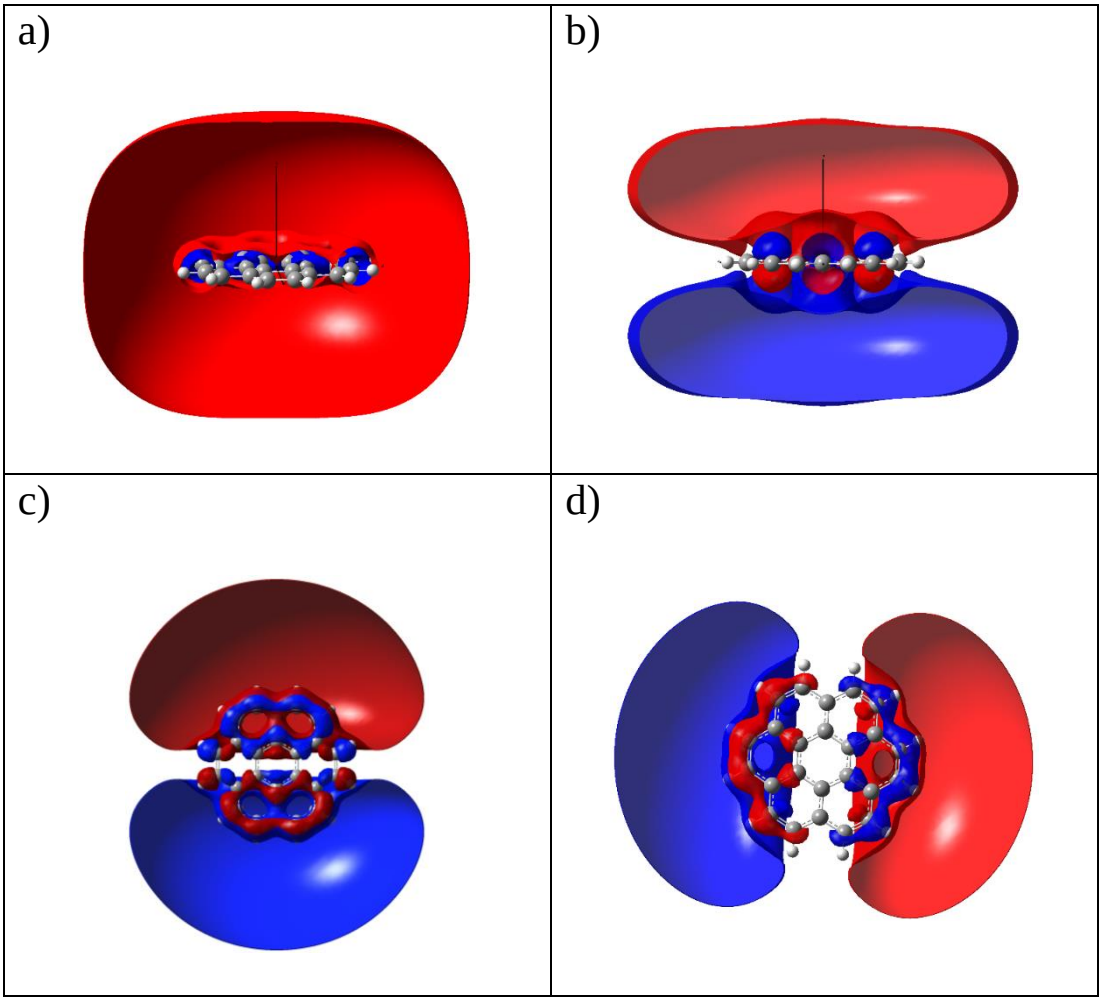

Figure 5.10: Dyson orbitals of a) s, b) p_z, c) p_y and d) p_x state of coronene computed by Benoît Mignolet at the TD-DFT/CAM-B3LYP/6-31(2+)+G(d,p) level (isocontour value of 0.002 $|e|/a^3$) . The pictures a) and b) include the molecular axes.

The Dyson orbital of the s state for coronene is not completely spherical but slightly elongated along the molecular plane (Figure 5.10 a). Hence, the modelled anisotropy value of the s state for coronene may diverge even more from the experimentally obtained values because the theoretical calculation of the PAD for large molecules with low symmetry is difficult (see chapter 1. 5).[75] This has been shown in previous chapters (1. 5 and 3. 1) where the modelled β values are following the trend of the experimental results but the values do not match exactly.

Nevertheless, based on the E_{bin}, the peaks 1-4 (Figure 5.7) can be assigned to the states with corresponding binding energies, as shown in Table 5.5. Additionally, the perfect agreement between the experimental and theoretical β value of the p_z state supports the assignment of peak 2 to the p state. Further measurements on coronene at different wavelengths are needed to recognise a trend in the anisotropy values which can be compared to the calculations, especially for the s and d states.

Furthermore, the thermal electron temperatures perpendicular to the laser polarisation of the coronene PES have been analysed and compared to the apparent temperatures of fullerenes (Figure 5.11).

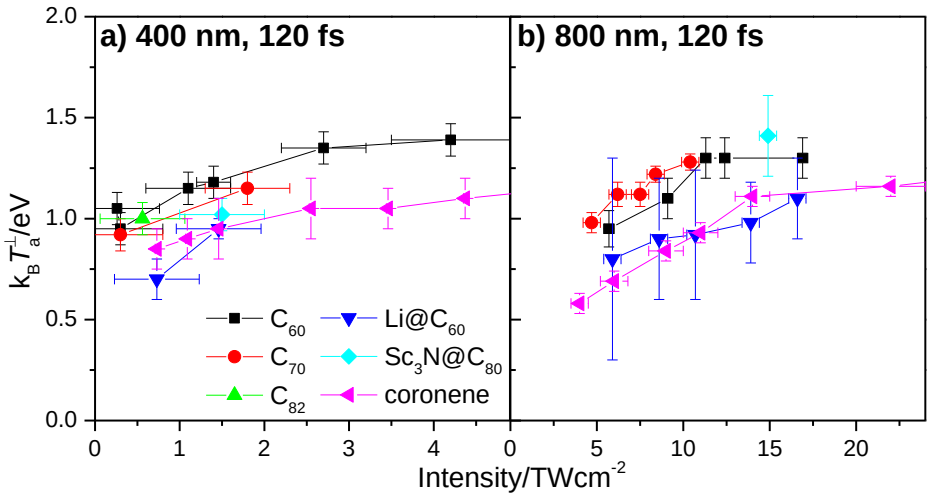

Figure 5.11: Comparison of the apparent temperatures perpendicular to the laser polarisation for coronene with C_{60}[35,64,74,77], C_{70}[74,77], C_{82}[77], Li@C_{60} and $Sc_3N@C_{80}$[77] using laser wavelengths of a) 400 nm, 120 fs and b) 800 nm, 120 fs.

For the laser wavelength of 400 nm and 800 nm the thermal electron temperature perpendicular to the laser polarisation direction is clearly lower for coronene compared to C_{60}, but similar to the endohedral fullerene, Li@C_{60} (Figure 5.11). The ionisation potential of coronene is about (7.21 ± 0.02) eV[158] which is lower than the C_{60} ($IP(C_{60})$ = 7.6 eV)[23]. Hence, the apparent thermal electron temperature is expected to be lower for coronene than C_{60}, as already seen for the apparent temperatures of Li@C_{60} (IP(Li@C_{60}) ≈ 6.4 eV)[119,125] and C_{60} (see chapter 1). For the investigation of the reasons behind the thermal electron temperatures of coronene being similar to Li@C_{60}, the parallel and perpendicular apparent temperatures to the laser polarisation direction of coronene and Li@C_{60} are compared to each other, as well as the corresponding modelled temperatures (Figure 5.12). The calculated temperatures of Li@C_{60} are the same as in Figure 4.6 while for coronene the following parameter were used and computed by Eleanor Campbell: $IP(C_{24}H_{12})$ ≈ 7.29 eV[159], 108 valence electrons, assuming the same time constant for coupling to vibrational degrees of freedom as for C_{60} with 240 fs[27], with a photon absorption cross-section of 0.15 Å^2 [63].

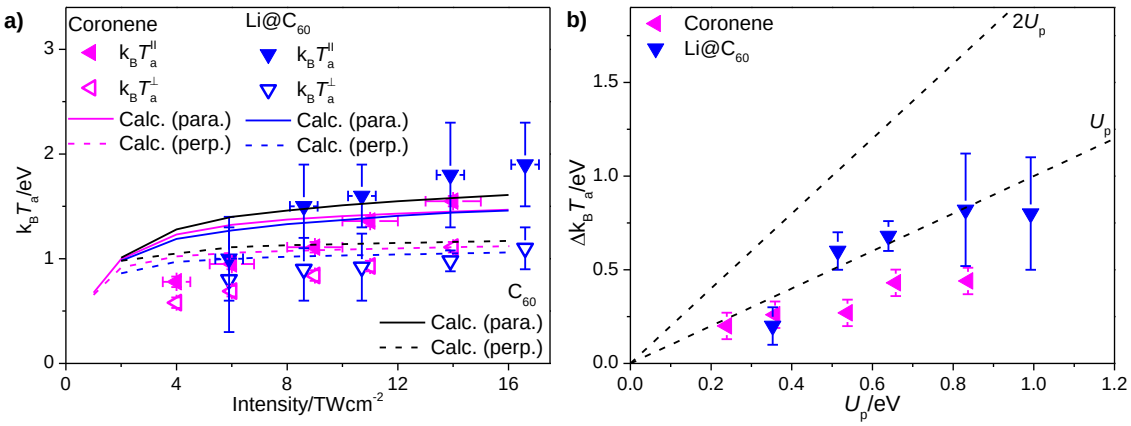

Figure 5.12: a) Plot of experimental apparent temperatures (points) obtained for coronene (pink points) and Li@C$_{60}$ (blue points) using 800 nm, (120 ± 10) fs against the laser intensity and compared to results from the transient thermal electron emission model[4,27,64] (lines) calculated by Eleanor Campbell (see chapter 1. 5). b) Difference between the parallel and perpendicular electron temperatures, obtained from plot a), plotted against the ponderomotive shift (equation (1.1)). The dashed lines in b) indicate the maximal gain in kinetic energy of the electrons from the vector field, $2U_p$, and a gain of U_p (see chapter 1. 5).

It has to be noted that the modelled temperatures of coronene are preliminary results as certain input parameters have been kept the same as for C$_{60}$. These parameters, like the time constant for coupling to vibrational degrees of freedom and the photon absorption cross-section, are unknown for coronene at the moment and can only be assumed. However, even the theoretically approximated apparent temperatures of coronene (pink lines) are quite close the modelled Li@C$_{60}$ temperatures (blue lines) and lower than the computed temperatures of C$_{60}$ (black lines) (Figure 5.12 a). This outcome is in agreement with the experimentally obtained apparent temperatures (Figure 5.11). According to the thermal model results, the apparent temperatures of coronene are supposed to be slightly higher than for Li@C$_{60}$, but these differences are too small to be detected as the experimental error is larger (Figure 5.12 a). Additionally, the coronene results of the thermal model are preliminary as mentioned before, because some input parameters are yet unknown for coronene. However, the experimental temperatures of coronene seem to be lower than for Li@C$_{60}$, and the temperature values are almost always within the error range of both molecules (Figure 5.12 a). The similarity in the apparent temperatures of coronene and Li@C$_{60}$ may be due to a combination of the lower density of states or lower number of electron for coronene and a higher IP than for Li@C$_{60}$. Nevertheless, the exact reasons need further studies, like on the time constant for coupling to vibrational degrees of freedom of coronene and Li@C$_{60}$.

The comparison of the differences between the parallel and perpendicular electron temperatures clearly shows a lower degree of asymmetry in the coronene thermal electron emission than for Li@C$_{60}$ or other studied fullerenes (Figure 5.12 b) and Figure 4.9). This observation needs further investigation as it seems that the asymmetry of the thermal electron emission is dependent on the molecular size or on the density of states.

6. Conclusions and Outlook

This thesis confirmed the presence of SAMOs in other fullerenes than C_{60} and C_{70}, as well as in endohedral fullerenes and polycyclic aromatic hydrocarbons. In this work investigated the ionisation and excitation mechanisms of fullerenes and PAHs in the gas phase using fs laser pulses. Previous work has identified the ionisation mechanisms on the fs timescale to be due to single photon ionisation of SAMO states and transient thermal electron emission. The same ionisation mechanisms has been found in C_{82}, the endohedral fullerenes, $Sc_3N@C_{80}$ and $Li@C_{60}$, and coronene within the present work using PES. The observed peak structure superimposed on a thermal background in the spectra has been attributed to one-photon ionisation of diffuse, excited electronic states. Based on the analysis of the PADs of the peaks and the similarity to the C_{60} and C_{70} spectra, these peaks have been assigned to s, p and d SAMO states, which was also supported by theoretical studies.

The structure of a fullerene, regarding molecular size and symmetry, has been found to have an effect on the SAMOs. The SAMO peaks are broader for higher fullerenes due to a splitting of the degenerate p and d states because of the decreased symmetry compared to I_h for C_{60}. Unfortunately, this splitting cannot be resolved in the current experimental PES setup as the bandwidth of the laser pulses is too broad for the close spacing of the non-degenerate states. In future experiments the laser pulses can be chirped or filtered to gain the desired resolution whilst maintaining the laser power and short pulse durations. The encapsulation of an atom or molecule increases the binding energy of the s SAMO for the studied fullerenes, $Li@C_{60}$ and $Sc_3N@C_{80}$, but does not affect the E_{bin} of the p and d SAMOs. Nevertheless, the PADs of the s state are not affected by the encapsulation of an atom or molecule inside the fullerene cage or changes of the cage size. However, the anisotropy values of the p SAMOs can be varied through insertion of an atom or molecule or variation of the cage size. On the contrary, alteration of the fullerene size influences the PAD of the d SAMO state, while the encapsulation of an atom or molecule does not have an effect. A deeper understanding of the link between the interaction of the encapsulated molecule and the SAMO states of the fullerenes requires further investigation of other endohedral fullerenes. This knowledge might enable the development of SAMO-based applications, especially $Li@C_{60}$, within molecular electronics like organic solar cells as acceptor molecules for example.[160–162]

Furthermore, the photoionisation probability ratios of the s/p and s/d SAMOs for C_{60} were characterised experimentally which were reproduced by TD-DFT calculations exceptionally well. This positive outcome supports the predictive potential of quantum chemistry techniques for such large and complex molecules, like fullerenes. Additionally, the assumption of an equal population of all SAMOs through fast energy redistribution after multiphoton excitation is endorsed. For a detailed comprehension of the population mechanisms involved in highly excited states like Rydberg states or SAMOs, time-resolved measurements would provide more information. Preparatory work was completed to accomplish this

and such measurements will be conducted in a follow up study. Since theoretical calculations on the electron dynamics of large molecules are currently impossible to conduct on such large molecules as fullerenes due to the enormous computational cost, initial TD-DFT studies were carried out on PAHs with a view to developing more detailed dynamical studies.

Theoretical studies within the present work predicted similar excited states to SAMOs in all studied PAHs. These TD-DFT computations were verified by experimental results obtained from coronene as part of this thesis and literature values of naphthalene. The binding energies of these SAMO-like states are decreasing with increasing molecular size, in particular for the s state. Molecules with a spherical shape have an increased stability of their SAMO-like states compared to PAHs of comparable molecular size which is expected due to the hollow core potential and the increased symmetry. Experimentally the SAMO-like states were identified in the coronene spectra, and a broad, underlying signal in the PES from valence states was detected. Further measurements, like absorption spectroscopy, are necessary to identify the origin of this broad signal. Also, findings from these coronene measurements should give a recognisable trend in the anisotropy values of the SAMO-like states, comparable to the calculations from this thesis. Hereafter, theoretical calculations on electron dynamics can be conducted for PAHs to complement future time-resolved experimental studies to get an insight into the excitation mechanisms of SAMO-like states.

Another ionisation mechanism of fullerenes, the thermal electron emission was analysed and verified. The transient thermal electron emission model and the electric field-induced barrier suppression model were verified within the present work by reproducing previous results on C_{60} at 800 nm and complementing the experimental data using 700 nm laser pulses. The thermal model was successfully applied to Li@C_{60} to reproduce the experimental trend in the apparent temperatures. Discrepancies between the model and the experimental values for the apparent temperatures parallel to the laser polarisation direction were observed. The reasons behind these deviations need further investigations. Other effects, such as internal polarisation, recollision effects or overlapping ATI peaks, might have to be included in the model which are not considered yet.

In conclusion, the comparison of the studied fullerenes assumed that the thermal electron emission mechanism becomes more dominant in the photoionisation of larger fullerenes. Since the thermal electron temperatures mainly decreased with increasing size of the fullerene cage, while the SAMO peaks become less pronounced. Nevertheless, not all studied fullerenes showed this trend for all laser wavelengths, like C_{82}, which has to be analysed in more detail for a better understanding. Also the transient thermal electron model can be applied to coronene to comprehend why the thermal electron temperatures of coronene are the same as for Li@C_{60}. The detailed understanding of the thermalisation process would improve the design of optoelectronics and energy-harvesting devices.[163]

6. 1. Pump-Probe Experiment Outlook

Previously it has been mentioned that preparatory work was completed to study the electron dynamics in the molecules to investigate their excitation and photoionisation mechanisms. The molecules are excited by a pump laser pulse and a delayed probe laser pulse photoionises the excited molecules. The created ions or photoelectrons can be detected and their spectra can give information about the properties of the electronic structure of the molecular system. By varying the delay between pump and probe pulse the dynamics in the molecular electronic structure can be recorded.

As mentioned in chapter 1. 2, the population mechanisms for the Rydberg states and SAMOs of fullerenes might be similar to those of other molecules analysed by Rydberg Fingerprint Spectroscopy.[19–22,33,48,79] Hence the molecules might absorb one or more photons and reach one or more excited intermediate states.[33] The Rydberg states and SAMOs of the previously excited molecules could be rapidly populated through effective IC from these intermediate states. [33,77] The lifetime of these intermediate states should be less than the laser pulse duration (about 120 fs) in the one-color experiments because the excitation and ionisation of the highly excited states occurred during one laser pulse.[7,33,50,77]

The experimental pump-probe setup, as described in chapter 2. 1. 2, was built to analyse the dynamics that lead to the population of the SAMOs and Rydberg states after exciting the fullerene molecules with fs laser pulses. The pump pulse at a wavelength of 200 nm is used to excite the fullerene molecules into an intermediate state from which the Rydberg states and SAMOs are populated through effective IC. Then the pulse with a wavelength of about 530 nm probes the Rydberg states and SAMOs of these excited molecules. The pump and probe laser beams were spatially overlapped through the vacuum chamber. To find the overlap of both laser pulses in time the mass spectra of C_{60} were recorded for different positions of the translation stage in the probe pulse setup. The ion signal intensity of C_{60}^+ was recorded as a function of the time delay between the pulses. Whenever the pulses overlapped in time, the ion signal increased (Figure 6.1).

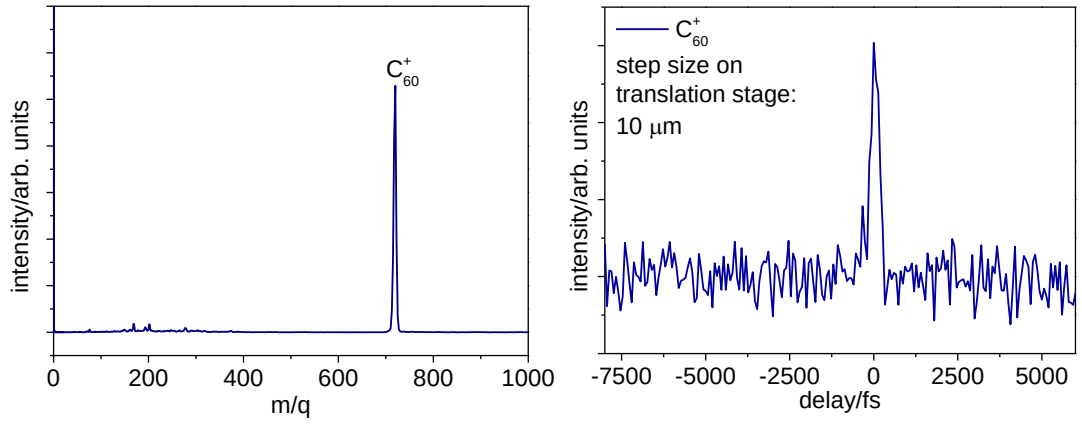

Figure 6.1: Mass spectra of C_{60} (left) and recorded C_{60}^+ ion signal intensity as a function of the delay between the pump and probe pulse (right); positive delay times represent the pump pulse arrives before the probe and negative times are vice versa.

Preliminary, the cross-correlation of the two laser pulses was roughly estimated to be about 230 fs based on a Gaussian fit to an OH^+ mass signal. A different molecule or a better technique needs to be explored to measure the cross-correlation of the laser pulses more reliably within the vacuum chamber. A simple exponential fit function was fitted to the C_{60}^+ spectrum using the obtained cross-correlation with a decay time of about 60 fs. However, the experiment has to be improved to get an accurate measurement of the cross-correlation of the laser pulses in the vacuum chamber. Unfortunately, no PES could be recorded due to a strong scattering of the 200 nm laser beam in the vacuum chamber causing an oversaturation of the VMI detector. For resolving this issue, baffles have been constructed for the viewports on the vacuum chamber to deflect any scattering of the 200 nm laser beam from the viewports. These have to be installed and tested on the experimental setup.

6. 2. General Outlook

A detailed understanding of the SAMOs and their properties will assist in the investigation of fundamental excitation and ionisation mechanisms within larger molecules comparable to fullerenes. This may help to understand electron dynamics or charge transfer processes in electronic materials which would in turn contribute to the design of new materials for specific applications. Additionally, this knowledge may play an important role in understanding the chemistry of neutral and charged fullerenes in space.

The successful prediction of ionisation properties of such a large and complex system as a fullerene by quantum chemistry using TD-DFT gives confidence in the predictive potential of this theory for probing the electron dynamics of complex molecular systems. This result supports the application of quantum chemistry for modelling electronic mechanisms in complex systems reliably. Since SAMOs have been

confirmed to be accessible in molecules smaller than fullerenes in the present work, theoretical calculations may be used to predict the electron dynamics during the excitation and ionisation of SAMOs. This technique can also be used for probing the interplay between direct and thermal ionisation and may provide important insights to help understand the electron dynamics of relevant molecules to applications such as acceptor molecules in organic solar cells. There is therefore a large scope for continued study in this field across a broad range of applications leading from fundamental understanding that has been obtained.

7. References

1. Hu, W., Tao, Y.-T. & Sirringhaus, H. Organic electronics–new physical chemistry insight. *Phys. Chem. Chem. Phys.* **14,** 14097–14098 (2012).

2. Nelson, J. Polymer: Fullerene bulk heterojunction solar cells. *Mater. Today* **14,** 462–470 (2011).

3. Kroto, H. W., Heath, J. R., O'Brien, S. C., Curl, R. F. & Smalley, R. E. C_{60}: buckminsterfullerene. *Nature* **318,** 162 (1985).

4. Campbell, E. E. B., Hansen, K., Hoffmann, K., Korn, G., Tchaplyguine, M., Wittmann, M. & Hertel, I. V. From above threshold ionization to statistical electron emission: The laser pulse-duration dependence of C_{60} photoelectron spectra. *Phys. Rev. Lett.* **84,** 2128–2131 (2000).

5. Zhao, J., Feng, M., Yang, J. & Petek, H. The superatom states of fullerenes and their hybridization into the nearly free electron bands of fullerites. *ACS Nano* **3,** 853–864 (2009).

6. Wurz, P. & Lykke, K. R. Multiphoton excitation, dissociation, and ionization of fullerene (C_{60}). *J. Phys. Chem.* **96,** 10129–10139 (1992).

7. Johansson, J. O., Henderson, G. G., Remacle, F. & Campbell, E. E. B. Angular-resolved photoelectron spectroscopy of superatom orbitals of fullerenes. *Phys. Rev. Lett.* **108,** 173401 (2012).

8. Chen, N., Beavers, C. M., Mulet-Gas, M., Rodriguez-Fortea, A., Munoz, E. J., Li, Y.-Y., Olmstead, M. M., Balch, A. L., Poblet, J. M. & Echegoyen, L. $Sc_2S@C_s(10528)$-C_{72}: A Dimetallic Sulfide Endohedral Fullerene with a Non Isolated Pentagon Rule Cage. *J. Am. Chem. Soc.* **134,** 7851–7860 (2012).

9. Campbell, E. E. B., Hansen, K., Hedén, M., Kjellberg, M. & Bulgakov, A. V. Ionisation of fullerenes and fullerene clusters using ultrashort laser pulses. *Photochem. Photobiol. Sci.* **5,** 1183–1189 (2006).

10. Poulin, J.-C., Fabre, C. & Rassat, A. STM Visualization of C_{84} Fullerene on Gold. *Microsc. Microanal. Microstruct.* **6,** 363–369 (1995).

11. Hansen, K. & Campbell, E. E. B. Radiative cooling of fullerenes. *J. Chem. Phys.* **104,** 5012–5018 (1996).

12. Kjellberg, M., Johansson, J. O., Jonsson, F., Bulgakov, A. V, Bordas, C., Campbell, E. E. B. & Hansen, K. Momentum-map-imaging photoelectron spectroscopy of fullerenes with femtosecond laser pulses. *Phys. Rev. A* **81,** (2010).

13. Shchatsinin, I., Laarmann, T., Zhavoronkov, N., Schulz, C. P. & Hertel, I. V. Ultrafast energy redistribution in C_{60} fullerenes: a real time study by two-color femtosecond spectroscopy. *J. Chem. Phys.* **129,** 204308-1–12 (2008).

14. Boyle, M., Laarmann, T., Hoffmann, K., Hedén, M., Campbell, E. E. B., Schulz, C. P. & Hertel, I. V. Excitation dynamics of rydberg states in C_{60}. *Eur. Phys. J. D* **36,** 339–351 (2005).

15. Shchatsinin, I., Laarmann, T., Stibenz, G., Steinmeyer, G., Stalmashonak, A., Zhavoronkov, N., Schulz, C. P. & Hertel, I. V. C_{60} in intense short pulse laser fields down to 9 fs: excitation on time scales below e-e and e-phonon coupling. *J. Chem. Phys.* **125,** 194320 (2006).

16. Pauly, H. *Atom, Molecule, and Cluster Beams I*. (Springer-Verlag Berlin Heidelberg, 2000).

17. Ehrler, O. T., Yang, J. P., Hättig, C., Unterreiner, A. N., Hippler, H. & Kappes, M. M. Femtosecond pump/probe photoelectron spectroscopy of isolated C_{60} negative ions. *J. Chem. Phys.* **125,** 74312 (2006).

18. Tomita, S., Andersen, J. U., Bonderup, E., Hvelplund, P., Liu, B., Nielsen, S. B., Pedersen, U. V., Rangama, J., Hansen, K. & Echt, O. Dynamic Jahn-Teller effects in isolated C_{60}^- studied by

near-infrared spectroscopy in a storage ring. *Phys. Rev. Lett.* **94,** 53002 (2005).

19. Minitti, M. P., Cardoza, J. D. & Weber, P. M. Rydberg fingerprint spectroscopy of hot molecules: structural dispersion in flexible hydrocarbons. *J. Phys. Chem. A* **110,** 10212–10218 (2006).

20. Gosselin, J. L. & Weber, P. M. Rydberg fingerprint spectroscopy: a new spectroscopic tool with local and global structural sensitivity. *J. Phys. Chem. A* **109,** 4899–4904 (2005).

21. Kuthirummal, N. & Weber, P. M. Structure sensitive photoionization via Rydberg levels. *J. Mol. Struct.* **787,** 163–166 (2006).

22. Kuthirummal, N. & Weber, P. M. Rydberg states: sensitive probes of molecular structure. *Chem. Phys. Lett.* **378,** 647–653 (2003).

23. Campbell, E. E. B. & Levine, R. D. Delayed Ionization and Fragmentation En Route to Thermionic Emission: Statistics and Dynamics. *Annu. Rev. Phys. Chem.* **51,** 65–98 (2000).

24. Hohmann, H., Callegari, C., Furrer, S., Grosenick, D., Campbell, E. E. B. & Hertel, I. V. Photoionization and Fragmentation Dynamics of C_{60}. *Phys. Rev. Lett.* **73,** 1919–1922 (1994).

25. Campbell, E. E. B., Raz, T. & Levine, R. D. Intemal energy dependence of the fragmentation patterns of C_{60} and C_{60}^{+}. *Chem. Phys. Lett.* **253,** 261–267 (1996).

26. Tchaplyguine, M., Hoffmann, K., Dühr, O., Hohmann, H., Korn, G., Rottke, H., Wittmann, M., Hertel, I. V. & Campbell, E. E. B. Ionization and fragmentation of C_{60} with sub-50 fs laser pulses. *J. Chem. Phys.* **112,** 2781–2790 (2000).

27. Hansen, K., Hoffmann, K. & Campbell, E. E. B. Thermal electron emission from the hot electronic subsystem of vibrationally cold C_{60}. *J. Chem. Phys.* **119,** 2513–2522 (2003).

28. Campbell, E. E. B., Ulmer, G. & Hertel, I. V. Delayed Ionization of C_{60} and C_{70}. *Phys. Rev. Lett.* **67,** 1986–1988 (1991).

29. Hertel, I. V., Laarmann, T. & Schulz, C. P. in *Adv. At. Mol. Opt. Physics, Vol 50* (eds. Bederson, B. & Walther, H.) **50,** 219–286 (Elsevier Academic Press Inc, 2005).

30. Boyle, M., Hoffmann, K., Schulz, C. P., Hertel, I. V., Levine, R. D. & Campbell, E. E. B. Excitation of Rydberg Series in C_{60}. *Phys. Rev. Lett.* **87,** 273401 (2001).

31. Feng, M., Petek, H. & Zhao, J. Atomlike, Hollow-Core-Bound Molecular Orbitals of C_{60}. *Science (80-.).* **320,** 359–362 (2008).

32. Pavlyukh, Y. & Berakdar, J. Angular electronic 'band structure' of molecules. *Chem. Phys. Lett.* **468,** 313–318 (2009).

33. Johansson, J. O. & Campbell, E. E. B. Probing excited electronic states and ionisation mechanisms of fullerenes. *Chem. Soc. Rev.* **42,** 5661–5671 (2013).

34. Mignolet, B. *Personal Communitcation*. (2013).

35. Bohl, E., Sokół, K. P., Mignolet, B., Thompson, J. O. F., Johansson, J. O., Remacle, F. & Campbell, E. E. B. Relative Photoionization Cross Sections of Super-Atom Molecular Orbitals (SAMOs) in C_{60}. *J. Phys. Chem. A* **119,** 11504–11508 (2015).

36. Bucksbaum, P. H., Freeman, R. R., Bashkansky, M. & Mcilratht, T. J. Role of the ponderomotive potential in above-threshold ionization. *J. Opt. Soc. Am. B* **4,** 760–764 (1987).

37. Posthumus, J. H. The dynamics of small molecules in intense laser fields. *Reports Prog. Phys.* **67,** 623–665 (2004).

38. Keldysh, L. V. Ionization in the field of a strong electromagnetic wave. *Sov. Phys. JETP* **20,** 1307–1314 (1965).

39. Campbell, E. E. B., Hoffmann, K., Rottke, H. & Hertel, I. V. Sequential ionization of C_{60} with femtosecond laser pulses. *J. Chem. Phys.* **1716,** 1716–1719 (2001).

40. Bauer, D., Ceccherini, F., Macchi, A. & Cornolti, F. C_{60} in intense femtosecond laser pulses: Nonlinear dipole response and ionization. *Phys. Rev. A* **64,** 63203 (2001).

41. Ondrey, G. S., Rose, C., Proch, D. & Kompa, K. L. Resonant multiphoton ionization dynamics of N_2 via the a $^1\Pi_g$(v=10–14) states: Preparation of state-selected N^+_2 X $^2\Sigma$+g(v^+=0–4) ions. *J. Chem. Phys.* **95,** 7823–7827 (1991).

42. Johansson, J. O., Bohl, E. & Campbell, E. E. B. Super-Atom Molecular Orbital Excited States of Fullerenes. *Philos. Trans. R. Soc. A* **374,** 1–13 (2016).

43. Schick, C. P. & Weber, P. M. Ultrafast Dynamics in Superexcited States of Phenol. *J. Phys. Chem. A* **105,** 3725–3734 (2001).

44. Rudolf, M. & Zhang, Z. Standoff detection of large organic molecules using Rydberg fingerprint spectroscopy and microwave Rayleigh scattering. *Opt. Lett.* **37,** 145–7 (2012).

45. Gosselin, J. L., Minitti, M. P., Rudolf, M., Sølling, T. I. & Weber, P. M. Energy flow and fragmentation dynamics of n,n-dimethylisopropylamine. *J. Phys. Chem. A* **110,** 4251–5 (2006).

46. Thiré, N., Cireasa, R., Blanchet, V. & Pratt, S. T. Time-resolved photoelectron spectroscopy of the CH(3)I B(1)E 6s [2] state. *Phys. Chem. Chem. Phys.* **12,** 15644–52 (2010).

47. Cardoza, J. D., Rudolf, M., Hansen, N. & Weber, P. M. Identification of isomeric hydrocarbons by Rydberg photoelectron spectroscopy. *J. Electron Spectros. Relat. Phenomena* **165,** 5–10 (2008).

48. Goto, M. & Hansen, K. Ionization of naphthalene via the Rydberg states using a femtosecond 775nm pulse. *Chem. Phys. Lett.* **522,** 23–27 (2012).

49. Cardoza, J. D., Rudolf, M. & Weber, P. M. Electronic spectroscopy and ultrafast energy relaxation pathways in the lowest Rydberg States of trimethylamine. *J. Phys. Chem. A* **112,** 10736–43 (2008).

50. Johansson, J. O., Henderson, G. G. & Campbell, E. E. B. Visible and ultraviolet photoelectron spectroscopy of fullerenes using femtosecond laser pulses. *EPJ Web Conf.* **41,** 2015 (2013).

51. Kruit, P. & Read, F. H. Magnetic field paralleliser for 2π electron-spectrometer and electron-image magnifier. *J. Phys. E.* **16,** 313–324 (1983).

52. Eppink, A. T. J. B. & Parker, D. H. Velocity map imaging of ions and electrons using electrostatic lenses: Application in photoelectron and photofragment ion imaging of molecular oxygen. *Rev. Sci. Instrum.* **68,** 3477–3484 (1997).

53. Johansson, J. O. Angle-resolved femtosecond photoelectron spectroscopy of fullerenes. (2010).

54. Whitaker, B. ed. Imaging in Molecular Dynamics: Technology and Applications. *Cambridge Univ. Press* (2003).

55. Yang, C.-H. On the Angular Distribution in Nuclear Reactions and Coincidence Measurements. *Phys. Rev.* **74,** 764–772 (1948).

56. Reid, K. L. Photoelectron angular distributions. *Annu. Rev. Phys. Chem.* **54,** 397–424 (2003).

57. Cooper, J. & Zare, R. N. Angular Distribution of Photoelectrons. *J. Chem. Phys.* **48,** 942–943 (1968).

58. Cooper, J. & Zare, R. N. Erratum: Angular Distribution of Photoelectrons. *J. Chem. Phys.* **49,** 4252 (1968).

59. Mabbs, R., Grumbling, E. R., Pichugin, K. & Sanov, A. Photoelectron imaging: an experimental window into electronic structure. *Chem. Soc. Rev.* **38,** 2169–2177 (2009).

60. Mehlig, K., Hansen, K., Hedén, M., Lassesson, A., Bulgakov, A. V & Campbell, E. E. B. Energy distributions in multiple photon absorption experiments. *J. Chem. Phys.* **120,** 4281–4288 (2004).

61. Ding, D., Compton, R. N., Haufler, R. E. & Klots, C. E. Multiphoton Ionization of C_{60}. *J. Phys. Chem.* **97,** 2500–2504 (1993).

62. Zhang, Y. & Stuke, M. Direct observation of transition from delayed ionization to direct ionization for free C_{60} and C_{70}: Thermionic emission? *Phys. Rev. Lett.* **70,** 3231–3234 (1993).

63. Johansson, J. O., Henderson, G. G. & Campbell, E. E. B. Dynamics of Thermal Electron Emission from Highly Excited C_{60}. *J. Phys. Chem. A* **118,** 8067–8073 (2014).

64. Johansson, J. O., Fedor, J., Goto, M., Kjellberg, M., Stenfalk, J., Henderson, G. G., Campbell, E. E. B. & Hansen, K. Anisotropic hot electron emission from fullerenes. *J. Chem. Phys.* **136,** (2012).

65. Kjellberg, M., Bulgakov, A. V, Goto, M., Johansson, J. O. & Hansen, K. Femtosecond electron spectroscopy of coronene, benzo[GHI]perylene, and anthracene. *J. Chem. Phys.* **133,** 74308 (2010).

66. Hansen, K. *Statistical Physics of Nanoparticles in the Gas Phase*. (Springer Netherlands, 2013). doi:10.1007/978-94-007-5839-1

67. Hansen, K., Campbell, E. E. B. & Echt, O. The frequency factor in statistical fullerene decay. *Int. J. Mass Spectrom.* **252,** 79–95 (2006).

68. Weidele, H., Kreisle, D., Recknagel, E., Schulze Icking-Konert, G., Handschuh, H., Gantefoer, G. & Eberhardt, W. Thermionic emission from small clusters : direct observation of the kinetic energy distribution of the electrons. *Chem. Phys. Lett.* **237,** 425–431 (1995).

69. Anisimov, S. I., Kapeliovich, B. L. & Perel'man, T. L. Electron emission from metal surfaces exposed to ultrashort laser pulses. *Sov. Phys. JETP* **39,** 375–377 (1974).

70. Bordas, C., Baguenard, B., Climen, B., Lebeault, M. A., Lépine, F. & Pagliarulo, F. Time-dependent spectrum of thermionic emission from hot C_{60}. *Eur. Phys. J. D* **34,** 151–155 (2005).

71. Lépine, F., Climen, B., Lebeault, M. a. & Bordas, C. Time-dependent delayed electron spectra: a direct measurement of total decay rate as a function of internal energy. *Eur. Phys. J. D* **55,** 627–35 (2009).

72. Hunsche, S., Starczewski, T., l'Huillier, a., Persson, a., Wahlström, C.-G., van Linden van den Heuvell, H. & Svanberg, S. Ionization and Fragmentation of C_{60} via Multiphoton-Multiplasmon Excitation. *Phys. Rev. Lett.* **77,** 1966–1969 (1996).

73. Huismans, Y., Cormier, E., Cauchy, C., Hervieux, P. -a., Gademann, G., Gijsbertsen, A., Ghafur, O., Johnsson, P., Logman, P., Barillot, T., Bordas, C., Lépine, F. & Vrakking, M. J. J. Macro-atom versus many-electron effects in ultrafast ionization of C_{60}. *Phys. Rev. A* **88,** 13201 (2013).

74. Henderson, G. G. *Femtosecond Laser Studies of Fullerenes and Nanotubes*. (2012).

75. Mignolet, B., Johansson, J. O., Campbell, E. E. B. & Remacle, F. Probing Rapidly Ionizing Super-Atom Molecular Orbitals in Fullerenes : A Computational and fs Photoelectron Spectroscopy Study. *ChemPhysChem* **14,** 3332–3340 (2013).

76. Mignolet, B. Control of attosecond electronic dynamics in molecules. (2014).

77. Johansson, J. O., Bohl, E., Henderson, G. G., Mignolet, B., Dennis, T. J. S., Remacle, F. & Campbell, E. E. B. Hot electron production and diffuse excited states in C_{70}, C_{82} and $Sc_3N@C_{80}$ characterised by angular-resolved photoelectron spectroscopy. *J. Chem. Phys.* **139,** 84309 (2013).

78. Boyle, M., Hedén, M., Schulz, C. P., Campbell, E. E. B. & Hertel, I. V. Two-color pump-probe study and internal-energy dependence of Rydberg-state excitation in C_{60}. *Phys. Rev. A - At. Mol. Opt. Phys.* **70,** 13–16 (2004).

79. Goto, M. & Hansen, K. Competitive ionization processes of anthracene excited with a femtosecond pulse in the multi-photon ionization regime. *J. Chem. Phys.* **135,** 214310-1–6

(2011).

80. Rulliere, C. *Femtosecond Laser Pulses: Principles and Experiments*. (2005).

81. Coherent. *Mantis Manual*.

82. Vasa, N. J., Tanaka, M., Okada, T., Maeda, M. & Uchino, O. Comparative study of spectral narrowing of a pulsed Ti:Sapphire laser using pulsed and CW injection seeding. *Appl. Phys. B Laser Opt.* **62,** 51–57 (1996).

83. LightConversion. *TOPAS White Manual*.

84. Skinner, D. R. & Whitcher, R. E. Measurement of the radius of a high-power laser beam near the focus of a lens. *J. Phys. E.* **5,** 237–238 (1972).

85. Khosrofian, J. M. & Garetz, B. a. Measurement of a Gaussian laser beam diameter through the direct inversion of knife-edge data. *Appl. Opt.* **22,** 3406–3410 (1983).

86. de Araújo, M. a C., Silva, R., de Lima, E., Pereira, D. P. & de Oliveira, P. C. Measurement of Gaussian laser beam radius using the knife-edge technique: improvement on data analysis. *Appl. Opt.* **48,** 393–396 (2009).

87. Rohmund, F., Bulgakov, A. V, Hedén, M., Lassesson, A. & Campbell, E. E. B. Photoionisation and photofragmentation of Li@C_{60}. *Chem. Phys. Lett.* **323,** 173–179 (2000).

88. Wiley, W. C. & McLaren, I. H. Time-of-Flight Mass Spectrometer with Improved Resolution. *Rev. Sci. Instrum.* **26,** 1150–1157 (1955).

89. Li, W., Chambreau, S. D., Lahankar, S. a. & Suits, A. G. Megapixel ion imaging with standard video. *Rev. Sci. Instrum.* **76,** 063106,1-7 (2005).

90. Chang, B.-Y., Hoetzlein, R. C., Mueller, J. A., Geiser, J. D. & Houston, P. L. Improved two-dimensional product imaging: The real-time ion-counting method. *Rev. Sci. Instrum.* **69,** 1665–1670 (1998).

91. Winkler, L. smoothc.mat. *MATLAB Cent.* (2005). at <http://uk.mathworks.com/matlabcentral/fileexchange/7951-smoothc-mat>

92. Roberts, G. M., Nixon, J. L., Lecointre, J., Wrede, E. & Verlet, J. R. R. Toward real-time charged-particle image reconstruction using polar onion- peeling. *Rev. Sci. Instrum.* **80,** 53104-1–7 (2009).

93. Zhao, K., Colvin, T., Hill, W. T. & Zhang, G. Deconvolving Two-Dimensional Images of Three-Dimensional Momentum Trajectories. *Rev. Sci. Instrum.* **73,** 3044–3050 (2002).

94. Kaminski, P., Wiehle, R., Renard, V., Kazmierczak, A., Lavorel, B., Faucher, O. & Witzel, B. Wavelength dependence of multiphoton ionization of xenon. *Phys. Rev. A* **70,** 53413-1–9 (2004).

95. Freeman, R. R., Bucksbaum, P. H., Milchberg, H., Darack, S., Schumacher, D. & Geusic, M. E. Above-Threshold Ionization with Subpicosecond Laser Pulses. *Phys. Rev. Lett.* **59,** 1092–1095 (1987).

96. Schyja, V., Lang, T. & Helm, H. Channel switching in above-threshold ionization of xenon. *Phys. Rev. A* **57,** 3692–3697 (1998).

97. Helm, H., Bjerre, N., Dyer, M. J., Huestis, D. L. & Saeed, M. Images of Photoelectrons Formed in Intense Laser Fields. *Phys. Rev. Lett.* **70,** 3221–3224 (1993).

98. Kramida, A., Ralchenko, Y., Reader, J. & Team, N. A. NIST Atomic Spectra Database (ver. 5.3), [Online]. National Institute of Standards and Technology, Gaithersburg, MD. *http//physics.nist.gov/asd [2016, Febr. 12]* (2015).

99. Hohenberg, P. & Kohn, W. Inhomogeneous Electron Gas. *Phys. Rev.* **136,** B864–B871 (1964).

100. Kohn, W. & Sham, L. J. Self-Consistent Equations Including Exchange and Correlation Effects.

Phys. Rev. **140,** A1133–A1138 (1965).

101. Runge, E. & Gross, E. K. U. Density-functional theory for time-dependent systems. *Phys. Rev. Lett.* **52,** 997–1000 (1984).

102. Frisch, M. J., Trucks, G. W., Schlegel, H. B., Scuseria, G. E., Robb, M. A., Cheeseman, J. R., Scalmani, G., Barone, V., Mennucci, B., Petersson, G. A., Nakatsuji, H., Caricato, M., Li, X., Hratchian, H. P., Izmaylov, A. F., Bloino, J., Zheng, G., Sonnenberg, J. L., Hada, M., Ehara, M., Toyota, K., Fukuda, R., Hasegawa, J., Ishida, M., Nakajima, T., Honda, Y., Kitao, O., Nakai, H., Vreven, T., Montgomery, J. A., J., Peralta, J. E., Ogliaro, F., Bearpark, M., Heyd, J. J., Brothers, E., Kudin, K. N., Staroverov, V. N., Kobayashi, R., Normand, J., Raghavachari, K., Rendell, A., Burant, J. C., Iyengar, S. S., Tomasi, J., Cossi, M., Rega, N., Millam, J. M., Klene, M., Knox, J. E., Cross, B. J., Bakken, V., Adamo, C., Jaramillo, J., Gomperts, R., Stratmann, R. E., Yazyev, O., Austin, A. J., Cammi, R., Pomelli, C., Ochterski, J. W., Martin, R. L., Morokuma, K., Zakrzewski, V. G., Voth, G. A., Salvador, P., Dannenberg, J. J., Dapprich, S., Daniels, A. D., Farkas, Ö., Foresman, J. B., Ortiz, J. V., Cioslowski, J. & Fox, D. J. Gaussian 09 (Revision C), Gaussian, Inc., Wallingford CT. (2009).

103. Mignolet, B., Kus, T. & Remacle, F. in *Imaging Manip. Mol. Orbitals* (eds. Grill, L. & Joachim, C.) 41–54 (Springer-Verlag Berlin Heidelberg, 2013).

104. Peach, M. J. G., Benfield, P., Helgaker, T. & Tozer, D. J. Excitation energies in density functional theory: An evaluation and a diagnostic test. *J. Chem. Phys.* **128,** 44118 (2008).

105. Peach, M. J. G., Helgaker, T., Sałek, P., Keal, T. W., Lutnæs, O. B., Tozer, D. J. & Handy, N. C. Assessment of a Coulomb-attenuated exchange–correlation energy functional. *Phys. Chem. Chem. Phys.* **8,** 558–562 (2006).

106. Wang, X. Q., Wang, C. Z., Zhang, B. L. & Ho, K. M. Electronic structures of C_{82} fullerene isomers. *Chem. Phys. Lett.* **217,** 199–203 (1994).

107. Khamatgalimov, A. R. & Kovalenko, V. I. Electronic Structure and Stability of Fullerene C_{82} Isolated-Pentagon-Rule Isomers. *J. Phys. Chem. A* **115,** 12315–12320 (2011).

108. Hino, S., Matsumoto, K., Hasegawa, S., Iwasaki, K., Yakushi, K., Morikawa, T., Takahashi, T., Seki, K., Kikuchi, K., Suzuki, S., Ikernoto, I. & Achiba, Y. Ultraviolet photoelectron spectra of C_{82} and KxC_{82}. *Phys. Rev. B* **48,** 8418–8423 (1993).

109. Stevenson, S., Rice, G., Glass, T., Harich, K., Cromer, F., Jordan, M. R., Craft, J. & Dorn, H. C. Metallofullerenes in High Yield and Purity. *Nature* **80,** 80–82 (1999).

110. Hennrich, F. H., Michel, R. H., Fischer, A., Richard-Schneider, S., Gilb, S., Kappes, M. M., Fuchs, D., Bürk, M., Kaoru Kobayashi & Nagase, S. Isolation and Characterization of C_{80}. *Angew. Chemie Int. Ed. English* **35,** 1732–1734 (1996).

111. Cummins, T. R., Bürk, M., Schmidt, M., Armbruster, J. F., Fuchs, D., Adelmann, P., Schuppler, S., Michel, R. H. & Kappes, M. M. Electronic states and molecular symmetry of the higher fullerene C_{80}. *Chem. Phys. Lett.* **261,** 228–233 (1996).

112. Wang, C.-R., Sugai, T., Kai, T., Tomiyama, T. & Shinohara, H. Production and isolation of an ellipsoidal C_{80} fullerene. *Chem. Commun.* **1,** 557–558 (2000).

113. Huang, T., Zhao, J., Feng, M., Petek, H., Yang, S. & Dunsch, L. Superatom orbitals of $Sc_3N@C_{80}$ and their intermolecular hybridization on Cu(110)-(2×1)-O surface. *Phys. Rev. B* **81,** 1–8 (2010).

114. Zhang, M., Harding, L. B., Gray, S. K. & Rice, S. A. Quantum States of the Endohedral Fullerene $Li@C_{60}$. *J. Phys. Chem. A* **112,** 5478–5485 (2008).

115. Popok, V. N., Gromov, A., Jonsson, M., Taninaka, A., Shinohara, H. & Campbell, E. E. B. Electronic properties of thin films sublimed from $La@C_{82}$ and $Li@C_{60}$. *Nano* **3,** 155–160 (2008).

116. Lu, X., Feng, L., Akasaka, T. & Nagase, S. Current status and future developments of

endohedral metallofullerenes. *Chem. Soc. Rev.* **41,** 7723–7760 (2012).

117. Gromov, A., Ostrovskii, D., Lassesson, A., Jonsson, M. & Campbell, E. E. B. Fourier Transform Infrared and Raman Spectroscopic Study of Chromatographically Isolated Li@C_{60} and Li@C_{70}. *J. Phys. Chem. B* **107,** 11290–11301 (2003).

118. Aoyagi, S., Nishibori, E., Sawa, H., Sugimoto, K., Takata, M., Miyata, Y., Kitaura, R., Shinohara, H., Okada, H., Sakai, T., Ono, Y., Kawachi, K., Yokoo, K., Ono, S., Omote, K., Kasama, Y., Ishikawa, S., Komuro, T. & Tobita, H. A layered ionic crystal of polar Li@C_{60} superatoms. *Nat. Chem.* **2,** 678–83 (2010).

119. Broclawik, E. & Eilmes, A. Density functional study of endohedral complexes M@C_{60} (M=Li, Na, K, Be, Mg, Ca, La, B, Al): Electronic properties, ionization potentials, and electron affinities. *J. Chem. Phys.* **108,** 3498 (1998).

120. Popok, V. N., Azarko, I. I., Gromov, A., Jönsson, M., Lassesson, A. & Campbell, E. E. B. Conductance and EPR study of the endohedral fullerene Li@C_{60}. *Solid State Commun.* **133,** 499–503 (2005).

121. Dunlap, B. I., Ballester, J. L. & Schmidt, P. P. Interaction between C_{60} and endohedral alkali atoms. *J. Phys. Chem.* **96,** 9781 (1992).

122. Li, Y. S. & Tomanek, D. How free are encapsulated atoms in C_{60}? *Chem. Phys. Lett.* **221,** 453–458 (1994).

123. Jiménez-Fabián, I. & Jalbout, A. F. Fullerene as an electron buffer: Charge transfer and solvent interactions. *J. Comput. Theor. Nanosci.* **5,** 512–516 (2008).

124. Gromov, A., Krawez, N., Lassesson, A., Ostrovskii, D. I. & Campbell, E. E. B. Optical properties of endohedral Li@C_{60}. *Curr. Appl. Phys.* **2,** 51–55 (2002).

125. Lassesson, A., Hansen, K., Jönsson, M., Gromov, A., Campbell, E. E. B., Boyle, M., Pop, D., Schulz, C. P., Hertel, I. V., Taninaka, A. & Shinohara, H. A femtosecond laser study of the endohedral fullerenes Li@C_{60} and La@C_{82}. *Eur. Phys. J. D* **34,** 205–209 (2005).

126. Komatsu, K., Wang, G. W., Murata, Y., Tanaka, T., Fujiwara, K., Yamamoto, K. & Saunders, M. Mechanochemical Synthesis and Characterization of the Fullerene Dimer C_{120}. *J. Org. Chem.* **63,** 9358–9366 (1998).

127. Kusch, C., Krawez, N., Tellgmann, R., Winter, B. & Campbell, E. E. B. Thermal desorption spectroscopy of fullerene films containing endohedral Li@C_{60}. *Appl. Phys. A Mater. Sci. Process.* **66,** 293–298 (1998).

128. Denis, P. A. Chemical reactivity of lithium-doped fullerenes. *J. Phys. Org. Chem.* **25,** 322–326 (2012).

129. Yagi, H., Ogasawara, N., Zenki, M., Miyazaki, T. & Hino, S. Photoemission study of Li@C_{60}. *Chem. Phys. Lett.* **651,** 124–126 (2016).

130. Wan, Z., Christian, F. & Anderson, S. L. Collision of Li^+ and Na^+ with C_{60}: Insertion, fragmentation, and thermionic emission. *Phys. Rev. Lett.* **69,** 1352–1355 (1992).

131. Tomita, S., Andersen, J. U., Hansen, K. & Hvelplund, P. Stability of Buckminsterfullerene, C60. *Chem. Phys. Lett.* **382,** 120–125 (2003).

132. Concina, B., Tomita, S., Andersen, J. U. & Hvelplund, P. Delayed ionisation of C_{70}. *Eur. Phys. J. D* **34,** 191–194 (2005).

133. Bohl, E., Sokół, K. P., Mignolet, B., Thompson, J. O. F., Johansson, J. O., Remacle, F. & Campbell, E. E. B. Supporting Information: Relative Photoionization Cross-sections of SAMOs in C_{60}. *J. Phys. Chem. Lett.* **119,** 11504–11508 (2015).

134. Samson, J. a. R., Haddad, G. N. & Kilcoyne, L. D. Absorption and dissociative photoionization cross sections of NH_3 from 80 to 1120 Å. *J. Chem. Phys.* **87,** 6416–6422 (1987).

135. Cool, T. a., Wang, J., Nakajima, K., Taatjes, C. a. & Mcllroy, A. Photoionization cross sections for reaction intermediates in hydrocarbon combustion. *Int. J. Mass Spectrom.* **247,** 18–27 (2005).

136. Wang, J., Yang, B., Cool, T. a., Hansen, N. & Kasper, T. Near-threshold absolute photoionization cross-sections of some reaction intermediates in combustion. *Int. J. Mass Spectrom.* **269,** 210–220 (2008).

137. Zhou, Z., Zhang, L., Xie, M., Wang, Z., Chen, D. & Qi, F. Determination of absolute photoionization cross-sections of alkanes and cyclo-alkanes. *Rapid Commun. mass Spectrom.* **24,** 1335–1342 (2010).

138. Campbell, E. E. B., Fanti, M., Hertel, I. V., Rolf Mitzner & Zerbetto, F. The hyperpolarisability of an endohedral fullerene: Li@C_{60}. *Chem. Phys. Lett.* **288,** 131–137 (1998).

139. Bak, K. L., Koch, H., Oddershede, J., Christiansen, O. & Sauer, S. P. a. Atomic integral driven second order polarization propagator calculations of the excitation spectra of naphthalene and anthracene. *J. Chem. Phys.* **112,** 4173 (2000).

140. Chai, J.-D. & Head-Gordon, M. Long-range corrected hybrid density functionals with damped atom–atom dispersion corrections. *Phys. Chem. Chem. Phys.* **10,** 6615–6620 (2008).

141. Zhao, Y. & Truhlar, D. G. Density functional for spectroscopy: No long-range self-interaction error, good performance for Rydberg and charge-transfer states, and better performance on average than B3LYP for ground states. *J. Phys. Chem. A* **110,** 13126–13130 (2006).

142. Becke, A. D. Density-functional thermochemistry.III. The role of exact exchange. *J. Chem. Phys.* **98,** 5648 (1993).

143. Yanai, T., Tew, D. P. & Handy, N. C. A new hybrid exchange-correlation functional using the Coulomb-attenuating method (CAM-B3LYP). *Chem. Phys. Lett.* **393,** 51–57 (2004).

144. Schmidt, W. Photoelectron spectra of polynuclear aromatics. V. Correlations with ultraviolet absorption spectra in the catacondensed series. *J. Chem. Phys.* **66,** 828 (1977).

145. Duncan, M. A., Dietz, T. G. & Smalley, R. E. Two-color photoionization of naphthalene and benzene at threshold. *J. Chem. Phys.* **75,** 2118 (1981).

146. George, G. A. & Morris, G. C. The intensity of absorption of naphthalene from 30 000 cm^{-1} to 53 000 cm^{-1}. *J. Mol. Spectrosc.* **26,** 67–71 (1968).

147. Biegasiewicz, K. F., Griffiths, J. R., Savage, G. P., Tsanaktsidis, J. & Priefer, R. Cubane: 50 Years Later. *Chem. Rev.* **115,** 6719–6745 (2015).

148. Markevitch, A. N., Moore, N. P. & Levis, R. J. The influence of molecular structure on strong field energy coupling and partitioning. *Chem. Phys.* **267,** 131–140 (2001).

149. Prinzbach, H., Weiler, A., Landenberger, P., Wahl, F., Worth, J., Scott, L., Gelmont, M., Olevano, D. & v. Issendorff B. Gas-phase production and photoelectron spectroscopy of the smallest fullerene, C_{20}. *Nature* **407,** 60–63 (2000).

150. Prinzbach, H., Wahl, F., Weiler, A., Landenberger, P., Wörth, J., Scott, L. T., Gelmont, M., Olevano, D., Sommer, F. & von Issendorff, B. C_{20} carbon clusters: fullerene-boat-sheet generation, mass selection, photoelectron characterization. *Chem. - An Eur. J.* **12,** 6268–6280 (2006).

151. Salama, F., Joblin, C. & Allamandola, L. J. Electronic absorption spectroscopy of matrix-isolated polycyclic aromatic hydrocarbon cations. II. The phenanthrene cation ($C_{14}H_{10}^{+}$) and its 1-methyl derivative. *J. Chem. Phys.* **101,** 10252–10262 (1994).

152. Raymonda, J. W. Rydberg States in Cyclic Alkanes. *J. Chem. Phys.* **56,** 3912 (1972).

153. Robin, M. B. *Higher Excited States of Polyatomic Molecules*. (Academic Press, 1974).

154. Vörös, M. & Gali, A. Optical absorption of diamond nanocrystals from ab initio density-

functional calculations. *Phys. Rev. B - Condens. Matter Mater. Phys.* **80,** 161411 (2009).

155. Shang, Q. Y. & Bernstein, E. R. (σ3s) Rydberg states of cylcohexanes, bicyclo[2.2.2]octane, and adamantane. *J. Chem. Phys.* **100,** 8625–8632 (1994).

156. Rudakov, F. & Weber, P. M. Ultrafast structural and isomerization dynamics in the Rydberg-exited Quadricyclane: Norbornadiene system. *J. Chem. Physicshysics* **136,** 134303 (2012).

157. Xing, X., Gedanken, A., Sheybani, A. & McDiarmid, R. The 198-225-nm Transition of Norbornadiene. *J. Phys. Chem.* **98,** 8302–8309 (1994).

158. Schröder, D., Loos, J., Schwarz, H., Thissen, R., Preda, D. V., Scott, L. T., Caraiman, D., Frach, M. V. & Böhme, D. K. Single and double ionization of corannulene and coronene. *Helv. Chim. Acta* **84,** 1625–1634 (2001).

159. Clar, E., Robertson, J. M., Schlogl, R. & Schmidt, W. Photoelectron Spectra of Polynuclear Aromatics. 6. Applications to Structural Elucidation: "Circumanthracene". *J. Am. Chem. Soc.* **103,** 1320–1328 (1981).

160. Kawashima, Y., Ohkubo, K. & Fukuzumi, S. Efficient Charge Separation in $Li^+@C_{60}$ Supramolecular Complexes with Electron Donors. *Chem. - An Asian J.* **10,** 44–54 (2015).

161. Gan, L., Zhang, Q., Cheng, Y. & Schwingenschloegl, U. Photovoltaic Heterojunctions of Fullerenes with MoS_2 and WS_2 Monolayers. *J. Phys. Chem. Lett.* **5,** 1445–1449 (2014).

162. Yamada, M., Ohkubo, K., Shionoya, M. & Fukuzumi, S. Photoinduced Electron Transfer in a Charge-Transfer Complex Formed between Corannulene and $Li^+@C_{60}$ by Concave−Convex π−π Interactions. *J. Am. Chem. Soc.* **136,** 13240–13248 (2014).

163. Ma, Q., Andersen, T. I., Nair, N. L., Gabor, N. M., Massicotte, M., Lui, C. H., Young, A. F., Fang, W., Watanabe, K., Taniguchi, T., Kong, J., Gedik, N., Koppens, F. H. L. & Jarillo-Herrero, P. Tuning ultrafast electron thermalization pathways in a van der Waals heterostructure. *Nat. Phys. Lett.* **12,** 455–459 (2016).

164. Popov, A. a & Dunsch, L. Hindered cluster rotation and ^{45}Sc hyperfine splitting constant in distonoid anion radical $Sc_3N@C_{80}^-$, and spatial spin-charge separation as a general principle for anions of endohedral fullerenes with metal-localized lowest unoccupied molecular orbitals. *J. Am. Chem. Soc.* **130,** 17726–42 (2008).

8. Appendices

8. 1. Appendix A – Laser Intensity Calibration Factors

Laser intensity calibration factors obtained for different wavelengths and pulse durations as described in chapter 2. 1. 3 and 2. 2. 2.

Table 8.1: Summary of the laser intensity calibration factors

Laser wavelength	Pulse duration	Calibration factor in $\frac{W/cm^2}{\mu J}$
400 nm	(120 ± 10) fs	$(1.82 \pm 0.22) \cdot 10^{11}$
500 nm	(90 ± 10) fs	$(1.35 \pm 0.34) \cdot 10^{11}$
520 nm	(90 ± 10) fs	$(6.1 \pm 1.2) \cdot 10^{11}$
540 nm	(35 ± 10) fs	$(8.8 \pm 1.8) \cdot 10^{11}$
570 nm	(39 ± 1) fs	$(6.5 \pm 2.1) \cdot 10^{11}$
600 nm	(90 ± 10) fs	$(0.89 \pm 0.04) \cdot 10^{11}$
625 nm	(44 ± 5) fs	$(5.62 \pm 0.37) \cdot 10^{11}$
700 nm	(78 ± 10) fs	$(2.03 \pm 0.48) \cdot 10^{11}$
800 nm	(120 ± 10) fs	$(6.21 \pm 0.13) \cdot 10^{11}$

8. 2. Appendix B – Peak Fitting Analysis Procedure

After fitting the thermal electron background to the PES as described in section 4. 2, the thermal background is subtracted from the spectrum for the peak fitting procedure (Figure 8.1).

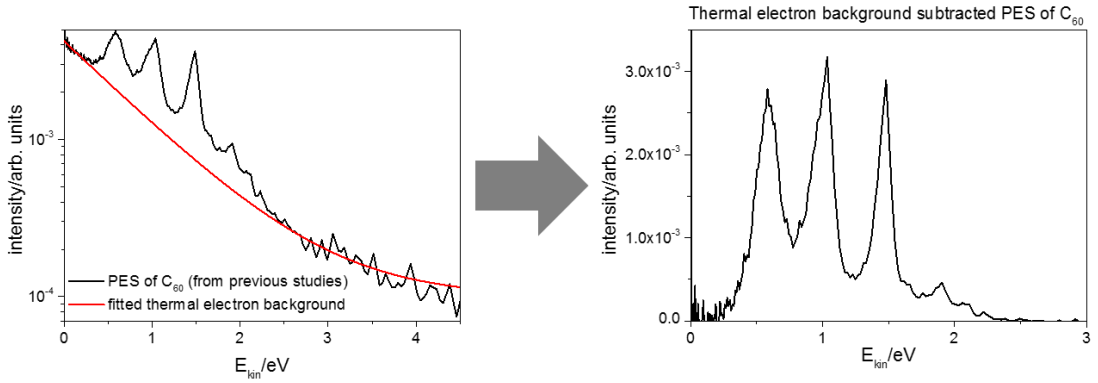

Figure 8.1: Example of PES of C_{60} at 500 nm, (90 ± 10) fs, (4.5 ± 0.3) TW/cm² from previous studies[74] with the fitted thermal electron background on the left, note that it is on a logarithmic intensity scale. On the right is the according PES shown after the thermal electron background subtraction.

Lorentzian functions are fitted to the peaks in the PES by eye to obtain the peak position, area and width. In this procedure it is important that the summation of all peak functions aligns with the experimental spectrum.

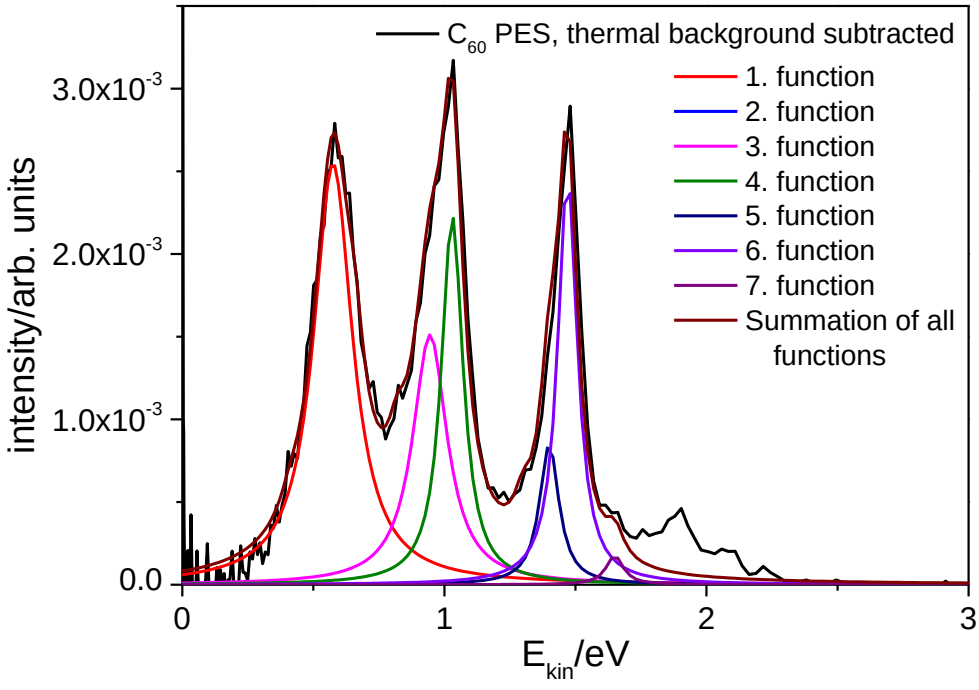

Figure 8.2: Peak fitting result of the thermal electron background subtracted C_{60} PES from Figure 8.1.

In some cases more than one Lorentzian function are needed to fit a peak reasonably well, but the number of used functions should not exceed the number of possible orbitals based on the assignment of the peak (like one function for a s peak or three functions for a p peak etc.). If more than one function is used to fit a peak, the summation of the applied peaks is used to obtain the peak position, area and width including the error propagation from the individual peaks.

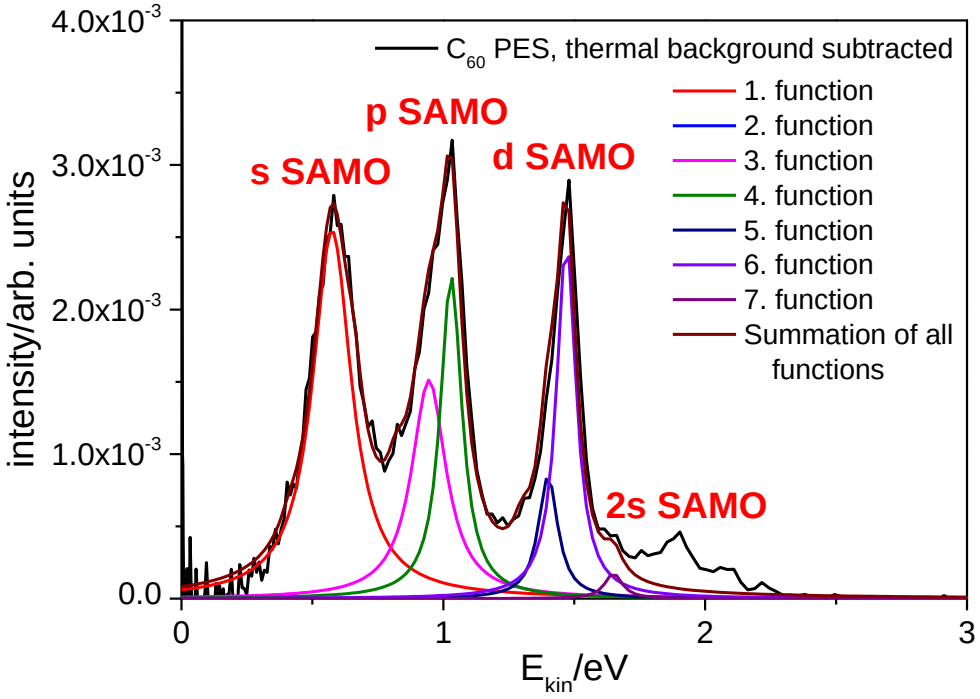

Figure 8.3: Same spectrum as Figure 8.2 including the assignment of the peaks.

8. 3. Appendix C – Negative Mode LD FT-ICR Mass Spectrum of Li@C$_{60}$ Sample

LD FT-ICR mass spectrum of the Li@C$_{60}$[PF$_6$] sample taken at the same conditions as in chapter 3. 2. 3, Figure 3.14, just in the negative mode to detect anions.

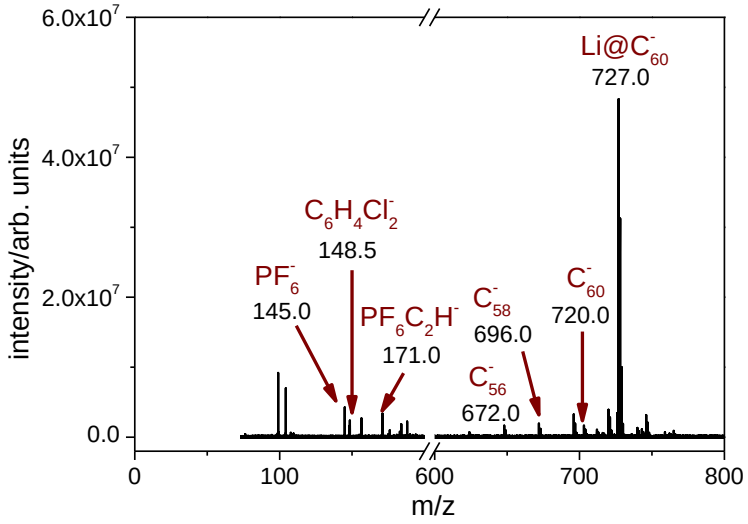

Figure 8.4: Negative mode LD FT-ICR mass spectrum of Li@C$_{60}$[PF$_6$] including the assignment of some peaks.

8. 4. Appendix D – Mass Spectra of Li@C_{60} using 600 nm Laser Pulses

Mass spectra series of Li@C_{60}[PF_6] recorded at several laser intensities (as labelled in the graph) using 600 nm, (90 ± 10) fs at T_{oven} = (301 ± 3) ºC.

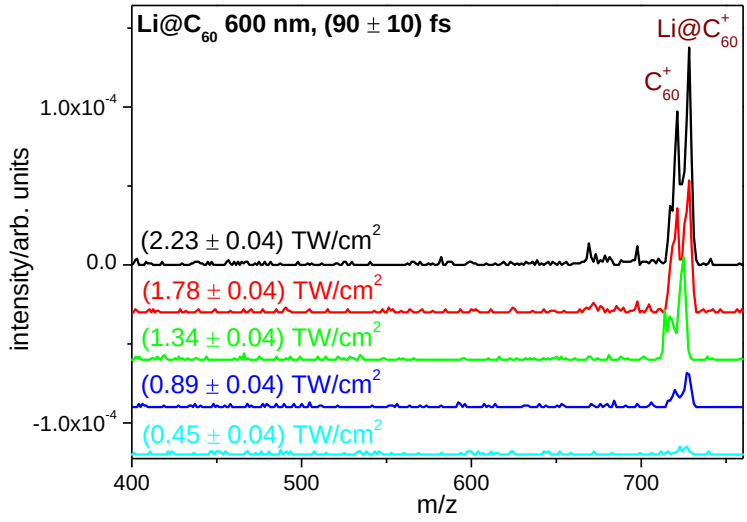

Figure 8.5: Mass spectra of Li@C_{60} using 600 nm, (90 ± 10) fs at different laser intensities as indicated in the graph.

8. 5. Appendix E – Mass Spectra Series at different Laser Intensities of $Li@C_{60}$

Mass spectra of $Li@C_{60}$ taken at 540 nm using different laser intensities to probe the laser intensity dependence of the ion yield.

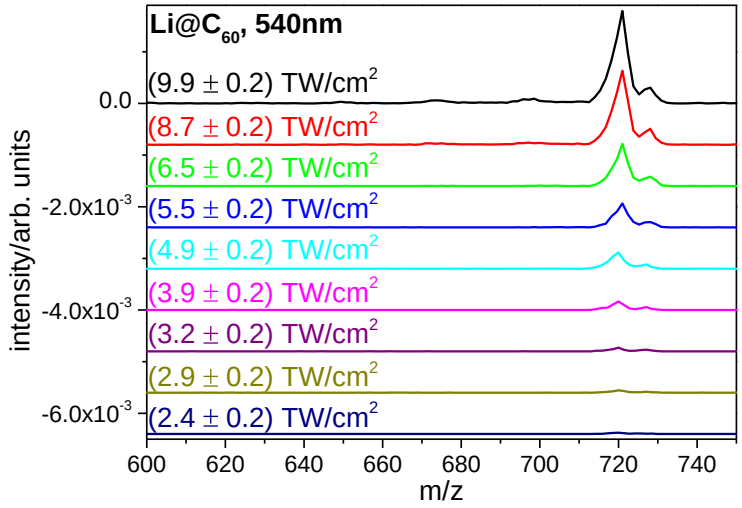

Figure 8.6: Series of $Li@C_{60}$ mass spectra at 540 nm, (35 ± 10) fs, T_{oven} = (386 ± 3) °C and laser intensities as labelled.

8. 6. Appendix F – PES of Li@C_{60} at 600 nm and 800 nm

Angle integrated PES of Li@C_{60} at 600 nm, (90 ± 10) fs, (1.0 ± 0.5) TW/cm^2 and 800 nm, (120 ± 10) fs, (4.0 ± 0.6) TW/cm^2.

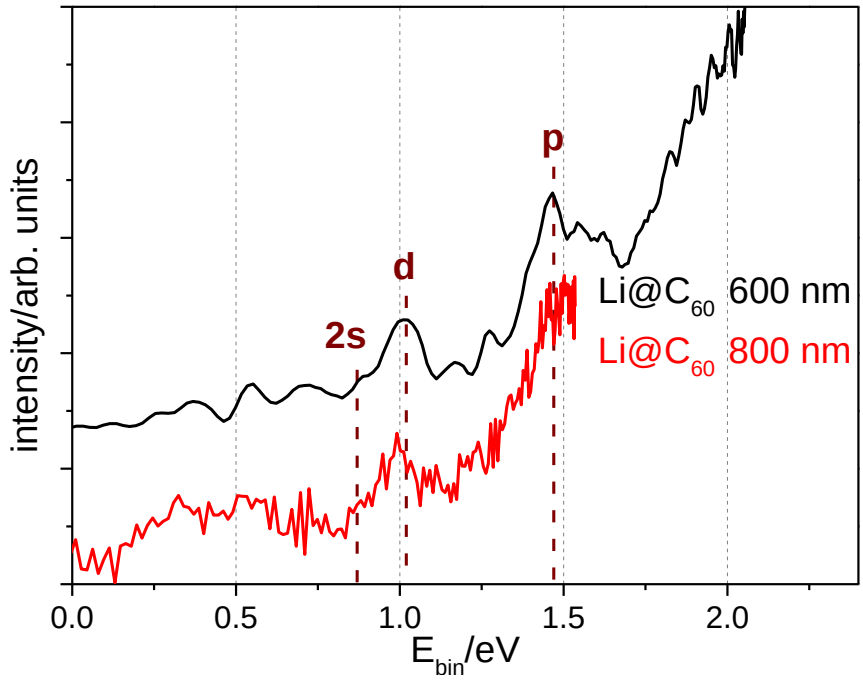

Figure 8.7: Angle integrated PES of Li@C_{60} at 600 nm and 800 nm with the peak assignment.

8. 7. Appendix G – PES of C_{60} at 700 nm

Angular-resolved PES of C_{60} at 700 nm and at different laser intensities are analysed to investigate the thermal electron background. The recorded spectra have a high noise level for lower laser intensities due to the decreased sample signal. The fitted apparent temperatures parallel ($T_a^{\parallel}$) and perpendicular ($T_a^{\perp}$) to the laser polarisation direction are a) $T_a^{\parallel}$ = (0.83 ± 0.10) eV, $T_a^{\perp}$ = (0.75 ± 0.12) eV; b) $T_a^{\parallel}$ = (1.00 ± 0.20) eV, $T_a^{\perp}$ = (0.65 ± 0.30) eV; c) $T_a^{\parallel}$ = (1.08 ± 0.08) eV, $T_a^{\perp}$ = (0.72 ± 0.05) eV.

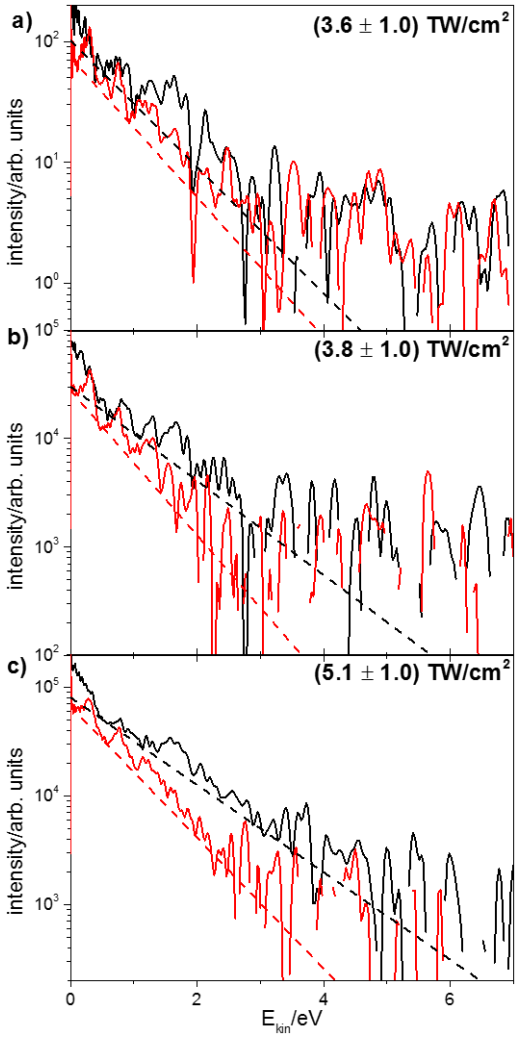

Figure 8.8: Angular-resolved PES of C_{60} at 700 nm, (78 ± 10) fs, at different laser intensities as labelled in the graphs. The black solid line is the PES parallel to the laser polarisation direction and the red solid line is the PES perpendicular to it. The corresponding dashed lines are the fitted thermal electron background according to equation (4.1). Note that the intensity scale is logarithmic.

8. 8. Appendix H – Publications

The publications are attached in the following order:

- Johansson, J. O., Bohl, E., Henderson, G. G., Mignolet, B., Dennis, T. J. S., Remacle, F. & Campbell, E. E. B. Hot electron production and diffuse excited states in C_{70}, C_{82} and $Sc_3N@C_{80}$ characterised by angular-resolved photoelectron spectroscopy. *J. Chem. Phys.* **139,** 084309 (2013).
- Bohl, E., Sokół, K. P., Mignolet, B., Thompson, J. O. F., Johansson, J. O., Remacle, F. & Campbell, E. E. B. Relative Photoionization Cross Sections of Super-Atom Molecular Orbitals (SAMOs) in C_{60}. *J. Phys. Chem. A* **119,** 11504–11508 (2015).
- Johansson, J. O., Bohl, E. & Campbell, E. E. B. Super-Atom Molecular Orbital Excited States of Fullerenes. *Philos. Trans. R. Soc. A* **374,** 1–13 (2016).

Hot electron production and diffuse excited states in C_{70}, C_{82}, and $Sc_3N@C_{80}$ characterized by angular-resolved photoelectron spectroscopy

J. Olof Johansson,[1] Elvira Bohl,[1] Gordon G. Henderson,[1] Benoit Mignolet,[2] T. John S. Dennis,[3] Francoise Remacle,[2] and Eleanor E. B. Campbell[1,a)]
[1]*EaStCHEM, School of Chemistry, University of Edinburgh, Edinburgh EH9 3JJ, United Kingdom*
[2]*Département de Chimie, B6c, Université de Liège, B4000 Liège, Belgium*
[3]*School of Physics and Astronomy, Queen Mary University of London, Mile End Road, London E1 4NS, United Kingdom*

(Received 1 July 2013; accepted 5 August 2013; published online 27 August 2013)

Angular-resolved photoelectron spectroscopy using wavelength-tuneable femtosecond laser pulses is presented for a series of fullerenes, namely, C_{70}, C_{82}, and $Sc_3N@C_{80}$. The photoelectron kinetic energy distributions for the three molecules show typical thermal electron spectra with a superimposed peak structure that is the result of one-photon ionization of diffuse low-angular momenta states with electron density close to the carbon cage and that are related to so-called super atom molecular orbitals. Photoelectron angular distributions confirm this assignment. The observed structure is less prominent compared to the thermal electron background than what was observed in C_{60}. It can be concluded that hot electron emission is the main ionization channel for the larger and more complex molecules for these excitation conditions. © *2013 AIP Publishing LLC*. [http://dx.doi.org/10.1063/1.4818987]

I. INTRODUCTION

A fundamental understanding of the electronic structure and photoinitiated electron dynamics in large organic molecules and carbon nanomaterials is important for optimizing their properties for use in molecular electronics and organic photovoltaics. C_{60} is an excellent model system for acceptor molecules, such as $PC_{60}BM$, due to its high symmetry and simple chemical composition, which simplifies theoretical modelling.[1] Photoelectron spectroscopy studies of gas-phase fullerenes after ca. 100 fs laser excitation have shown that an efficient energy redistribution produces hot electrons leading to the emission of thermal electrons with a characteristic Boltzmann-like photoelectron spectrum (PES).[2] Superimposed on the thermal electron background, a series of clear peaks converging on the ionization energy can be observed that were initially assigned to one-photon ionization of Rydberg states with large orbital angular momenta ($\ell = 3$, 5, and 7).[3] Photoelectron angular distributions (PADs) have been shown to be a powerful tool to clearly identify the states giving rise to some of this peak structure in PES and could, in combination with a recent computational study by Mignolet *et al.*, show that the peak structure seen in fs spectra is due to excitation of diffuse, excited states.[4,5] These diffuse states are Rydberg-like states with low orbital angular momenta ($\ell = 0$, 1, and 2)[4] and at least two radial nodes in the wavefunction ($n = 3$). The lowest-lying s-state predominantly consists of the excitation of the s "Super Atom Molecular Orbital" (s-SAMO) that was originally studied by Feng *et al.*[6] using scanning tunnelling spectroscopy of fullerenes supported on metal substrates. Higher-lying states, such as the p and d states, are further away from the core, in contrast to the s-SAMO, and therefore show a mixture of SAMO and more conventional Rydberg character, where the long range Coulomb force dominates the interaction.[5] It is not clear how much of the SAMO-character is retained in larger and more complex fullerenes, although there have been a few studies, mainly theoretical, that have identified SAMOs in systems other than C_{60}.[7,8]

Recently, Grancini *et al.*[9] found that in a solar cell composed of a polymer donor and $PC_{60}BM$ acceptor, above-gap excitation in the donor produces hot, delocalised interfacial charge transfer states that result in much more efficient charge dissociation. The diffuse SAMOs, giving rise to nearly free-electron bands in solids,[7] could potentially play a key role in the diffuse charge transfer states mediating the efficient charge dissociation observed.[9] A deeper understanding of the nature of the excited states and the hot electron dynamics in model acceptor materials may therefore lead to improved light-harvesting devices.

To probe the influence of molecular size and symmetry on both the thermal electron emission and diffuse excited states, we have carried out measurements on a series of fullerenes with lower symmetry than C_{60}, namely, C_{70}, C_{82}, and the endohedral fullerene $Sc_3N@C_{80}$. Experimentally, gas-phase studies are ideally suited for understanding the fundamental aspects of these states, since there are no solvents or surfaces present that perturb the electronic structure. The paper is organized as follows. In Sec. II, the experimental setup is briefly described and we show how binding energies and PADs are extracted from the measurements. We also briefly describe the computational methodology used

a)Author to whom correspondence should be addressed. E-mail: eleanor.campbell@ed.ac.uk.

to compute the excited states and compare with the experimental binding energies. In Sec. III, PES with clear thermal electron signatures are presented for the molecules studied. Subsequently, the focus is shifted to assigning the peaks superimposed on the thermal background, which is possible by comparing to results for C_{60}. PES and PADs are therefore first presented for C_{60} and then for C_{70}, C_{82}, and $Sc_3N@C_{80}$.

II. METHODS

A. Experimental setup

The experimental setup is similar to the one presented in Ref. 10. Neutral gas-phase fullerenes from purified powder of C_{60}, C_{70}, C_{82}, and $Sc_3N@C_{80}$ were prepared from an effusive oven at a temperature of ca. 500 °C inside a vacuum chamber with pressure below 10^{-8} mbar. The output from a non-collinear optical parametric amplifier (NOPA), pumped by a regenerative titanium sapphire amplifier (producing 800 nm, 120 fs laser pulses of 3.8 mJ pulse energy), was passed into the vacuum chamber at right angles to the effusive molecular beam. The pulse duration after passing through a half-wave plate, Glan-laser polarizer, and a vacuum viewport was approximately 90 fs. The wavelength range used from the NOPA was 500–750 nm, but was complimented by the fundamental and second harmonic of the regenerative amplifier (800 and 400 nm, respectively). Mass spectra were collected with a time-of-flight mass spectrometer. For all spectra presented in this paper, the laser power was adjusted so that the lowest possible detectable signal was obtained, which typically meant that only singly charged molecular parents were observed. Typical mass spectra are shown in Figure 1. The intact molecular ion was the most abundant species in the mass spectra, although for C_{82} a small fraction of C_{84} was observed as well. The electrons were extracted onto a position sensitive detector consisting of a pair of microchannel plates and a phosphor screen using a standard velocity-map imaging (VMI) electrode configuration.[11] The resulting VMI images were inverted using a modified version of Polar Onion-Peeling (POP)[12] that included up to the tenth Legendre polynomial in the inversion procedure.

B. Data analysis

Data collected using 120 fs, 400 nm, and 1.1 TW cm^{-2} intensity are presented in Figure 2 for C_{60}. For this pulse duration and intensity, the PES typically show thermal electron emission, as characterized by an exponential kinetic energy distribution.[13] A series of peaks can be seen superimposed on the thermal electron background, and in order to extract angular distributions for these peaks, it is first necessary to remove the thermal electron background. We do this by dividing the inverted VMI image into 10° angular segments, which is shown in Figure 2 for the segments corresponding to 0°–10° (parallel to the laser polarization direction), 40°–50°, and 80°–90° (perpendicular to the laser polarization direction). Clear peaks are observed along the laser polarization direction for this wavelength. Perpendicular to the laser polarization direction, an exponential distribution is observed (plotted in log-lin scale) due to thermal electron emission, although some residual peak structure is still visible. An exponential distribution is fitted to the 80°–90° angular segment and subsequently subtracted from all other angular segments. For longer wavelengths and higher intensities, the thermal electron background becomes asymmetric because of the laser field's influence on the emitted electrons,[13] which complicates the thermal background subtraction. Also, above-threshold ionization (ATI) peaks superimposed on the

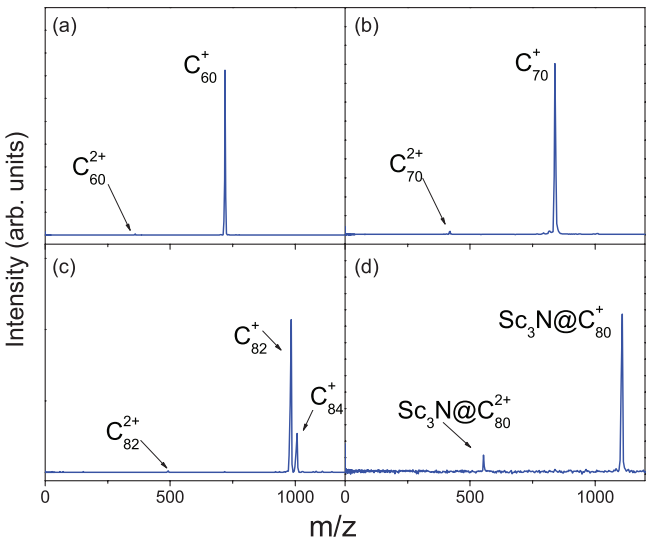

FIG. 1. Mass spectra obtained for the different molecules (indicated in the figure) with typical laser excitation conditions where the intact molecular ion is the dominant species in the mass spectrum. The laser wavelengths and intensities were (a) 500 nm, 4.7 TW cm^{-2}; (b) 520 nm, 2.9 TW cm^{-2}; (c) 519 nm, 2.8 TW cm^{-2}; and (d) 506 nm, 4.1 TW cm^{-2}. The pulse duration was approximately 90 fs.

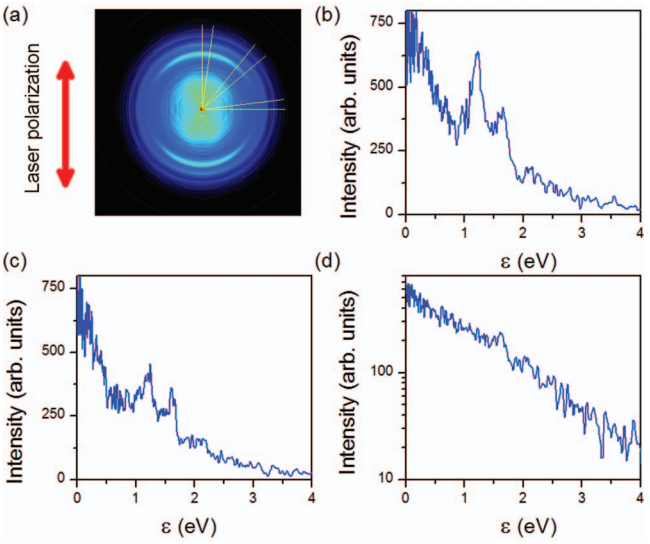

FIG. 2. (a) Inverted VMI image obtained after ionizing C_{60} with 120 fs, 400 nm laser excitation of 1.1 TW cm^{-2} (weighted by the radius for display purposes). ε is the electron kinetic energy. The yellow lines represent the angular segments that the image is divided into for producing the PES along the (b) 0°–10°, (c) 40°–50°, and (d) 80°–90° angular segments. Note that the perpendicular segment (80°–90°) is plotted in log-lin scale to emphasise the (exponential) thermal electron background.

TABLE I. Computed binding energies of the lowest SAMO states of C_{60}.

Functional	Basis	s-state E_{bind} (eV)	p-state E_{bind} (eV)	d-state E_{bind} (eV)
B3LYP	6-31 + G(d)	2.14	1.26	0.77
CAM-B3LYP	6-31 + G(d)	2.10	1.14	0.62
CAM-B3LYP	6-31 + G(d) + diffuse functions (Mignolet *et al.*[5])	2.35	1.46–1.72	1.14–1.35

background further obscure the thermal signal.[2,14] Therefore, for longer wavelengths (approximately >650 nm), where a higher intensity is needed due to a lower value of the photon absorption cross-section, an exponential distribution is fitted for each angular segment. By keeping the laser power to a minimum, however, the asymmetric effects are also kept to a minimum.

Once the thermal background has been subtracted, Lorentzian peaks are fitted to the spectra and the peak intensity vs. angle can be used to extract the angular distributions for each peak. We have found, using pulses of the order of 100 fs, that most angular distributions are very simple. In fact, we can fit the PADs with an equation used for single-photon ionization of a randomly distributed sample[15]

$$I(\theta) \propto [1 + \beta P_2(\cos\theta)], \quad (1)$$

where θ is the emission angle with respect to the laser polarization direction and P_2 is a second order Legendre polynomial that is weighted by the anisotropy parameter β (which can range from −1 to 2). Typically, Legendre polynomials of order up to $2n$ are needed to describe the PAD from a multiphoton process, where n is the number of photons involved in the ionization process.[16] Given the ionization potential of C_{60}, one would expect a polynomial order up to at least 10 for 800 nm ionization. Of course, it is possible to fit the PADs to higher order Legendre polynomials, however, including higher orders does not significantly improve the fits. The coefficient for the fourth Legendre polynomial is typically less than 10% of the fitted coefficient for the second order polynomial (i.e., the β value), which is less than the estimated 10% uncertainty in peak intensity. We therefore use Eq. (1) to fit the data. By changing the laser wavelength, it is possible to measure the kinetic energy dependence of the β-parameter for a given peak. This gives us the possibility to not only compare computed binding energies to experimental ones, but also compare the anisotropy kinetic energy dependence to calculations to assign peaks in PES.[1,4]

C. Computational details

C_{60}, C_{70}, and C_{84} (D_2 isomer) were optimized without imposing symmetry at the B3LYP/6-31+G(d) level. The geometries of C_{60}, C_{70}, and C_{84} were found to belong to the I_h, D_{5h}, and D_2 point groups, respectively. The excited states were computed by time-dependent density functional theory (TD-DFT) at the TD-DFT/B3LYP/6-31+G(d) level for a band of 500 excited states above the ground state, with symmetry imposed. All computations were carried out with GAUSSIAN 09.[17]

The functional B3LYP and the 6-31+G(d) basis set were selected in order to be able to carry out a systematic study of the SAMO states of increasingly large fullerenes. Functionals corrected for long-range electronic interactions, like the functional CAM-B3LYP used in Mignolet *et al.*,[5] are better suited for describing highly excited states with a diffuse character. However, the computation of the correction term of CAM-B3LYP increases significantly the computation time and slows down the convergence, which precludes its use for the larger fullerenes C_{70} and C_{84} when a band of 500 excited states is needed. The use of a smaller basis set, compared to what was used previously[5] for C_{60}, is motivated by the same considerations. The present basis set is large enough to describe the lower-lying SAMOs of the three fullerenes computationally investigated in this study and therefore allows for a systematic comparison of their binding energies. For C_{60}, we were able to compute the binding energies in B3LYP and CAM-B3LYP for two basis sets (see Table I). With the 6-31+G(d) basis set, the B3LYP binding energies are slightly higher than the CAM-B3LYP binding energies but the energy differences between the states remain similar (within 0.1 eV). The addition of diffuse functions increases the binding energies,[5] but overall the energetic order of the lowest SAMO states is stable. In addition, the computed photoelectron angular distributions, which strongly depend on the symmetry properties of the SAMO states, do not change substantially when using the smaller basis set. The same is true of the anisotropy parameter, β. The SAMOs of C_{70} do not exhibit a spherical symmetry but rather a cylindrical one. Therefore, the p and d manifolds of the SAMOs in C_{70} are not exactly degenerate. The p_z-SAMO orbital is lower in energy than the p_x and p_y ones, and the d_{z2} SAMO is lower than d_{zx} and d_{zy} that are, in turn, lower than d_{xy} and d_{x2-y2}.

A detailed description of the calculations of PADs was presented previously.[5] The PADs for C_{60} and C_{70} were computed for a randomly oriented sample by rotating the molecular frame of the molecule to obtain a random orientation with respect to the laboratory frame. The computed PADs were subsequently analysed using Eq. (1) to obtain the β-parameters which were then compared to experiments.

III. RESULTS AND DISCUSSION

A. Thermal electron emission

Thermal electron emission from fullerenes has previously only been studied in C_{60}, C_{70}, and, to a much lesser extent, La@C_{82} after 800 nm excitation.[10,18] The resulting PES show an exponential background distribution $I(\varepsilon) \propto \exp(-\varepsilon/k_B T_a)$, characterised by an apparent temperature

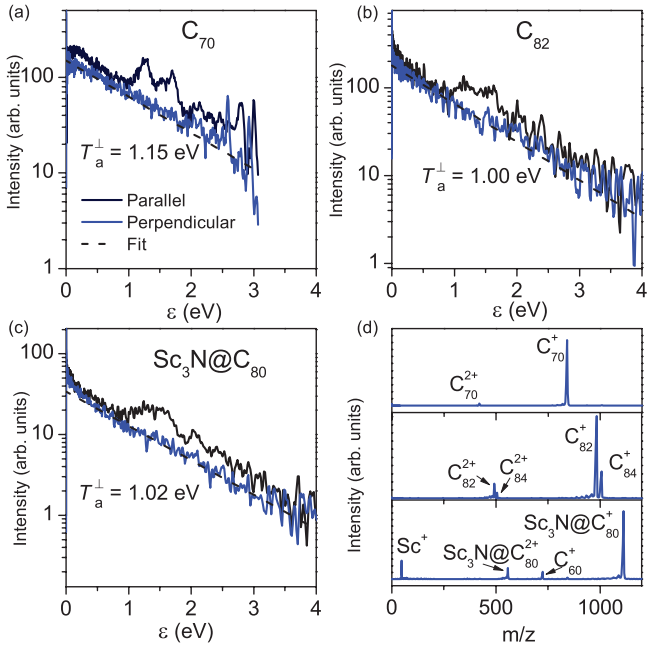

FIG. 3. PES along and perpendicular to the laser polarisation direction obtained after 400 nm, 120 fs for (a) C_{70}, 6.4 TW cm^{-2}; (b) C_{82}, 6.3 TW cm^{-2}; and (c) $Sc_3N@C_{80}$, 8.4 TW cm^{-2}. The spectrum in (a) was obtained under slightly different VMI extraction conditions to what is normally used and so the spectrum is only reliable up to ca. 2.5 eV. The corresponding mass spectra are presented in (d).

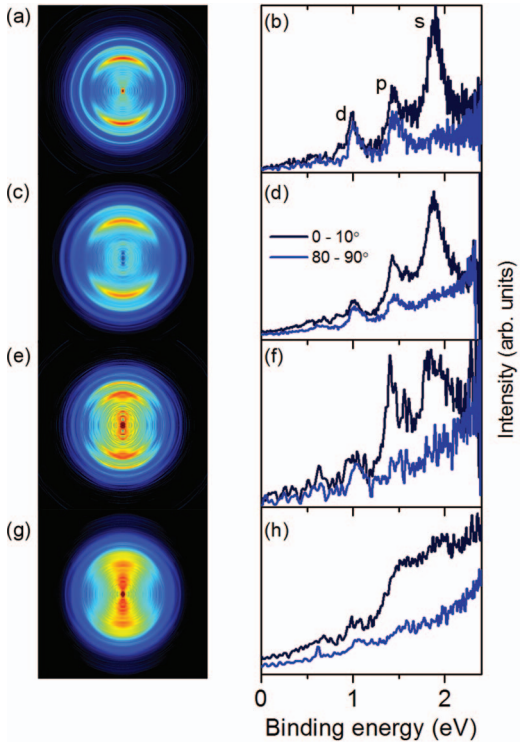

FIG. 4. Inverted VMI images and angle-resolved PES parallel and perpendicular to the laser polarization direction for [(a) and (b)] C_{60} excited with 500 nm, 4.7 TW cm^{-2}; [(c) and (d)] C_{70} excited with 520 nm, 2.9 TW cm^{-2}; [(e) and (f)] C_{82} excited with 519 nm, 2.8 TW cm^{-2}; and [(g) and (h)] $Sc_3N@C_{80}$ excited with 506 nm, 4.1 TW cm^{-2}.

T_a (k_B is Boltzmann's constant).[1,19] Angular-resolved PES, together with the corresponding mass spectra, obtained for C_{70}, C_{82}, and $Sc_3N@C_{80}$ after 120 fs, 400 nm excitation are presented in Figure 3. The spectra can, just as shown previously in the case of C_{60} and C_{70},[10] be fitted to an exponential distribution for all wavelengths studied, indicating a thermal ionization mechanism. The fitted apparent temperatures perpendicular to the laser polarization direction ($T_a^{\perp}$) are similar for all molecules, verifying the thermal nature of the electron signal, since the temperature should only be weakly dependent on the excitation spectrum of each molecule. The C_{70} temperatures are higher than for the other molecules studied here but that can be expected, since fewer electrons result in a lower heat capacity, which in turn results in higher apparent temperatures for similar excitation intensities, as is the case for C_{60}/C_{70}.[10] The results provide further evidence that efficient redistribution of excitation energy leading to thermal electron emission is a dominant ionization mechanism in fullerenes after fs laser excitation. Interestingly, this has also been shown to be the case for polycyclic aromatic hydrocarbons (PAHs),[20] which demonstrates that rapid electron thermalization occurs in a large range of organic molecules and carbon nanomaterials.

B. Identification of SAMOs

To assign the peaks observed superimposed on the thermal background in Figure 3, it is useful to compare to C_{60}, since angular-resolved photoelectron spectroscopy has been successful in identifying excited states due to the high symmetry of this molecule, leading to an almost atomic-like behaviour of the PADs with clear signatures of s- and p-states.[4] Therefore, an inverted VMI image and the corresponding angular-resolved PES parallel and perpendicular to the laser polarization direction are shown in Figures 4(a) and 4(b) for C_{60} after 500 nm, 4.7 TW cm^{-2} laser excitation. Three peaks clearly stand out and are labelled according to the assignment made in Refs. 4 and 5, namely, s-, p-, and d-states. The rich peak structure converging on the ionization energy,[3] corresponding to higher-lying states, is not resolved in this particular spectrum as the peaks become more densely spaced and the spectrometer resolution decreases with increasing kinetic energy (corresponding to decreasing binding energy in Figure 4). The Rydberg/SAMO states have orders of magnitude higher photoionization rates (of the order of 10^{14} s^{-1}) than those of the more localized valence states (with ionization rates of the order of 10^{10} s^{-1}), and will therefore ionize much more efficiently during the ca. 100 fs laser pulse, which is the reason why these particular states are observed in the fs PES.[5] The large overlap between the neutral and ionic states implies that the vibrational energy is conserved upon ionization, in analogy with Rydberg fingerprint spectroscopy,[21] which produces clear peak structure despite the high vibrational temperature at which the molecules are typically prepared experimentally. The peak structure is independent of wavelength and intensity, as is the case for the "fingerprint spectra" presented in this work. In Rydberg fingerprint spectroscopy, a highly excited state is initially populated and through internal conversion (IC), a large range of states is subsequently populated.[21–23] As soon as a SAMO/Rydberg state

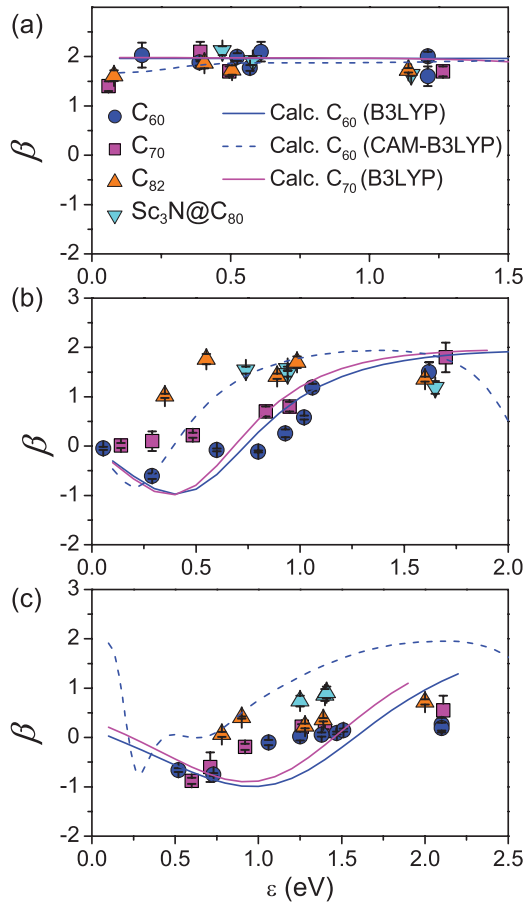

FIG. 5. Photoelectron angular distributions (PADs) for (a) s-states, (b) p-states, and (c) d-states, characterised by the fitted β value for the range of molecules studied. The lines show the calculated β-values for C_{60} and C_{70} at the TD-DFT/B3LYP/6-31+G(d) level for a randomly oriented sample (see Sec. II). The C_{60} CAM-B3LYP results from Ref. 5 are shown for comparison. Please note the difference in scale for the x-axes.

is populated through various IC processes, it will ionize due to the high ionization rate. For fullerenes in the laser interaction zone where SAMO/Rydberg states are not populated on the timescale of the laser pulse, the excited valence states do not photoionize due to the vanishingly small ionization rate, and will therefore contribute to the rapid heating of the molecules which eventually leads to hot electron production and subsequent thermal electron emission.[5]

The PADs for the three peaks, extracted from the angular dependent peak intensities, can be fitted according to Eq. (1) allowing the β-values to be extracted. The kinetic-energy dependent β-values, measured for a range of different wavelengths, are plotted in Figure 5 for the s, p, and d states. The s-state is clearly identified since $\beta \approx 2$ for all kinetic energies. The β-values for the p-state show a characteristic behaviour similar to what is calculated for the p-SAMO state.[4,5]

In Ref. 4, results for C_{70} were presented for one wavelength (400 nm). Here, we have repeated these measurements and also extended the wavelength range. The measured VMI and PES for C_{70} are very similar to C_{60} for all wavelengths measured, as shown in Figures 4(c) and 4(d) for 520 nm excitation. We have therefore assigned the three prominent peaks as s-, p-, and d-states in C_{70} as well. The binding energies are slightly lower for C_{70}, as shown in Table II. The TD-DFT computations show SAMO states in C_{70} with binding energies close to what was found for C_{60} in agreement with experiments (see Sec. II). Due to the lower symmetry of C_{70}, the calculated p-state is split into a p_z state and two degenerate p_x and p_y states. The PADs extracted from the angle-resolved PES are also similar to those of C_{60}, as seen in Figure 5. In particular, the s-state shows $\beta \approx 2$ independent of kinetic energy, which provides further support for this assignment. However, β-values for the p-state are slightly larger than for C_{60}. The calculated PADs are in reasonable agreement with the experimental values (Figure 5).

TABLE II. Summary of experimental and computed (see Sec. II) binding energies of the lowest-lying Rydberg states of the fullerenes studied.

		s-state E_{bind} (eV)	p-state E_{bind} (eV)	d-state E_{bind} (eV)
C_{60}	Expt.	1.90(1)	1.47(2)	1.02(1)
	Calc.	2.14	1.26	0.77
C_{70}	Expt.	1.86(2)	1.42(2)	0.99(3)
	Calc.	2.20	1.19–1.24	0.73–0.79
C_{82}	Expt.	1.90(4)	1.42(5)	1.03(3)
C_{84}	Calc.	2.12	1.22–1.28	0.72–0.83
$Sc_3N@C_{80}$	Expt.	1.94(5)	1.50(4)	1.04(2)

A similar set of peaks for C_{82} is observed at the same binding energies as for C_{60}, although less pronounced compared to the thermal electron background (Figures 4(e) and 4(f)). Based on the binding energies and PADs, in particular for the s-state (Figure 5), it is reasonable to assign the same set of peaks to s, p, and d states of C_{82}. Zhao *et al.* reported that the s-SAMO binding energy in C_{82} is 0.2 eV higher than in C_{60}.[7] By contrast, computations performed by us have identified SAMO-like electronic states in C_{84} at very similar energies to C_{60} and it is therefore natural to assume that the same is true for C_{82} since electronic states (TD-DFT) are more relevant than molecular orbitals (DFT) in laser spectroscopy experiments. Similarly to the difference between C_{60} and C_{70}, we observe that the PAD for the p-state of C_{82} is slightly different from that of C_{60} and C_{70}.

In our experiments on $Sc_3N@C_{80}$, bands with maxima corresponding to the peak positions observed for the other fullerenes are just discernible, as shown in Figures 4(g) and 4(h). The β-values, in particular for the s-band, are consistent with those for the other fullerenes. We have therefore assigned the peaks/bands in the spectra to the same states that are observed in the other fullerenes studied. DFT computations of $Sc_3N@C_{80}$ indicate the presence of SAMO-like orbitals with an approximate binding energy of 0.5 eV,[8] in contrast to what we present here. Similarly to C_{70} and C_{82}, the β-values for the p-band are different from C_{60} and appear to be higher and peak at a lower kinetic energy for the larger, less symmetric molecules. The difference in molecular structure is obviously not large enough to significantly influence the binding energy (Table II), however, PADs are very sensitive to small changes to the molecular potential, which could explain the difference in the PADs. Also, electron-electron correlations between the

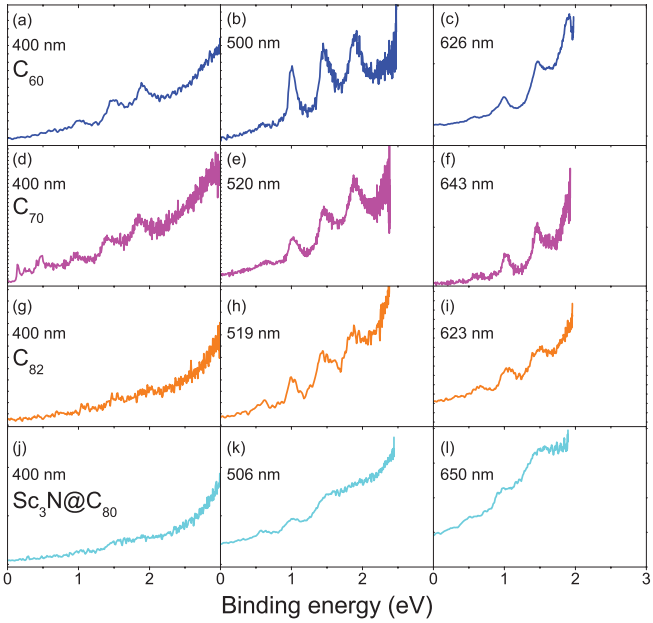

FIG. 6. Angle-integrated PES for a series of wavelength regions. Molecules and wavelengths are indicated in the figure.

outgoing electron and the residual electrons can influence the β-values, however, $\beta \approx 2$ for the s-states indicates that this is not a significant contribution for these states.

C. Angle-integrated PES

More insights are gained by comparing the angle-integrated PES, since angle-resolved spectra along a certain direction can either show a large or small contribution from a given peak depending on the β-value. Angle-integrated spectra for three typical wavelength regions are shown in Figure 6. There is a slight spread in the wavelength due to experimental conditions, however, the spectra in each region are typically very similar. As previously mentioned, the peak structure becomes less pronounced with decreasing molecular symmetry and increasing size. The underlying thermal background signal is more dominant for the larger molecules, as expected for larger particles, which will show more bulk-like properties. The binding energy does not change considerably (Table II) and it can be concluded that the binding energies of the states are not largely influenced by details of the molecular structure. This is in agreement with Rydberg Fingerprint spectroscopy that does not show a large change in binding energy of similar molecular species. This is also supported by the TD-DFT computations that do not predict a larger energy difference than what is observed experimentally.[4,5]

IV. CONCLUSIONS

In conclusion, we have presented results obtained using a combination of velocity-map imaging and Rydberg fingerprint spectroscopy to study diffuse, excited electronic states of C_{70}, C_{82}, and $Sc_3N@C_{80}$. Due to the similarity to C_{60} spectra, and, in particular, PADs characterised by $\beta \approx 2$, we have been able to assign peaks in the spectra to s-, p- and d-states. We observe an increasing thermal-to-Rydberg ratio in the spectra for increasing molecular size and complexity (but lower symmetry).

We have shown that the Rydberg fingerprint experimental technique combined with PADs has the possibility to identify potentially important diffuse states in carbon nanomaterials and complex organic molecules. The technique can also be used for probing the interplay between direct and thermal ionization and may provide important insights to help understand the electron dynamics of molecules of relevance to applications such as acceptor molecules in organic solar cells.

ACKNOWLEDGMENTS

J.O.J., E.B., and E.E.B.C. gratefully acknowledge financial support from the Leverhulme Foundation (RPF-298 "PES of hollow nanomaterials") and fruitful discussions with T. Ridley. F.R. and B.M. acknowledge support from the Fonds de la Recherche Fondamentale Collective FRFC 2.4545.12. F.R. is a Director of Research and B.M. is a PhD fellow of Fonds National de la Recherche Scientifique (FNRS, Belgium).

[1] J. O. Johansson and E. E. B. Campbell, Chem. Soc. Rev. **42**, 5661 (2013).
[2] E. E. B. Campbell, K. Hansen, K. Hoffmann, G. Korn, M. Tchaplyguine, M. Wittmann, and I. V. Hertel, Phys. Rev. Lett. **84**, 2128 (2000).
[3] M. Boyle, K. Hoffmann, C. P. Schulz, I. V. Hertel, R. D. Levine, and E. E. B. Campbell, Phys. Rev. Lett. **87**, 273401 (2001).
[4] J. O. Johansson, G. Henderson, F. Remacle, and E. E. B. Campbell, Phys. Rev. Lett. **108**, 173401 (2012).
[5] B. Mignolet, O. Johansson, E. E. B. Campbell, and F. Remacle, "Probing rapidly-ionizing super-atom molecular orbitals in C60: A computational and femtosecond photoelectron spectroscopy study," ChemPhysChem (in press).
[6] M. Feng, J. Zhao, and H. Petek, Science **320**, 359–362 (2008).
[7] J. Zhao, M. Feng, J. Yang, and H. Petek, ACS Nano **3**, 853–864 (2009).
[8] T. Huang, J. Zhao, M. Feng, H. Petek, S. Yang, and L. Dunsch, Phys. Rev. B **81**, 085434 (2010).
[9] G. Grancini, M. Maiuri, D. Fazzi, A. Petrozza, H.-J. Egelhaaf, D. Brida, G. Cerullo, and G. Lanzani, Nature Mater. **12**, 29–33 (2012).
[10] M. Kjellberg, O. Johansson, F. Jonsson, A. V. Bulgakov, C. Bordas, E. E. B. Campbell, and K. Hansen, Phys. Rev. A **81**, 023202 (2010).
[11] C. Bordas, F. Paulig, H. Helm, and D. L. Huestis, Rev. Sci. Instrum. **67**, 2257–2268 (1996).
[12] G. M. Roberts, J. L. Nixon, J. Lecointre, E. Wrede, and J. R. R. Verlet, Rev. Sci. Instrum. **80**, 053104 (2009).
[13] J. O. Johansson, J. Fedor, M. Goto, M. Kjellberg, J. Stenfalk, G. Henderson, E. E. B. Campbell, and K. Hansen, J. Chem. Phys. **136**, 164301 (2012).
[14] M. Tchaplyguine, K. Hoffmann, O. Duhr, H. Hohmann, G. Korn, H. Rottke, M. Wittmann, I. V. Hertel, and E. E. B. Campbell, J. Chem. Phys. **112**, 2781–2789 (2000).
[15] J. Cooper and R. N. Zare, J. Chem. Phys. **48**, 942–943 (1968).
[16] K. L. Reid, Annu. Rev. Phys. Chem. **54**, 397–424 (2003).
[17] M. J. Frisch, G. W. Trucks, H. B. Schlegel *et al.*, GAUSSIAN 09, Revision A.1, Gaussian, Inc., Wallingford, CT, 2009.
[18] A. Lassesson, K. Hansen, M. Joensson, A. Gromov, E. E. B. Campbell, M. Boyle, D. Pop, C. P. Schulz, I. V. Hertel, A. Taninaka, and H. Shinohara, Eur. Phys. J. D **34**, 205–209 (2005).
[19] K. Hansen, K. Hoffmann, and E. E. B. Campbell, J. Chem. Phys. **119**, 2513–2522 (2003).
[20] M. Kjellberg, A. V. Bulgakov, M. Goto, O. Johansson, and K. Hansen, J. Chem. Phys. **133**, 074308 (2010).
[21] J. L. Gosselin and P. M. Weber, J. Phys. Chem. A **109**, 4899–904 (2005).
[22] V. Blanchet, K. Raffael, G. Turri, B. Chatel, B. Girard, I. A. Garcia, I. Wilkinson, and B. J. Whitaker, J. Chem. Phys. **128**, 164318 (2008).
[23] P. Piecuch, J. A. Hansen, D. Staedter, S. Faure, and V. Blanchet, J. Chem. Phys. **138**, 201102 (2013).

THE JOURNAL OF PHYSICAL CHEMISTRY A

Article

pubs.acs.org/JPCA

Relative Photoionization Cross Sections of Super-Atom Molecular Orbitals (SAMOs) in C_{60}

Elvira Bohl,[†] Katarzyna P. Sokół,[†,§] Benoit Mignolet,[‡] James O. F. Thompson,[†] J. Olof Johansson,[†] Francoise Remacle,[‡] and Eleanor E. B. Campbell*[,†,∥]

[†]EaStCHEM, School of Chemistry, University of Edinburgh, Edinburgh EH9 3FJ, U.K.

[‡]Department of Chemistry, B6c, University of Liège, B4000, Liège, Belgium

Supporting Information

ABSTRACT: The electronic structure and photoinduced dynamics of fullerenes, especially C_{60}, is of great interest because these molecules are model systems for more complex molecules and nanomaterials. In this work we have used Rydberg Fingerprint Spectroscopy to determine the relative ionization intensities from excited SAMO (Rydberg-like) states in C_{60} as a function of laser wavelength. The relative ionization intensities are then compared to the ratio of the photoionization widths of the Rydberg-like states, computed in time-dependent density functional theory (TD-DFT). The agreement is remarkably good when the same photon order is required to energetically access the excited states. This illustrates the predictive potential of quantum chemistry for studying photoionization of large, complex molecules as well as confirming the assumption that is often made concerning the multiphoton excitation and rapid energy redistribution in the fullerenes.

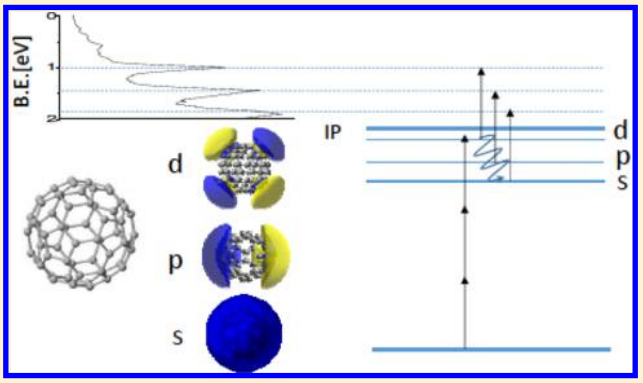

INTRODUCTION

Gas phase photoelectron spectroscopy provides a powerful tool to probe in detail the fundamental electronic structure and photoinduced dynamical properties of isolated molecules.[1] The advent of new light sources such as tunable ultrafast laser systems or Free Electron Lasers is providing ever more advanced possibilities for experimentally probing photoinduced electron dynamics on increasingly complex systems.[2] For planning and reliably interpreting the results of such advanced experiments, it is essential to develop theoretical methods that are able to accurately predict the outcome so that we understand the nuances and fundamental factors involved in taking such a measurement. This work focuses upon the comparison of experimental measurements and theoretical predictions of photoionization cross sections from excited electronic states of a complex molecule, C_{60}. It has recently been suggested that there could be significant challenges in interpreting femtosecond photoionization experiments as the detection sensitivity could significantly depend on changes in the photoionization cross-section as the system evolves.[3] Fullerenes are interesting model systems to help develop both the new experimental possibilities and the associated theoretical techniques. The high symmetry of C_{60}, making it accessible for high level theoretical investigation, combined with its interesting electronic properties and ease of experimental handling,[4] provides an attractive but challenging subject for study.

In earlier studies it has been shown that one-color femtosecond photoelectron spectra of gas phase fullerenes typically show 3 or 4 prominent peaks corresponding to binding energies in the range 1−2 eV, superimposed on a thermal electron background.[5−7] Theoretical photoionization angular distributions of a band of 500 neutral excited states computed in TD-DFT confirmed that the peaks observed in the photoelectron spectra are due to single photon ionization from excited "SAMO" (super-atom molecular orbital) states.[6,8] The SAMO states are singly excited states where an electron is (indirectly) promoted from the highest occupied molecular orbital (HOMO) to a "SAMO" s, p, or d orbital. The SAMOs in fullerenes were first identified in low-temperature scanning tunnelling spectroscopy studies of C_{60} on a copper surface and described as diffuse Rydberg-like orbitals with the charge distribution centered on the center of the hollow carbon cage.[9] They can be considered as low-lying mixed Rydberg/valence states with a dominant Rydberg contribution[10] and significant charge density within the cage.[8] The high symmetry and hollow character of C_{60} leads to the beautiful and simple atomic nature of the Dyson orbitals of the SAMO states, shown in Figure 1, and a correspondingly distinct photoelectron angular distribution for the s-orbitals.[8] The Dyson orbitals are one-particle orbitals computed as the overlap between the neutral and

Received: October 21, 2015
Revised: November 5, 2015
Published: November 9, 2015

DOI: 10.1021/acs.jpca.5b10339
J. Phys. Chem. A 2015, 119, 11504−11508

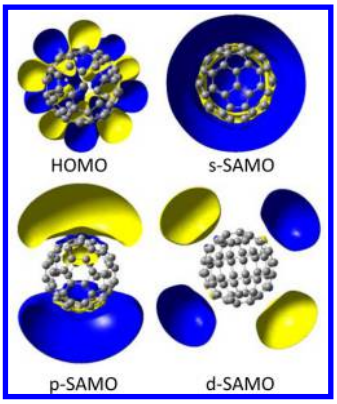

Figure 1. Cuts in the isocontour amplitudes ($0.002|el/a_0^3$) of the HOMO and Dyson orbitals of the s, p, and d SAMO states of C_{60}. The electronic structure of the 500 lowest excited states was computed at the TD-DFT/CAM-B3LYP/6-31(+)G(d)-Bq(6-31(6+)G(d)) level. Computational details are given in ref 8.

cation many-electron wave functions and represent the probability amplitude of the electron that is ionized.[8,11] They are used to calculate photoionization intensities and photoelectron angular distributions, as described in detail for C_{60} in an earlier publication.[8] For C_{60} the SAMO Dyson orbitals are very similar to the SAMO molecular orbitals.

The prominence of the SAMO peaks and the development of the thermal background in the photoelectron spectra[4] was attributed to the much larger photoionization widths (orders of magnitude larger than for the valence states) that were predicted for the SAMO states for the low photon energies used in the experiments.[8] These large photoionization widths are consistent with the recent observation of the correlation between photoionization cross-section and polarizability volume for a range of organic molecules.[3] The predicted photoionization widths for the fullerene SAMOs corresponded to ionization lifetimes on the order of 10 fs whereas the ionization lifetimes of non-SAMO states (including the valence states) were predicted to be on the order of picoseconds−nanoseconds and thus considerably longer than the laser pulse duration.[8]

In the work presented here, we report photoelectron spectra obtained for a wider range of laser wavelengths than previously reported. We determine the relative photoionization intensities from the SAMO states as a function of laser wavelength and compare them to calculations of the photoionization widths (proportional to the photoionization cross sections) using the TD-DFT approach described previously.[8] This provides an additional stringent test of the theoretical calculations and the very good agreement between experiment and theory illustrates the predictive detail that can be captured for complex polyatomic systems. In addition, the results provide strong support for the very rapid energy redistribution within fullerenes that is often invoked to interpret experimental results.[12]

EXPERIMENTAL AND THEORETICAL METHODS

Photoelectron spectra were obtained using a velocity map imaging spectrometer based on the design of Parker and coworkers.[13] The experimental apparatus has been described in more detail previously.[4,14] C_{60} (99.95% purity, SES Research) was introduced into the vacuum chamber as an effusive molecular beam produced by heating the sample in an oven to ∼500 °C.

A regenerative amplified Ti:sapphire laser system (800 nm fundamental output, pulse 110 fs duration) was used to pump a commercial noncollinear optical parametric amplifier (NOPA) providing a tunable light source in the visible range. The pulse durations were sub-100 fs at the interaction region and wavelength dependent. Data provided in the Supporting Information show that the pulse duration does not significantly influence the results in the range accessed in these experiments (ca. 30−90 fs, Figure S2 and S3). For experiments involving 800 or 400 nm light, the NOPA was bypassed, and the 800 nm light was frequency doubled using a 0.5 mm thick BBO crystal cut at 29°. The laser intensity and polarization were controlled using a combination of a half-wave plate and a Glan-laser polarizer and focused into the chamber using a 30 cm focal length, fused silica lens. The laser intensity was chosen for each wavelength to provide a good signal-to-noise ratio in the photoelectron spectra while ensuring that fragmentation and double ionization peaks were of negligible intensity in the corresponding mass spectra. It was typically within the range $10^{11}-10^{12}$ Wcm^{-2}.

The laser intersects the effusive molecular beam at right angles and the photoelectrons are extracted using a set of electrostatic lenses and detected using an integrated 40 mm dual MCP/Phosphor detector (Photonis, ADP 3040FM 12/10/8 60:1). The image is recorded using a CCD camera (AVT, Stingray Model F146B), controlled via a LabVIEW program. The recorded images were centroided[15] and integrated for 10^6-10^7 laser shots. Once recorded, the images were inverted using a POP inversion algorithm,[16] which was modified to include Legendre polynomials up to the 10th order. The conversion from velocity to energy was calibrated using the well-known peaks from multiphoton ionization via Freeman-type resonances in Xe.[17]

The peaks in the photoelectron spectra were fitted using Lorentzian functions (with 2 functions with small energy separations used to get an optimum fit for the p- and d-SAMO bands, in agreement with the slight splitting of these bands observed in the calculations).[8] The binding energies and peak widths were not changed for fitting the spectra obtained for different laser wavelengths, only the relative intensities. The error bars indicate the uncertainty in both the subtraction of the thermal background and the Lorentzian peak fits.

The details of the theoretical calculations have been presented in a previous publication.[8] Briefly, the electronic structure of the 500 lowest excited states of neutral C_{60} was computed at the TD-DFT/CAM-B3LYP/6-31(+)G(d)-Bq(6-31(6+)G(d)) level. The binding energies of the first s, p, and d and second s band of SAMO states as well as the predicted photoelectron angular distributions were shown previously to be in good agreement with the experimental values.[8] In the photoionization process, the Dyson orbital represents the probability amplitude of the electron that is ionized. The calculated photoionization width is the square modulus of the dipole coupling between the Dyson orbital, ϕ_I^{Dyson}, and the outgoing plane wave, ε_Ω, integrated over the emission angle of the ejected electron, Ω, and multiplied by the density of plane waves at the energy of the emitted electron $\rho(\varepsilon)$.

$$\Gamma_I(\varepsilon) = \rho(\varepsilon) \int d\Omega \, |\langle \varepsilon_\Omega | - \mathbf{E}\cdot\mathbf{r} | \phi_I^{Dyson} \rangle|^2 \quad (1)$$

DOI: 10.1021/acs.jpca.5b10339
J. Phys. Chem. A 2015, 119, 11504−11508

The photoionization widths between the electronic states and the ground state of the cation (5-fold degenerate) were computed using a basis of orthogonalized plane waves to describe the wave function of the ionized electron. The photoionization width was computed for each state taking into account the random orientation of the C_{60} molecule with respect to the electric field. An electric field of 4.7×10^6 V cm^{-1} was used for the calculations, corresponding to a laser intensity of 3×10^{11} W cm^{-2}, similar to the values used in the experiments. Detailed information on the theoretical methodology is available in ref 8. Note that the ionization width, Γ, is proportional to the photoionization rate and directly related to the photoionization cross-section. It does not refer to the width of the peaks in the experimental photoelectron spectra.

To compare the experimental results with the theoretical predictions, we calculated the ratios of the experimental SAMO peaks for a given laser wavelength and compared them to the calculated ratios of the photoionization widths for the corresponding SAMOs at the appropriate electron kinetic energies. Because we are comparing ratios, the laser electric field term cancels and we can compare data sets taken at different laser intensities. Systematic studies of the influence of fluctuations in experimental parameters, such as laser pulse duration, laser intensity and fullerene oven temperature, were carried out to check that these do not influence the value of the determined intensity ratios. These studies are documented in the Supporting Information.

RESULTS AND DISCUSSION

The experimental photoelectron spectra, Figure 2 and Supporting Information Figure S1, show the presence of peaks corresponding to ionization from the SAMO states independent of the excitation wavelength, as is typical for Rydberg Fingerprint Spectroscopy.[18] The excitation mechanism is not fully understood but it must involve multiphoton excitation and efficient coupling to a wide range of energetically accessible states. The SAMOs will be preferentially ionized on the time scale of the laser excitation,[8] for reasons discussed above, and because their potential energy surface will be similar to that of the cation, the ionization transition is expected to conserve vibrational energy, thus leading to a peak in the spectrum corresponding to the electronic binding energy of the SAMO. If sufficient energy has been absorbed by the valence electrons, the molecule may thermally ionize instead of undergoing direct photoionization, leading to the thermal background that is observed in the spectra (Supporting Information), before the electronic excitation has time to couple significantly to vibrational degrees of freedom.[14]

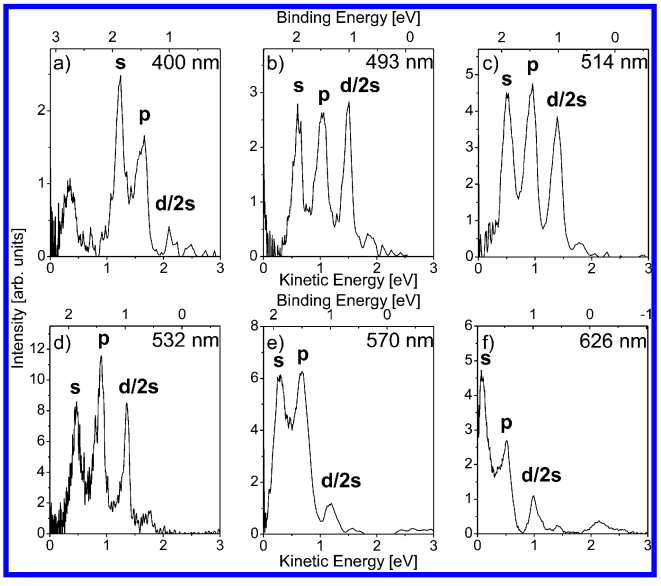

Figure 2. One-color femtosecond photoelectron spectra of C_{60} at selected wavelengths after thermal electron background subtraction. The spectra are plotted in terms of both electron kinetic energy (lower axis) and electron binding energy (upper axis). The binding energy is defined as the difference between the photon energy and the photoelectron kinetic energy. Peaks corresponding to ionization from the s, p, and d/2s SAMOs are marked.

Representative examples of the photoelectron spectra are shown in Figure 2. The full set of spectra, prior to subtraction of the thermal background are provided in Figure S1. The peaks were identified as arising from SAMOs in an earlier publication by comparing theoretical binding energies and photoelectron angular distributions with experimental photoelectron spectra.[6] The peaks appear at identical electron binding energies (upper *x*-axes) for all investigated laser wavelengths. The prominent peak with a binding energy of ca. 1.9 eV corresponds to the first s-SAMO band, the next peak corresponds to the first p-SAMO band (binding energy ca. 1.5 eV) and the following peak to a combination of the first d-SAMO band and second s-SAMO band that cannot be clearly distinguished in these angle-integrated spectra (binding energies of ca. 1 and 0.9 eV, respectively).[6]

In Figure 3, the calculated photoionization widths of the lowest SAMO states are plotted as a function of photoelectron kinetic energy. The photoionization width (rate) decreases strongly as the photoelectron kinetic energy increases up to a photoelectron kinetic energy of 2 eV, in contrast to the calculations for the non-SAMO states[8] (not shown) that show an increasing photoionization width (starting from a much lower value), in agreement with identified trends found in absolute photoionization cross-section measurements for different molecular systems.[19−22] The ionization widths (rates) are predicted to be similar for the SAMO and non-SAMO states for photoelectron energies beyond 2.5 eV, converging to a value of ≤0.01 eV.[8] However, this corresponds to a photoionization lifetime that is greater than 300 fs, significantly longer than the laser pulse duration, and one would not expect to see clear peak

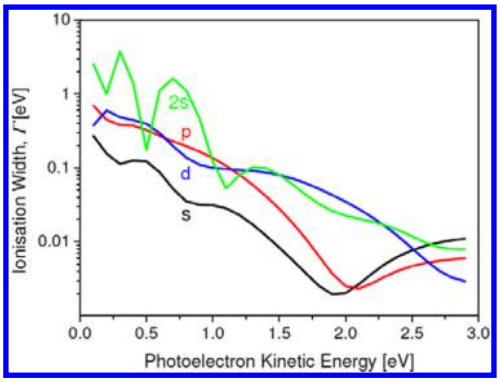

Figure 3. Calculated photoionization widths as a function of photoelectron kinetic energy for the lowest-lying SAMO states (black = s, red = p, blue = d, green =2s) using TD-DFT. For more details of the theoretical methods see ref 8.

DOI: 10.1021/acs.jpca.5b10339
J. Phys. Chem. A 2015, 119, 11504−11508

structure in the spectra, in agreement with the experimental results in Figures 2 and S1.

We are unable to determine absolute photoionization cross sections in the experiment. However, the ratio of the SAMO intensities can be used to compare with the corresponding ratios of the calculated photoionization widths for each value of the photon energy. Note that the photoelectron kinetic energies are different for ionization from the different SAMO states in each experiment (carried out with a fixed photon energy).

Figure 4 shows the results of this comparison of the measured ratios with the predicted ratios of the s to p and s to d

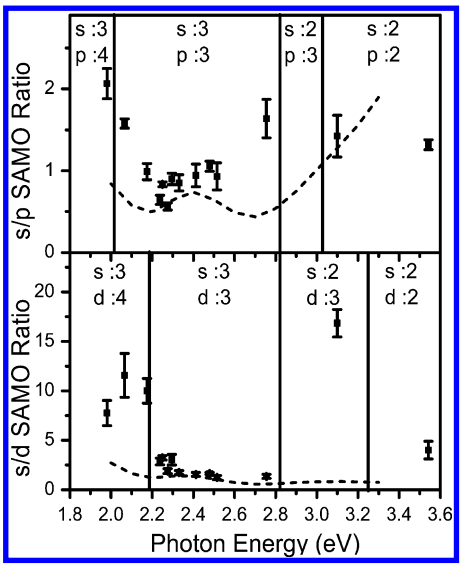

Figure 4. Comparison of relative experimental SAMO peak intensities (squares) and the theoretical photoionization width ratios of SAMO states plotted as a function of laser photon energy. Upper panel: ratio of the s and p peak intensities. Lower panel: ratio of the s and d peak intensities. Theoretical values shown by dashed lines (ratio of average values calculated for each band).[8] The numbers at the top of the plots indicate the number of photons needed to access the s and the p or d SAMO states, respectively (not taking into consideration the substantial amount of vibrational energy that is present in the hot fullerenes from the oven).

SAMO intensities, computed as the ratio of the ionization widths of the SAMO states.[8] There is a clear correlation between the predicted trend and the experimentally measured results within the regions where the excited states can be accessed by the *same number of photons*. Outside these regions, the s-band can be accessed by one less photon than the higher states. In this case the s-band intensity would be expected to be significantly higher than the higher-lying states and the measured ratios are correspondingly higher. This subtlety is not predicted by the calculations because they do not include the population mechanism but simply assume that all states are populated with the same probability. The results are quite remarkable in that they are implying that this assumption (at least for the SAMO population) does hold as long as the photon order needed to energetically access the states is the same. What is apparent is that these calculations are, with surprisingly good accuracy, able to predict the photoionization probability in addition to the photoelectron angular distribution as a function of kinetic energy as shown earlier.[8]

The experimental ratios for the d and 2s SAMO peaks do not agree so well with the calculations (Figure S8). These states have similar binding energies and thus would be accessed by the same number of photons throughout the range investigated. Here, the experimentally determined d-peak intensity is considerably larger than the 2s whereas the calculations predict very similar intensities for these two peaks. It should also be noted, however, that the d and 2s peaks are very difficult to distinguish in the experimental spectra and also that the calculations indicate strong oscillations in the 2s photoionization width (Figure 3). The assignment of the 2s peak is based on the determined angular distribution.[6]

CONCLUSION

The femtosecond photoelectron spectra of C_{60} have been reported for different laser wavelengths. The experimentally determined intensity ratios of the s, p, and d SAMO features in the spectra can be reproduced by taking the ratios of the photoionization widths, predicted using TD-DFT. The success of this theory at predicting the ionization properties of a system that is as large and complex as a fullerene is remarkable and provides confidence in the predictive potential of quantum chemistry techniques for probing the electronic dynamics of complex molecular systems.

ASSOCIATED CONTENT

Supporting Information

The Supporting Information is available free of charge on the ACS Publications website at DOI: 10.1021/acs.jpca.5b10339.

Additional content providing all photoelectron spectra used for the analysis prior to subtraction of the thermal background contribution, test of relative SAMO photoionization peak intensities as a function of various experimental parameters (laser pulse duration, oven temperature, laser pulse intensity) and the comparison of the experimental peak intensity and theoretical photoionization width ratios for the d and 2s SAMOs (PDF)

AUTHOR INFORMATION

Corresponding Author

*E. E. B. Campbell: e-mail, Eleanor.Campbell@ed.ac.uk; tel, 0044131 650 4729.

Present Addresses

[§]Department of Chemistry, University of Cambridge, Lensfield Road, Cambridge CB2 1EW, U.K.

[‖]Also at: Division of Quantum Phases and Devices, School of Physics, Konkuk University, 143-701 Seoul, Korea.

Notes

The authors declare no competing financial interest.

ACKNOWLEDGMENTS

E.B, K.P.S, J.O.F.T, J.O.J., and E.E.B.C. gratefully acknowledge financial support from the Leverhulme Trust (RPF-298 "PES of hollow nanomaterials"). J.O.J. is a Royal Society of Edinburgh/BP Trust Research Fellow and acknowledges financial support from the RSE. The work of F.R. and B.M. was supported by FRFC (Fonds National de la Recherche Collective) 2.4545. B.M. is a Post-Doctoral Fellow (Charge de recherches) of Fonds National de la Recherche Scientifique (FNRS Belgium). F.R. thanks FNRS for its support.

DOI: 10.1021/acs.jpca.5b10339
J. Phys. Chem. A 2015, 119, 11504−11508

REFERENCES

(1) Suzuki, T. Femtosecond Time-Resolved Photoelectron Imaging. *Annu. Rev. Phys. Chem.* **2006**, *57*, 555−592.

(2) Chergui, M. Emerging Photon Technologies for Chemical Dynamics. *Faraday Discuss.* **2014**, *171*, 11−40.

(3) Thompson, J. O. F.; Saalbach, L.; Crane, S. W.; Paterson, M. J.; Townsend, D. Ultraviolet Relaxation Dynamics of Aniline, N, N-Dimethylaniline and 3,5-Dimethylaniline at 250 nm. *J. Chem. Phys.* **2015**, *142*, 114309.

(4) Johansson, J. O.; Campbell, E. E. B. Probing Excited Electronic States and Ionisation Mechanisms of Fullerenes. *Chem. Soc. Rev.* **2013**, *42*, 5661−5671.

(5) Boyle, M.; Hoffmann, K.; Schulz, C. P.; Hertel, I. V.; Levine, R. D.; Campbell, E. E. B. Excitation of Rydberg Series in C_{60}. *Phys. Rev. Lett.* **2001**, *87*, 273401.

(6) Johansson, J. O.; Henderson, G. G.; Remacle, F.; Campbell, E. E. B. Angular-Resolved Photoelectron Spectroscopy of Superatom Orbitals of Fullerenes. *Phys. Rev. Lett.* **2012**, *108*, 173401.

(7) Johansson, J. O.; Bohl, E.; Henderson, G. G.; Mignolet, B.; Dennis, T. J. S.; Remacle, F.; Campbell, E. E. B. Hot Electron Production and Diffuse Excited States in C_{70}, C_{82}, and $Sc_3N@C_{80}$ Characterized by Angular-Resolved Photoelectron Spectroscopy. *J. Chem. Phys.* **2013**, *139*, 084309.

(8) Mignolet, B.; Johansson, J. O.; Campbell, E. E. B.; Remacle, F. Probing Rapidly-Ionizing Super-Atom Molecular Orbitals in C_{60}: A Computational and Femtosecond Photoelectron Spectroscopy Study. *ChemPhysChem* **2013**, *14*, 3332−3340.

(9) Feng, M.; Zhao, J.; Petek, H. Atomlike, Hollow-Core-Bound Molecular Orbitals of C_{60}. *Science* **2008**, *320*, 359−362.

(10) Reisler, H.; Krylov, A. I. Interacting Rydberg and Valence States in Radicals and Molecules: Experimental and Theoretical Studies. *Int. Rev. Phys. Chem.* **2009**, *28*, 267−308.

(11) Dauth, M.; Wiessner, M.; Feyer, V.; Schöll, A.; Puschnig, P.; Reinert, F.; Kümmel, S. Angle Resolved Photoemission from Organic Semiconductors: Orbital Imaging Beyond the Molecular Orbital Interpretation. *New J. Phys.* **2014**, *16*, 103005.

(12) Hansen, K.; Hoffmann, K.; Campbell, E. E. B. Thermal Electron Emission from the Hot Electronic Subsystem of Vibrationally Cold C_{60}. *J. Chem. Phys.* **2003**, *119*, 2513−2522.

(13) Eppink, A. T. J. B.; Parker, D. H. Velocity Map Imaging of Ions and Electrons Using Electrostatic Lenses: Application in Photoelectron and Photofragment Ion Imaging of Molecular Oxygen. *Rev. Sci. Instrum.* **1997**, *68*, 3477−3484.

(14) Johansson, J. O.; Henderson, G. G.; Campbell, E. E. B. Dynamics of Thermal Electron Emission from Highly Excited C_{60}. *J. Phys. Chem. A* **2014**, *118*, 8067−8073.

(15) Ogi, Y.; Kohguchi, H.; Niu, D.; Ohshimo, K.; Suzuki, T. Super-Resolution Photoelectron Imaging with Real-Time Subpixelation by Field Programmable Gate Array and Its Application to NO and Benzene Photoionization. *J. Phys. Chem. A* **2009**, *113*, 14536−44.

(16) Roberts, G. M.; Nixon, J. L.; Lecointre, J.; Wrede, E.; Verlet, J. R. Toward Real-Time Charged-Particle Image Reconstruction Using Polar Onion-Peeling. *Rev. Sci. Instrum.* **2009**, *80*, 053104.

(17) Schyja, V.; Lang, T.; Helm, H. Channel Switching in above-Threshold Ionization of Xenon. *Phys. Rev. A: At., Mol., Opt. Phys.* **1998**, *57*, 3692−3697.

(18) Gosselin, J. L.; Weber, P. M. Rydberg Fingerprint Spectroscopy: A New Spectroscopic Tool with Local and Global Structural Sensitivity. *J. Phys. Chem. A* **2005**, *109*, 4899−4904.

(19) Samson, J. A. R.; Haddad, G. N.; Kilcoyne, L. D. Absorption and Dissociative Photoionization Cross Sections of NH_3 from 80 to 1120 Å. *J. Chem. Phys.* **1987**, *87*, 6416.

(20) Cool, T. A.; Wang, J.; Nakajima, K.; Taatjes, C. A.; McIlroy, A. Photoionization Cross Sections for Reaction Intermediates in Hydrocarbon Combustion. *Int. J. Mass Spectrom.* **2005**, *247*, 18−27.

(21) Wang, J.; Yang, B.; Cool, T. A.; Hansen, N.; Kasper, T. Near-Threshold Absolute Photoionization Cross-Sections of Some Reaction Intermediates in Combustion. *Int. J. Mass Spectrom.* **2008**, *269*, 210.

(22) Zhou, Z.; Zhang, L.; Xie, M.; Wang, Z.; Chen, D.; Qi, F. Determination of Absolute Photoionization Cross-Sections of Alkanes and Cyclo-Alkanes. *Rapid Commun. Mass Spectrom.* **2010**, *24*, 1335−42.

DOI: 10.1021/acs.jpca.5b10339
J. Phys. Chem. A 2015, 119, 11504−11508

SUPPORTING INFORMATION

Relative Photoionization Cross-Sections of SAMOs in C_{60}

Elvira Bohl[1], Katarzyna Sokół[1†], Benoit Mignolet[2], James O.F. Thompson[1], J. Olof Johansson[1], Francoise Remacle[2] and Eleanor E.B. Campbell[1,‡]

[1] EaStCHEM, School of Chemistry, University of Edinburgh, Edinburgh EH9 3FJ, U.K.

[2] Department of Chemistry, B6c, University of Liège, B4000, Liège, Belgium.

1. Full Data Series

The complete series of angle-integrated photoelectron spectra used to extract the data shown in Figures 2 and 4 of the paper are shown in Figure S1. The thermal background has not been subtracted from these plots but the fit used to determine the background contribution is shown as a red line.

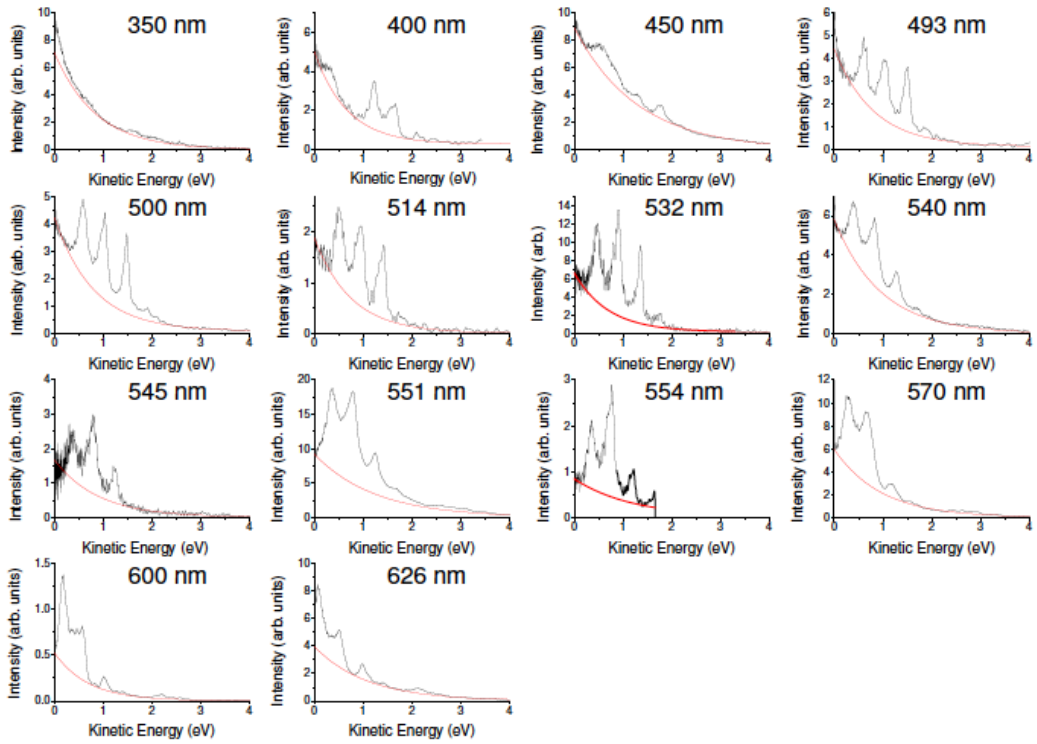

Fig. S1. Photoelectron spectra for different laser wavelengths. The red line shows the fit used to subtract the thermal background.

† Present Address: Department of Chemistry, University of Cambridge, Lensfield Road, Cambridge CB2 1EW, U.K.

‡ Also at: Division of Quantum Phases and Devices, School of Physics, Konkuk University, 143-701 Seoul, Korea,

2. Dependence on Experimental Parameters

The following tests were carried out to ensure that the results did not depend critically on fullerene oven temperature, laser pulse duration or laser pulse intensity within the ranges typically used in the photoionization experiments.

A. – LASER PULSE DURATION DEPENDENCE

Measurements were performed at a set wavelength and oven temperature (542 nm (corresponding to 2.3 eV), 505 °C) to ascertain the influence of laser pulse duration upon the relative s-SAMO, p-SAMO and d-SAMO signals. The results are reported in Figure S2. The data plotted in black correspond to a laser pulse duration of 38±1 fs and the data plotted in red to 99±2 fs, in both cases the laser pulse fluence was 0.4 Jcm^{-2}.

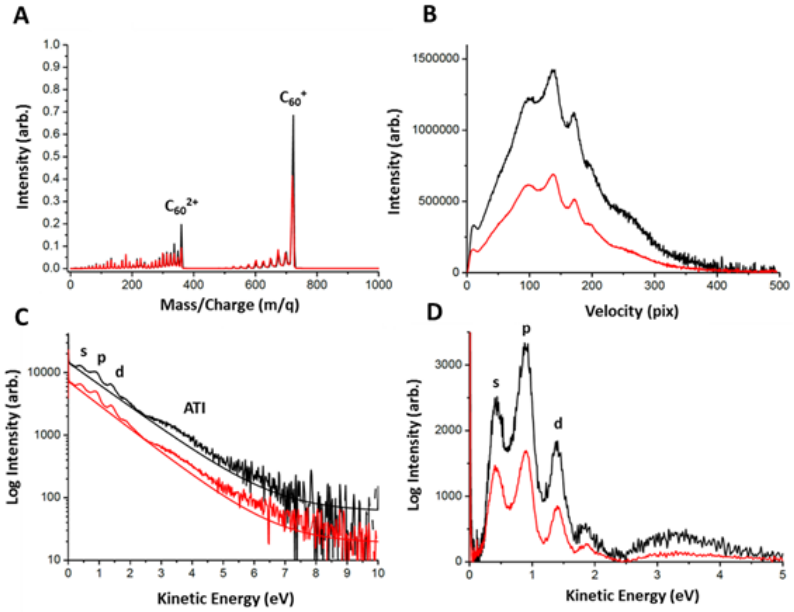

Figure S2 - (A) TOF mass spectra, (B) Photoelectron velocity distribution, (C) PES (intensity plotted on a log scale) with fitted thermal electron background, (D) PES with thermal electron background subtracted. The spectra in black and red correspond to a pulse duration of 38 ±1 fs (10.5 $TWcm^{-2}$) & 99±2 fs (4 $TWcm^{-2}$) respectively. The signal above 2.5 eV is due to above threshold ionization (ATI).

The comparison between the data at the two pulse durations is shown in Figure S3.

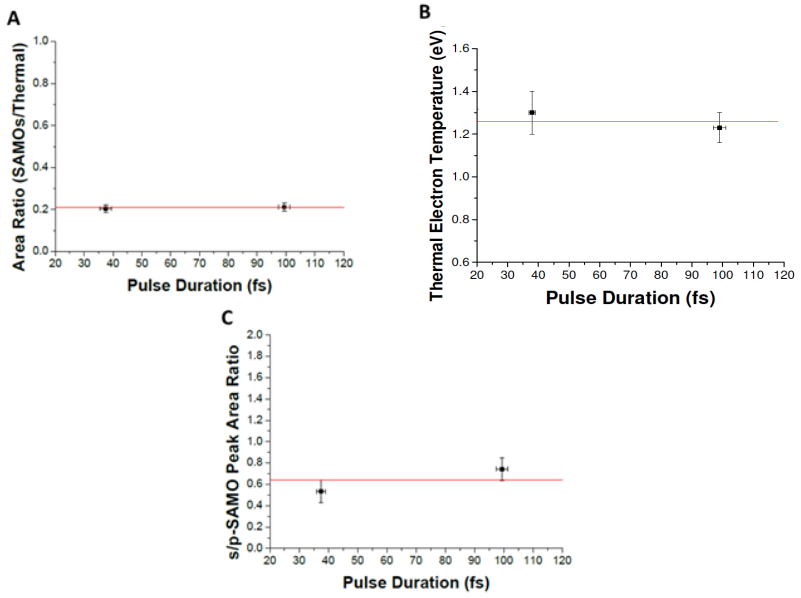

Figure S3 - Plots showing the pulse duration dependence of (A) overall s, p and d-SAMO photoionization intensity relative to thermal electron emission, (B) thermal electron temperature and (C) s/p-SAMO photoionization intensity ratio. Data taken from spectra in Fig. S2. Red lines are horizontal lines to guide the eye.

From these results it was deduced that the pulse duration is not a significant factor determining the relative intensity of the SAMO states. Although there appears to be a slight increase of the s/p ratio for the longer pulse duration, this is still, just, within the experimental error bars.

B. – INITIAL INTERNAL ENERGY DEPENDENCE

Since earlier studies have shown the importance of initial vibrational energy for the population and detection of the SAMO peaks [1], measurements were performed at a set wavelength, pulse duration and laser intensity (540 nm (corresponding to 2.3 eV), 35 fs, and 8.20 ± 0.05 $TWcm^{-2}$) for a number of different oven temperatures, although still for significantly higher vibrational temperatures than the low temperature beam studied in Ref 1, to investigate any influence the oven temperature and hence the internal energy of C_{60} may have on the SAMO ratios. Figure S4 details the results of these measurements.

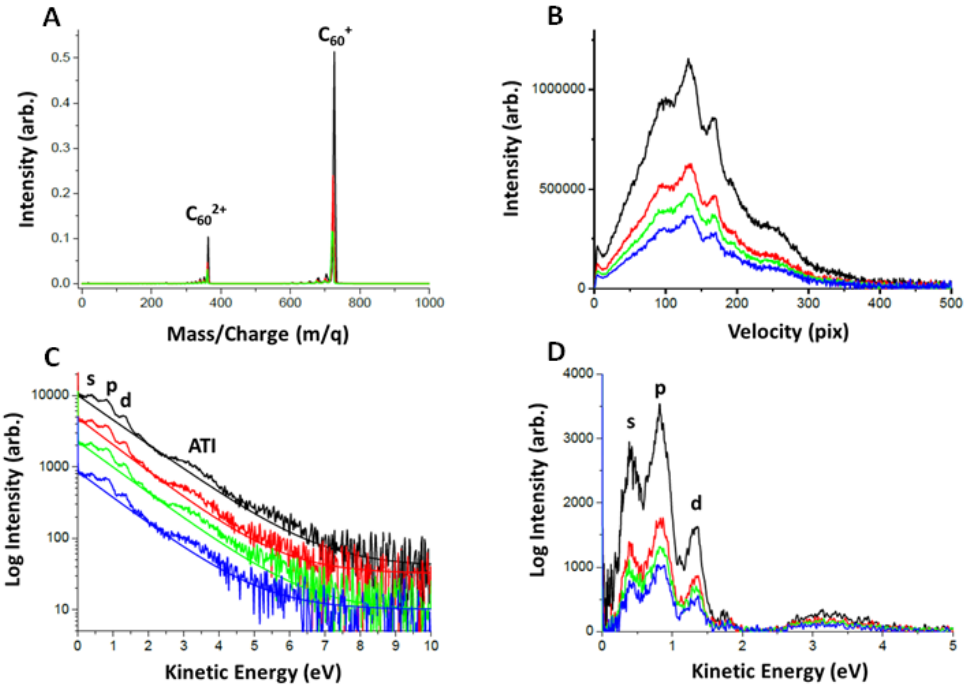

Figure S4 - (A) TOF mass spectra, (B) Photoelectron velocity distribution, (C) PES (intensity plotted on a log scale) with fitted thermal electron background, (D) PES with thermal electron background subtracted. The spectra are coloured black, red, green and blue to differentiate the different oven temperatures of 505 °C, 485 °C, 460 °C & 435 °C respectively.

The comparison between the different oven temperatures is presented in Figure S5.

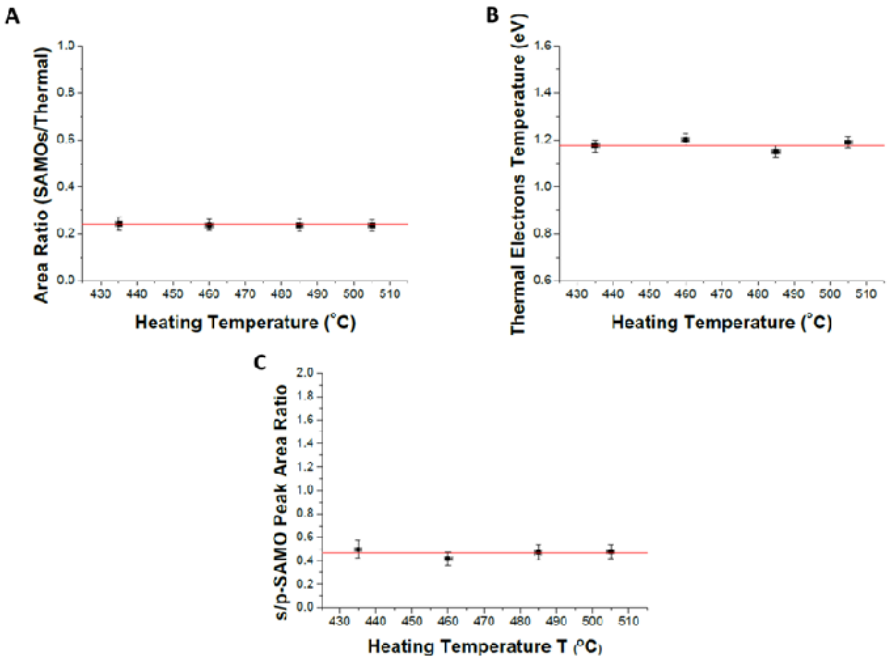

Figure S5 - Plots showing the oven temperature dependence of (A) overall s, p and d-SAMOs photoionization intensity relative to thermal electron emission, (B) thermal electron temperature and (C) s/p-SAMOs intensity ratio. Data from the spectra in Fig. S4. Horizontal red lines to guide the eye.

From these measurements it was determined that the oven temperature, whilst an important factor in optimising the total count rate (by controlling the target density), is not a critical factor, for the temperature range studied, in determining the relative difference in the observed photoelectron intensities of the SAMO states.

C. – LASER INTENSITY DEPENDENCE

Measurements were performed at a set wavelength, pulse duration and oven temperature (540 nm (corresponding to 2.3 eV), 35 fs, and 505 °C) for a number of different laser intensities to investigate the effects of laser power density on the relative observed signal levels from the SAMO states. Figure 5 details these results taken at 5.8 ± 0.1, 4.7 ± 0.1, 3.9 ± 0.06, 3.2 ± 0.05 and 1.8 ± 0.03 TWcm^{-2}.

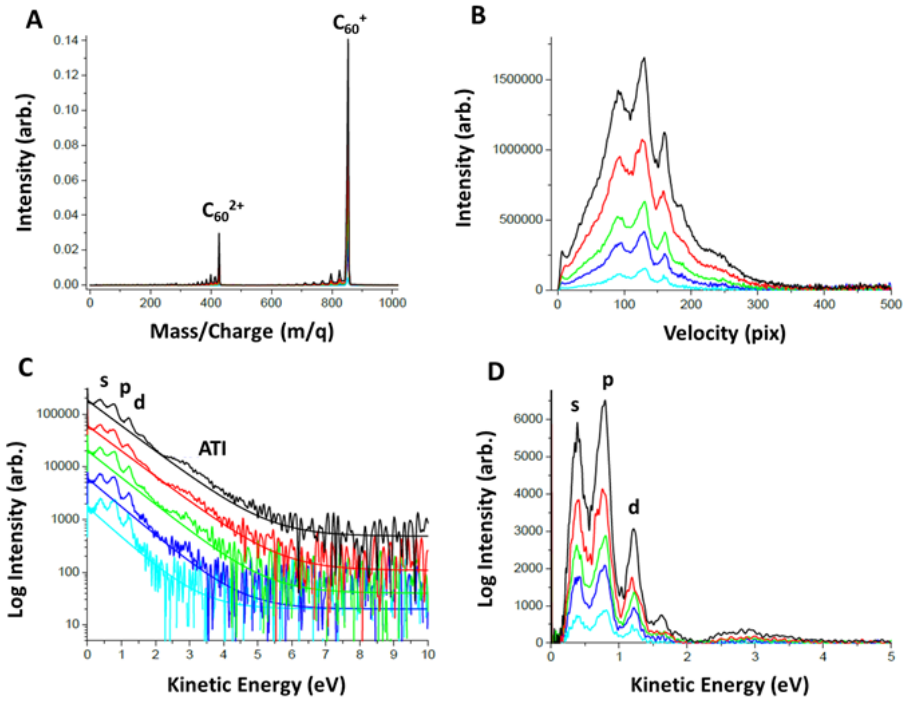

Figure S6 - (A) TOF mass spectra, (B) Photoelectron velocity distribution, (C) PES (intensity plotted on a log scale) with fitted thermal electron background, (D) PES with thermal electron background subtracted. The spectra are colour coded as black, red, green, blue and cyan for the measurements recorded at 5.77, 4.70, 3.93, 3.20, 1.82 TWcm^{-2} respectively.

The comparison of the different laser intensities is shown in Figure S7.

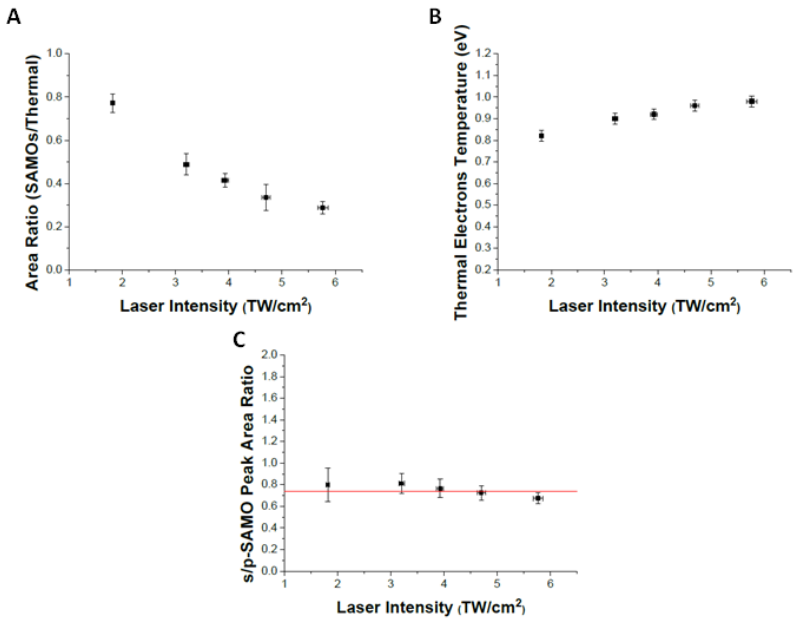

Figure S7 - Plots showing the laser intensity dependence of (A) overall s, p and d-SAMO photoionisation intensity relative to thermal electron emission, (B) thermal electron temperature and (C) s/p-SAMOs photoionization intensity ratio. Horizontal red line to guide the eye. Data from the spectra in Fig S6.

From this comparison it can be seen that there is a significant dependence of the relative magnitude of the SAMO states with respect to the total thermal background on laser pulse intensity. The trend shows that the total thermal background signal increases more rapidly with increasing laser intensity (fluence), and hence increasing electron temperature [2,3], than the SAMO signal. However the relative intensities of the SAMO states with respect to each other remain constant as a function of laser intensity for the range investigated.

3. Ratio of d and 2s SAMO Intensities

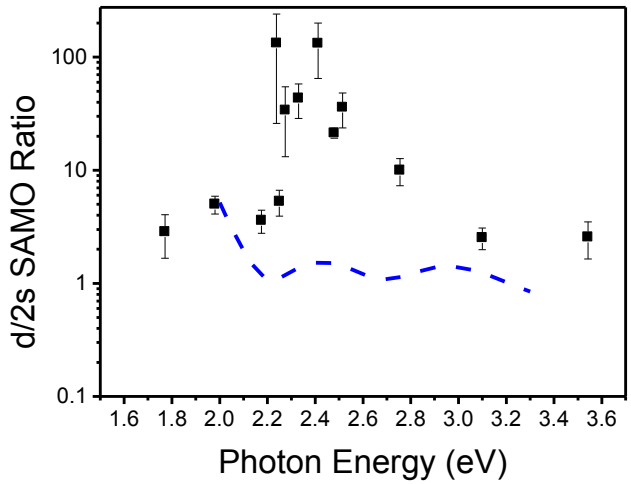

Fig. S8. Comparison of relative experimental d and 2s SAMO peak intensities with theoretical ionization width ratios (average band values) as a function of photon energy.

REFERENCES

1. Boyle, M., et al., *Excitation dynamics of Rydberg states in C_{60}.* The European Physical Journal D - Atomic, Molecular, Optical and Plasma Physics, 2005. **36**(3): p. 339-351.
2. Kjellberg, M., et al., *Momentum-map-imaging photoelectron spectroscopy of fullerenes with femtosecond laser pulses.* Physical Review A, 2010. **81**(2): p. 023202.
3. Hansen, K., K. Hoffmann, and E.E.B. Campbell, *Thermal electron emission from the hot electronic subsystem of vibrationally cold C_{60}.* The Journal of Chemical Physics, 2003. **119**(5): p. 2513-2522.

PHILOSOPHICAL TRANSACTIONS A

rsta.royalsocietypublishing.org

Review

Cite this article: Johansson JO, Bohl E, Campbell EEB. 2016 Super-atom molecular orbital excited states of fullerenes. *Phil. Trans. R. Soc. A* **374**: 20150322.
http://dx.doi.org/10.1098/rsta.2015.0322

Accepted: 10 March 2016

One contribution of 12 to a theme issue 'Fullerenes: past, present and future, celebrating the 30th anniversary of Buckminster Fullerene'.

Subject Areas:
chemical physics

Keywords:
fullerene, super-atom molecular orbitals, photoelectron angular distributions

Author for correspondence:
Eleanor E. B. Campbell
e-mail: eleanor.campbell@ed.ac.uk

Super-atom molecular orbital excited states of fullerenes

J. Olof Johansson[1], Elvira Bohl[1] and Eleanor E. B. Campbell[1,2]

[1]EaStCHEM and School of Chemistry, University of Edinburgh, David Brewster Road, Edinburgh EH9 3FJ, UK
[2]Division of Quantum Phases and Devices, School of Physics, Konkuk University, 143-701 Seoul, South Korea

JOJ, 0000-0002-9320-447X; EEBC, 0000-0002-4656-3218

Super-atom molecular orbitals are orbitals that form diffuse hydrogenic excited electronic states of fullerenes with their electron density centred at the centre of the hollow carbon cage and a significant electron density inside the cage. This is a consequence of the high symmetry and hollow structure of the molecules and distinguishes them from typical low-lying molecular Rydberg states. This review summarizes the current experimental and theoretical studies related to these exotic excited electronic states with emphasis on femtosecond photoelectron spectroscopy experiments on gas-phase fullerenes.

This article is part of the themed issue 'Fullerenes: past, present and future, celebrating the 30th anniversary of Buckminster Fullerene'.

1. Introduction

In the past 30 years since their discovery [1] fullerenes and, in particular, C_{60} have become very important model systems for studying the properties of complex molecules and nanoparticles in the gas phase. Their ease of handling combined with their high symmetry and chemical simplicity, consisting of only the element carbon, has made them attractive systems for pushing both experimental and theoretical techniques to provide a deeper understanding of the electronic and dynamical properties of matter on the nanoscale. Fullerenes also have the intriguing characteristic that, depending on the experimental circumstances, they can appear to show properties more associated with bulk matter

THE ROYAL SOCIETY PUBLISHING

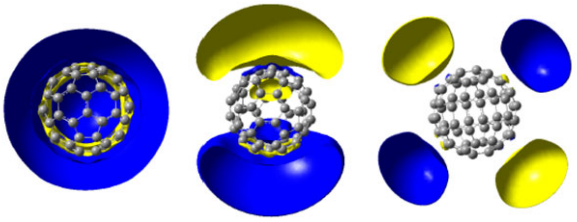

Figure 1. Cuts in the isocontour amplitudes of the Dyson orbitals (representing the probability density of the electron that is ionized) of the *s*-, *p*- and *d*-SAMO states of C_{60}. Adapted from [3].

(such as thermionic electron emission) or can appear almost atomic like [2]. In this review, we are focusing on the atomic-like nature of diffuse excited electronic states of fullerenes, known as 'super-atom molecular orbitals' (SAMOs). SAMOs can be considered to be similar to low-lying mixed valence/Rydberg states, often encountered in molecules; however, the hollow and highly symmetric nature of C_{60} provides a spherically symmetric potential with a shallow attractive region in the centre of the molecule. As a consequence of this, the wave functions of the lowest members of the lowest angular momenta Rydberg series have significant electron density inside the cage and, in contrast with typical molecular Rydberg states, the electron density is centred on the centre of the hollow cage rather than on the atomic cores that form the molecule. The associated molecular orbitals, therefore, bear a close resemblance to large, diffuse, nanometre-scale hydrogenic atomic orbitals (figure 1).

The unusual nature of the SAMOs was first pointed out by Petek and co-workers when they used low-temperature ultrahigh-vacuum scanning tunnel microscopy (STM) to image the orbitals of C_{60} deposited on Cu [4]. The same group also showed the formation of nearly free electron bands when fullerenes aggregated to form a two-dimensional crystal on the metal surface, indicating that these could be interesting systems for molecular electronics applications if the excitation energy of the SAMOs could be tuned to be closer to the Fermi energy. The excited SAMOs were observed earlier in gas-phase C_{60} by femtosecond photoelectron spectroscopy; however, they were not specifically identified as such [5], and they have also been observed in two-photon photoemission experiments on C_{60} layers deposited on surfaces [6].

The STM studies have been reviewed previously [7] so here we focus on reviewing the properties of the SAMO states in isolated gas-phase molecules where there is no perturbation from the presence of a substrate. We start by briefly reviewing the experimental and theoretical techniques that have been used to obtain information about these excited states in gas-phase molecules before describing the results and finishing with a comparison of experimental photoelectron angular distributions (PADs) with calculations using a simple model potential.

2. Methods

The details of the experimental techniques have been provided in previous publications [5,8,9] and will be only briefly described here. The original studies that reported the excitation and subsequent single-photon ionization of Rydberg states in C_{60} were carried out with a combined linear time-of-flight photoelectron spectrometer and a time-of-flight mass spectrometer (MS) [5,10]. In these earlier studies, the angular dependence of the electron emission was not studied. The emphasis was placed on the determination of the binding energies of the higher lying members of the Rydberg series that were well resolved using 800 nm laser pulses with 1.5 ps duration. In more recent studies, the time-of-flight photoelectron spectrometer was replaced by a velocity map imaging (VMI) spectrometer, illustrated in figure 2 [8,9]. This incorporates a position-sensitive detector consisting of a set of multichannel plates followed by a phosphor

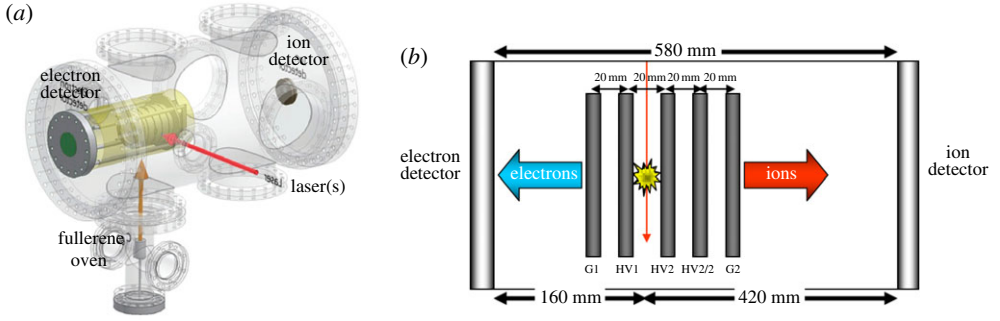

Figure 2. (*a*) Schematic of VMI/MS apparatus. (*b*) Sketch of the electron/ion optics from above. (Online version in colour.)

screen. A CCD camera records the positions at which the electrons arrive on the phosphor screen. The electron extraction voltages are set to produce a two-dimensional projection of the emitted electron cloud on the detector [11]. The resulting images recorded by the CCD camera are inverted to obtain the initial velocity and angular distribution of the electrons using a standard algorithm, either BASEX [12], *p*-BASEX [13] or polar-onion peeling [14] modified to include up to the tenth Legendre polynomial in the inversion procedure. The great advantage of VMI is that it allows the simultaneous recording of the electron velocity and the PAD. The velocity scale is calibrated by recording the above-threshold ionization spectrum of Xe. The Xe photoelectron spectra also serve as a convenient calibration for the 800 nm laser power [15]. The thermal background was subtracted from the spectra [2] and the SAMO peaks were fitted with Lorentzian functions.

The laser pulses were obtained from a regenerative amplified Ti : sapphire laser (*ca* 110 fs, 800 nm). Additional wavelengths were provided by frequency doubling or tripling the fundamental output or by using the fundamental output to pump a commercial noncollinear optical parametric amplifier (NOPA) providing a tuneable light source in the visible range. The pulse durations from the NOPA were in the range of 30–90 fs. The laser light was linearly polarized with the electric vector aligned in the vertical direction. In order to obtain a good signal to noise ratio for the SAMO peaks while minimizing the background contribution due to thermoelectronic ionization [16], the laser intensity typically was within the range 10^{11}–10^{12} W cm^{-2}.

A number of theoretical approaches for the calculation of the SAMO states have been reported. The early studies focused on characterizing the one-electron SAMO orbitals using plane-wave density functional theory (DFT) electronic structure calculations [4,7,17]. A many-body perturbative approach provided evidence for the enhanced stability and long lifetime of the states [18]. Time-dependent (TD)-DFT calculations were described in detail by Mignolet *et al*. [19]. In these studies, the electronic structure of the 500 lowest excited states of neutral C_{60} was computed at the TD-DFT/B3LYP/6+31 G(d) [8] or the TD-DFT/CAM-B3LYP/6-31(+)G(d)-Bq(6-31(6+)G(d)) level [19].

Photoelectron spectra, including PADs, were computed by first calculating the Dyson orbitals. The Dyson orbitals are one-particle orbitals computed as the overlap between the neutral and cation many electron wave functions and represent the probability amplitude of the electron that is ionized [19,20]. They are used to calculate photoionization intensities and PADs, as described in detail for C_{60} by Mignolet *et al*. [19]. For C_{60} the SAMO Dyson orbitals, figure 1, are very similar to the SAMO molecular orbitals. As the SAMO and Rydberg excited states are composed of several excitations from the highest occupied molecular orbital to several SAMO and/or Rydberg orbitals, the Dyson orbitals of the SAMO and Rydberg states are thus a linear combination of the SAMO/Rydberg molecular orbitals of the same symmetry. The first band of *s*-SAMO states has a principal quantum number $n = 3$, while the lowest-lying members of the *p*- and *d*-bands in these calculations, figure 1, have $n = 4$ and 5, respectively, i.e. all wave functions of the lowest-lying SAMO states contain two radial nodes.

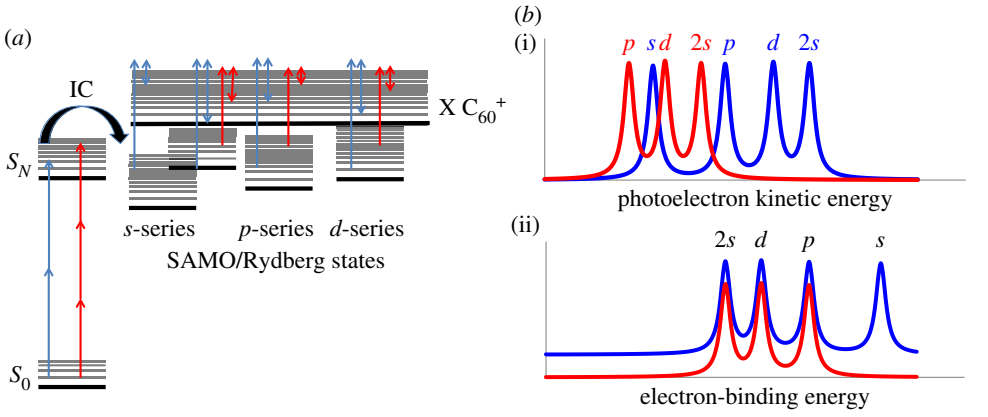

Figure 3. Schematic illustration of the 'Rydberg fingerprint spectroscopy' technique used to probe the SAMO and Rydberg excited states of the fullerenes. (*a*) Multiphoton excitation is followed by very efficient state couplings and population of a wide range of excited states with varying amounts of vibrational energy. Narrow lines indicate vibrational excitation. Only the first two members of the *s*-series and the first members of the *p*- and *d*-series are shown for clarity. The single-headed arrows indicate two different photon energies. The double-headed arrows indicate the photoelectron kinetic energies. Note that the photon energy corresponding to the red arrow is too low to ionize the lowest-lying *s*-state. (*b*) (i) Schematic of the photoelectron spectra that would be observed for the two-photon energies shown in (*a*). (ii) Corresponding electron binding energies. (Online version in colour.)

3. Rydberg fingerprint spectroscopy

The term 'Rydberg fingerprint spectroscopy' was coined by Weber and co-workers [21]. It refers to the sensitivity of molecular Rydberg electron-binding energies to the molecular structure and has been proposed as an analytical technique to distinguish molecular isomers [22] and also as a means of probing isomerization dynamics on a femtosecond time scale [23]. It was based on the observation that well-resolved peaks could be observed in the photoelectron spectra of organic molecules corresponding to low-lying molecular Rydberg states when using femtosecond lasers for photoionization [24,25]. At the same time, similar observations were made for the excitation and ionization of Rydberg states of C_{60} [5]. For large molecules like C_{60} where there is a very high density of excited electronic and vibrational states, the excitation is practically independent of the wavelength of the laser used for excitation. An additional advantage of the technique is that, due to the similarity of the Rydberg and cation potential energy surfaces, the final photoionization step is essentially vibration conserving and the method can work with molecules that have a high initial vibrational energy. A simplified, schematic illustration of the technique is shown in figure 3. High-lying excited states are very rapidly and efficiently coupled to other excited states, aided by the high degree of vibrational excitation within the molecule and the transient electric field of the laser pulse [26]. This allows the population of a wide band of excited states with varying amounts of vibrational energy, including excited valence states, the fullerene SAMO states and higher lying Rydberg states. Within the same laser pulse, once excited, these SAMO/Rydberg states can be single-photon ionized by the absorption of an additional photon.

As the excited states are incoherently populated, the final step in the photoionization process can be considered to be a single-photon ionization from the excited states. In this case, the PAD for a random orientation of the molecule can be described as [27]:

$$I(\theta) \propto (1 + \beta P_2(\cos\theta)), \tag{3.1}$$

where β is an anisotropy parameter, taking values within the range -1 to $+2$, and $P_2(\cos\theta)$ is the second order Legendre polynomial.

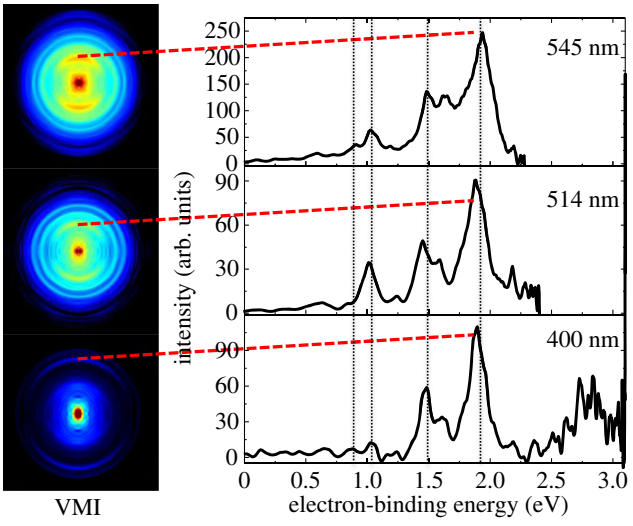

Figure 4. VMI images and the corresponding angle-integrated photoelectron spectra for C_{60}, plotted as a function of electron-binding energy, for ionization with three different laser wavelengths: 545 nm, 514 nm and 400 nm (top to bottom).

4. Fullerene super-atom molecular orbitals and Rydberg states

Owing to the unique hollow nature of the fullerenes, the low-lying members of Rydberg series, the SAMOs, which are the main interest here, are rather unusual in having the electron density centred on the centre of the hollow molecular core rather than on the atomic constituents of the molecule. SAMOs arise because of the hollow core potential defined by the spherical C_{60} carbon cage. The overall potential is a sum of two contributions: the deep Coulomb wells centred on each carbon atom and a shallow attractive potential induced by the long-range-dispersion interactions between electrons localized on two opposite sides of the cage. While only the former is sufficient to define the σ and π molecular orbitals, the shallow attractive potential within the cage is essential for correctly describing SAMO states. In particular, the lowest-lying members of the *s*- and *p*-series are considered to have significant electron density within the centre of the molecule (figure 1). The *s*-SAMO has even been identified theoretically for anions [28,29]. This clearly distinguishes the SAMO states from the higher lying Rydberg states. The unique nature of the potential was discussed in analogy with image potential states of graphene in the context of the STM experiments carried out by the Petek group [7]. For states with higher principal quantum numbers, the electron density is almost entirely outside the carbon cage and the electron-binding energies and properties more closely resemble those of conventional Rydberg series.

A series of VMI images and the corresponding angle-integrated photoelectron spectra, plotted as a function of electron-binding energy ($E_{\mathrm{bind}} = h\nu - E_{\mathrm{kin}}$, where $h\nu$ is the photon energy) rather than photoelectron kinetic energy (E_{kin}), are shown in figure 4 for C_{60} for three different laser wavelengths. The peak structure is clearly seen in all three spectra with the most prominent peak (assigned to the excitation of the first *s*-SAMO band) being indicated by the dashed lines. The positions of the maxima of the first *p*- and *d*-bands and the second *s*-band are indicated by the vertical dashed lines. This series of measurements nicely illustrates the non-resonant nature of the excitation of the SAMO states as well as the single-photon ionization from the excited states that underpins the analysis and interpretation.

The experimentally measured electron-binding energies are given in table 1 along with calculated values. The plane-wave DFT values [4] were only given with respect to the calculated lowest unoccupied molecular orbital value and are, therefore, just given as energy differences between the states. The experimental assignment was based partly on the calculated binding energies and partly on the PADs. The experimental angular distributions were extracted by

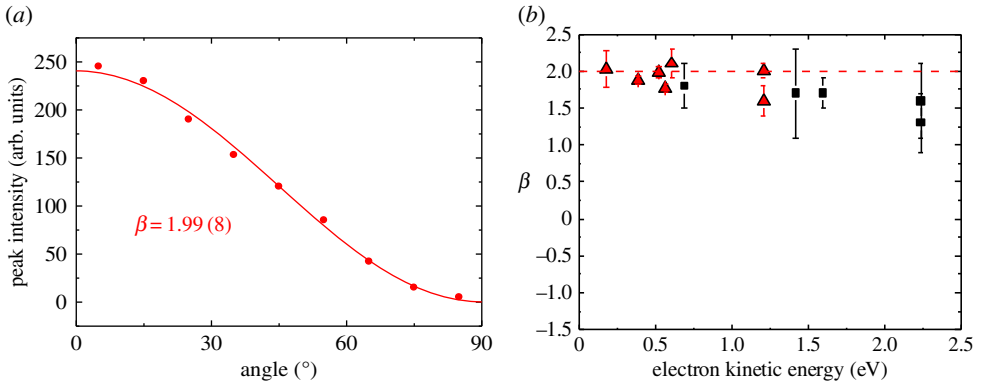

Figure 5. (*a*) Photoelectron angular distribution for the peak in the 400 nm photoelectron spectrum shown in figure 4 at a binding energy of 1.9 eV. (*b*) Value of the anisotropy parameter, β, as a function of photoelectron kinetic energy for the peaks assigned to the first (red, triangles) and second (black, squares) members of the *s*-SAMO series. The data point corresponding to the plot in (*a*) appears at an electron kinetic energy of $E_{kin} = h\nu - E_{bind} = 3.1 - 1.9 = 1.2$ eV. (Online version in colour.)

Table 1. Comparison of experimental and theoretical binding energies for the C_{60} SAMOs.

	SAMO-binding energy (eV)						
	s	Δ_{sp}	*p*	Δ_{pd}	*d*	$\Delta_{ds'}$	*s*′
experiment [8]	1.90 ± 0.01	0.43	1.47 ± 0.02	0.45	1.02 ± 0.01	0.15	0.87 ± 0.02
B3LYP 6-31+G(d) [8]	2.15	0.89	1.26	0.49	0.77	−0.01	0.78
CAM-B3LYP 6-31+G(D)+diff. [19]	2.35	0.89–0.63	1.46–1.72	0.11–0.58	1.14–1.35	0	1.14–1.35
plane-wave DFT [4]		0.66		0.55		−0.1	
model potential	1.9	0.3	1.6	0.6	1.0	0.1	0.9

dividing the VMI data into angular segments and integrating the relevant peak intensity in each case [9]. An example for the peak at a binding energy of 1.9 eV, indicated in figure 4, is shown in figure 5*a* for the 400 nm data with the data fitted to equation (3.1).

The value extracted for the anisotropy parameter, β, for the peaks with binding energies of 1.9 ± 0.1 eV shows that the outgoing electron is very close to a pure *p*-wave. This is expected for single-photon ionization from an *s*-state with zero orbital angular momentum ($\ell = 0$). An additional confirmation of the assignment of this peak is obtained when considering the extracted value of β as a function of the kinetic energy of the outgoing electron. For ionization from an *s*-state, the value of β should not change as the electron kinetic energy changes because the outgoing wave should always be a *p*-wave. The non-resonant excitation mechanism for the SAMOs allows us to test this by simply changing the wavelength of the laser. The results are shown in figure 5*b* for the peaks assigned to the first (binding energy 1.9 eV) and second (binding energy 0.87 eV) members of the *s*-series. The situation is less straightforward for ionization from states with higher values of the orbital angular momentum because more than one exit channel is possible ($\Delta\ell = \pm 1$) and the value will change as the velocity of the outgoing electron changes. In this situation, comparison with the theoretical results helps to assign the peaks.

A comparison of the experimentally determined anisotropy parameters and TD-DFT calculations for the B3LYP/6+31 G(d) and CAM-B3LYP/6-31(+)G(d)-Bq(6-31(6+)G(d)) level is shown in figure 6 for C_{60}, and C_{70} with additional experimental values for C_{82} and $Sc_3N@C_{80}$.

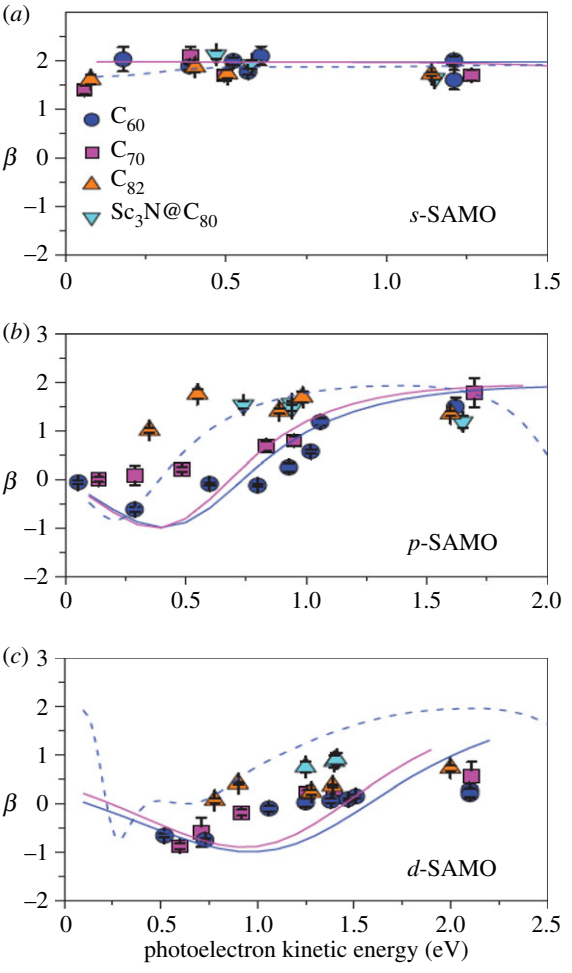

Figure 6. Photoelectron angular distributions (PADs) for (*a*) *s*-states, (*b*) *p*-states and (*c*) *d*-states, characterized by the fitted β-value for experiments on C_{60} (circles), C_{70} (squares), C_{82} (up-triangles) and $Sc_3N@C_{80}$ (down-triangles). The full lines show the calculated β-values for C_{60} and C_{70} at the B3LYP/6-31+G(d) level [8]. The dashed lines are C_{60} CAM-B3LYP/6-31(+)G(d)-Bq(6-31(6+)G(d)) results [19]. Adapted from [9].

Both the experimental and theoretical results are almost identical for C_{60} and C_{70}. Although the CAM-B3LYP/6-31(+)G(d)-Bq(6-31(6+)G(d)) calculations provide better agreement with the experimental binding energies, the B3LYP/6-31+G(d) angular distributions are in better agreement with the measurements for the *p*-SAMO. The *d*-SAMO measurements lie in between the two sets of calculations. The predicted angular distributions are very sensitive to the diffusivity of the wave functions. The angular distributions for ionization from the *p*-SAMO are significantly shifted for low kinetic energies for C_{82} and $Sc_3N@C_{80}$ with respect to C_{60} and C_{70}. A smaller, but still significant, shift is also seen for the *d*-SAMO.

Photoelectron spectra parallel and perpendicular to the laser polarization direction are compared for the different fullerenes whose β-values are plotted in figure 6, obtained at a wavelength of around 500 nm, in figure 7. The binding energies of the SAMO peaks are very similar in all cases (table 1). It should be noted that the ionization energies of the higher fullerenes and the endohedral species are all significantly lower than that of C_{60}; therefore, the excitation energy of the SAMO states must be lowered by the same amount. The main difference in the photoelectron spectra is a broadening of the peak widths and a more prominent double-peak structure for the *p*-SAMO band due to the decreasing symmetry as the size of the fullerene cage

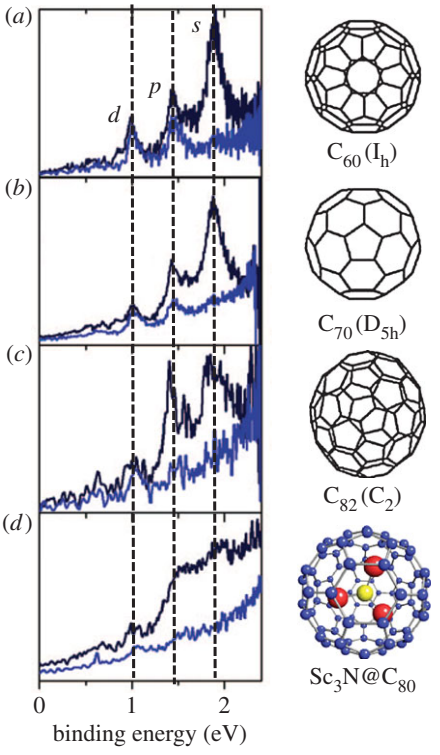

Figure 7. Photoelectron spectra parallel (black) and perpendicular (blue) to the laser polarization direction of (*a*) C_{60}, 500 nm, 4.7 TW cm^{-2}, (*b*) C_{70}, 520 nm, 2.9 TW cm^{-2}, (*c*) C_{82}, 519 nm, 2.8 TW cm^{-2} and (*d*) $Sc_3N@C_{80}$, 506 nm, 4.1 TW cm^{-2}. Adapted from [9].

is increased. The peak structure for the first *s*- and *p*-SAMO bands is almost completely smeared out for the endohedral fullerene, $Sc_3N@C_{80}$ [9].

The TD-DFT calculations also provided insight into the dominance of peaks corresponding to single-photon ionization of SAMO bands over valence bands in the photoelectron spectra. The photoionization widths between the excited electronic states and the ground state of the cation were computed using a basis of orthogonalized plane waves to describe the wave function of the ionized electron [19]. The photoionization width was computed for each state taking into account the random orientation of the C_{60} molecule with respect to the electric field. The calculated photoionization width is proportional to the photoionization rate and directly related to the photoionization cross section (it does not refer to the width of the peaks in the photoelectron spectrum).

For the relatively low photoelectron kinetic energies that are studied in these experiments, the photoionization cross section from the SAMO states is orders of magnitude larger than ionization from the non-SAMO valence excited states (figure 8). The calculated photoionization widths can be converted to photoionization lifetimes of the order of femtoseconds for the SAMO states but picoseconds to nanoseconds for the non-SAMO states [19]. This explains very clearly why the SAMO peaks are so dominant for ionization with visible laser wavelengths. Even though the non-SAMO states will be populated, the probability that they will be single-photon ionized on the time scale of the laser pulse (50–100 fs) is vanishingly small.

The ratio of calculated photoionization widths has been compared to relative experimental ionization intensities [3]. The results, figure 9, show very good agreement between the theoretical ratios and the experimental ratios for photon energies where the same number of photons can access both states. Outside these regions, the *s*-band can be accessed by one less photon than the higher states. In this case, the *s*-band intensity would be expected to be significantly higher than

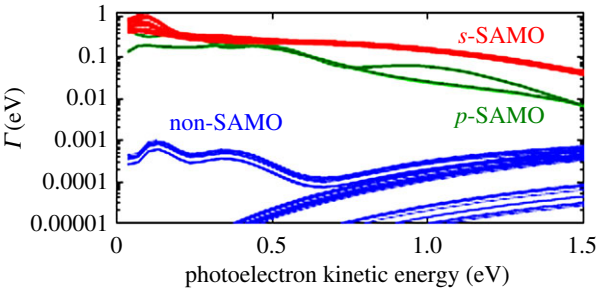

Figure 8. Photoionization widths, Γ, plotted on a logarithmic scale versus the photoelectron kinetic energy. Adapted from [19]. (Online version in colour.)

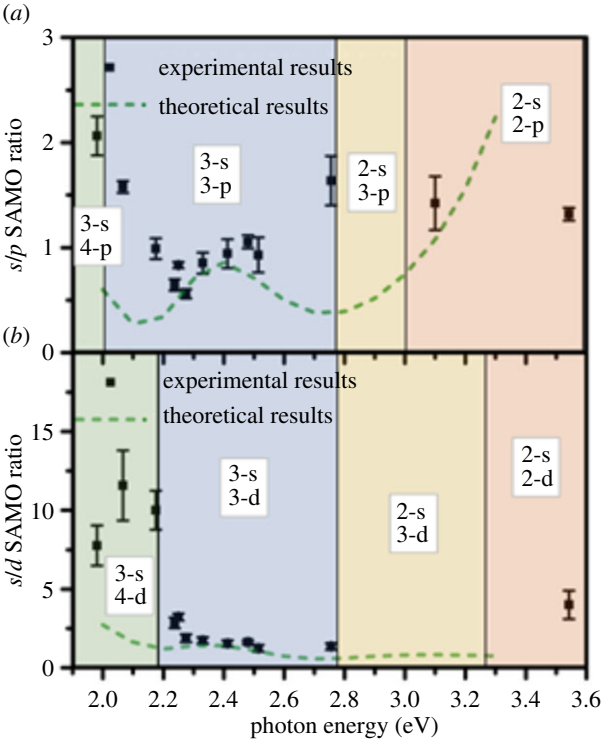

Figure 9. Comparison of relative experimental SAMO peak intensities (squares) and the theoretical photoionization width ratios of SAMO states plotted as a function of laser photon energy. (*a*) Ratio of the *s*- and *p*-peak intensities. (*b*) Ratio of the *s*- and *d*-peak intensities. Theoretical values shown by dashed lines (ratio of average values calculated for each band). The numbers in each panel indicate the number of photons needed to access the *s* and the *p*- or *d*-SAMO states, respectively. Adapted from [3]. (Online version in colour.)

the higher lying states and the measured ratios are correspondingly higher. This is not accounted for by the calculations because they do not include the population mechanism but simply assume that all states are populated with the same probability. The results are quite remarkable because they are implying that this assumption (at least for the SAMO population) does hold as long as the photon order needed to energetically access the states is the same. What is apparent is that the TD-DFT calculations are, with good accuracy, able to predict the photoionization probability in addition to the PAD as a function of kinetic energy as discussed earlier.

The rapid decrease in the photoionization width of the SAMO/Rydberg states as the photoelectron kinetic energy increases (figure 8) also explains why the higher-lying Rydberg

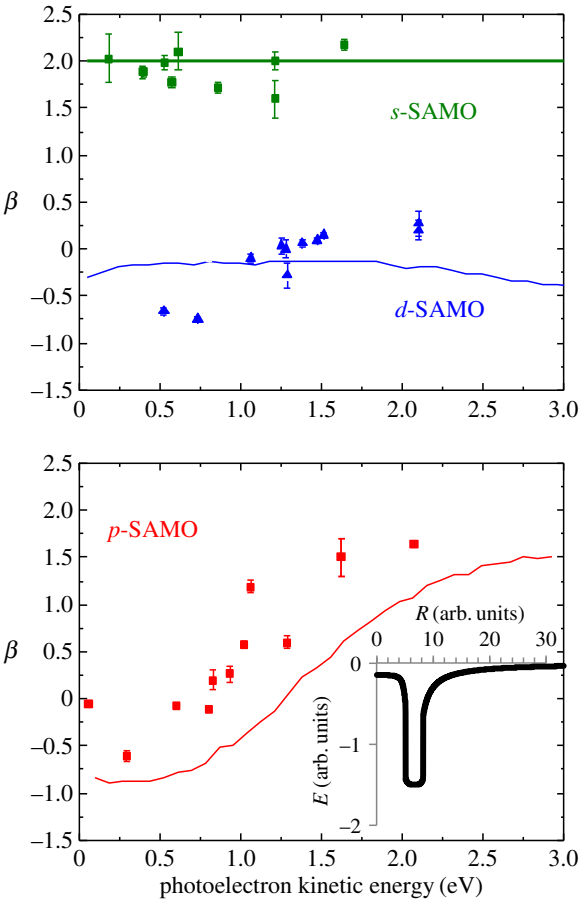

Figure 10. Comparison of experimental anisotropy parameters, β, with calculations using the simple phenomenological model potential shown in the inset. Note that the β value for the *s*-SAMO is independent of the potential, which can be seen from equation (5.1). (Online version in colour.)

states that were the subject of the early studies [5,10,30] are much less prominent for excitation with visible light. Excitation and ionization with 800 nm, 1.5 ps bandwidth limited picosecond laser pulses produced photoelectron spectra where the higher-lying states were well resolved [5]. The assignment of the peaks was made by comparing the experimental binding energies with the numerical solution of the Schrödinger equation using a simple model potential [5]. In the light of the detail that can be obtained in angle-resolved studies using VMI, it would be useful to revisit the study of the higher-lying Rydberg states using picosecond ionization.

5. Photoelectron angular distributions from a phenomenological potential

There have been a number of attempts to model C_{60} and $X@C_{60}$ photoionization using simple, spherically symmetric, phenomenological potentials [5,7,31–33]. Usually in these studies, the depth, width and shape of the potential well are adjusted to fit the experimental results and has often taken the form of a quasi-square well potential at the position of the carbon atoms. For example, the model used to calculate the Rydberg binding energies, discussed above, was based on a quasi-rectangular potential at the position of the carbon atoms, published by Puska & Nieminen [34]. In order to illustrate the use of a phenomenological potential to model the PADs, we have adapted a phenomenological square well potential to have a shallow attractive core and adjusted the parameters to obtain good agreement with the SAMO-binding energies. We then

numerically solve the Schrödinger potential within Matlab, following the method described by Falkensteiner *et al.* [35]. The eigenenergies for the lowest *s*-, *p*- and *d*-SAMO states are given in table 1. The corresponding wave functions were then used to calculate the PADs following the method described by Bartels *et al.* [36].

The anisotropy parameter, β, is defined within the Bethe–Cooper–Zare theory [27,37] as

$$\beta = \frac{\ell(\ell-1)R_-^2 + (\ell+1)(\ell+2)R_+^2 - 6\ell(\ell+1)R_-R_+\cos\delta}{(2\ell+1)(\ell R_-^2 + (\ell-1)R_+^2)}, \tag{5.1}$$

where

$$R_\pm = \int \psi_\mathrm{f}^\pm(r)\psi_\mathrm{i}(r)r^3\,\mathrm{d}r \tag{5.2}$$

are the radial matrix elements, ψ_i and ψ_f are the initial and final state wave functions, ℓ is the orbital angular momentum quantum number of the initial state, r is the radial coordinate and $\delta = \delta_+ - \delta_-$ is the difference of the Coulomb phase shifts of the final state wave functions ψ_f, defined by their asymptotic behaviour [38]. The subscripts $\pm$ refer to the $\ell+1$ and $\ell-1$ transitions.

$$R_\pm \simeq \sqrt{\frac{2}{\pi k}}\frac{1}{r}\cos\left(kr - (\ell\pm1)\frac{\pi}{2} + \frac{\log(2kr)}{k} + \delta_\pm + \sigma_\pm\right) \quad \text{for } r\to\infty. \tag{5.3}$$

Here, k is the magnitude of the wavevector and σ is the Coulomb phase ($=\arg\Gamma(1+\ell-i/k)$) [39].

The results for the lowest *s*-, *p*- and *d*-SAMOs are shown in figure 10. The spherically symmetric radial potential used for the calculations is shown as an inset in the lower plot. The results are rather close to the experimental values. It should be noted that although quasi-square well potentials have been used to model fullerene photoionization they are not very physical and a cusp-like potential has been suggested as a more realistic approximation [40]. The good agreement achieved here gives some confidence that a systematic comparison of the eigenenergies and angular distributions obtained from the available model potentials should provide a means of selecting the most appropriate and generally applicable model potential for C_{60}.

6. Conclusion

Thirty years after their discovery, fullerenes continue to be valuable model systems and serve to develop new experimental and theoretical techniques that can probe ever more complex systems. The fullerene SAMO excited electronic states that have been reviewed here provide large, challenging systems for quantum chemistry but, most attractively, the high symmetry and nature of the C_{60} molecules also make it possible to apply much simpler models that provide more intuitive insight into the factors that influence the binding energy of these interesting states. The increased knowledge of the properties of these states may lead to design of materials for specific charge transport applications and may also play an important role in understanding the chemistry of neutral and charged fullerenes in space.

Authors' contributions. J.O.J. and E.B. carried out the experimental work, analysed the experimental data and contributed to data interpretation. J.O.J. solved the Schrödinger equation for the simple jellium model and calculated the corresponding PADs. E.E.B.C. designed the experiments, supervised the research, contributed to data interpretation and wrote the manuscript.

Competing interests. We declare we have no competing interests.

Funding. Funding from the Leverhulme Trust (RPF-298 'PES of hollow nanomaterials') is gratefully acknowledged. E.E.B.C. acknowledges the support of a JILA Visiting Fellowship. J.O.J. is a Royal Society of Edinburgh/BP Trust research fellow.

Acknowledgements. We thank Françoise Remacle and Benoit Mignolet (University of Liège) for supplying the TD-DFT calculations and for many fruitful discussions. We also thank James Thompson, Gordon Henderson and Katarzyna Sokóş for their contributions to the experiments.

References

1. Kroto HW, Heath JR, O'Brien SC, Curl RF, Smalley RE. 1985 C_{60}: Buckminsterfullerene. *Nature* **318**, 162–163. (doi:10.1038/318162a0)
2. Johansson JO, Campbell EEB. 2013 Probing excited electronic states and ionisation mechanisms of fullerenes. *Chem. Soc. Rev.* **42**, 5661–5671. (doi:10.1039/C3CS60047E)
3. Bohl E, Sokół KP, Mignolet B, Thompson JOF, Johansson JO, Remacle F, Campbell EEB. 2015 Relative photoionization cross sections of super-atom molecular orbitals (SAMOs) in C_{60}. *J. Phys. Chem. A* **119**, 11 504–11 508. (doi:10.1021/acs.jpca.5b10339)
4. Feng M, Zhao J, Petek H. 2008 Atom like, hollow-core-bound molecular orbitals of C_{60}. *Science* **320**, 359–362. (doi:10.1126/science.1155866)
5. Boyle M, Hoffmann K, Schulz CP, Hertel IV, Levine RD, Campbell EEB. 2001 Excitation of Rydberg series in C_{60}. *Phys. Rev. Lett.* **87**, 273401. (doi:10.1103/PhysRevLett.87.273401)
6. Dutton GJ, Dougherty DB, Jin W, Reutt-Robey JE, Robey SW. 2011 Superatom orbitals of C_{60} on Ag(111): two-photon photoemission and scanning tunneling spectroscopy. *Phys. Rev. B* **84**, 195435. (doi:10.1103/PhysRevB.84.195435)
7. Feng M, Zhao J, Huang T, Zhu X, Petek H. 2011 The electronic properties of superatom states of hollow molecules. *Acc. Chem. Res.* **44**, 360–368. (doi:10.1021/ar1001445)
8. Johansson JO, Henderson G, Remacle F, Campbell EEB. 2012 Angular-resolved photoelectron spectroscopy of superatom orbitals of fullerenes. *Phys. Rev. Lett.* **108**, 173401. (doi:10.1103/PhysRevLett.108.173401)
9. Johansson JO, Bohl E, Henderson GG, Mignolet B, Dennis TJS, Remacle F, Campbell EEB. 2013 Hot electron production and diffuse excited states in C_{70}, C_{82}, and $Sc_3N@C_{80}$ characterized by angular-resolved photoelectron spectroscopy. *J. Chem. Phys.* **139**, 084309. (doi:10.1063/1.4818987)
10. Boyle M, Laarmann T, Hoffmann K, Hedén M, Campbell EEB, Schulz CP, Hertel IV. 2005 Excitation dynamics of Rydberg states in C_{60}. *Eur. Phys. J. D* **36**, 339–351. (doi:10.1140/epjd/e2005-00281-7)
11. Bordas C, Paulig F, Helm H, Huestis DL. 1996 Photoelectron imaging spectrometry: principle and inversion method. *Rev. Sci. Instrum.* **67**, 2257–2268. (doi:10.1063/1.1147044)
12. Dribinski V, Ossadtchi A, Mandelshtam VA, Reisler H. 2002 Reconstruction of Abel-transformable images: the Gaussian basis-set expansion Abel transform method. *Rev. Sci. Instrum.* **73**, 2634–2642. (doi:10.1063/1.1482156)
13. Garcia GA, Nahon L, Powis I. 2004 Two-dimensional charged particle image inversion using a polar basis function expansion. *Rev. Sci. Instrum.* **75**, 4989–4996. (doi:10.1063/1.1807578)
14. Roberts GM, Nixon JL, Lecointre J, Wrede E, Verlet JRR. 2009 Toward real-time charged-particle image reconstruction using polar onion-peeling. *Rev. Sci. Instrum.* **80**, 053104. (doi:10.1063/1.3126527)
15. Schyja V, Lang T, Helm H. 1998 Channel switching in above-threshold ionization of xenon. *Phys. Rev. A* **57**, 3692–3697. (doi:10.1103/PhysRevA.57.3692)
16. Johansson JO, Fedor J, Goto M, Kjellberg M, Stenfalk J, Henderson GG, Campbell EEB, Hansen K. 2012 Anisotropic hot electron emission from fullerenes. *J. Chem. Phys.* **136**, 164301. (doi:10.1063/1.4704828)
17. Zhao J, Feng M, Yang J, Petek H. 2009 The superatom states of fullerenes and their hybridization into the nearly free electron bands of fullerites. *ACS Nano* **3**, 853–864. (doi:10.1021/nn800834k)
18. Pavlyukh Y, Berakdar J. 2011 Communication: superatom molecular orbitals: new types of long-lived electronic states. *J. Chem. Phys.* **135**, 201103. (doi:10.1063/1.3665089)
19. Mignolet B, Johansson JO, Campbell EEB, Remacle F. 2013 Probing rapidly-ionizing super-atom molecular orbtals in C_{60}: a computational and femtosecond photoelectron spectroscopy study. *ChemPhysChem* **14**, 3332–3340. (doi:10.1002/cphc.201300585)
20. Dauth M, Wiessner M, Feyer V, Schöll A, Puschnig P, Reinert F, Kümmel S. 2014 Angle resolved photoemission from organic semiconductors: orbital imaging beyond the molecular orbital interpretation. *New J. Phys.* **16**, 103005. (doi:10.1088/1367-2630/16/10/103005)
21. Gosselin JL, Weber PM. 2005 Rydberg fingerprint spectroscopy: a new spectroscopic tool with local and global structural sensitivity. *J. Phys. Chem. A* **109**, 4899–4904. (doi:10.1021/jp0503866)
22. Cardoza JD, Rudakov FM, Hansen N, Weber PM. 2008 Identification of isomeric hydrocarbons by Rydberg photoelectron spectroscopy. *J. Electron Spectrosc. Relat. Phenom.* **165**, 5–10. (doi:10.1016/j.elspec.2008.06.003)

23. Rudakov FM, Weber PM. 2012 Ultrafast structural and isomerization dynamics in the Rydberg-exited quadricyclane: norbornadiene system. *J. Chem. Phys.* **136**, 134303. (doi:10.1063/1.3697472)
24. Schick CP, Weber PM. 2001 Ultrafast dynamics in the three-photon, double-resonance ionization of phenol via the S_2 electronic state. *J. Phys. Chem. A* **105**, 3735–3740. (doi:10.1021/jp003304g)
25. Tsubouchi M, Whitaker BJ, Wang L, Kohguchi H, Suzuki T. 2001 Photoelectron imaging on time-dependent molecular alignment created by a femtosecond laser pulse. *Phys. Rev. Lett.* **86**, 4500–4503. (doi:10.1103/PhysRevLett.86.4500)
26. Zhang GP, Sun X, George TF. 2003 Laser-induced ultrafast dynamics in C_{60}. *Phys. Rev. B* **68**, 165410. (doi:10.1103/PhysRevB.68.165410)
27. Cooper J, Zare RN. 1968 Angular distribution of photoelectrons. *J. Chem. Phys.* **48**, 942–943. (doi:10.1063/1.1668742)
28. Klaiman S, Gromov EV, Cederbaum LS. 2013 Extreme correlation effects in the elusive bound spectrum of C_{60}^-. *J. Phys. Chem. Lett.* **4**, 3319–3324. (doi:10.1021/jz4018514)
29. Voora VK, Cederbaum LS, Jordan KD. 2013 Existence of a correlation bound s-type anion state of C_{60}. *J. Phys. Chem. Lett.* **4**, 849–853. (doi:10.1021/jz400195s)
30. Boyle M, Hedén M, Schulz CP, Campbell EEB, Hertel IV. 2004 Two-color pump-probe study and internal-energy dependence of Rydberg-state excitation in C_{60}. *Phys. Rev. A* **70**, 051201. (doi:10.1103/PhysRevA.70.051201)
31. Dolmatov VK, Baltenkov AS, Connerade JP, Manson ST. 2004 Structure and photoionization of confined atoms. *Rad. Phys. Chem.* **70**, 417–433. (doi:10.1016/j.radphyschem.2003.12.024)
32. Madjet ME, ChakrabortY HS, Rost JM, Manson ST. 2008 Photoionization of C_{60}: a model study. *J. Phys. B* **41**, 105101. (doi:10.1088/0953-4075/41/10/105101)
33. Phaneuf RA *et al.* 2013 Probing confinement resonances by photoionizing Xe inside a C_{60} molecular cage. *Phys. Rev. A* **88**, 053402. (doi:10.1103/PhysRevA.88.053402)
34. Puska MJ, Nieminen RM. 1993 Photoabsorption of atoms inside C_{60}. *Phys. Rev. A* **47**, 1181–1186. (doi:10.1103/PhysRevA.47.1181)
35. Falkensteiner P, Grosse H, Schöberl F, Hertel P. 1985 Solving the Schrödinger equation for bound states. *Comput. Phys. Commun.* **34**, 287–293. (doi:10.1016/0010-4655(85)90005-0)
36. Bartels C, Hock C, Huwer J, Kuhnen R, Schwöbel J, von Issendorff B. 2009 Probing the angular momentum character of the valence orbitals of free sodium nanoclusters. *Science* **323**, 1323–1327. (doi:10.1126/science.1168080)
37. Cooper J, Zare RN. 1968 Erratum: angular distribution of photoelectrons. *J. Chem. Phys.* **49**, 4252. (doi:10.1063/1.1670761)
38. Bethe HA, Salpeter EE. 1977 *Quantum mechanics of one- and two-electron atoms*. New York, NY: Plenum Publishing Corporation.
39. Hertel IV, Schulz CP. 2015 *Atoms, molecules and optical physics 1*. Berlin, Germany: Springer.
40. Baltenkov AS, Manson ST, Msezane AZ. 2015 Jellium model potentials for the C_{60} molecule and the photoionization of endohedral atoms, A@C_{60}. *J. Phys. B* **48**, 185103. (doi:10.1088/0953-4075/48/18/185103)